Nano-rectennas for harnessing infrared energy

Thesis submitted in accordance with the requirements of the
University of Liverpool for the degree of Doctor in Philosophy
in the Faculty of Science and Engineering by

Serdar B. Tekin

June 2023

Department of Electrical Engineering and Electronics

Abstract

A significant effort has been invested in the research of self-biased rectenna (rectifying antenna) devices that are capable of rectifying very high frequency signal and can function without the aid of an external bias. The latter makes these nanostructures strong candidates for energy harvesting alternative to photovoltaic (PV) technology. The development of high frequency rectifier, which is capable of transforming infrared (IR) alternating-current (AC) radiation into usable direct-current (DC) electricity is the primary focus of the rectenna design. One of the most promising candidates as the rectifier in a rectenna device is known as metal-insulator-metal (MIM) diode, which has been given serious consideration. The ultra-fast quantum mechanical (QM) tunnelling mechanism of MIM diodes makes them suitable for high-frequency rectification applications.

Despite their potential, MIM tunnel rectifiers are currently exhibiting very low AC to DC power conversion efficiencies, much less than 1%. This is mainly due to the poor coupling efficiency (η_c) between the antenna and the diode components being limited by the diode's cut-off frequency (f_c). The cut-off frequency is determined by the R_dC_d time constant where capacitance (C_d) and the resistance (R_d) of the diode are inversely proportional. Then, the η_c is calculated from the resistances of the diode (R_d) and antenna ($R_a = \sim 100\ \Omega$) elements, along with the C_d at a specific angular frequency (ω). In order to overcome this trade-off, a careful metal/oxide barrier height engineering must be maintained while scaling down devices and reducing the insulator thickness to decrease the C_d and the R_d simultaneously.

In this thesis, various MIM diode combinations have been fabricated and tested using different metal (Au, Ti, Al, Zn and Cr) and oxide (Al_2O_3, Nb_2O_5, Ta_2O_5, ZnO, TiO_2 and NiO) combinations with the aim of optimising the MI^nM (n = 1, 2, 3) structures. Initially, tunnelling diodes with single (MIM) and triple insulator (MI^3M) configurations have been fabricated using atomic layer deposition (ALD), radio-frequency (RF) sputtering and shadow mask evaporation methods. ALD has offered excellent control of insulator film thickness and quality. The shadow mask patterning has also provided a fast and easy fabrication method for processing several MIM configurations. The key performance metrics of the diodes including zero-bias

dynamic resistance (R_0), zero-bias responsivity (β_0), asymmetry (η) and non-linearity (f_{NL}) have been determined from DC current voltage (I-V) measurements.

Single insulator Au/Al_2O_3/Ti and Au/Al_2O_3/Zn diodes displayed β_0 of -0.6 A/W and 1.6 A/W, respectively indicating that they can be employed for self-biased energy harvesting applications. Besides this, Au/ZnO/Au diode exhibited extremely low zero-bias dynamic resistance (R_0 = 540 Ω) compared to the Al_2O_3 based diodes with the same area (10^4 μm^2) which makes this insulator a potential candidate for THz operations. Furthermore, the effect of resonant tunnelling (RT) on the rectification performance of cascaded (Nb_2O_5/Ta_2O_5/Al_2O_3) and non-cascaded (Ta_2O_5/Nb_2O_5/Al_2O_3) triple insulator rectifiers has been demonstrated. The MI^3M rectifiers have shown state of the art low-voltage β of 4.3 A/W at 0.35 V and η of 6 at 0.1 V. The effect of RT was stronger at higher bias region where an η of ~120 was obtained beyond 1 V.

Variable angle spectroscopic ellipsometry (VASE) has been used during the fabrication process of the devices to measure the oxide thickness, observe the film quality and extract the optical constants (refractive index n, extinction coefficient k). Band gaps (E_g) of the deposited oxide layers have also been extracted using Tauc Lorentz method after finding the absorption coefficient (α), real (ε_1) and imaginary (ε_2) parts of the dielectric function with respect to the photon energy. The results of sub-band gap point by point VASE analysis show two ε_2 peaks, at 1.3 eV referring to hydrogen bridge defect (Si-H-Si) in the SiO_2 layers which corresponds to the oxygen (O_2) vacancies; and at 2.9 eV referring to the negatively charged O_2 vacancies intrinsic to the SiO_2/Si interface. The latter were found to correlate with the higher gate to source current on the actual devices. This study is a clear demonstration of point-by-point VASE analysis for understanding the defect related gate oxide behaviour of Si power MOSFETs.

Furthermore, the scaled MIM diodes based on TiO_2, ZnO and NiO thin films using photolithography and radio-frequency (RF) magnetron sputtering have been fabricated to further improve the η_c of the devices. The electron affinities of these oxides have been found from the combination of X-ray photoelectron spectroscopy (XPS), VASE measurement and then used to reliably model the I-V characteristics of the fabricated diodes. The impact of scaling the device area down to 1 μm^2 has been shown to be

crucial for enhancing the η_c. A Au/ZnO/Cr diode, having 1 μm^2 device area, showed the best rectification performance with a $R_0 = 71$ k Ω, $\beta_0 = 0.28$ A/W, and a projected $\eta_c = 2.4 \times 10^{-5}$ % for operation at 28.3 terahertz (THz).

The novelty of this thesis is that it presents experimentally enhanced performance metrics of the MIM tunnel rectifiers such as; reduced diode resistance, increased asymmetry and device responsivity by engineering the barriers, as well as improved diode coupling efficiency by scaling down the devices. Furthermore, a new process flow for fabricating nanometre (nm) scale rectenna devices using scanning probe thermal lithography tool has been proposed to develop more efficient devices at 28.3 THz.

Acknowledgments

First of all, I owe my primary supervisor Prof. Ivona Z. Mitrovic a great debt of gratitude for giving me the opportunity to work in this project and making my dreams come true. I am very thankful for all her guidance and support at every stage of my PhD, as well as her trust to give me responsibilities which improved my self-confidence and perspective. I am proud to work with her for all this time. I also would like to express my respect and appreciation to my secondary supervisor Prof. Steve Hall for all his advice to strengthen my work and proofreading my studies. As my other secondary supervisor, I would like to thank Prof. Paul Chalker from Materials Science and Engineering Department for providing me laboratory opportunities to support my work. I also would like to thank School of EEECS, University of Liverpool, UK for my PhD scholarship. Many thanks to all BOSE group members and our supervisors for helping me a lot over the past four years. In particular, I would like to thank; Dr Naser Sedghi for his contributions and all our discussions, Saeed Almalki, Harry Finch, Dr Ayendra Weerakkody and Dr Partha Das for their collaboration and contributions, Dr Zhongming Cao and Dr Siti Supardan for their support and sharing their experiences, Dr David Donaghy for managing our laboratory and his technical support. Also, special thanks to my colleagues and my friends Adeem Alshammari and Valentina Casadei for their friendship and encouragement during our PhDs. Additionally, I would like to thank; Prof Vin Dhanak from Stephenson Institute, for the XPS measurements and his collaboration, Dr Matthew Werner from Material Science and Engineering for fabricating my devices via ALD and his contribution to my publications, Dr Liam O'Brien from Physics and Dr Andrea Vezzoli from Chemistry departments for letting me use their laboratory facilities, Andreas Hemmetter from AMO, Germany and Nexperia semiconductor company for providing me samples and contributing to my studies. I am also very grateful to my former colleague Dr Evren Kaya and my MSc supervisor Prof Seref Kalem for their support and encouragement to start my PhD, I learnt a lot from them. Also, special thanks to Prof Manus Hayne from Lancaster University for providing me a new position in his research group by the end of my PhD and helping me to strengthen my future career. Finally, special thanks to my family for their continuous support, patience, and love. I wouldn't have come this far without them, and I am always proud of being their son and brother. Also, as another special member of my family, I would like to thank Gizem Acar for her warm heart, all her positive energy, endless support, and unconditional love. I am profoundly thankful for having you by my side.

Table of contents

4. Experimental methods………………………………..…..…100

5. Physical and electrical characterisation of metal oxide thin films………………………………………………………………..124

List of Figures

List of Tables

Abbreviations

Abs – Absolute

AC – Alternate current

ACNTC – Antenna-coupled nano-thermocouples

Al – Aluminium

Au – Gold

Al_2O_3 – Aluminium oxide

AlO_x – Native aluminium oxide

ALD – Atomic layer deposition

Ar – Argon

BE – Binding energy

C – Capacitance

CB – Conduction band

CBO – Conduction band offset

CV – Capacitance-voltage

Cr – Chromium

DC – Direct current

DIW – De-ionized water

DOS – Density of states

DT – Direct tunnelling

E_{QW} – Energy of the bound state in the quantum well

fs – femtosecond

FNT – Fowler-Nordheim tunnelling

IE – Ionisation Energy

IR – Infrared

IV – Current-voltage

KE – Kinetic energy

KK – Kramers-Kronig

MIG – metal-insulator-graphene

MIM – Metal-insulator-metal

MI^2M – Metal- insulator-insulator-metal

MI^3M – Metal-insulator-insulator-insulator-metal

MOSFET – Metal oxide semiconductor field effect transistor

MSE – Mean standard error

MW – Microwave

Nb – Niobium

Nb_2O_5 – Niobium oxide

Nb(OEt)5 – Niobium ethoxide

Ni – Nickel

NiO – Nickel oxide

PF – Poole-Frenkel

PR – Photoresist

PV – Photovoltaics

PVD – Physical vapour deposition

QM – Quantum mechanical

R_a – Dynamic resistance

R_d – Dynamic resistance

R_l – Load resistance

RF – Radio frequency

RT – Resonant tunnelling

SE – Schottky emission

SEM – Secondary electron microscopy

Si – Silicon

SMU – Semiconductor measurement unit

ST – Step tunnelling

Ta – Tantalum

TAT – Trap-assisted-tunnelling

Ta_2O_5 – Tantalum oxide

Ta(OEt)5 – Tantalum ethoxide

Ti – Titanium

TiO_2 – Titanium dioxide

TMA – try-methyl-aluminium

TWD – Travelling wage diode

UV – Ultraviolet

V_A – Alternating voltage

VASE – Variable angle spectroscopic Ellipsometry

VB – Valence band

VBM – Valence band maximum

V_{oc} – Open circuit voltage

WKB – Wentzel-Kramers-Brillouin

XPS – X-ray photoelectron spectroscopy

Zn – Zinc

ZnO – Zinc oxide

Publications and contributions

1. **S. B. Tekin**, P. Das, A. D. Weerakkody, N. Sedghi, S. Hall, I. Z. Mitrovic, P. R. Chalker, M. Werner, and J. S. Wrench, "Single and Triple Insulator Tunnel Rectifiers for Infrared Energy Harvesting," *2020 Joint International EUROSOI Workshop and International Conference on Ultimate Integration on Silicon (EUROSOI-ULIS)*, pp. 1-4, 2020, doi: 10.1109/EUROSOI-ULIS49407.2020.9365388 (Digital presentation)

2. **S. B. Tekin**, N. Sedghi, S. Hall, I. Z. Mitrovic, "Effect of Electron Affinity on ALD MI^{2}M Resonant Tunneling Rectifiers". *51st IEEE Semiconductor Interface Specialists Conference*, 2020. (Abstract) (Poster presentation)

3. **S. B. Tekin**, A. D. Weerakkody, N. Sedghi, S. Hall, M. Werner, J. S. Wrench, P. R. Chalker, and I. Z. Mitrovic, "Single and triple Insulator metal-insulator-metal diodes for infrared rectennas," *Solid-State Electronics*, vol. 185, p. 108096, 2021, doi: 10.1016/j.sse.2021.108096

4. S. Almalki, **S. B. Tekin**, N. Sedghi, S. Hall, and I. Z. Mitrovic, "Applicability of Sc_2O_3 versus Al_2O_3 In MIM RECTIFIERS for IR rectenna," *Solid-State Electronics*, vol. 184, p. 108082, 2021, doi: 10.1016/j.sse.2021.108082

5. I. Z. Mitrovic, S. Almalki, **S. B. Tekin**, N. Sedghi, P. R. Chalker, and S. Hall, "Oxides for Rectenna Technology," *Materials*, vol. 14, no. 18, p. 5218, 2021, doi: 10.3390/ma14185218

6. **S. B. Tekin**, S. Almalki, A. Vezzoli, L. O'Brien, S. Hall, P. R. Chalker, I. Z. Mitrovic Optimization of MIM Rectifiers for Terahertz Rectennas. *ECS Transactions. IOP Publishing*, vol 108, no. 69, p. 69, 2022, doi: 10.1149/10802.0069ecst (Digital presentation)

7. **S. B. Tekin**, S. Almalki, A. Vezzoli, L. O'Brien, S. Hall, P. R. Chalker, I. Z. Mitrovic, "Scaled MIM rectifiers for infrared rectennas". *UK Semiconductors 2022 Conference*, 2022. (Abstract) (Oral presentation)

8. **S.B. Tekin**, S. Almalki, H. Finch, A. Vezzoli, L. O'Brien, V.R. Dhanak, S. Hall, and I.Z. Mitrovic, "Electron affinity of metal oxide thin films of TiO2, ZnO and NiO and their applicability in 28.3 THz rectenna devices". The manuscript has been accepted for publication under Journal of Applied Physics after minor revision.

Chapter 1

1. Introduction

1.1 Motivation

At sea level, our planet receives about 1000 W/m^2 of sunlight when the sky is clear. Over 50% of this solar energy is primarily composed of infrared radiation (IR) [1]. Therefore, renewable energy sources are crucial components to achieve global zero-carbon economy goals in the future century. The development of sustainable energy technologies and materials has already seen a surge in study. The IR region, which spans the wavelengths of 1.5 to 20 µm, is the most significant spectrum because it is re-emitted by the earth's surface as IR radiation between 8 and 14 µm, with a peak emissivity at 10.6 µm, or in other words 28.3 THz as shown in Fig. 1.1 [2]. The current solar cell-based energy harvesting sources are unable to fully utilise this radiation. This is because only the energy from the visible spectrum (400 to 750 nm) of the sun has been captured using conventional photovoltaic (PV) technology. Moreover, IR radiation can be used to generate energy day or night, unlike solar panels, which are restricted by the amount of sunlight and weather conditions [1,3].

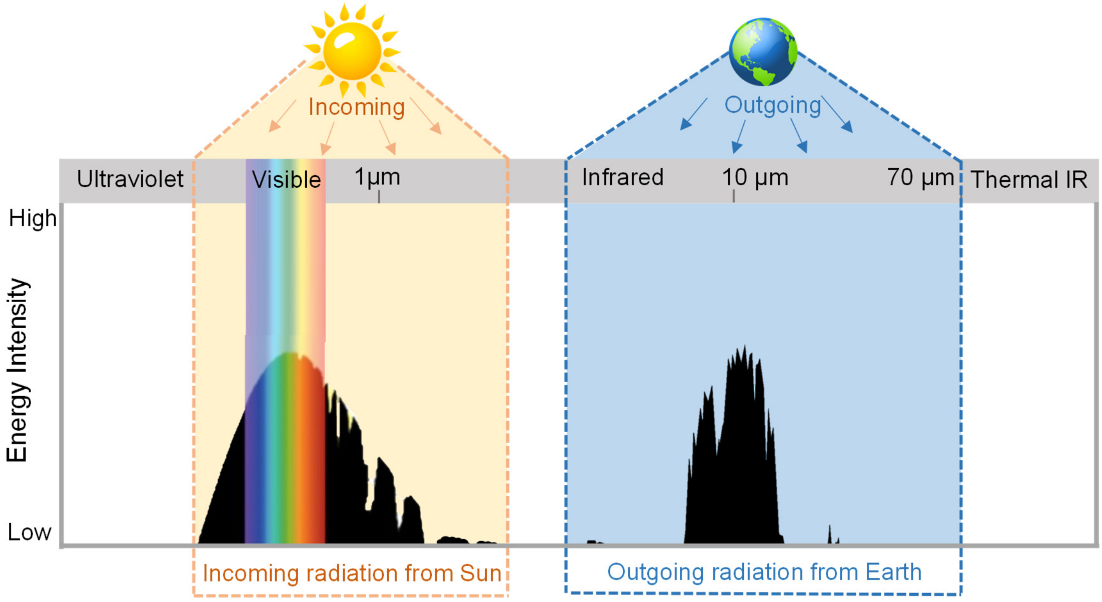

Figure 1.1. A simplified diagram of the incoming and outgoing atmospheric radiation [2].

Scientists have been intrigued by the concept of a rectifying antenna (rectenna) for many years due to its efficient design and functioning in the IR range [4,5]. Rectennas have the potential to theoretically achieve 100% conversion efficiency, which is a significant difference from PV technology where the band gap of the semiconductor is the limiting factor [3,6,7]. However, only the collection of energy at microwave (MW) and radio frequencies (RF) has been demonstrated to be successful (>85% conversion efficiency in MW frequencies) so far with the use of an antenna and rectifying diode [8]. The maximum up to date overall conversion efficiency at 28.3 THz have been obtained as ~ 10^{-8}% using MI^2M based nano-rectenna devices with a detectivity of ~10^5 Jones ($\mathrm{cm}\sqrt{\mathrm{Hz}}\mathrm{W}^{-1}$) [9]. On the other hand, the IR is abundant in the environment that is emitted by several heat sources such as sun, earth's surface, electronic devices and human body. Hence, IR energy harnessing can have various potential applications in different fields. One of these applications is capturing and converting thermal radiation or waste heat into usable electricity to reduce the energy consumption in several industries such as transportation, manufacturing or electronics [1]. Another potential application of rectennas can be their usage in wireless power transfer applications. They can be integrated with devices such as sensors and wearable electronics which makes it possible to harvest IR energy for powering these devices without any batteries or wired connections [10]. Also, they can be utilised in environmental sensing applications such as thermal imaging or non-contact temperature sensing by detecting and monitoring the temperature, heat distributions and thermal gradient parameters [11,12]. Internet of things (IoT) and autonomous systems can also be other application fields for nano-rectenna devices due to the growing need for compact and self-powered energy sources. Nano-rectennas can harvest energy from the ambient IR radiation, enabling long-term and sustainable operation of these devices without the need for frequent battery replacements. As a result, the rectenna technology is at the cutting edge of high-frequency electronics and nanophotonics applications, including IR and optical detectors [11,12], biosensors [10] and optical transceivers in communication systems [13].

Rectennas' ability to function at higher IR/THz frequencies has been limited by the absence of a diode nanostructure that can be coupled to antennas to work efficiently. The potential practical rectification mechanism relies on the quantum tunnelling effect of electrons with fast response times of the order of femtoseconds (fs). This idea is used in metal-insulator-insulator-metal (MIM) diodes, which need to be engineered for improved quantum mechanical (QM) tunnelling and reduced in size to nanometer scale for efficient THz operation. These devices can now be moved towards the THz regime owing to development of nanotechnology, which has enabled patterning down to the nanoscale.

The focus of this study is to enhance the diode architectures and provide a better understanding of their feasibility for integrating with rectenna systems. The objectives include specifying the technical requirements, improving the rectification capabilities of THz rectifiers, downsizing these devices to make a projected efficiency assumption and demonstrating the practicality of the rectenna technology at optical frequencies to open the way for energy harvesting from the re-emitted IR radiation by the earth's surface.

1.2 THz/IR nano-rectenna concept

Figure 1.2 shows the components of an optical rectenna array, comprising receiving nano-antennas and rectifying diodes. As mentioned in the previous section, a MIM diode has been regarded as a leading contender for the rectenna system, and it is the primary subject of this study.

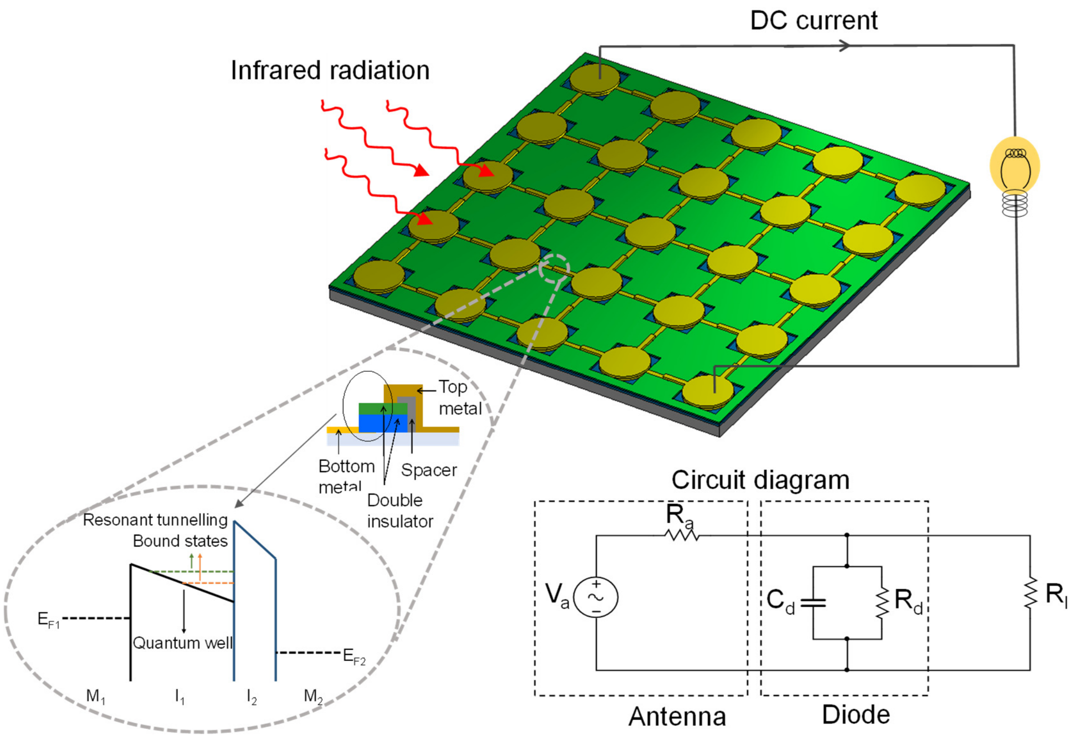

Figure 1.2. Schematic of a rectenna array and the equivalent circuit diagram of a single rectenna device [1].

The rectification process occurs by capturing the alternating-current (AC) electromagnetic (EM) signal by the antenna arms and converting into useful direct-current (DC) with the integrated MIM rectifier. Figure 1.2 also depicts a rectenna's simplified equivalent circuit. It consists of an alternating voltage source (V_a) with an associated antenna resistance (R_a) in series with the diode component composed of dynamic resistance (R_d) and diode capacitance (C_d) in parallel with the load resistance (R_l).

The resistance difference between the forward and reverse bias currents facilitates energy transfer via the diode rectifier. As a result, the incoming AC signal is transformed into a DC current. As explained by Moddel *et al.* [6], the overall rectenna efficiency can be estimated by

$$\eta = \eta_a \eta_s \eta_c \eta_j \tag{1.1}$$

where η_a is the coupling efficiency of incident EM radiation to the receiving antenna, η_s is the efficiency of collected energy in the diode-antenna junction, η_c is the power coupling efficiency between the diode and antenna, η_j is the diode rectifying efficiency which is determined by device responsivity (A/W). Responsivity represents the rectified DC current per incident radiation power [6].

It is possible to determine the power coupling efficiency (η_c) between the diode and the antenna at a specific angular frequency (ω) by

$$\eta_c = \frac{4\frac{R_a R_d}{(R_a+R_d)^2}}{1+\left[\omega\frac{R_a R_d}{(R_a+R_a)}C_d\right]^2} \tag{1.2}$$

where R_a and R_d are antenna and diode resistances, respectively and C_d is the diode capacitance. It is also important to note that the antenna reactance is assumed to be negligible in comparison to the diode reactance in this equation. However, at high frequencies (>1 THz), this effect can diminish the coupling efficiency by a factor of ~10 [14]. An impedance match between the diode and the antenna ($R_a = R_d$) is essential for a high power coupling efficiency. Low dynamic resistance and diode capacitance are necessary for efficient THz rectification. The cut-off frequency (f_c) can be calculated as

$$f_c = \frac{1}{2\pi R_d C_d} \tag{1.3}$$

According to Eqn. 1.4, fabricating an MIM diode with a small area (in nm scale) or utilizing a thick dielectric layer (in the range of a few nanometers) can reduce the diode capacitance,

$$C_d = \frac{A\varepsilon_r\varepsilon_o}{d} \tag{1.4}$$

where d is the thickness of the insulator, ε_r is dielectric permittivity, ε_o is permittivity of vacuum and A is the diode area. However, increasing the oxide thickness will result in a higher diode resistance, which reduces the probability of electrons to tunnel through a larger energy barrier. In other words, the insulator thickness should be in the region of a few nanometers to ensure that electron tunnelling dominates other parasitic conduction mechanisms. Therefore, the electrical properties of a diode are determined by the choice of materials for the metals and insulators, as well as by the thickness of the insulator.

The current responsivity (β_i) of a diode junction can also be used to express its efficiency (η_j) in the classical region. In the semi-classical approach, the quantum efficiency of the diode junction is denoted by β_i^{sc}. This phenomenon is explained by the photon-assisted tunneling (PAT) formulation, which is used to determine the response of a rectenna under illumination [15]. Therefore, the diode's rectification performance can be expressed as

$$\eta_j = V_D\beta_i^{sc} = \frac{V_D}{V_{ph}}\left[\frac{I_{dark}(V_D+V_{ph})-2I_{dark}(V_D)+I_{dark}(V_D-V_{ph})}{I_{dark}(V_D+V_{ph})-I_{dark}(V_D-V_{ph})}\right] \tag{1.5}$$

where V_D is the operating voltage, V_{ph} is the electric potential that corresponds to photon energy and I_{dark} is the diode's I-V characteristic in a dark environment. In the classical region, the β_i^{sc} is equal to the classical formulation of the responsivity ($I''(V)/I'(V)$) of a diode where I' and I'' are the first and second derivatives of the current [15]. Therefore, β_i^{sc} becomes closely related with the device asymmetry which is the ratio of the forward and reverse current. Hence, the overall diode efficiency is given by

$$\eta_{diode} = \eta_c \eta_j. \tag{1.6}$$

Having a self-biased rectenna that operates without any external bias, or a "zero-bias" is another crucial factor. Moreover, in order to increase the collected power to useful levels in practice, rectenna arrays are needed which result in more efficient output DC power. The key performance metrics of a MIM diode can be determined from its I-V characteristics. These are diode's dynamic resistance (R_d), responsivity (β), asymmetry (η_{asym} or η) and non-linearity (f_{NL}) [3,6,12,16]. The dynamic resistance, in other words, differential resistance (R_d) is calculated by differentiating the current with respect to applied bias voltage which is expressed as follows

$$R_d = \left[\frac{dI}{dV}\right]^{-1} \tag{1.7}$$

The rectification ability of a diode is indicated by its responsivity (β). In other words, it is the ratio of the DC current generated from the incident AC power on the diode and it is calculated by

$$\beta = \frac{1}{2}\frac{I''(V)}{I'(V)} \tag{1.8}$$

The absolute ratio of positive (I^+) to negative current (I^-), or vice versa, at a specific voltage, is defined as the asymmetry (η).

$$\eta = \frac{|I^+|}{|I^-|} \text{ or } \frac{|I^-|}{|I^+|} \tag{1.9}$$

Lastly, the device non-linearity (f_{NL}), measured as the ratio of static to dynamic resistances, is another critical MIM diode parameter as shown in Eqn. 1.10. Nonlinear DC I-V characteristics are necessary for efficient IR frequency rectification.

$$f_{NL} = \frac{dI/dV}{I/V} = \frac{V}{I} R_D \tag{1.10}$$

As the MIM diodes are aimed to be used as THz rectifiers, their rectification performance, especially the zero-bias dynamic resistance (R_0) and responsivity (β_0) are the focus of interest. The performance of the rectenna devices for IR energy harvesting can be enhanced by optimising the parameters provided by Eqns. (1.7)–(1.10) from the DC I–V characteristics of the MIM diodes.

1.3 Other emerging THz rectifiers

There are other alternative structures for THz energy harvesting besides the tunnel rectifiers such as plasmonic rectennas, Seebeck nano-antenna, graphene geometric and metal-insulator-graphene (MIG) based rectifiers. These different types are discussed in this section.

1.3.1 Plasmonic rectennas

One alternative candidate is known as plasmonic diode. Similar to the tunnel diodes, it consists of a metal-insulator-metal (MIM) where the diode acts as a waveguide to propagate light waves. In this structure, a MIM device is exposed to THz radiation, which stimulates oscillating electron waves on one of the metal electrodes, known as surface plasmons, as they move close to the metal's surface. As shown in Fig. 1.3 (a), upon the illumination, the incoming photons excite the electrons in the metal electrode to higher energy states (hot electrons) above the Fermi level and leave same number of holes (hot holes) behind. Then, the excited electrons accumulate at the metal-insulator interface.

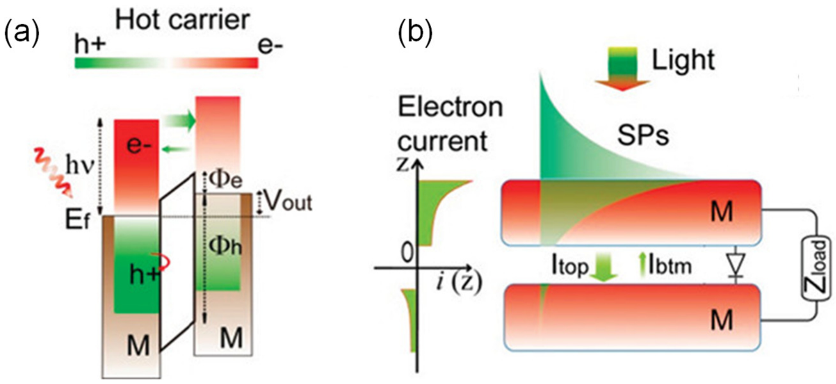

Figure 1.3. Basic schematics of energy conversion using hot electron injection. (a) Energy band diagram of the MIM diode showing the hot electron injection over the energy barrier. (b) A MIM diode under illumination having different hot electron density between the top and the bottom electrodes [17].

The absorption of the excited plasmons in the top metal produces a high density of hot electrons that can tunnel or inject over the barrier and generate current [17,18]. When the absorption in one electrode is greater than the other, the DC current is produced as shown in Fig. 1.3 (b). For an efficient energy conversion, the absorption needs to be confined only in one electrode [17].

A specific type of plasmonic rectenna is a travelling wave diode (TWD) rectenna that can be produced in the same manner as tunnel diodes by altering the design and the process flow. The difference between a classical lumped element (planar) diode and a TWD is shown in Fig. 1.4. A lumped element diode (Fig. 1.4 (a)), is placed between the feed points of the antenna patches and the signal flows through the diode uniformly via the propagation of the plasmonic waves between the patches. On the other hand, the TWD effectively functions as a rectifying transmission line for the surface plasmons. As shown in Fig. 1.4 (b), one side of the TWD element is placed between the antenna patches and the energy accumulates at the antenna's feed point when it is radiated by incident electromagnetic waves. Hence, a coupled surface plasmon is generated and propagates along with the MIM interface. There are two possible modes of propagations which are symmetric and antisymmetric. In order to operate in the IR region, the antisymmetric surface plasmon mode is used at the MIM interface. Therefore, the electron tunneling is provided by the electric field confinement in the insulator region which results in rectification [19].

Pelz *et al.* [19] developed a TWD made of double NiO/Nb_2O_5 insulators sandwiched between Ni and CrAu metals to show that the transmission line impedance can get beyond the constraints of traditional lumped element MIM diodes' RC time constants at optical frequencies.

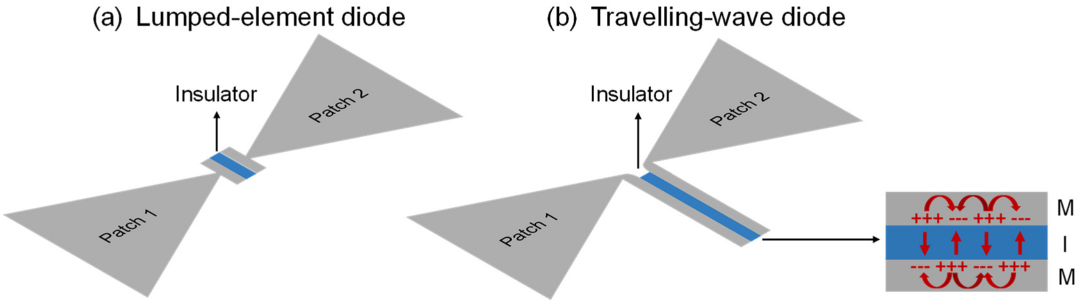

Figure 1.4. Basic schematics of (a) lumped element MIM rectenna, and (b) TWD with the transmission line between the bowtie antenna patches and the device cross-section showing the propagation of surface plasmons in an antisymmetric mode along the diode interface [19].

In the suggested method, the antenna excites a surface plasmon wave, which then travel down the extended MIM diode to produce a transmission line. As a result, the MIM diode rectifies the propagating wave. This TWD structure exhibited a peak response of 130 A/W and a detectivity of $D^* = 1.0 \times 10^4$ Jones ($\mathrm{cm}\sqrt{\mathrm{Hz}}\mathrm{W}^{-1}$) in the optical experiments which is a detector performance parameter and can be calculated by

$$D^* = \beta_{sys}\sqrt{A_{Abs}}\sqrt{R_d/4kT} \tag{1.11}$$

where β_{sys} represents the system responsivity which is the DC output current for an applied incident power, A_{Abs} represents the absorption area of the rectenna, R_d is the diode resistance, k stands for the Boltzmann's constant and T represents the temperature [19]. These structures have the advantage of enabling the use of even basic planar MIM devices as solar energy harvesters where the DC photocurrent is generated by the hot electrons in the MIM device as opposed to rectennas which need high-frequency rectification. In contrast to planar MIM diodes, the transmission line's input impedance determines the impedance of the device rather than the capacitance of the MIM diode. In other words, the capacitive lumped element MIM impedance is no longer present because the antenna is rather integrated with a rectifying transmission line, and the antenna perceives the input impedance of the transmission line. As a result, the coupling efficiency (η_c) calculated by Eqn. 1.2 no longer applies. The η_c of a TWD is determined by [20]

$$\eta_c = \frac{4R_{twd}R_a}{(R_{twd}+R_a)^2+(X_{twd}+X_a)^2} \tag{1.12}$$

where R_{twd} and X_{twd} represents the real and imaginary parts of the TWD's input impedance, while R_a and X_a are the real and imaginary parts of the antenna's impedance.

The efficiency of TWDs is currently lower than theoretically predicted values. Their performance is primarily constrained by the plasmonic decay caused by the increasing resistance of the metals at high frequencies.

1.3.2. Seebeck nano-antennas

Antenna integrated nano-thermocouple (ACNTC) rectifiers are being researched as an alternative to tunnel diode rectifiers because of their potential for infrared (IR) rectification through the Seebeck effect. The Seebeck effect is defined as the change in temperature between two electrical conductors that causes a voltage difference between the two materials. In several studies, it has been observed that there is a linear relationship between the Seebeck coefficients (response of a material to a temperature difference) of metals and the open circuit voltage (V_{oc}) induced by the temperature difference at the junction [21–28]. The V_{oc} can be expressed as

$$V_{oc} = (S_1 - S_2)(T_h - T_c) = \Delta S . \Delta T \tag{1.13}$$

where S_1 and S_2 represents the Seebeck coefficients of the conductors, while T_h and T_c are the temperatures of the hot and cold junctions [22,26].

There are several different Seebeck antenna and junction designs in the literature where the Seebeck effect was the dominant conduction mechanism rather than tunnelling. One example of basic Seebeck nano-antenna schematic composed of two different metals and a dipole antenna at the junction is shown in Fig. 1.5. In this design, the dipole antenna collects IR electromagnetic radiation, which then cause the current in the antenna to flow and heat the NTC's hot junction. The Seebeck effect is then used by the NTC to transform the heat produced by the dissipated antenna currents into detectable electric signals. The non-zero relative Seebeck coefficient (RSC) in NTCs is either caused by the intersection of metals having different absolute Seebeck coefficients or by cross-sectional discontinuity in single-metal thermocouples [26].

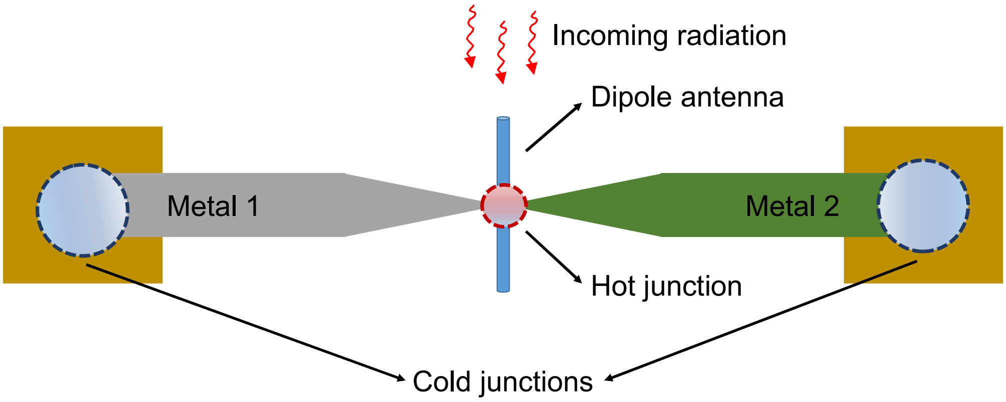

Figure 1.5. Basic schematic of a dipole ACNTC [26].

In terms of simplicity and cost effectivity, Seebeck nano-antennas are advantageous since they do not require any insulating layers. They can also be integrated into array structures. Bareiß *et al.* [22] demonstrated the Seebeck thermal effect at 28.3 THz on their fabricated individual and array type rectenna structures composed of Au and Ti metals using e-beam lithography and lift-off techniques. It was found that there was 5.8 mK average temperature difference between the junctions. Also, a constant correlation between the metals' Seebeck coefficient and the open-circuit voltage (V_{oc}), which is equal to the average temperature difference between the two junctions, was observed. The authors mentioned that the detected V_{oc} was relatively weak due to the small difference between the Seebeck coefficients of Au and Ti and can be improved using different metals with larger Seebeck coefficient difference.

Briones *et al.* [23] proposed a simulation based work on Seebeck nano-antennas in order to demonstrate the optical to electrical energy conversation in mid-IR range. They analysed two types of antenna structures which are square and Archimedean spiral antennas those are shown in Fig. 1.6. They used Ti and Ni metals due to the large difference in their Seebeck coefficients (S_{Ni} = -19.5 μV/K and S_{Ti} = 7.9 μV/K) at the interface and as well as low thermal conductivities (κ_{Ni}= 90 W/mK and κ_{Ti} = 21.9 W/mK) to optimize the thermal energy harvesting. The metals were located on a silicon oxide half-space to provide thermal insulation. Around 215 mK and 340 mK temperature difference with the corresponding generated low-voltage signals of 5.74 μV and 9.08 μV were reported for square and Archimedean spiral antennas, respectively. The estimated DC power and the total harvesting efficiency for the square antenna were reported as 1.7 aW and 4.8×10^{-7}%, while they were 4aW and 3.4×10^{-6}% for Archimedean spiral antenna.

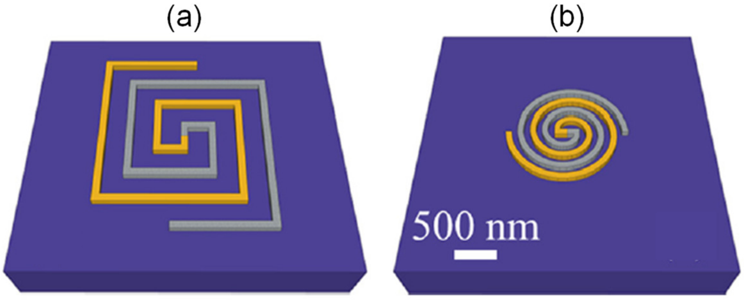

Figure 1.6. Schematic representations of the (a) square spiral and (b) Archimedean spiral Seebeck nano-antennas [23].

It was indicated that the response of the devices can be improved by decreasing the effective thermal conductivity of the substrate.

Russer *et al.* presented a comprehensive experimental and theoretical work on dipole antenna integrated single-metal nano-thermocouples (Fig. 1.7 (a)) for IR detection. They fabricated an array (Fig. 1.7(b)) of ACNTs using 50 nm to 200 Pd metal wire segments connected in series to increase the V_{oc}. A linearly polarised 10.6 µm CO_2 laser was used as the illumination source. They measured 0.86 µV/K relative Seebeck coefficient. Also, according to their simulations, nano-thermocouples could have picosecond response time being advantageous for THz detection [25].

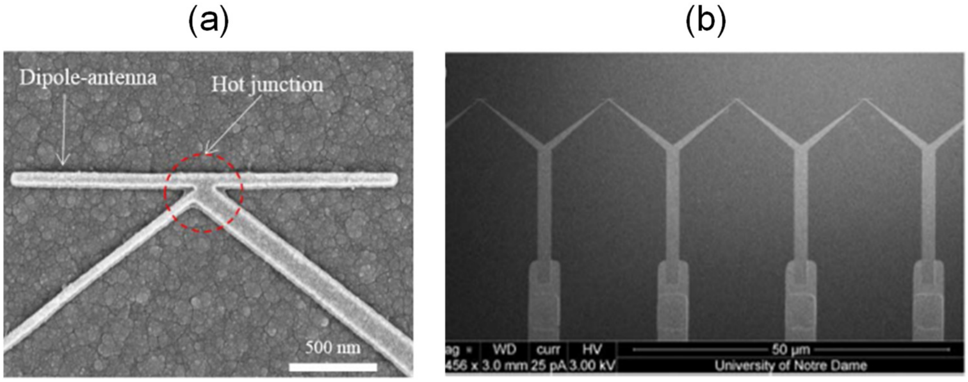

Figure 1.7. SEM image of the (a) single and (b) array from of the ACNTC structures [25].

Szakmany *et al*. [27] also fabricated single-metal ACNTCs integrated with two different primary and secondary dipole antennas over different cavities with the aim of detecting 28.3 THz frequency. The device schematics, as well as an SEM image of these structures are shown in Figs. 1.8 (a) and (b). The cavities were formed by etching the Si substrates using focused ion beam (FIB) with the aim of increasing the sensitivity of the ACNTC IR detectors. It was reported that the cavities prevent unwanted cooling of the hot junction by thermally separating the antenna and the substrate. Besides this, the detector sensitivity was substantially increased by the cavity design due to the constructive interference of the incoming radiation reflected back to the antenna. According to this study, the sensitivity of the ACNT IR detectors can be enhanced 2 orders of magnitude with these modifications.

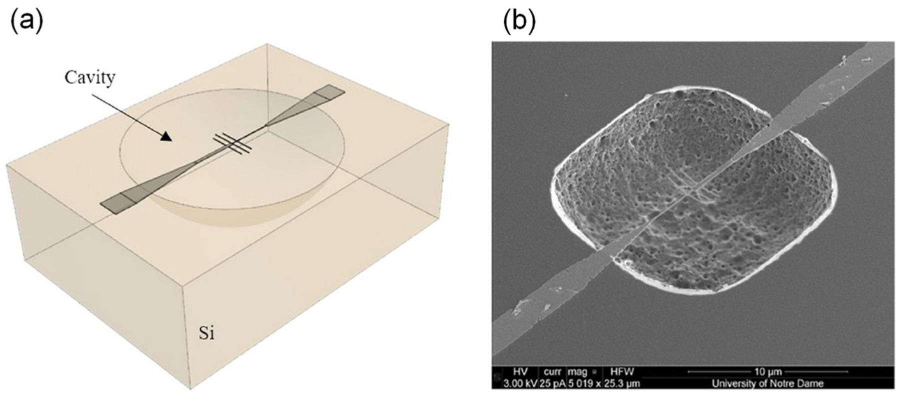

Figure 1.8. (a) Schematic representation, and (b) SEM image of the ACNTC structure with the cavity [27].

Several promising results have been obtained from the above mentioned studies. These include detecting a generated V_{oc} signal using the Seebeck effect as the conduction mechanism, increasing the temperature difference between the hot and cold junctions using materials having large Seebeck coefficient difference, designing different type of antenna structures to improve the efficiency of the incident radiation, and altering the substrate material to enhance the sensitivity. However, there are limiting factors such as the type of the antenna, material choice and thermal losses in the metals which requires further investigation of these structures.

1.3.3. Graphene geometric diodes

Graphene geometric diodes are another promising alternative for THz rectification due to their planar structure with low capacitance and higher tolerance to large power compared to MIM diodes. The resistance of these structures is also relatively low since the monolayer graphene is a highly conductive material. Therefore, the relatively low capacitance and resistance of the geometric diodes help to improve the impedance match between the antenna and the rectifier. It has been reported that the RC time constant of the geometric diodes can be lowered to 10^{-15} s which makes them promising for the THz operations [29].

The cross-section and the top view of a graphene geometric diode, proposed in Ref. [30], are shown in Fig. 1.9. In this kind of structure, similar to other proposed devices, a thermal oxide layer on the substrate material is used to ensure proper isolation and the uniformity of the devices. Then, the metal layers are patterned and deposited using lithography, deposition and lift-off techniques. After that, a graphene monolayer is grown on the metal electrodes and patterned by another set of nanolithography and etching steps as shown in Fig. 1.9 (a). The geometry of the graphene monolayer grown on the metal electrodes is shown in Fig. 1.9 (b). A funnel-like structure is seen on the left (forward) part of the graphene layer, whereas a straightforward rectangle is placed on the right (backward). The forward current is produced when charge carriers on the graphene layer travel forward and cross the neck's width. The vertical wall reflects these charge carriers on their way back, which causes the backward current to be substantially lower than the forward current. Therefore, the diode behavior and consequently the rectification ability is provided by the asymmetry between the forward and reverse currents.

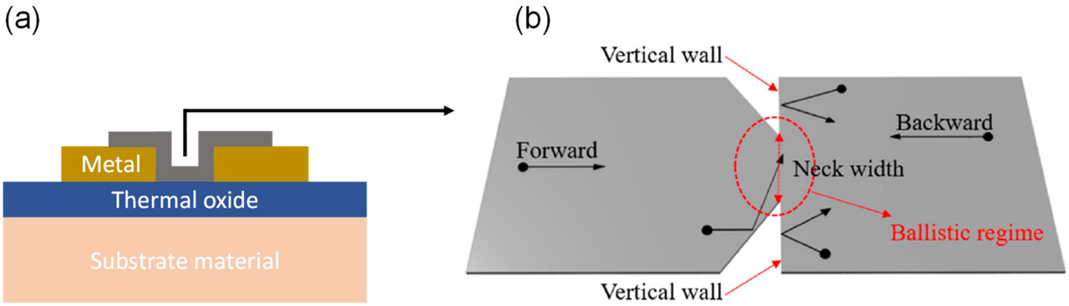

Figure 1.9. (a) Cross-section and (b) the top view of an example graphene geometric diode [30].

Wang *et al.* [30] presented a CVD grown monolayer graphene based geometric diode for THz rectenna applications with the aim of having reduced capacitance and resistance to increase the device cut-off frequency (f_c). They studied the effect of different neck widths on the device performance. The maximum β_0 and R_0 were obtained as 0.0628 A/W and ~5×10^3 Ω, respectively for the 50 nm neck width. According to the authors, this is the highest reported β_0 for the graphene geometric diodes which is still lower than more mature technologies. Compared to the conventional MIM diodes, the AC to DC rectification ability of geometric diodes depends on the asymmetric geometry of the graphene layer rather than the potential barriers and the device junction. In another study, Araby *et al.* [31] examined different types of graphene based diodes integrated with antennas for harvesting IR energy.

The performance of these devices may occasionally be constrained by the neck width, which is the narrowest point in the device and where the potential barrier is located. The efficiency of the charge transport depends particularly on the shape and size of the neck width. Fermi velocity is the speed of charge carriers (such electrons and holes) close to the material's Fermi level. In a graphene geometric diode, the charge carriers' behaviour in the presence of a potential barrier depends on their Fermi velocities and this can be another limiting factor for the performance of these structures. This is due to the fact that a high Fermi velocity increases the possbilitiy of charge carriers colliding with each other, or with the other defects, which could result in energy loss and lower efficiency. The MFP is the typical distance a charge carrier can travel before scattering when it collides with other impurities or defects. The increased probability of scattering, as the charge carriers pass through the device, can limit the efficiency of charge transport if the MFP length is relatively short compared to the neck width. As a result, the overall efficiency of the device is affected [30].

1.3.4. Metal-insulator-Graphene (MIG) based rectifiers

Another novel graphene based approach is the metal-insulator-graphene (MIG) diode for high frequency rectification. Hemmetter *et al.* [32], presented a one-dimensional (1D) MIG integrated rectenna composed of Ti/TiO_2/G layers on flexible polyimide film for THz detection as shown in Fig. 1.10. In this design, the graphene layer is encapsulated between the same type of oxide layers which works as an electrode. In a MIG design, a thin insulating layer is sandwiched between the graphene and a metal electrode. Therefore, the asymmetry of the device is determined by the difference between the electrical properties of the graphene and the metal layer. It is also mentioned that the reason of using TiO_2 as the insulating layer is the ease of depositing high quality TiO_2 layer by plasma enhanced atomic layer deposition (PE-ALD) on the graphene layer.

The effective junction area is given by the thickness of the graphene layer and the channel width. As an advantage of this structure, the capacitance is reduced by forming a 1D diode junction at the graphene edge which facilitates operation in THz frequency range.

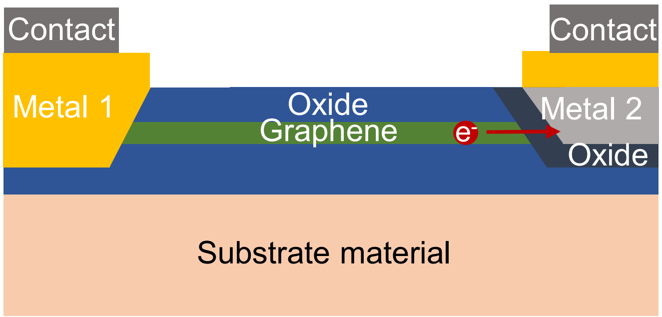

Figure 1.10. 1D-metal-insulator-graphene (MIG) diode [32].

The proposed device could operate up to 170 GHz frequency and exhibited a maximum responsivity of 80 V/W at 167 GHz with a noise equivalent power (NEP) of 80 pW/$\sqrt{Hz}$ in free space measurements under ambient conditions [32]. The NEP is calculated using the voltage noise (V_{noise}) and the responsivity (β_{THz}) at a specific frequency and expressed as

$$NEP = V_{noise}/\beta_{THz} \tag{1.14}$$

Compared to MIM diodes, the MIG devices exhibited a higher responsivity and reduced junction capacitance due to the 1D graphene channel. As another advantage, they can be fabricated on flexible substrates. However, the current optical tests have been done at a relatively low frequency of ~170 GHz. Further improvements in these devices is necessary to function effectively at 28.3 THz. This could be done by changing the oxide material, reducing its thickness or introducing multiple insulator structures instead of single oxide layer and replacing the top metal electrode. Thus, the MIG barriers may be engineered for having a better coupling efficiency at higher frequencies such as 28.3 THz.

1.3.5 Multiwall carbon nanotube (MWCNT) rectenna devices

Carbon nanotube tunnel diode arrays are another scalable contender for high frequency applications. As shown in Fig. 1.11, the device architecture consists of an array of vertically aligned multiwall carbon nanotubes (MWCNTs) coated with a thin insulating layer using ALD, followed by the top metal electrode deposition. At each MWCNT tip, a MWCNT-insulator-metal (MWCNT-I-M) structure is formed and the area of the tip determines the diode junction area. Considering the extremely small diameter of the CNTs (~10 nm), the diode area, consequently the capacitance can be dramatically reduced which is an advantage for the THz operations. On the other hand, the main constraint of these devices is the extremely high diode resistance.

According to the preliminary results, a single MWCNT-I-M exhibited a dynamic resistance of ~1TΩ, which is equal to an overall resistance of 7.5 kΩ cm^2 considering ~10^{10} diodes per area [33]. In another study, Shah *et al.* [34] managed to reduce the resistance down to 100 Ω cm^2 by altering the MWCNT tip junction, as well as using various top metal electrodes and reducing the insulator thickness.

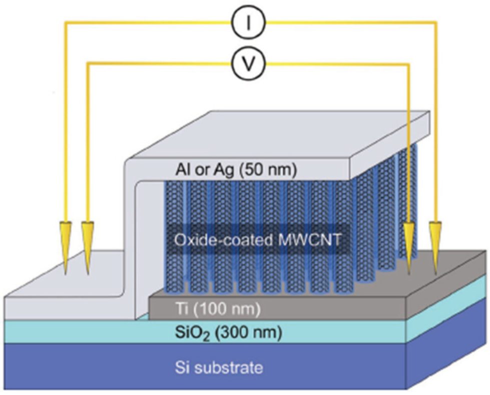

Figure 1.11. Device schematic of a MWCNT-I-M diode array [35].

Anderson *et al.* [35] presented a MWCNT-I-M tunnel diode using Al and Ag metals together with double-insulator Al_2O_3/HfO_2 layers to improve the diode performance metrics with the aid of resonant and step tunneling. The fabricated devices were tested using two different laser sources having wavelengths of 1064 nm and 638 nm which pass through a diffuser and generate stable illumination. A responsivity of 7.6 V/W was reported from the optical measurements which makes these devices a potential contender for photodetection applications. Additionally, they further reduced the dynamic resistance of these diodes ~75% compared to the previous structures.

In a more recent study [36], the performance metrics of the CNT based rectennas were aimed to further improve using a quad-insulator layer between the CNT and Al electrodes. The device schematics, SEM image of the structure and energy band alignment of the $Al_2O_3/ZrO_2/Al_2O_3/ZrO_2$ layers are shown in Fig. 1.12.

It was mentioned that the proposed quad-insulator structure has a more complex tunnelling behavior compared to double insulator structures and various conduction mechanisms can be seen at different biases. On the other hand, very high asymmetry

(η = 245 at 0.8 V), as well zero-bias responsivity (β_0 = 4.3 A/W) were obtained from the DC I-V measurements. However, the R_0 of the device was reported as 10^7 Ω cm^2 which is much higher than the previous configurations.

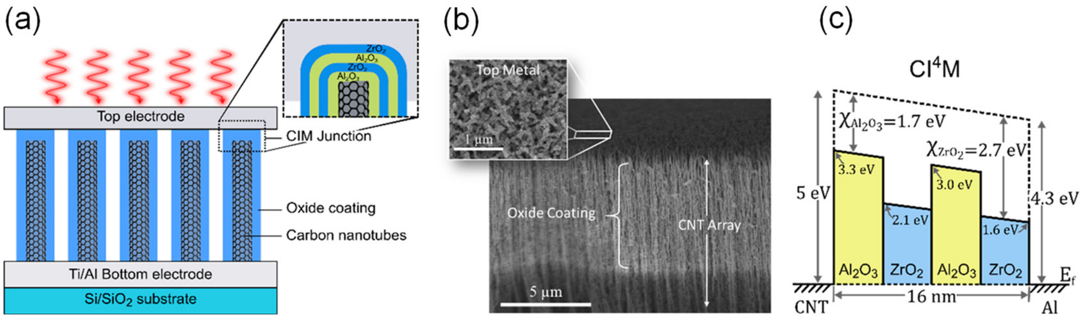

Figure1.12. (a) Schematic of CNT rectenna design, (b) SEM image of the CNT array structure, and (c) energy band diagram of the quad-insulator $Al_2O_3/ZrO_2/Al_2O_3/ZrO_2$ layers [36].

In the most recent study [37], they obtained 0.65 µA/W optical responsivity at 638 nm wavelength by altering the previous design. The process flow of this method is shown in Fig. 1.13. In the new structure, Polydimethylsiloxane (PDMS) and poly(3,4-ethylenedioxythiophene) polystyrene sulfonate (PEDOT:PSS) polymer layers act as the bottom and top electrodes, respectively. Also, a new combination of Al_2O_3-HfO_2-Al_2O_3-HfO_2 quad-insulator layers are sandwiched between these electrodes. However, it was mentioned that the R_0 of this structure is also too high which was around 0.1–1.0 MΩ cm^2.

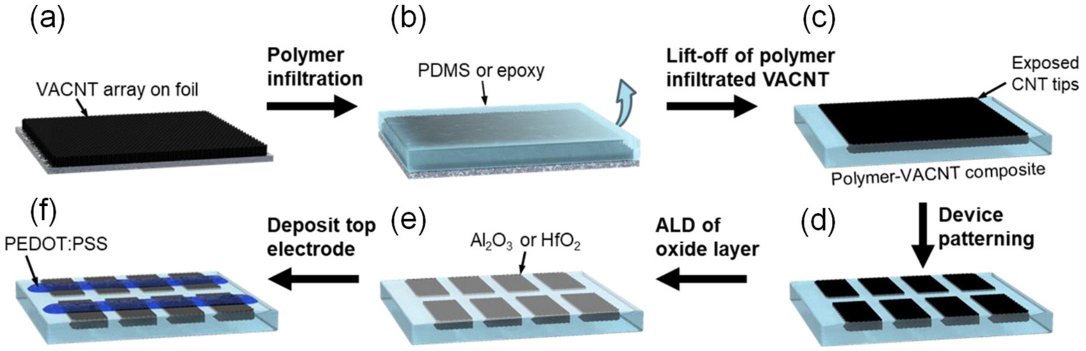

Figure 1.13. Process flow of CNT diodes showing (a) VACNT array on metal foil, (b) infiltration of VACNTs with polymer or epoxy, (c) removal of polymer infiltrated VACANT from foil, (d) device patterning, (e) oxide deposition, and (f) top electrode deposition [37].

The high zero-bias resistance of these structures seems to be the main challenge and must be improved to be able to operate at 28.3 THz frequency. Besides this, considering the manufacturing complexity of these structures, MIM tunnel diodes currently look more promising in terms of device performance and ease of fabrication.

It is evident from the number of research on the MIM tunnel rectifiers that despite being an emerging technology, it is more mature than the other THz rectifier types. Apart from this demand, current state-of-the art MIM diodes are more efficient in terms of rectification performance at 28.3 THz. Plasmonic diodes, such as TWD and graphene geometric diodes, are mainly attractive due the possibility of reducing the diode capacitance and the resistance to improve the coupling efficiency. For the TWDs, this is done by omitting the capacitive lumped element MIM structure and using the input impedance of the transmission line to have a better match with the antenna element. The best achieved DC rectification performance of R_0 = 380 Ω and β_0 = 0.46 A/W was obtained using a Ni/NiO/Nb_2O_5/CrAu TWD [19], but it is also mentioned that the overall performance of the rectenna is still suffering due to the poor absorption efficiency. Besides this, the primary factor that is limiting the efficiency of these devices is the plasmonic decay caused by the increasing resistance of the metals at high frequencies. Currently, the TWD efficiency is less than the theoretical predictions.

Graphene geometric diodes are also aiming to improve the impedance match, as well as to increase the RC time constant by taking the advantage of the graphene properties. This is because the resistance of these structures is relatively low due to the high conductivity of the graphene layer. The highest achieved β_0 was found to be 0.0628 A/W with a R_0 of ~5 kΩ [30] where the β_0 is considerably lower than the values obtained using MIM diodes. Another disadvantage of these devices is the fabrication complexity which needs additional graphene growth techniques such as chemical vapour deposition (CVD).

Another graphene-based technology is the 1D MIG diode. Similar to the TWD and graphene geometric diodes, this structure has the benefit of lower capacitance that facilitates operations in the THz frequency range by creating a 1D diode junction at the graphene edge. The maximum reported β_0 of 80 V/W was obtained from the optical measurements at 167 GHz using a Ti/TiO_2/G diode stack [32]. Although this is a very high responsivity, the cut-off frequency of the device still has to be improved to operate at 28.3 THz.

As another alternative, ACNTCs are being investigated due to their potential to generate DC current utilising the Seebeck effect between two different electrical conductors. As they do not need any insulating layers, ACNTCs are advantageous in terms of cost effectivity and ease of fabrication. The antenna type, material choice and thermal losses are the limiting factors of the ACNTCs. There are several studies focused on designing the most efficient antenna structures, fabricating arrays and optimising the thermal energy conversion using metals having a larger Seebeck coefficient difference. However, the obtained results are not yet comparable with the MIM diode's performance metrics.

Finally, MWCNT rectenna is another emerging type that consists of a MWCNT-insulator-metal (MWCNT-I-M) diode structure. These structures aim to reduce the diode capacitance using CNTs having very small diameters (~10 nm) as the bottom electrodes. However, they currently suffer with very high diode resistances which is a critical disadvantage for THz operations. For the above-mentioned reasons, as the most promising type, MIM tunnel rectifiers are the main scope of this thesis.

1.3 Thesis outline

The motivation of this thesis is to study the performance of several MIM tunnel rectifiers to pave the way for IR energy harvesting by developing optimised nano-rectenna devices. In this scope, a background information of THz/IR nano-rectennas has been given with the explanation of the main performance metrics of MIM diodes in Chapter 1. Besides the tunnel rectifiers, several other emerging nano-rectenna structures including plasmonic, Seebeck, graphene geometric, MIG and MWCNT based rectennas have been introduced and their performance metrics were compared with the MIM diodes. The outline of the thesis is as follows.

Chapter 2 reports a detailed literature review on the MI^{n}M diodes including typical materials used in the diode fabrication, a comparison of state-of-the-art devices in the literature and several design considerations of the THz rectifiers.

In Chapter 3, typical conduction mechanisms in MIM diodes are studied including; Schottky emission (SE), Poole-Frenkel emission (PF), direct tunnelling (DT), Fowler-Nordheim tunnelling (FNT), Resonant tunnelling (RT) and Step tunnelling (ST). In addition, the working principles of an in-house MATLAB model that has been used to generate the current voltage (I-V) characteristics of MI^nM diodes, as well as to observe the RT states are explained. Lastly, a circular patch dipole antenna design and simulations for 28.3 THz frequency in CST Studio software are presented.

Chapter 4 describes the experimental methods used in this work which includes the details of material deposition, device patterning via shadow mask and photolithography processes, and the characterisation methods; (i) Variable Angle Spectroscopic Ellipsometry (VASE), (ii) X-ray photoelectron spectroscopy (XPS), and (iii) current voltage (I-V) electrical characterisation.

In Chapter 5, a sub-band gap analysis has been done on thermal SiO_2/Si wafers with the aim of observing potential defects in SiO_2 gate oxide layers for Si power MOSFETs. Besides this, VASE measurements have been used to measure the thickness, film uniformity, optical constants, as well as the band gap (E_g) of RF sputtered thin films. Moreover, a VASE analysis has been done on TiO_2 thin films prepared using plasma-enhanced (PE) and thermal atomic layer deposition (ALD). The extracted band gaps have been compared with the sputtered TiO_2 films in this work. XPS measurements have also been performed on the sputtered metal oxide thin films to understand the film quality, stoichiometry and to extract their electron affinities (χ). Additionally, possibility of Poole-Frenkel (PF) and Schottky Emission (SE) conduction mechanisms have been checked in Al_2O_3 based MIM rectifiers to find the dominant conduction mechanism in the MIM diodes.

Chapter 6 demonstrates novel single (MIM) and triple (MI^3M) metal-insulator-metal diodes fabricated by shadow mask evaporation, atomic layer deposition (ALD) and radio-frequency (RF) sputtering. Several insulators (Al_2O_3, ZnO, Ta_2O_5, Nb_2O_5) have been studied in different MI^nM configurations. In addition, the resonant tunnelling was observed in MI^3M structures and modelled using the in-house simulation tool. The fabricated MI^3M devices show state-of-the-art rectification parameters and are the best published to date.

Chapter 7 presents the feasibility of three metal oxide thin films (TiO_2, ZnO, and NiO) to be integrated in rectennas operating at 28.3 THz. The obtained physical characterisation parameters were used in fitting the experimental I-V data and used to make a reliable assessment of the MIM diode performance in an IR rectenna. A projected coupling efficiency at 28.3 THz of 2.4×10^{-5} % has been demonstrated for ZnO based MIM rectifier which is 6 orders of magnitude higher than in previously demonstrated state-of-the-art ZnO based devices.

In Chapter 8, a summary of this thesis is given with future research suggestions on how to further optimize the MIM structures for an efficient THz rectenna operation. This includes the process flow of how to fabricate nano-scale rectennas via an advanced nano-fabrication tool (NanoFrazor) which is a thermal scanning probe lithography technique.

References

[1] I. Z. Mitrovic, S. Almalki, S. B. Tekin, N. Sedghi, P. R. Chalker, and S. Hall, "Oxides for Rectenna Technology," *Materials*, vol. 14, no. 18, p. 5218, 2021, doi: 10.3390/ma14185218.

[2] N. O. A. A. US Department of Commerce, "The Atmospheric Window," NOAA's National Weather Service, 2019. [Online]. Available: https://www.weather.gov/jetstream/absorb.

[3] S. Hall, I. Z. Mitrovic, N. Sedghi, Y. C. Shen, Y. Huang, and J. F. Ralph, "Energy Harvesting Using THz Electronics," *Functional Nanomaterials and Devices for Electronics, Sensors and Energy Harvesting*, pp. 241–265, 2014, doi: 10.1007/978-3-319-08804-4_12.

[4] R. L. Bailey, "A Proposed New Concept for a Solar-Energy Converter," *Journal of Engineering for Power*, vol. 94, no. 2, pp. 73–77, 1972, doi: 10.1115/1.3445660.

[5] B. Berland, "Photovoltaic Technologies Beyond the Horizon: Optical Rectenna Solar Cell, Final Report, 1 August 2001-30 September 2002 (Technical Report) | OSTI.GOV," *Photovoltaic Technologies Beyond the Horizon: Optical Rectenna Solar*

Cell, Final Report, 1 August 2001-30 September 2002 (Technical Report) | OSTI.GOV, 2003. https://www.osti.gov/biblio/15003607.

[6] G. Moddel, “Will Rectenna Solar Cells Be Practical?,” *Will Rectenna Solar Cells Be Practical? | Springer*, 2013.

[7] D. K. Kotter, S. D. Novack, W. D. Slafer, and P. J. Pinhero, “Theory and Manufacturing Processes of Solar Nanoantenna Electromagnetic Collectors,” *Journal of Solar Energy Engineering*, vol. 132, no. 1, 2010, doi: 10.1115/1.4000577.

[8] W. C. Brown, "Optimization of the Efficiency and Other Properties of the Rectenna Element," *1976 IEEE-MTT-S International Microwave Symposium*, 1976, pp. 142-144, doi: 10.1109/MWSYM.1976.1123673.

[9] A. Weerakkody, A. Belkadi, and G. Moddel, “Nonstoichiometric Nanolayered Ni/NiO/Al2O3/CrAu Metal–Insulator–Metal Infrared Rectenna,” *ACS Applied Nano Materials*, vol. 4, no. 3, pp. 2470–2475, 2021, doi: 10.1021/acsanm.0c03012.

[10] A. Kausar, A. Reza, T. Latef, M. Ullah, and M. Karim, “Optical Nano Antennas: State of the Art, Scope and Challenges as a Biosensor Along with Human Exposure to Nano-Toxicology,” *Sensors*, vol. 15, no. 4, pp. 8787–8831, 2015, doi: 10.3390/s150408787.

[11] M. N. Gadalla, M. Abdel-Rahman, and A. Shamim, “Design, Optimization and Fabrication of a 28.3 THz Nano-Rectenna for Infrared Detection and Rectification,” *Scientific Reports*, vol. 4, no. 1, 2014, doi: 10.1038/srep04270.

[12] G. Jayaswal, A. Belkadi, A. Meredov, B. Pelz, G. Moddel, and A. Shamim, “Optical rectification through an Al2O3 based MIM passive rectenna at 28.3 THz,” *Materials Today Energy*, vol. 7, pp. 1–9, 2018, doi: 10.1016/j.mtener.2017.11.002.

[13] I. E. Hashem, N. H. Rafat and E. A. Soliman, "Nanocrescent antenna as a transceiver for optical communication systems," 2014 IEEE International Symposium on Electromagnetic Compatibility (EMC), 2014, pp. 39-45, doi: 10.1109/ISEMC.2014.6898940.

[14] A. Belkadi, A. Weerakkody, and G. Moddel, “Demonstration of resonant tunneling effects in metal-double-insulator-metal (MI2M) diodes,” *Nature Communications*, vol. 12, no. 1, 2021, doi: 10.1038/s41467-021-23182-0.

[15] D. Matsuura, M. Shimizu, and H. Yugami, “High-current density and high-asymmetry MIIM diode based on oxygen-non-stoichiometry controlled homointerface structure for optical rectenna,” *Scientific Reports*, vol. 9, no. 1, 2019, doi: 10.1038/s41598-019-55898-x.

[16] P. Maraghechi, A. Foroughi-Abari, K. Cadien, and A. Y. Elezzabi, “Enhanced rectifying response from metal-insulator-insulator-metal junctions,” *Applied Physics Letters*, vol. 99, no. 25, p. 253503, 2011, doi: 10.1063/1.3671071.

[17] F. Wang and N. A. Melosh, “Plasmonic Energy Collection through Hot Carrier Extraction,” *Nano Letters*, vol. 11, no. 12, pp. 5426–5430, 2011, doi: 10.1021/nl203196z.

[18] Y. Abate, R. E. Marvel, J. I. Ziegler, S. Gamage, M. H. Javani, M. I. Stockman, and R. F. Haglund , “Control of plasmonic nanoantennas by reversible metal-insulator transition,” *Scientific Reports*, vol. 5, no. 1, 2015, doi: 10.1038/srep13997.

[19] B. Pelz and G. Moddel, “Demonstration of distributed capacitance compensation in a metal-insulator-metal infrared rectenna incorporating a traveling-wave diode,” *Journal of Applied Physics*, vol. 125, no. 23, p. 234502, 2019, doi: 10.1063/1.5083155.

[20] B. Pelz, M. Armanious, and G. Moddel, “Effects of transmission line geometry on traveling-wave metal-insulator-metal rectenna infrared detectors,” *Journal of Applied Physics*, vol. 126, no. 6, p. 064503, Aug. 2019, doi: 10.1063/1.5083154.

[21] M. Bareiß, B. N. Tiwari, A. Hochmeister, G. Jegert, U. Zschieschang, H. Klauk, B. Fabel, G. Scarpa, G. Koblmuller, G. H. Bernstein, W. Porod, and P. Lugli, "Nano Antenna Array for Terahertz Detection," in IEEE Transactions on Microwave Theory and Techniques, vol. 59, no. 10, pp. 2751-2757, 2011, doi: 10.1109/TMTT.2011.2160200.

[22] M. Bareiß, P. M. Krenz, G. P. Szakmany, B. N. Tiwari, D. Kalblein, A. O. Orlov, G. H. Bernstein, G. Scarpa, B. Fabel, U. Zschieschang, H. Klauk, W. Porod, and P. Lugli, “Rectennas Revisited,” *IEEE Transactions on Nanotechnology*, vol. 12, no. 6, pp. 1144–1150, 2013, doi: 10.1109/tnano.2013.2281373.

[23] E. Briones, J. Briones, A. Cuadrado, J. C. Martinez-Anton, S. McMurtry, M. Hehn, F. Montaigne, J. Alda, and F. J. Gonzalez, “Seebeck nanoantennas for solar energy harvesting,” *Applied Physics Letters*, vol. 105, no. 9, p. 093108, 2014, doi: 10.1063/1.4895028.

[24] B. Mora-Ventura, R. Díaz de León, G. García-Torales, J. L. Flores, J. Alda, and F. J. González, “Responsivity and resonant properties of dipole, bowtie, and spiral Seebeck nanoantennas,” *Journal of Photonics for Energy*, vol. 6, no. 2, p. 024501, 2016, doi: 10.1117/1.jpe.6.024501.

[25] J. A. Russer, C. Jirauschek, G. P. Szakmany, A. O. Orlov, G. H. Bernstein, W. Porod, P. Lugli, and P. Russer, "Antenna-coupled terahertz thermocouples," *2015 IEEE MTT-S International Microwave Symposium*, 2015, pp. 1-4, doi: 10.1109/MWSYM.2015.7166943.

[26] G. P. Szakmany, l. O. Orlov, G. H. Bernstein and W. Porod, "Recent development of antenna-coupled thermocouples," *2015 IEEE 15th International Conference on Nanotechnology (IEEE-NANO)*, 2015, pp. 592-595, doi: 10.1109/NANO.2015.7388673.

[27] G. P. Szakmany, A. O. Orlov, G. H. Bernstein, and W. Porod, “Cavity-Backed Antenna-Coupled Nanothermocouples,” *Scientific Reports*, vol. 9, no. 1, 2019, doi: 10.1038/s41598-019-46072-4.

[28] G. P. Szakmany, A. O. Orlov, G. H. Bernstein and W. Porod, "THz Wave Detection by Antenna-Coupled Nanoscale Thermoelectric Converters," *IEEE Transactions on Terahertz Science and Technology*, vol. 7, no. 5, pp. 582-585, 2017, doi: 10.1109/TTHZ.2017.2715420.

[29] Z. Zhu, S. Joshi, S. Grover, and G. Moddel, “Graphene geometric diodes for terahertz rectennas,” *Journal of Physics D: Applied Physics*, vol. 46, no. 18, p. 185101, Apr. 2013, doi: 10.1088/0022-3727/46/18/185101.

[30] H. Wang, G. Jayaswal, G. Deokar, J. Stearns, P. M. Costa, G. Moddel, and A. Shamim, “CVD-Grown Monolayer Graphene-Based Geometric Diode for THz Rectennas,” *Nanomaterials*, vol. 11, no. 8, p. 1986, Aug. 2021, doi: 10.3390/nano11081986.

[31] H. A. El-Araby, H. A. Malhat and S. H. Zainud-Deen, "Performance of nanoantenna-coupled geometric diode with infrared radiation," *2017 34th National Radio Science Conference (NRSC)*, 2017, pp. 15-21, doi: 10.1109/NRSC.2017.7893471.

[32] A. Hemmetter, X. Yang, Z. Wang, M. Otto, B. Uzlu, M. Andree, U. Pfeiffer, A. Vorobiev, J. Stake, M. C. Lemme, and D. Neumaier, “Terahertz Rectennas on Flexible Substrates Based on One-Dimensional Metal–Insulator–Graphene Diodes,” *ACS Applied Electronic Materials*, vol. 3, no. 9, pp. 3747–3753, Aug. 2021, doi: 10.1021/acsaelm.1c00134.

[33] A. Sharma, V. Singh, T. L. Bougher, and B. A. Cola, “A carbon nanotube optical rectenna,” *Nature Nanotechnology*, vol. 10, no. 12, pp. 1027–1032, Sep. 2015, doi: 10.1038/nnano.2015.220.

[34] E. H. Shah, B. Brown, and B. A. Cola, “A Study of Electrical Resistance in Carbon Nanotube–Insulator–Metal Diode Arrays for Optical Rectenna,” *IEEE Transactions on Nanotechnology*, vol. 16, no. 2, pp. 230–238, Mar. 2017, doi: 10.1109/tnano.2017.2656066.

[35] E. C. Anderson, T. L. Bougher, and B. A. Cola, “High Performance Multiwall Carbon Nanotube–Insulator–Metal Tunnel Diode Arrays for Optical Rectification,” *Advanced Electronic Materials*, vol. 4, no. 3, p. 1700446, Jan. 2018, doi: 10.1002/aelm.201700446.

[36] E. C. Anderson and B. A. Cola, “Photon-Assisted Tunneling in Carbon Nanotube Optical Rectennas: Characterization and Modeling,” *ACS Applied Electronic Materials*, vol. 1, no. 5, pp. 692–700, Apr. 2019, doi: 10.1021/acsaelm.9b00058.

[37] E. C. Anderson, A. P. Patel, J. J. Preston, and B. A. Cola, “Tunneling diodes based on polymer infiltrated vertically aligned carbon nanotube forests,” *Nanotechnology*, vol. 31, no. 40, p. 405202, Jul. 2020, doi: 10.1088/1361-6528/ab9bd6.

Chapter 2

2. Literature review on MI^{n}M (n = 1, 2, 3) rectifiers

2.1 Material selection and design considerations

The first and the fundamental step of engineering MIM diodes and optimizing these structures is to choose the correct material combinations since the electrical characteristics of a diode are controlled by the choice of materials for both the insulator and the metal. A review of oxides and metals commonly used for MIM diode fabrication is presented in section 2.1 in detail. Then, the state-of-the-art MI^{n}M devices in the literature have been listed with their associated performance metrics in section 2.2. Lastly, the design considerations, as well as the challenges in fabrication of these devices have been explained together with efficiency predictions. The outcomes of this chapter have been presented in the review paper by Mitrovic *et al.* [1] in *Materials* 2021, *14*(18), 5218, and I have contributed to the paper as a corresponding author.

2.1.1 Typical oxides used in MIM diodes

The band gaps of typical oxides used in the design and fabrication of MIM diodes are shown in Fig. 2.1.

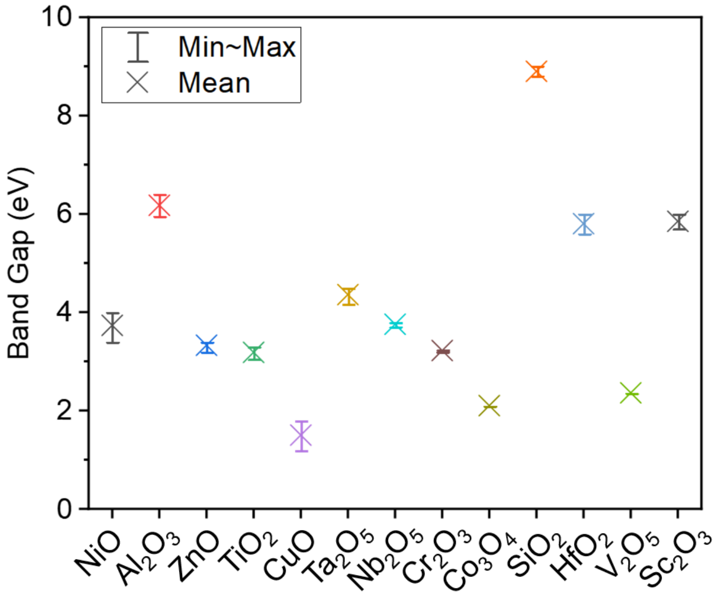

Figure 2.1. (a) Band gaps of typical oxides for MIM diodes. Full details are provided in Table 2.1 [1].

Table 2.1 also includes a complete set of information regarding the material properties. It has been observed that the reported measured values of the oxide band gap (Table 2.1) depend on the stoichiometry and structural characteristics (amorphous, crystalline, and polycrystalline) of films made using various deposition processes.

As shown in Table 2.1, amorphous Al_2O_3 thin films made by atomic layer deposition (ALD) [2] or molecular beam epitaxy [3] have a band gap of about 6.4 eV, but non-stoichiometric AlO_x deposited by radio frequency (RF) sputtering has a narrower band gap of 5.95 eV [4]. Another example is that the band gap of crystalline NiO was reported as 4.0 eV [5], however a more recent work measured a band gap of 3.4 eV for a 2 nm plasma oxidized NiO film [4]. It is also important to note that the variation of ±0.25 eV in the band gap values reported in Table 2.1 may also be caused by tolerances in using various characterization techniques; for example, for Ta_2O_5, 4.2 eV from ultraviolet-visible (UV-vis) absorbance spectra [6] as opposed to 4.4 eV measured by reflection electron energy loss spectroscopy [2] or variable angle spectroscopic ellipsometry [7].

Similar to the band gap analysis, a range of electron affinity (χ) values of the oxides commonly used in MIM diode fabrication are compared in Fig. 2.2 and the detailed reported values are summarized in Table 2.1.

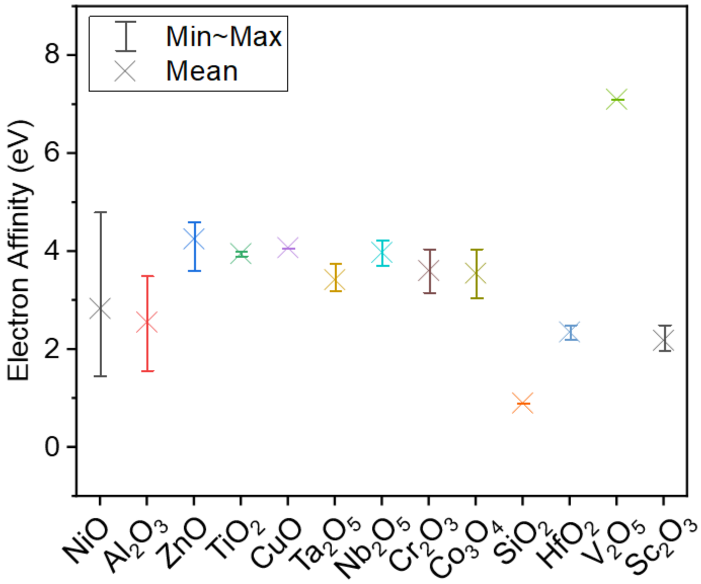

Figure 2.2. (a) Electron affinities of typical oxides for MIM diodes. Full details are provided in Table 2.1 [1].

It is important to keep in mind that the wide variability in published values for the electron affinities of Al_2O_3, NiO, ZnO, Co_3O_4, and Cr_2O_3 are likely due to the variations in fabrication conditions, as well as the measurement methods. For example, in comparison to previously published results on similarly fabricated NiO-based MIM diodes, a recent study [4] demonstrates a scaled (0.025 μm^2, Ni/~1.5 nm NiO/CrAu) MIM diode with a significantly lower R_0 ~ 630 Ω and a β_0 of 0.41 A/W, where the oxide is prepared by plasma oxidation. However, a comparable structure with a significantly larger area (1.45 μm^2, Ni/3 nm NiO/Cr) processed by Krishnan *et al.* [8], where the oxide is again grown by plasma oxidation, exhibited an R_0 of 500 kΩ. Another similar structure (Ni/NiO/Ni) was fabricated by Choi *et al.* [9] with a 4 nm thick plasma oxidised NiO layer and a highly reduced device area of 0.018 μm^2. The measured R_0 of this diode is 42.4 MΩ which is ~4 orders of magnitude larger than the one in Ref. [4] with a comparable β_0 of 0.41 A/W. In one of our recent studies [10], we also fabricated a NiO based MIM diode (CrAu/~6.8 nm NiO/CrAu) having 1 μm^2 device area where the oxide was RF sputtered. The resulting R_0 has been measured as 461 kΩ which is in agreement with the observed values in Ref. [8], while β_0 was found to be relatively improved to 0.76 A/W. The details of these results are explained in Chapter 7. The extremely low R_0 in Ref. [4] has been attributed to the very small barriers between the Ni/NiO (0.1 eV) and CrAu/NiO (0.07 eV) interfaces by finding these values from the simulated I-V curves of the MIM diodes using the hypothetical band diagram values in order to match the experimental I-V results. According to the theoretical I-V curve in Ref. [4], NiO has an χ of 4.8 eV, however in Ref. [11], a similar NiO film grown by plasma oxidation has an estimated χ of 2.05 eV.

Despite the fact that this method is frequently used in the literature, it results in a wide range of values for the metal/oxide barrier heights that conflict with those obtained from the physical characterisation of the related thin films, making it challenging to interpret the results. According to the other data that has been generated [12,13] using ultraviolet photoelectron spectroscopy (UPS) and X-ray photoemission spectroscopy (XPS) techniques, NiO's χ has been found to be 1.46 eV for the oxidised pure Ni targets with a laser vaporization cluster source [25], whereas for as-deposited NiO_x the χ has been measured as 2.1 eV [26]. These results unequivocally show that the electron affinity, as well as the band gap of NiO can vary depending on the surface treatment and the measurement method.

This uncertainty in the material properties of most common oxide contenders has been studied in the scope of this thesis. Depending on the surface conditions, changes in the work function and the electron affinity can be >1 eV for metals and semiconductors. It was mentioned by Weerakkody *et al.* [4] that the formation of electronic dipoles at the surface is most likely to be responsible for these variations, which alter the minimal energy required for an electron to leave the sample.

Table 2.1. Physical properties of metals and oxides: work function, electron affinity and band gap.

Metal	**Work Function (eV)**	**Oxide**	**Electron Affinity, χ (eV)**	**Band Gap, E_g (eV)**
Ni	4.9 [14,15], 4.99 [16], 5.04–5.35 [17]	NiO	1.46 [12], 2.05 [13], 3.0 [18], 4.8 [4]	3.4 [4], 3.8 [18], 4.0 [5]
Co	4.00 [14], 4.8 [16], 5.00 [19]	Al_2O_3	1.57 [20], 2.58 [21], 3.50 [22]	5.95 [4], 6.4 [3,23]
Ag	4.26 [20,24], 4.33 [15], 4.7 [14]	ZnO	3.6-3.7 [25], 4.3–4.5 [6], 4.6 [18]	3.2 [26], 3.38 [6], 3.4 [18]
Cu	4.5 [14,15], 4.63 [16], 4.65 [24]	TiO_2	3.9 [18,27]	3.05 [27], 3.2 [18], 3.3 [28]
Au	4.8 [14], 5.1 [24], 5.28 [15]	CuO	4.07 [29]	1.2–1.8 [30]
Al	4.2 [14,31], 4.28 [20,24]	Ta_2O_5	3.2 [27], 3.3 [18], 3.54 [20,32] 3.75 [6]	4.17 [6], 4.4 [2,27], 4.45 [7]
W	4.5 [14,33], 4.8 [16]	Nb_2O_5	3.72 [20], 4.23 [23]	3.71 [7], 3.8 [2]
Mo	4.2 [14], 4.4 [16], 4.6 [24]	Cr_2O_3	3.16–4.05 [23]	3.2 [34], 3.24 [35]
Zn	4.3 [14,24]	Co_3O_4	3.05–4.05 [36]	2.10 [37]
Pd	5.0 [14], 5.12 [15]	SiO_2	0.9 [18,27]	8.8 [2], 9.0 [18]
Pt	5.3 [14], 5.65 [24]	HfO_2	2.2 [18], 2.25	5.6 [2], 6.0 [27]
Cr	4.0 [16], 4.4 [14], 4.5 [24]	V_2O_5	7.1 [38]	2.36 [39]
Ta	4.1[14,16], 4.25 [24]	Sc_2O_3	2.06 [40], 1.98–2.5 [41]	5.7–6.0 [40]
Nb	4.1 [1], 4.3 [24]	-	-	-
V	4.44 [42]	-	-	-
Ti	3.7 [16], 4.1 [14], 4.33 [24]	-	-	-

2.1.2 Typical metals used in MIM diodes

Figure 2.3 and Table 2.1 display a variety of typical metals that have been employed in the manufacturing of MIM diodes together with the work function values that have been reported in the literature.

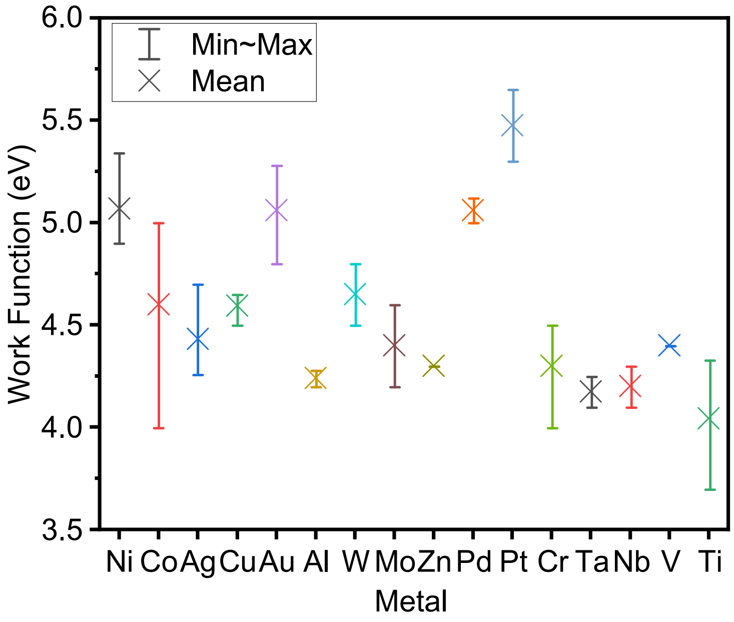

Figure 2.3. Work functions for typical metals used in a rectenna [1].

Co, Cr, and Ti have the lowest values, while a wide variety of values have been reported, particularly for the first two metals. In addition, ZCAN (ZrCuAlNi) and $TiAl_3$ [23,31,43] metallic thin films having multiple components, as well as conductive oxides such as indium tin oxide (ITO) and $SrRuO_3$ (SRO) and nitrides including TiN and NbN [44] can also function as electrodes in MIM diodes.

Another factor is that, metal conductivity decreases at THz frequencies. Therefore, the skin effect should be taken into account while fabricating rectennas for THz rectification. Equation. 2.1 is used to compute the skin depth (δ) for any metal [1]. To retain good conductivity in the metal at a high-frequency regime, the thickness of the metal should be ~ 5 times the skin depth value,

$$\delta = (\rho/\pi f \mu_o \mu_r)^{1/2} \tag{2.1}$$

where ρ is the metal's resistivity, μ_r is the metal's relative magnetic permeability, μ_o is the vacuum's magnetic permeability, and f is the frequency of operation.

As shown in Fig. 2.4, the δ for typically metals utilised in rectennas that can function at 28.3 THz were determined using ρ and μ_r reported in Refs. [21-26]. It is obvious that Ni has the lowest δ value, and some of the earliest rectennas have been demonstrated using NiO based diodes integrated with Ni Bowtie antennas [45,46].

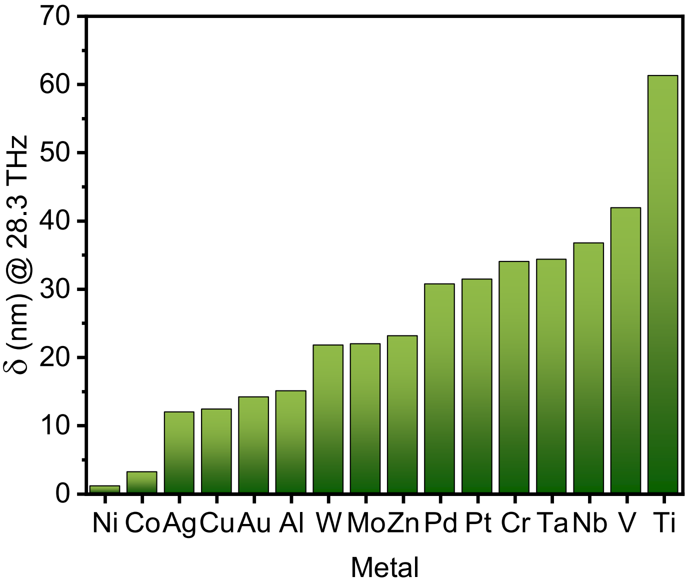

Figure 2.4. Skin depths of typical metals to operate at 28.3 THz [1].

However, compared to the challenges in MIM rectifiers, δ can be considered as a minor issue to overcome. This could be done by depositing an extra metal layer on the antenna regions suitable for specific frequencies to reduce the effect of the δ.

2.2 State-of-the-art devices

In order to provide readers a better idea regarding the applicability of MIM diodes in IR nano-rectennas, this section provides an overview of DC rectification parameters in single, double, and triple insulator MIM configurations.

2.2.1. Single insulator MIM diodes

As shown in Fig. 2.5, numerous MIM diodes with various metal/oxide combinations have been fabricated and tested. The details of these diodes including the material selection, fabrication methods, device combinations, oxide thicknesses, device areas and the performance metrics are also summarized in Table 2.2. As seen in Fig. 2.5 and Table 2.2, NiO and Al_2O_3 based devices have attracted the most research attention.

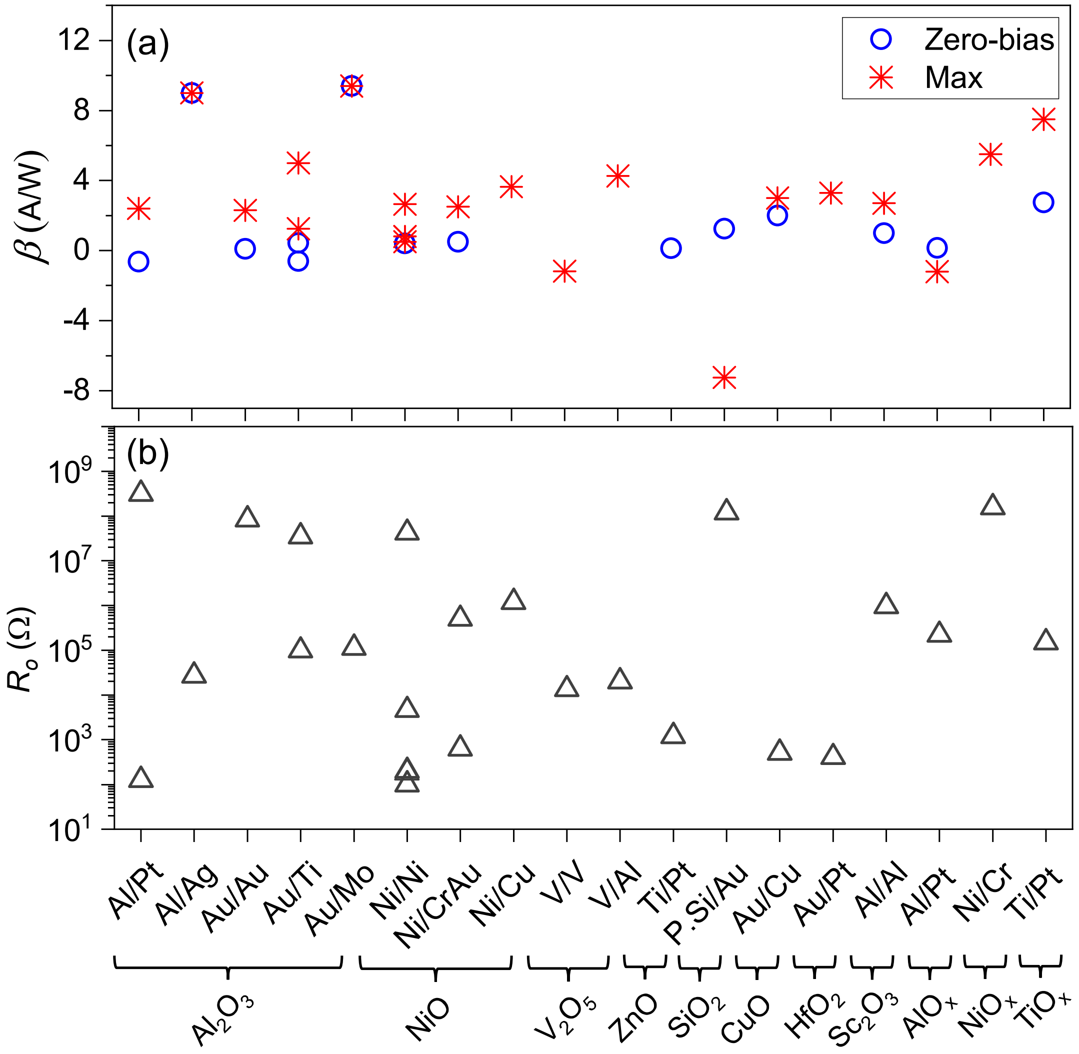

Figure 2.5. (a) Responsivity and (b) dynamic resistance for various MIM diodes. Full details are summarized in Table 2.2 [1].

Proof-of-concept studies by Wilke *et al.* [45] and Fumeaux *et al.* [46] initially demonstrated how to fabricate highly scaled diodes having 0.056 μm^2 and 0.012 μm^2 device areas, respectively based on NiO and integrated with dipole, bowtie, and spiral antennas. The electron microscope images of these three different structures are shown in Fig. 2.6. Despite the fact that they made the first demonstration of the operation of thin-film diodes as rectifiers at 28 THz radiation, there were problems with efficiency and reproducibility of the fabrication process in addition to low device responsivities.

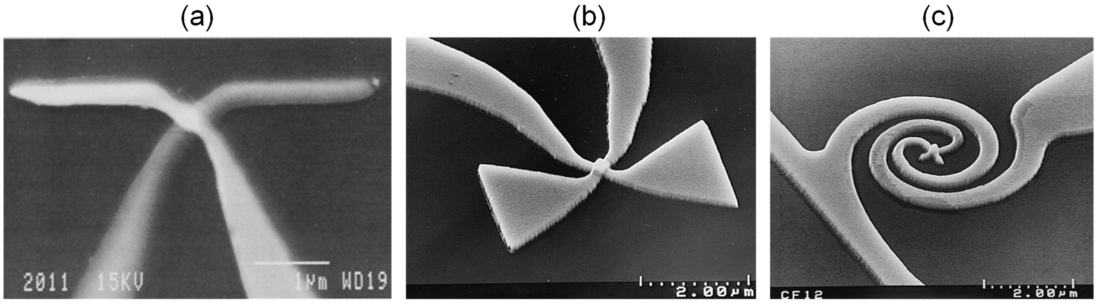

Figure 2.6. Electron microscope images of (a) dipole, (b) bowtie and (c) spiral rectenna structures [45,46].

In a later study, waveguide-integrated near-IR detectors composed of a multilayer Ni/Au stacks and NiO insulating layers were fabricated by Hobbs *et al.* [47] and achieved enhanced responsivity, as well as improved quantum efficiency ~6%. Choi *et al.* [9] used the geometric field enhancement method in a Ni/NiO/Ni based rectenna to reduce tunnelling resistance and increase the amplitude of the output AC signal. This diode's responsivity was higher than what had previously been reported. Several other metals including Ag [48], Pt [49], CrAu [8,50], Cu [51], and Mo [11] have also been used to fabricate NiO-based diodes. Ni/CrAu electrodes were used to produce a very sensitive diode by Krishnan *et al.* [8] that had a 1.45 μm^2 device area. The devices exhibited a β_{max} of 2.5 A/W at 0.1 V and a R_0 of 500 kΩ. Zhang *et al.* [51] produced diodes with a scaled device area of 0.008 μm^2 by combining Ni/Cu nanorods as electrodes and thermally oxidized 2-12 nm NiO which resulted in a β_{max} of 3.65 A/W at 0.1 V, but also a very high R_0 of 1.2 MΩ. The schematic representation of this Ni/NiO/Cu diode fabrication process on the anodic aluminum oxide (AAO) substrates including metal electrodeposition and native oxidation are shown in Fig. 2.7.

In another study [48], it was shown that the β_{max} could be improved up to 4.25 A/W using the same deposition method for 6 nm NiO and replacing Ni/Cu with Ni/Ag electrodes. When Ni/Mo electrodes were combined with plasma oxidized NiO thin films on flexible substrates, Kaur *et al.* [11] observed that the dynamic resistance can be decreased to 6 kΩ. As another approach, Ni/NiO/Au diodes prepared using Langmuir-Blodgett technique have been reported to exhibit extremely high sensitivity ($S = 2\times\beta$) of 35 V^{-1} and resistivity of 100 at 0.6 V [52]; however, zero-bias values of these devices were not reported.

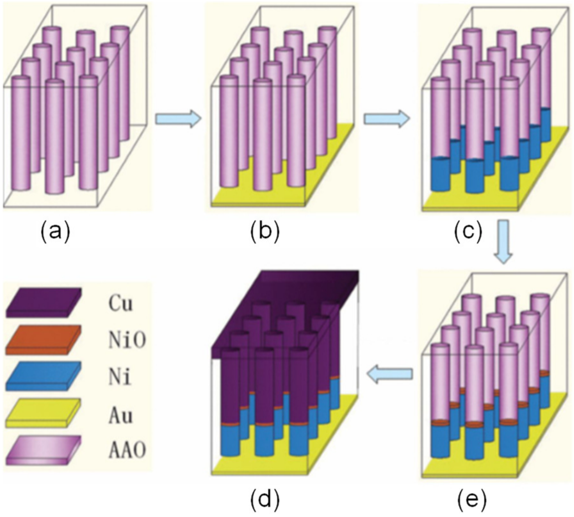

Figure 2.7. Fabrication steps of MIM diodes including (a) AAO substrate, (b) Au layer deposition, (c) Ni electrode deposition, (d) NiO native oxidation and (e) Cu electrode deposition [51].

The best performance with the single insulator based diodes was demonstrated by Weerakkody *et al.* [4] utilizing Ni/~1.5 nm NiO/CrAu configuration with a device area of 0.025 µm^2. They reported a η_c of 0.29% due to a much lower R_0 (~630 Ω) in contrast to previously observed values on comparable diodes which was also mentioned in section 2.1.1.

As reported in Table 2.2, another oxide candidate for THz energy harvesting applications is Al_2O_3. A slot-antenna with integrated Al/Al_2O_3/Pt diode has been shown by Kinzel *et al.* [53] having a R_0 of 124.6 Ω. A dipole antenna-coupled, Al/Al_2O_3/Pt based detector processed with electron beam (e-beam) lithography and shadow mask evaporation was developed by Bean *et al.* [54]. The specific detectivity of this device (2.15×10^6 cmHz$^{1/2}$W^{-1}) at 28.3 THz radiation was found to be higher than the performance of an IR detector based on Ni/NiO/Ni (1×10^6 cmHz$^{1/2}$W^{-1}) [55]. Table 2.2 shows the summary of the device area, oxide thickness, and deposition method for state-of-the-art MIM diodes as well as their rectification properties.

Table 2.2. List of the rectification parameters for state-of-the-art MIM diodes, including the device area, oxide thickness, and deposition method.

Oxides	**Metals**	β_0 **(A/W)**	β_{MAX} **(A/W)**	R_0 **(Ω)**	η	**Area (μm²)**	**Thickness (nm)**	**Deposition Technique**
NiO	Ni/Ni [45]	-	0.8	200	-	0.056	3.3	Sputtering
	Ni/Ni [46]	-	-	100	-	0.012	~3.5	Sputtering
	Ni/Ni [55]	-	0.825	180	-	0.075	3.5	Sputtering
	Ni/Ni [58]	-	0.5	~4.6 k	-	0.01192	2.5	Plasma oxidation
	Ni/Ni [9]	–0.41	–2.65	42 M	-	0.018	<4	Plasma oxidation
	Ni/Au [59]	2.8	4.56	-	-	0.64	2.2	Plasma oxidation
	Ni/Au [52]	-	17.5	-	22 at 0.6 V	4.4×10^{-5}	2.6–4.2	Langmuir-Blodgett
	Ni/Ag [48]	2.9	4.25	-	4.7 at 1.0 V	3.1×10^{-4}	6	Thermal oxidation
	Ni/Pt [49]	–1.5	–6.5	-	-	0.075	1–2	Native oxidation
	Ni/CrAu [8]	0.5	2.5	500 k	-	1.45	~3	Plasma oxidation
	Ni/CrAu [50]	-	-	-	6 at 0.2 V	100	5.5	Plasma oxidation
	Ni/CrAu [4]	0.41	-	629	-	0.025	~1.5	Plasma oxidation
	Ni/Cu [51]	-	3.65	1.2 M	-	0.008	12	Thermal oxidation
	Ni/Mo [11]	-	-	6 k	-	-	2.4	Plasma oxidation
Al_2O_3	Al/Al [49]	0.05	–0.7	-	-	-	1–2	Controlled oxidation
	Al/Ni [49]	0.25	0.5	-	-	-	1–2	Controlled oxidation
	Al/Ti [49]	0.3	1.0	-	-	-	1–2	Controlled oxidation
	Al/Pt [49]	0.5	0.65	-	-	-	1–2	Controlled oxidation
	Al/Pt [60]	0.5	2.25	-	-	0.0025	2–2.5	Controlled oxidation
	Al/Pt [54]	–0.64	2.4	312 M	-	0.004	1–2.5	O_2 exposure
	Al/Pt [53]	-	-	125	-	-	1–2	O_2 exposure
	Al/Ag [56]	9.0	9.0	27 k	1.2 at 0.6 V	1,760,000	-	Plasma oxidation
	Au/Mo [57]	9.4	9.4	113 k	-	1.0	~6	Sputtering
	Au/Au [61]	0.1	2.3	83 M	1.3 at 1.2 V	10,000	3	ALD
	Au/Ti [22]	0.44	1.25	98 k	-	0.04 *	1.5	ALD
	Au/Ti [61]	–0.6	5	35 M	1.7 at 1.5 V	10,000	3	ALD
AlO_x	Al/Gr [62]	-	-	600	2500 at 1 V	-	~3	Thermal oxidation
	Al/Pt [63]	~0.15	–1.2	~220 k	-	0.0056 *	~2 nm	O_2 exposure
TiO_x	Ti/Pt [64]	2.75	7.5	~150 k	-	-	-	Plasma oxidation
	Gr/Ti [65]	-	-	-	9000 at 1 V	12	-	Thermal oxidation
NiO_x	Ni/Cr [66]	-	5.5	157 M		400	7	Sputtering
ZnO	Ti/Pt [67]	0.125	-	1.2 k	-	90,000	4	ALD
	AuCr/Ni [68]	-	16	-	12 at 0.78 V	100	~4	Langmuir-Blodgett
V_2O_5	V/Al [42]	-	4.26	20 k	-	4.0	3	Sputtering
	V/V [69]	-	–1.18	13.4 k	-	4.0	1.45	Sputtering
SiO_2	PolySi/Au [70]	~1.25	–7.25	120 M	5 at 0.4 V	0.35	1.38	Boiling water oxidation
	PolySi/PolySi [71]	~1.5	–15.5	-	-	6×10^{-5}	-	Boiling water oxidation
Nb_2O_5	Nb/Pt [72]	-	10	-	1500 at 0.5 V	45,239 *	15	Anodic oxidation
	Nb/Pt [73]	-	8.45	-	7700 at 0.5 V	6400 *	15	Anodic oxidation
CuO	Au/Cu [74]	2.0	3.0	500	-	0.004489	0.7	ALD
TiO_2	Ti/Pd [11]	-	-	100 k	-	-	3	Plasma oxidation
Cr_2O_3	Au/Cr [75]	-	4.0	-	-	-	5	Electron beam evaporation
HfO_2	Au/Pt [76]	-	3.29	405	-	4.0	6	ALD
Sc_2O_3	Al/Al [77]	1.0	2.7	960 k	1.3 at 1.2 V	10,000	3	Sputtering

* Device area calculated based on stated dimensions.

Among the Al_2O_3 based MIMs, the Al/Ag [56] and Au/Mo [57] metal electrodes provided the maximum observed β_0 of ~ 9 A/W. A bowtie nano-antenna paired with an Au/Al_2O_3/Ti diode was utilized by Jayaswal *et al.* [22] to develop a 28.3 THz rectenna. The bowtie rectenna composed the Al_2O_3 layer sandwiched between the Au and Ti antenna patches, as well as the device cross-section are shown in Fig. 2.8. They achieved an overall efficiency of 2.05×10^{-14} with a β_0 of 0.44 A/W and a R_0 of 98 kΩ.

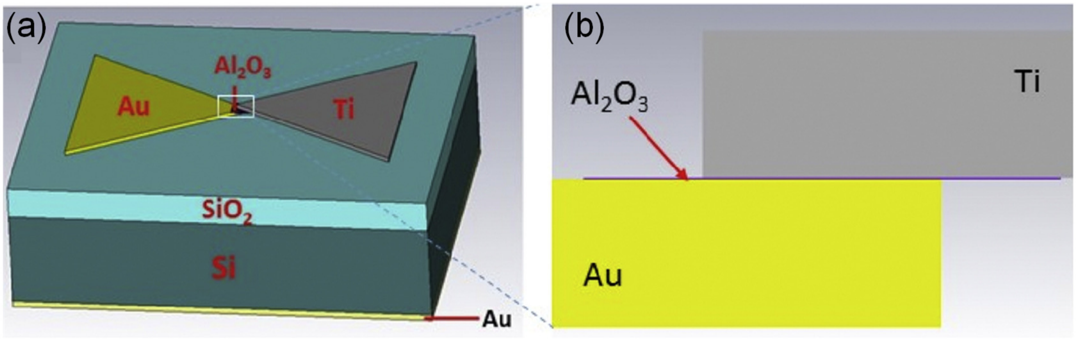

Figure 2.8. (a) 3D image of the fabricated MIM diode integrated rectenna, and (b) the device cross-section [22].

Several studies of non-stoichiometric MIMs based on AlO_x [62,63], TiO_x [64,65], and NiO_x [66] have been done, and in these studies, the fabrication parameters have been modified to control the oxide thickness and, as a result, to improve the performance metrics such as higher β_0 and lower R_0. Shirawastava *et al.* [62] obtained an extremely high asymmetry ($\eta = 2500$) and low R_0 using graphene (Gr) based Al/AlOx/Gr diodes. Also, an Al/AlOx/Pt diode coupled to a dipole antenna has been shown to have an IR detectivity of 9.65×10^6 cmHz$^{1/2}$W^{-1} [63].

Other oxides, including ZnO [67,68], V_2O_5 [55,69], SiO_2 [70,71], Nb_2O_5 [72,73], CuO [74], TiO_2 [11], Cr_2O_3 [75], HfO_2 [76], and Sc_2O_3 [77], have also been studied for utilising in THz MIM rectifiers. Fabrication of planar-type MIM tunnelling diodes has been facilitated using e-beam lithography and boiling water oxidation methods, resulting in high diode sensitivity of -31 V^{-1} for Poly Si/PolySi [71] and 14.5 V^{-1} for PolySi/Au [70] electrodes, but with an excessively high R_0 (in MΩs). For Nb/Nb_2O_5/Pt [73] and Gr/TiO_x/Ti [65] diodes, very high asymmetry values of 7700 at 0.5 V and 9000 at 1 V have been observed, respectively. However, no β_0 and R_0 information were provided for these devices. A Au/0.7 nm CuO/Cu diode with β_0 = 2 A/W and

R_0 = 500 Ω was demonstrated by Gadalla *et al.* [74]. A comparably low R_0 (405 Ω) has been accomplished using a Au/6 nm HfO_2/Pt diode [76].

In summary, although some diodes exhibit excellent responsivity, they also have high dynamic resistance, which is unfavourable for IR energy rectification. Using multiple insulators is an alternative strategy for improving the MIM diodes' figures of merit; this strategy is covered in the next section.

2.2.2. Multiple insulator MI^{n}M diodes

The use of multiple insulator diodes (MI^{n}M) in a rectenna system can increase the nonlinearity of the I-V characteristics and subsequently improve the performance of the THz rectifiers [78]. Resonant tunneling (RT) and step tunneling (ST) are two quantum mechanical tunnelling mechanisms that enable MI^{n}M diodes to have a high responsivity while maintaining a low resistance [7,20,61,79].

RT is a quantum mechanical conduction mechanism in which an electron can tunnel through an energy barrier between two regions of a semiconductor or dielectric material with the aid of a quantum well. In RT, a quantum well within the potential barrier act as a resonant energy state, allowing the electrons to tunnel through the barrier easier than standard tunnelling mechanisms. The electrons can tunnel through the barrier if their energies match the quantized energy levels of the quantum well. Hence, this can lead to a current-voltage (I-V) characteristic with lower differential resistance, as well as improved asymmetry and responsivity which is critical in a variety of high-frequency applications [7,20].

Similar to RT, ST occurs when semiconductor or insulator heterostructures stacked on top of each other and create a potential step at the interface between the layers. In this configuration, a step reduction in the tunnel distance occurs under an applied bias. Hence, the tunnelling starts to occur via only the wider band gap insulator layer. This makes it possible for the double insulator tunnel barriers to tune the I-V asymmetry and nonlinearity [31]. The detailed working principles of RT and ST are explained in Chapter 3. It should be noted that there is a limited number of publications on the benefits of these conduction mechanisms in nano-rectenna applications which are summarized in this chapter.

The responsivity and zero-bias dynamic resistance values of double MI^{2}M and triple MI^{3}M insulator diodes are displayed in Fig. 2.9. Table 2.3 includes a complete summary of the rectification characteristics, area, and deposition method of these diodes. It is clear that lower band gap oxides, such as HfO_2 [31,80], Ta_2O_5 [7,23,81], Nb_2O_5 [7,20], and most recently NiO [4,82], have been investigated in combination with Al_2O_3 which is one of the important MIM oxide candidates especially due to its lower dynamic permittivity at 28.3 THz which will be explained in detail in the next section. In addition, NiO has been utilised in combination with other compounds such as TiO_2 [17], Nb_2O_5 [83], and ZnO [66]. In more recent studies, TiO_2 MI^{2}M diodes with ZnO [84], TiO_x [85], and Co_3O_4 [19] were also investigated, and so are the films with nitrogen-doped TiO_2 and Al_2O_3 such as a Pt/NTiO$_x$/NAlO$_x$/Al diode [86].

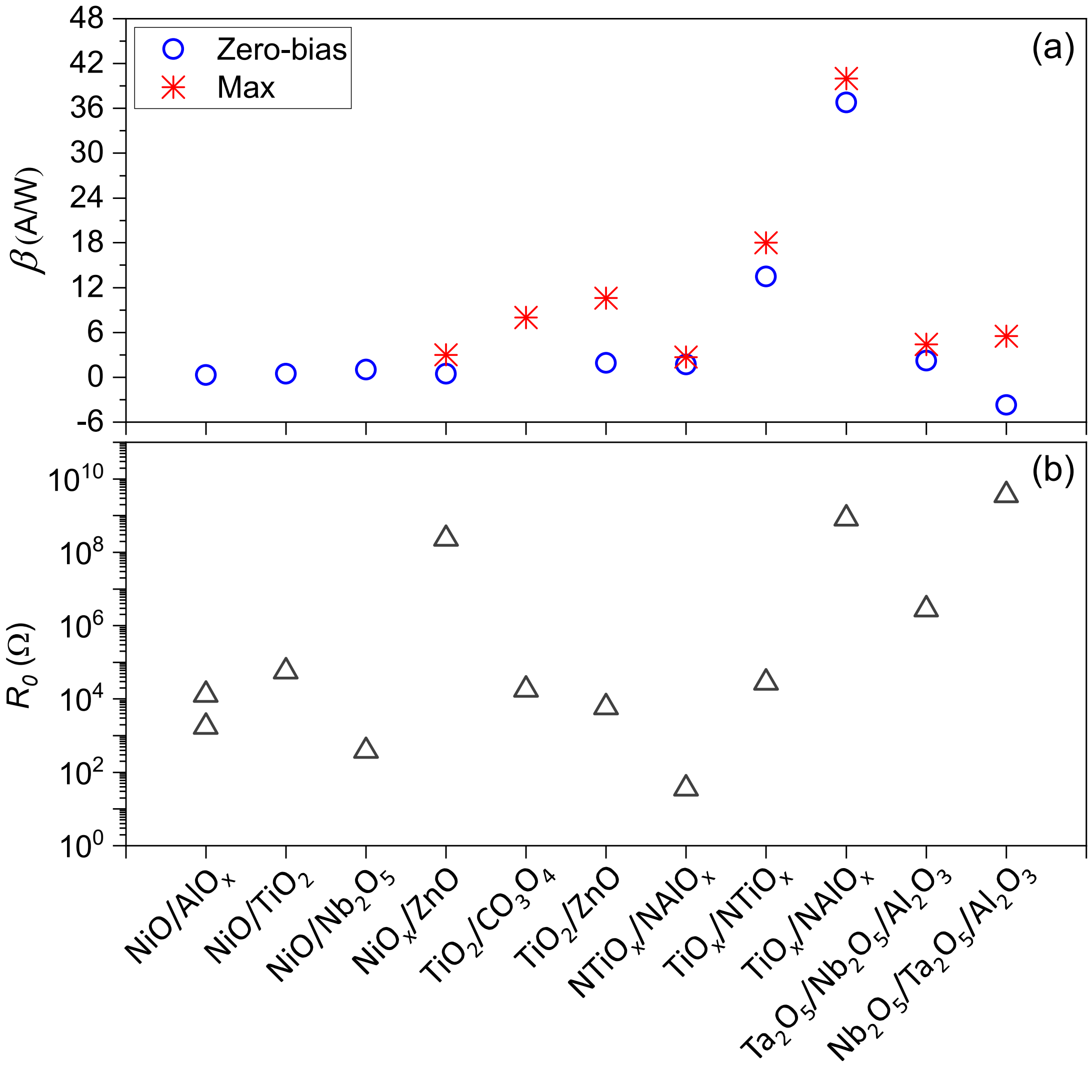

Figure 2.9. (a) Responsivity and (b) zero-bias dynamic resistance for MI^{n}M diodes. Full details are summarized in Table 2.3. [1]

Maraghechi *et al.* [87] demonstrated that by using Cr/Al_2O_3/HfO_2/Cr configuration, the rectifying performance of a double insulator diode can be superior to that of a single insulator device. The device cross-section and the energy band diagram of the MI^{2}M structure are shown in Fig. 2.10. Despite the fact that their diode showed an asymmetry (η) of >10 at 3 V which is very promising, the non-linearity (f_{NL}) of the I-V data at low bias wasn't enhanced and it could be further improved by lowering the metal/oxide barrier heights.

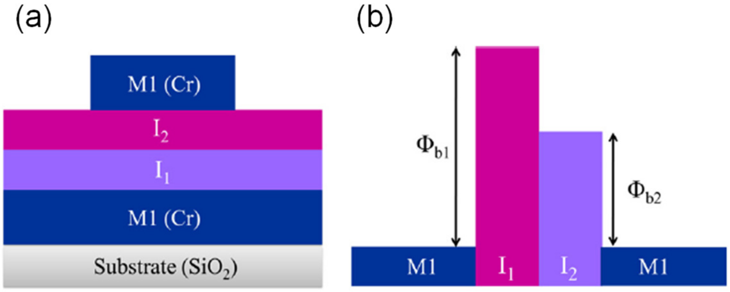

Figure 2.10. Schematics of MI^{2}M (a) device cross-section and (b) the energy band diagram presented in Ref. [87].

Alimardani *et al.* [23,31] made progress by experimentally proving the step tunnelling mechanism in MI^{2}M diodes made of Al_2O_3/HfO_2 and Al_2O_3/Ta_2O_5, respectively, with a work function difference of 0.6 eV between the Al and ZCAN electrodes. At lower voltages, enhanced asymmetry (η = 10 at 0.45 V) and f_{NL} were obtained, but the zero-bias rectification characteristics were not recorded. Energy band alignments of these two different MI^{2}M structures demonstrating the RT, flat band condition and ST with the associated applied biases are shown in Fig. 2.11.

It is seen from the figures that the dominance of both conduction mechanisms is observed at relatively high voltages which is a disadvantage for energy harvesting applications. This is due to the high barrier heights between the metal/oxide layers and should be modified by lowering the barriers to efficiently operate around zero-bias.

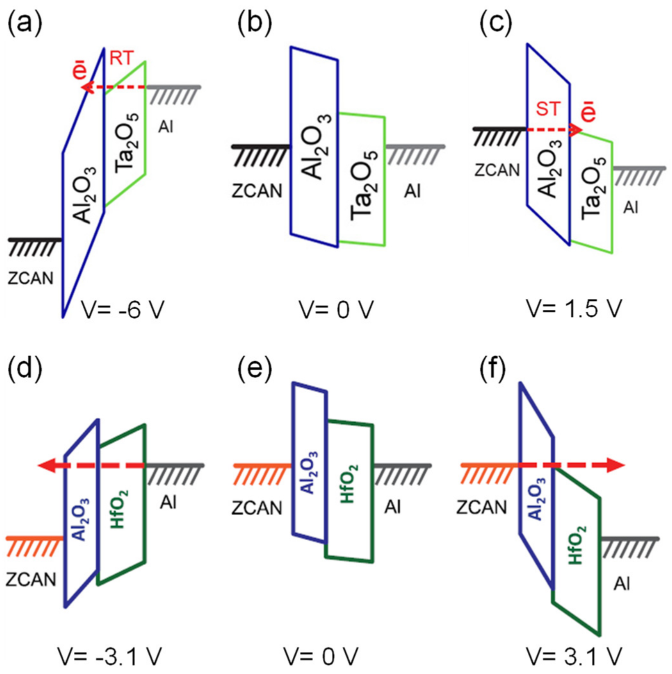

Figure 2.11. Energy band diagrams of (a)-(c) ZCAN/Al_2O_3/Ta_2O_5/Al and (d)-(f) ZCAN/Al_2O_3/HfO_2/Al diodes showing the RT, flat band and ST conditions [23,31].

Furthermore, Al/Al_2O_3/Ta_2O_5/Al device has been reported to exhibit high η (18 at 0.35 V) and a β_{max} of 6 A/W [7]. A spike in the I-V data at ~2 V has been attributed to resonant tunneling (RT). This behaviour was also noticed in a Ni/NiO_x/ZnO/Cr diode, where it showed remarkable η of 16 at 0.5 V and β_{max} of 8 A/W [66]. In addition, Mitrovic *et al.* [20] have shown that the Nb/4 nm Nb_2O_5/1 nm Al_2O_3/Ag diode has a superior low-bias η of 35 at 0.1 V and a β_{max} of 5 A/W at 0.25 V. In Fig. 2.12, the energy band diagrams including the flat band condition, as well as the RT and ST conditions of the Nb/Nb_2O_5/Al_2O_3/Ag are shown. Furthermore, in line with the experimental band alignment and a theoretical model, it was discovered that the work function difference of the Nb/Ag electrodes facilitated the start of strong resonance at less than 1 V as shown in Fig. 2.12 (b).

The impact of RT on asymmetric Al/Ta_2O_5/Al_2O_3/Cr diodes with different oxide thickness ratios has also been examined by Noureddine *et al.* [81]. They found a strong relationship between the simulated bound states at the Ta2O_5/Al_2O_3 conduction bands and the thickness ratio of the insulating layers. Low turn-on voltages (~0.17 V) have improved the rectification properties of the diodes [88].

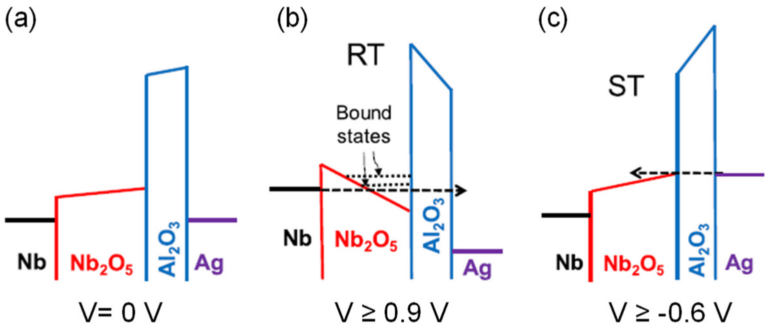

Figure 2.12. Energy band diagrams of ZCAN/Al_2O_3/Ta_2O_5/Al diode showing the (a) flat band condition at V= 0 V, (b) RT at V ≥ 0.9 V and (c) ST at V ≥ -0.6 V [20].

It is important to note that none of the devices described above had the desired minimum area for coupling with the antenna component. Instead, the research was focused on improving the asymmetry and the non-linearity of these devices by engineering different metal/oxide barriers.

The correlation between resistance and responsivity in MI^2M devices was investigated by Herner *et al.* [19] by testing Co/Co_3O_4/TiO_2/Ti diodes prepared with a range of thicknesses and annealing temperatures. When annealing the samples up to 256 °C in air, a substantial decrease in the dynamic resistance with a modest decrease in the responsivity was reported. Their most efficient diodes exhibited a β_0 of 2.2 A/W and a R_0 of 18 kΩ. In another work [17], the zero-bias rectification performance of a diode based on Co_3O_4 was compared with a structure composed of Ni/NiO/TiO_2/Cr. A quantum mechanical MIM diode simulator was used in this study to investigate the relationship between responsivity and resistance by altering the insulator thickness for both diodes. As opposed to RT, ST has been observed to be the more dominant conduction mechanism in both architectures. However, it has been mentioned that RT is critical for lowering the dynamic resistance which could be accomplished by increasing the Co_3O_4 thickness but this also increases the operation voltages. The use of a "geometric diode" has also been proposed as an alternative [17,89], where these structures were explained in section 1.3.3. but they are not a covered in the scope of thesis.

As also explained earlier, Pelz *et al.* [83] developed a travelling-wave diode (TWD) made of Ni/NiO/Nb_2O_5/CrAu to show that the transmission line impedance can get beyond the constraints of the traditional MIM diodes' RC time constant at optical frequencies. The design and the SEM image of this TWD are shown in Figs. 2.13 (a) and (b). An R_0 of 380 Ω and β_0 of 0.46 A/W were recorded from DC I-V measurements. In addition, the TWD showed a β_{max} of 130 µA/W with a detectivity of 1.0×10^4 jones in the optical measurements.

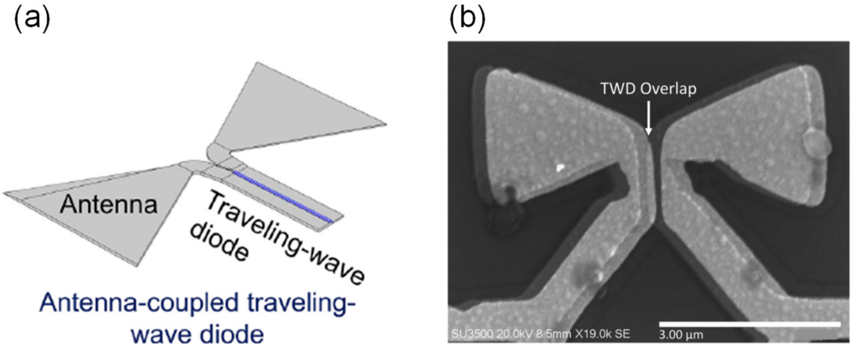

Figure 2.13. (a) TWD rectenna design and (b) the SEM image of the structure [83].

A Ti/TiO_2/ZnO/Al diode was demonstrated by Elsharabasy *et al.* [84] which had a peak β_{max} of 10.6 A/W at 0.15 V where the β_0 was 1.9 A/W with an R_0 of 5.9 kΩ. Their genetic algorithm-determined optimum rectenna design parameters were found to have theoretical 5.5% coupling efficiency, 6.4 A/W responsivity, and 34 THz cut-off frequency. In a recent study, Matsuura *et al.* [85] presented asymmetric Pt/TiO_2/$TiO_{1.4}$/Ti diodes made of stoichiometric and non-stoichiometric oxide layers with the goal of enhancing the current density and consequently the asymmetry. In a later study [85], the performance of non-stoichiometric TiO_x-based diodes was substantially improved. The diodes showed a current density of 4.6×10^6 A/m^2 with a peak asymmetry of 7.26 at 0.45 V.

Weerakkody *et al.* [4] followed a similar approach and determined that Ni/NiO/AlO_x/CrAu diodes could achieve low R_0 (1.75 kΩ) and fairly high β_0 (0.31 A/W). This was done by manipulating the deposition conditions of Al_2O_3 during sputtering to increase the ratio of Al^{3+} ions. Therefore, the alumina has a higher electron affinity (3.26 eV [20]) than the standard stoichiometric Al_2O_3 (~1.6 eV) which results in significantly lower barrier height at the NiO/AlO_x interface. In order to function at 28.3 THz, a bowtie antenna was coupled with this diode (Fig. 2.14) and demonstrated a considerable improvement in overall conversion efficiency (3.7×10^{-8}%) and detectivity of (1.7×10^5 $cmHz^{1/2}W^{-1}$).

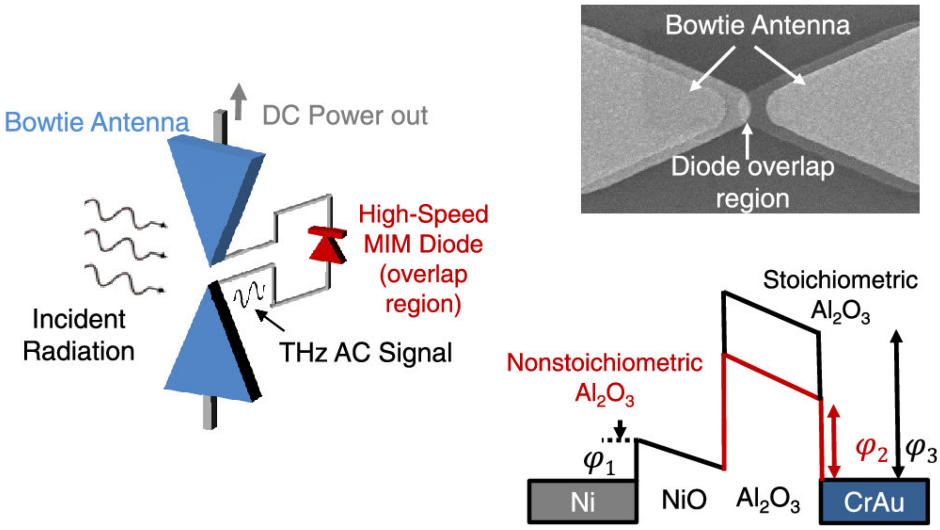

Figure 2.14. Schematics of bowtie antenna integrated Ni/NiO/AlO_x/CrAu diode with the energy band diagram and SEM image of the diode overlap region [4].

Another recent development is the ability to achieve resonant tunnelling at nearly zero-bias, allowing for the operation of Ni/NiO/AlO_x/CrAu diodes when illuminated at ~30 THz by the antenna component [82]. Low R_0 (13 kΩ) and high β_0 (0.5 A/W) were achieved at the same time by adjusting the depth and width of the quantum well of a 0.035 μm^2 diode by altering the insulator thickness. The highest achieved coupling efficiency (η_c) of 5.1% and a power conversion efficiency of 1.7×10^{-8}% is shown by the resulting bowtie rectifier for diodes when RT has taken place.

Defect engineering in MI^2M diodes is another recent strategy [86]. When TiO_2 and Al_2O_3 are doped with nitrogen (N_2) using plasma-assisted atomic layer deposition (PA-ALD), electron traps are created. These traps can help with unidirectional, defect-mediated Poole-Frenkel (PF) conduction and trap assisted tunneling (TAT) in multi-insulator structures. The rectification performance of doped diodes has seen to be improved, but it should be remembered that electron transport is much slower than tunnelling, which could constrain the frequency response. The best performing Pt/$NTiO_x$/$NAlO_x$/Al diode showed a R_0 of 36 Ω and a β_0 of 1.7 A/W.

Table 2.3 A summary of device and rectification parameters for multiple insulator MI^{n}M diodes, n = 2, 3 including device area, oxide thickness in the insulator stack and oxide deposition technique.

Oxides	**Metals**	**β_0 (A/W)**	**β_{MAX} (A/W)**	**R_0 (Ω)**	**η**	**Area (μm^2)**	**Thickness (nm)**	**Deposition Technique**
Al_2O_3/HfO_2	ZCAN/Al [31]	-	-	-	>10 at 0.8 V	8 × 10^5	2.5/1	ALD
	Cr/Cr [87]	-	~2.5	-	~10 at 3 V	2 × 10^5 *	2/2	ALD
Al_2O_3/Ta_2O_5	ZCAN/Al [23]	-	-	-	10 at 0.45 V 187 at 1.2 V	8 × 10^5	2.5/2.5	ALD
	Al/Al [7]	-	6.0	-	18 at 0.35 V	1 × 10^4	1/4	Sputtering/ALD
	Cr/Al [81]	-	-	>10^7 M	~8 at ~1 V	1 × 10^4	1/4	ALD
Al_2O_3/Nb_2O_5	Ag/Nb [20]	-	8.0	-	35.2 at 0.06 V	1 × 10^4	1/4	Sputtering
	Al/Al [7]	-	9.0	-	7.6 at ~0 V	1 × 10^4	1/4	Sputtering/ALD
NiO/AlO_x	Ni/CrAu [4]	0.31	-	1.75 k	-	0.025	2/1.1	Sputtering
	Ni/CrAu [82]	0.5	-	13 k	-	0.035	4/1	Sputtering
NiO/TiO_2	Ni/Cr [17]	~1.0	-	56 k	-	0.071	-	Sputtering/ O_2 ambient
NiO/Nb_2O_5	Ni/CrAu [83]	0.46	~3.0	380	~1.15 at 0.2 V	0.1552 *	3/2	Sputtering/ O_2 ambient
NiO_x/ZnO	Ni/Cr [66]	-	8.0	234 M	16 at 0.5 V	400 *	7/7	Sputtering
ZnO/TiO_2	Al/Ti [84]	1.9	10.6	5.9 k	-	72.27 *	0.5/1.65	ALD
TiO_2/Co_3O_4	Ti/Co [19]	2.2	4.4	18 k	1.2 at 0.1 V	0.071	2.7/2.5	Plasma oxidation/sputtering
$TiO_2/TiO_{1.4}$	Pt/Ti [85]	-	-	-	7.26 at 0.45 V	900	3/2	Annealing/ALD
$NTiO_x/NAlO_x$	Pt/Al [86]	1.7	2.7	36	1 at 0.5 V	100	7/3	PA-ALD
$Ta_2O_5/Nb_2O_5/Al_2O_3$	Al/Al [90]	-	5.1	-	12 at 0.1 V	1 × 10^4	2/2/1	ALD
$Ta_2O_5/Nb_2O_5/Al_2O_3$	Al/Al [61]	1.2	4.3	2.8 M	4.3 at 1.6 V	1 × 10^4	1/3/1	ALD
$Nb_2O_5/Ta_2O_5/Al_2O_3$	Al/Al [61]	–3.7	5.5	3.6 G	117 at 1.6 V 6 at 0.1 V	1 × 10^4	1/3/1	ALD

*Device area calculated based on stated dimensions.

According to the most recent theoretical work by Elsharabasy *et al.* [91], MI^{2}M diode responsivity can be improved by taking metal/oxide characteristics into account and adjusting the diode resistance to 100 Ω to have a perfect impedance match between the diode and the antenna. The optimization was carried out to assure zero-bias operation, and it was discovered that the Ti/1 nm TiO_2/1 nm Nb_2O_5/Ti diode has the closest configuration to the ideal diode according to the simulation results of R_0 = 108.6 Ω and β_0 = 4.99 A/W. Using this design, for a diode area of 0.01 μm^2, the predicted RC time constant was calculated to be 9 fs, resulting in a cut-off frequency (f_c) of 17 THz.

Besides the MI^2M structures, there have been a relatively limited number of investigations conducted on triple-insulator (MI^3M) diodes. The RT effect was explored and published for the first time by Maraghechi *et al.* [92] in Cr/Cr_2O_3/HfO_2/Al_2O/Cr and Cr/Cr_2O_3/Al_2O_3/HfO_2/Cr diode stacks in cascaded and non-cascaded formations, respectively. In our later studies [61,90], both cascaded (Al/Nb_2O_5/Al_2O_3/Ta_2O_5/Al) and non-cascaded (Al/Ta_2O_5/Nb_2O_5/Al_2O_3/Al) diode configurations have been developed by combining ultra-thin (1–3 nm) metal oxide films of Al_2O_3, Ta_2O_5 and Nb_2O_5. ALD has been used to facilitate sub-nm thickness control, low oxide defect density, excellent stoichiometry, and superior uniformity. The diodes exhibited dominant RT behaviour at low voltages ~0.35 V for non-cascaded design. These devices have been the best performing MI^3M diodes in the literature with superior low-voltage β_{max} of 5 A/W at 0.2 V and η of 12 at 0.1 V. The details of these devices are explained in Chapter 6 in detail.

2.3 Design considerations of THz rectifiers

In this section, the challenges in the MIM diode fabrication for THz energy harvesting and the efficiency considerations are covered. With this scope, the pros and cons of several deposition methods for the insulators used in the MIM fabrication and are summarised in detail. In addition, a theoretical prediction for the antenna/diode coupling efficiency is presented for four different oxide candidates.

2.3.1 Challenges in fabricating THz rectifiers

As indicated in Eqn. 1.3, a trade-off between various physical properties of diodes usually restricts practical implementation in rectennas for having a high f_c and harvesting IR energy. The patterning of nano-scale devices, coupling efficiency, and diode integration with the antenna are only a few key challenges that need to be solved. Other problems include a precise manufacturing process with smooth metal electrodes and high-quality ultra-thin oxides. The oxide uniformity and subsequently the electrical behaviour of the diodes are influenced by the surface roughness of the metal electrodes. As a result, the performance of the devices is being limited. In this section, several challenges in the fabrication process of the nano-rectennas are listed.

2.3.1.1 Bottom electrode surface roughness and native oxidation

The bottom metal electrode's surface roughness and the technique used to grow the oxide layer have a significant impact on the quality of the prepared oxide. The effect of growth conditions on the bottom electrode surface roughness presented in Ref. [32] is shown in Fig. 2.15. The atomic force microscopy (AFM) images of the Al deposited Si substrates are demonstrated before and after optimizing the substrate cleaning and the thermal evaporation growth conditions.

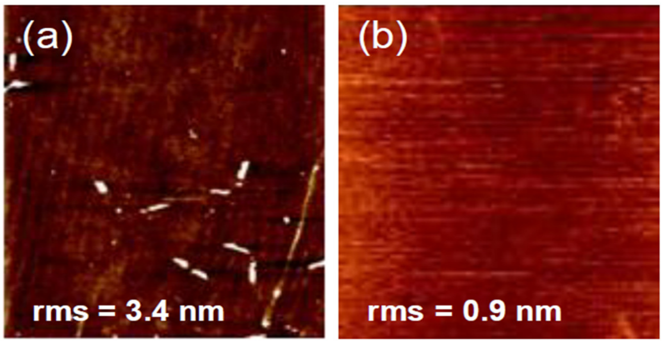

Figure 2.15. AFM images of Al thin films for 1600 μm^2 scan area (a) before and (b) after the optimization of cleaning process and the thermal evaporation growth conditions [32].

Native oxidation [49] can be considered as the simplest method, but typically produces low-quality, uneven oxides because of the changing humidity and the ambient atmosphere. Most of the fabricated diodes presented in Tables 2.2 and 2.3 have oxide thicknesses less than 5 nm, which aids in quantum-mechanical tunneling.

2.3.1.2 Oxide uniformity

The list of various oxide growth methods including native, plasma, thermal, boiling water, O_2 exposure, and anodic oxidation are also presented. In another method, the bottom electrodes undergo thermal oxidation [48,51,62], which involves heating process to a high temperature and allowing the oxides to grow on the metals.

A slight variation in the oxide thickness has a significant impact on the probability of tunnelling and the associated current density of the diode. Non-uniform insulating layers in MIM diodes can cause variability in the current density which results in lack of repeatability. Also, any defects in the oxide films can lead to the emergence of unwanted conduction mechanisms including Schottky (SE) and Poole Frenkel (PF) emissions or trap-assisted tunnelling (TAT). Therefore, it is crucial to make insulators that is uniform, ultra-thin, and free of defects for the efficient and consistent functioning of a diode.

Plasma oxidation [8,9,11,19,50,56,58,59,64], on the other hand, is more consistent and repeatable technique because it allows for precise control over process variables including power, oxygen flow rate and oxidation time. In this method, a He-based process gas is delivered into the region between the electrodes and the plasma is generated by applying an RF power at a specific frequency [93]. The schematic representation of a typical plasma oxidation setup is shown in Fig. 2.16. It has also been demonstrated that anodic oxidation or anodization yields high-quality oxidised metal surfaces with accurate thickness control [72,73].

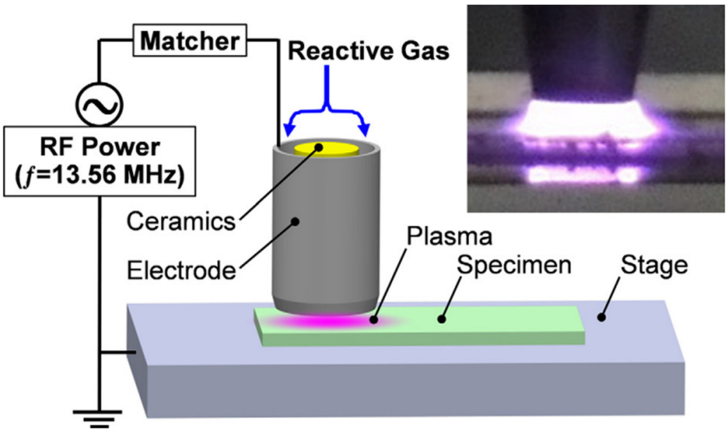

Figure 2.16. Schematic representation of a plasma oxidation setup [93].

Other methods, such Langmuir-Blodgett [52,68] , have also been studied for oxide deposition in MIM diodes. However, this technique has primarily been used to make insulator films based on organic materials which allows for simple and inexpensive oxide deposition with proper thickness control. Figure 2.17 illustrates the fabrication of inorganic NiO thin films from an organic nickel acetate precursor using the LB approach and their utilization as an insulating layer of a MIM tunnel diode.

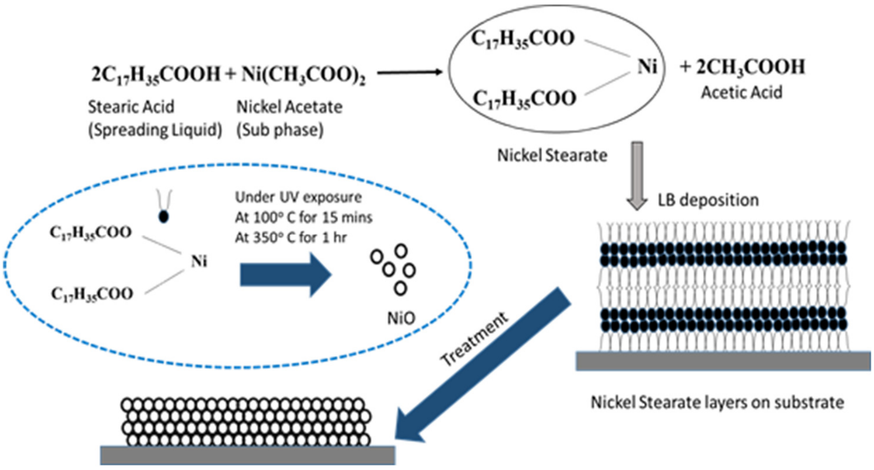

Figure 2.17. Schematic representation of NiO synthesis using LB method [52,68].

Direct deposition of an insulator on the bottom electrode material with various deposition techniques such as sputtering (Fig. 2.18 (a)) [4,7,69,77,82,83,17,20,42,45,46,55,57,66], e-beam evaporation (Fig. 2.18 (b)) [75] or ALD [7,22,85–87,90,23,31,61,67,74,76,81,84] could be a better approach to overcome the limitations of oxide growth on the bottom metal.

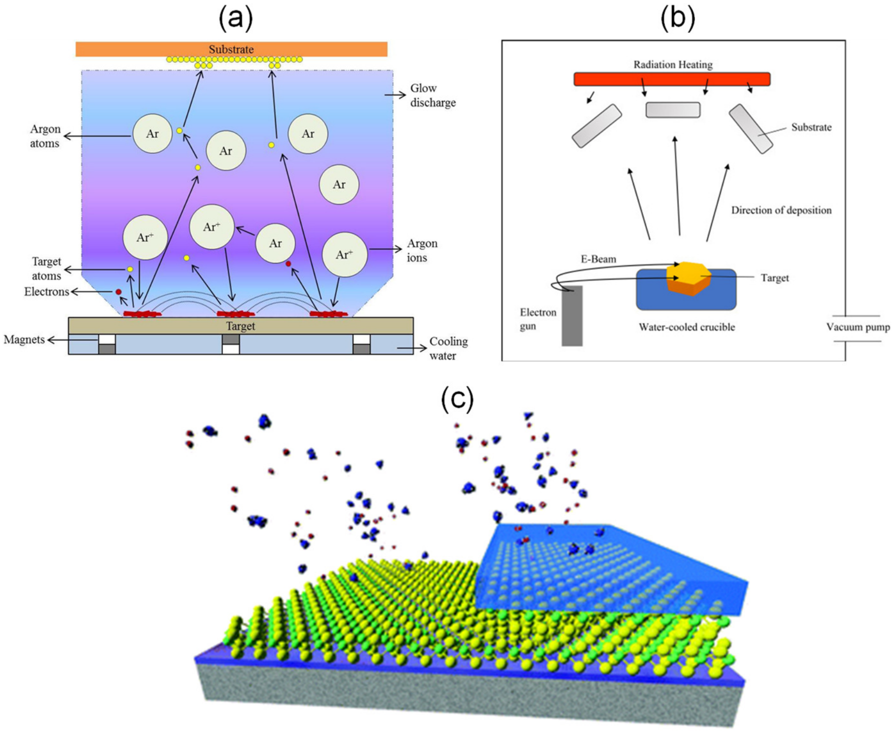

Figure 2.18. Schematics of (a) RF sputtering, (b) e-beam evaporation and (c) ALD setups [94–96].

Atomic layer deposition (ALD) (Fig. 2.18 (c)), among many other deposition techniques, provides the finest oxide quality with low defect density, high stoichiometry, and superior uniformity [90].

2.3.1.3 Device scaling

Apart from the deposition methods, the most sophisticated ultra-fine mask-less lithographic techniques, especially e-beam lithography (Fig. 2.19 (a)), are necessary for nano-scale patterning in order to facilitate small diode areas. Another alternative approach, which is thermal scanning probe lithography (Fig. 2.19 (b)), for patterning nano-scale devices is presented in this work. Hence, a minimal capacitance can be obtained while maintaining a diode resistance in the order of a few hundred Ωs to match the antenna impedance.

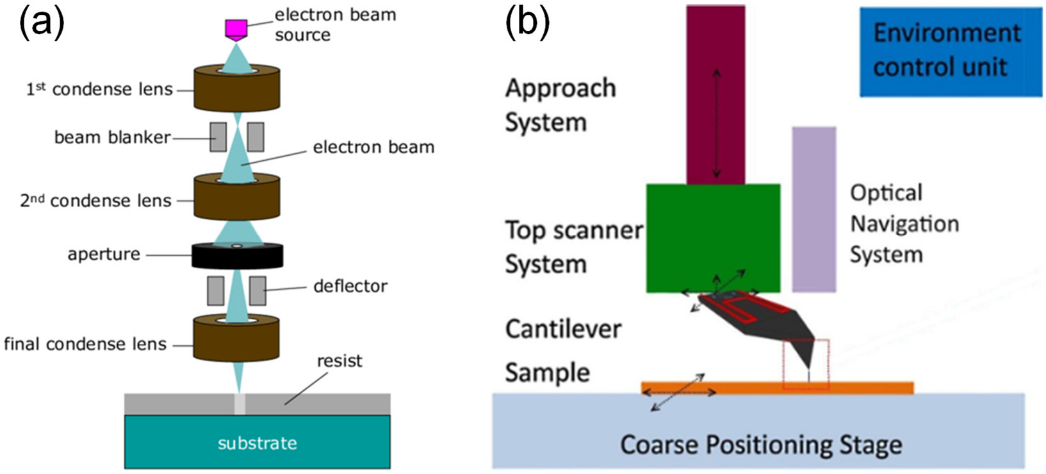

Figure 2.19. Schematics of e-beam lithography and thermal scanning probe lithography techniques [97,98].

2.3.2 Estimation of diode-antenna coupling efficiency (η_c)

The properties of thin films such as uniformity, crystallinity, stoichiometry and homogeneity are highly dependent on the deposition method as explained in the previous section in detail. As a result, the electron affinity, band gap and dielectric permittivity of even the same materials can change depending on the processing conditions.

The static (ε) and dynamic permittivity ($\varepsilon_r = n^2$, where n is the refractive index at a specific frequency) values of the most prominent oxides utilised in MIM diodes for rectennas, including NiO, Al_2O_3, ZnO, TiO_2, CuO, Ta_2O_5, Nb_2O_5, Cr_2O_3, SiO_2, HfO_2, V_2O_5, and Sc_2O_3 are summarized in Table 2.4. The dynamic permittivity (**ε_r**) of the oxides at specific frequencies (28.3 THz in our case) is used to predict the power transfer efficiency of an AC voltage source integrated with a MIM diode in order to further investigate the coupling efficiency of these oxides for rectifying THz signals.

Table 2.4. Static and dynamic permittivity (at 28.3 THz) of most common oxides used in MIM diodes for rectennas.

Oxide	**Static Permittivity (ε)**	**Dynamic Permittivity (ε_r) @ 28.3 THz**
NiO	7.9–16.7 [102], 11.9 [103,104]	3.24 [105]
Al_2O_3	7 [106], 7.6 [107], 8.3 [108], 8.9 [109], 9 [110], 10 [7,20,111,112]	0.8 [4,99]
ZnO	8.5 [113,114], 9.4–10.4 [113]	2.4 [101]
TiO_2	15-25 [115], 60 [116], 70 [117], 80 [110,118], 88–102 [119], 100 [120]	1.4 [99]
CuO	10^3–10^5 [121]	2.4 [74,100]
Ta_2O_5	20 [79], 23.9 [109], 25 [119]	-
Nb_2O_5	25 [7,20,79]	-
Cr_2O_3	10.3 [122], 11.8–13.3 [123]	-
SiO_2	3.9 [110]	4.7 [99]
HfO_2	14 [124], 18 [125], 25 [110]	-
V_2O_5	11.5–22.3 [126]	-
Sc_2O_3	8.5–9.3 [127], 14 [128,129]	-

Table 2.4 lists the reported **ε_r** values at 28.3 THz obtained from various techniques such as spectroscopic ellipsometry [4,99], transmission [100] and reflectance [101] measurements for NiO, Al_2O_3, ZnO, TiO_2, CuO, Ta_2O_5, Nb_2O_5, and SiO_2. Some oxides with very high static permittivity, like CuO, have very low dynamic permittivity, which allows their utilization in rectenna devices [74].

As shown in Eqn. 1.2, the coupling efficiency (η_c) in a rectenna system can be calculated at a specific frequency. Assuming that an antenna has ~ 100 Ω resistance to be able to capture 28.3 THz frequency. The coupled diode must have a similar resistance with the antenna in the scenario of a perfect impedance match between the diode and the antenna (100 Ω).

In Fig. 2.20, the η_c between diode and the antenna is shown as a function of the resistance and the area at 28.3 THz for the most common oxide contenders (Al_2O_3, TiO_2, ZnO and NiO). In the calculations, the oxide thickness was set at 3 nm. The dynamic resistance (R_D) and area (A) parameters were swept between 100-1 kΩ and 0.01-1 μm^2, respectively. For the capacitance calculations indicated in Eqn. 1.4, the high-frequency ε_r values (Table 2.4) of oxides were used. Figures 2.20 (a) and (b) illustrate that the Al_2O_3 and TiO_2 emerge as strong candidates with the maximum coupling efficiency higher than the other two oxides due to their smaller ε_r.

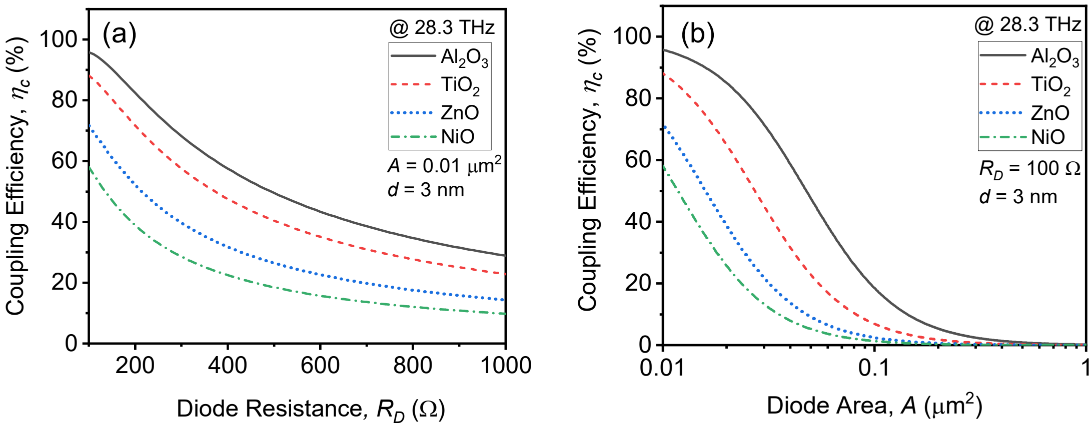

Figure 2.20. Calculated coupling efficiency for the MIM rectenna device as a function of (a) resistance and (b) area at 28.3 THz using 3 nm oxide thickness and dynamic permittivity values as stated in Table 2.4.

Another point is that, even though the diode resistance is set to be 100 Ω, the area appears to be more critical parameter, as the coupling efficiency is significantly reduced (< 1%) when the area is increased to 1 μm^2. Figure 2.20 represents the optimum device scenario that is still challenging to manufacture; i.e. a highly scaled MIM diode with a small capacitance in atto-farad (aF) level and a dynamic resistance of a few 100s of Ωs that operate effectively at 28.3 THz. The main focus of this thesis is on (i) engineering the metal/oxide barriers using several oxide materials, (ii) depositing ultra-thin films and (iii) fabricating scaled MIM diodes to boost the coupling efficiency of these devices beyond the state-of-the-art.

2.4 Conclusion

In this chapter, a detailed literature review of the state-of-the-art MI^nM (n = 1, 2, 3) diodes that are used in THz rectennas has been presented. This includes the utilization of numerous oxides in MIM diodes along with an overview of each oxide's electron affinity, band gap, and permittivity. Also, the most common metals used in MIM devices, as well as their work functions and skin depths have been summarized. It can be seen that there are several values electron affinity (such as from 1.46 eV to 4.8 eV for NiO) and work function (from 4.0 eV to 5.0 eV for Co) reported in the literature for the same type of materials depending on different growth and characterization methods. Since the barrier height of the engineered metal and oxide layers have a fundamental role on the device performance, it is crucial to know its exact value to reliably assess the rectification performance of the fabricated devices. Otherwise, it is not possible to have a repeatable process. It was seen that Al_2O_3 and NiO are the two most common oxides used in the MIM diode fabrication, as well as their combinations with the other oxides. This is usually due to their low dynamic permittivity values at 28.3 THz which increases the coupling efficiency.

The main goal of this research is to improve the rectification performance of diodes by increasing the asymmetry and zero-bias responsivity while decreasing the zero-bias dynamic resistance. There are several studies where very low R_0 values were obtained such as 125 Ω for the $Al/Al_2O_3/Pt$ and 100 Ω for the Ni/NiO/Ni diodes but their β_0 values haven't been optimized due to the trade-off between the dynamic resistance and responsivity. Since the single insulator MIM diodes are facing this limitation, alternatively, multiple insulator diode structures are becoming attractive due to the potential of resonant and step tunnelling mechanisms to break this trade-off. In RT, as the electrons propagate through the localized energy states in a QW formed by combining different insulating layers, the dynamic resistance can be decreased while maintaining a high asymmetry and responsivity. Also, the asymmetry and non-linearity of the I-V behavior can be improved via ST due to the reduction in the tunneling distance in one direction. For example, a double insulator $Ti/TiO_2/Co_3O_4/Co$ diode exhibited a high β_0 of 2.2 A/W with an 18 kΩ R_0 at a relatively small device area (0.071 μm^2) which makes it promising to integrate with THz rectennas. In another study, a very low R_0 of 380 Ω was reported for the Ni/NiO/Nb_2O_5/Cr diode with a relatively good β_0 of 0.46 A/W for 0.1552 μm^2 device area. In one of our works which is also included in this thesis, we achieved a considerably high β_0 of -3.7 A/W using a triple insulator Al/Nb_2O_5/Ta_2O_5/Al_2O_3/Al configuration with the aid of resonant tunnelling with relatively high β_0 which could be improved by lowering the barrier heights. Until now, the best achieved experimental rectenna performance belongs to a double insulator Ni/NiO/AlO_x/Au MI^{2}M diode integrated with a bowtie antenna which exhibited a coupling efficiency of 5.1% and an overall power conversion efficiency of 1.7 × 10^{-8}% at 30 THz. According to the DC I-V characterisation, this diode has a R_0 of 13 kΩ and a β_0 of 0.5 A/W. Another recent theoretical work demonstrates that a higher β_0 of 4.99 A/W with a lower R_0 can be achieved using a Ti/TiO_2/Nb_2O_5/Ti diode with 0.01 μm^2 device area which could result in more efficient rectification. As discussed, despite the number of limitations, there is a substantial research ongoing in this field to develop the most efficient MIM rectifier for THz rectennas. In section 2.3, a coupling efficiency has been calculated. The use of most promising oxides such as Al_2O_3, TiO_2, ZnO and NiO has been evaluated in terms of dynamic permittivity.

This review clearly shows that different combinations of multiple insulator MI^{n}M diode structures are the most promising ones for several reasons in comparison to the single insulator MIM rectifiers, as well as the other emerging THz rectifier types. These include better rectification performance in terms of asymmetry, zero-bias responsivity and reduced dynamic resistance with the aid of RT and ST. Plasmonic, graphene geometric, 1D MIG based and MWCNT rectennas are mainly focused on reducing the diode capacitance by altering the diode design. However, they are currently inefficient in terms of rectification performance compared to MIM tunnel rectifiers. Another disadvantage of these rectifier types (particularly for the graphene geometric, 1D MIG based and MWCNT rectennas) is the device complexity which requires more challenging fabrication processes. On the other hand, Seebeck nano-antennas are advantageous in terms of cost effectivity and ease of fabrication since they do not need an insulating layer, but they also suffer from thermal losses. Also, their state-of-the-art performance is not yet comparable with MIM diode's performance metrics.

References

[1] I. Z. Mitrovic, S. Almalki, S. B. Tekin, N. Sedghi, P. R. Chalker, and S. Hall, "Oxides for Rectenna Technology," *Materials*, vol. 14, no. 18, p. 5218, 2021, doi: 10.3390/ma14185218.

[2] N. Alimardani, S. W. King, B. L. French, C. Tan, B. P. Lampert, and J. F. Conley, "Investigation of the impact of insulator material on the performance of dissimilar electrode metal-insulator-metal diodes," *Journal of Applied Physics*, vol. 116, no. 2, p. 024508, 2014, doi: 10.1063/1.4889798.

[3] I. Z. Mitrovic, M. Althobaiti, A. D. Weerakkody, V. R. Dhanak, W. M. Linhart, T. D. Veal, N. Sedghi, S. Hall, P. R. Chalker, D. Tsoutsou, and A. Dimoulas, "Ge interface engineering using ultra-thin La2O3and Y2O3films: A study into the effect of deposition temperature," *Journal of Applied Physics*, vol. 115, no. 11, p. 114102, 2014, doi: 10.1063/1.4868091.

[4] A. Weerakkody, A. Belkadi, and G. Moddel, "Nonstoichiometric Nanolayered Ni/NiO/Al2O3/CrAu Metal–Insulator–Metal Infrared Rectenna," *ACS Applied Nano Materials*, vol. 4, no. 3, pp. 2470–2475, 2021, doi: 10.1021/acsanm.0c03012.

[5] E. Z. Kurmaev, R. G. Wilks, A. Moewes, L. D. Finkelstein, S. N. Shamin, and J. Kuneš, "Oxygen x-ray emission and absorption spectra as a probe of the electronic structure of strongly correlated oxides," *Physical Review B*, vol. 77, no. 16, 2008, doi: 10.1103/physrevb.77.165127.

[6] Z. Liu, Y. Liu, X. Wang, W. Li, Y. Zhi, X. Wang, P. Li, and W. Tang, "Energy-band alignments at ZnO/Ga2O3 and Ta2O5/Ga2O3 heterointerfaces by X-ray photoelectron spectroscopy and electron affinity rule," *Journal of Applied Physics*, vol. 126, no. 4, p. 045707, 2019, doi: 10.1063/1.5112067.

[7] A. D. Weerakkody, N. Sedghi, I. Z. Mitrovic, H. van Zalinge, I. Nemr Noureddine, S. Hall, J. S. Wrench, P. R. Chalker, L. J. Phillips, R. Treharne, and K. Durose, "Enhanced low voltage nonlinearity in resonant tunneling metal–insulator–insulator–metal nanostructures," *Microelectronic Engineering*, vol. 147, pp. 298–301, 2015, doi: 10.1016/j.mee.2015.04.110.

[8] S. Krishnan, H. La Rosa, E. Stefanakos, S. Bhansali, and K. Buckle, “Design and development of batch fabricatable metal–insulator–metal diode and microstrip slot antenna as rectenna elements,” *Sensors and Actuators A: Physical*, vol. 142, no. 1, pp. 40–47, 2008, doi: 10.1016/j.sna.2007.04.021.

[9] K. Choi, F. Yesilkoy, G. Ryu, S. H. Cho, N. Goldsman, M. Dagenais, and M. Peckerar, “A Focused Asymmetric Metal–Insulator–Metal Tunneling Diode: Fabrication, DC Characteristics and RF Rectification Analysis,” *IEEE Transactions on Electron Devices*, vol. 58, no. 10, pp. 3519–3528, 2011, doi: 10.1109/ted.2011.2162414.

[10] S. B. Tekin, S. Almalki, A. Vezzoli, L. O’Brien, S. Hall, P. R. Chalker, and I. Z. Mitrovic, “(Digital Presentation) Optimization of MIM Rectifiers for Terahertz Rectennas,” *ECS Transactions*, vol. 108, no. 2, pp. 69–79, 2022, doi: 10.1149/10802.0069ecst.

[11] A. Kaur and P. Chahal, “RF Characterization of NiO and TiO2 Based Metal-Insulator-Metal (MIM) Diodes on Flexible Substrates,” *IEEE Access*, vol. 6, pp. 55653–55660, 2018, doi: 10.1109/access.2018.2871635.

[12] W. F. Gale and T. C. Totemeier, Eds., *Smithells Metals Reference Book*. 2003. doi: 10.1604/9780750675093.

[13] B. E. Nieuwenhuys, R. Bouwman, and W. M. H. Sachtler, “The changes in work function of group Ib and VIII metals on xenon adsorption, determined by field electron and photoelectron emission,” *Thin Solid Films*, vol. 21, no. 1, pp. 51–58, 1974, doi: 10.1016/0040-6090(74)90089-3.

[14] M. T. Greiner and Z.-H. Lu, “Thin-film metal oxides in organic semiconductor devices: their electronic structures, work functions and interfaces,” *NPG Asia Materials*, vol. 5, no. 7, pp. e55–e55, 2013, doi: 10.1038/am.2013.29.

[15] S. B. Herner, A. Belkadi, A. Weerakkody, B. Pelz and G. Moddel, "Responsivity–Resistance Relationship in MIIM Diodes," in IEEE Journal of Photovoltaics, vol. 8, no. 2, pp. 499-504, 2018, doi: 10.1109/JPHOTOV.2018.2791421.

[16] H. Wu and L.-S. Wang, “A study of nickel monoxide (NiO), nickel dioxide (ONiO), and Ni(O2) complex by anion photoelectron spectroscopy,” *The Journal of Chemical Physics*, vol. 107, no. 1, pp. 16–21, 1997, doi: 10.1063/1.474362.

[17] E. L. Ratcliff, J. Meyer, K. X. Steirer, A. Garcia, J. J. Berry, D. S. Ginley, D. C. Olson, A. Kahn, and N. R. Armstrong, “Evidence for near-Surface NiOOH Species in Solution-Processed NiOx Selective Interlayer Materials: Impact on Energetics and the Performance of Polymer Bulk Heterojunction Photovoltaics,” *Chemistry of Materials*, vol. 23, no. 22, pp. 4988–5000, 2011, doi: 10.1021/cm202296p.

[18] J. Robertson, “Band offsets, Schottky barrier heights, and their effects on electronic devices,” *Journal of Vacuum Science & Technology A: Vacuum, Surfaces, and Films*, vol. 31, no. 5, p. 050821, 2013, doi: 10.1116/1.4818426.

[19] S. B. Herner, A. D. Weerakkody, A. Belkadi, and G. Moddel, “High performance MIIM diode based on cobalt oxide/titanium oxide,” *Applied Physics Letters*, vol. 110, no. 22, p. 223901, 2017, doi: 10.1063/1.4984278.

[20] I. Z. Mitrovic, A. D. Weerakkody, N. Sedghi, J. F. Ralph, S. Hall, V. R. Dhanak, Z. Luo, and S. Beeby, “Controlled modification of resonant tunneling in metal-insulator-insulator-metal structures,” *Applied Physics Letters*, vol. 112, no. 1, p. 012902, 2018, doi: 10.1063/1.4999258.

[21] M. L. Huang, Y. C. Chang, C. H. Chang, T. D. Lin, J. Kwo, T. B. Wu, and M. Hong, “Energy-band parameters of atomic-layer-deposition Al2O3⁄InGaAs heterostructure,” *Applied Physics Letters*, vol. 89, no. 1, p. 012903, 2006, doi: 10.1063/1.2218826.

[22] G. Jayaswal, A. Belkadi, A. Meredov, B. Pelz, G. Moddel, and A. Shamim, “Optical rectification through an Al2O3 based MIM passive rectenna at 28.3 THz,” *Materials Today Energy*, vol. 7, pp. 1–9, 2018, doi: 10.1016/j.mtener.2017.11.002.

[23] N. Alimardani and J. F. Conley, “Enhancing metal-insulator-insulator-metal tunnel diodes via defect enhanced direct tunneling,” *Applied Physics Letters*, vol. 105, no. 8, p. 082902, 2014, doi: 10.1063/1.4893735.

[24] H. B. Michaelson, “The work function of the elements and its periodicity,” *Journal of Applied Physics*, vol. 48, no. 11, pp. 4729–4733, 1977, doi: 10.1063/1.323539.

[25] M. C. Gwinner, Y. Vaynzof, K. K. Banger, P. K. H. Ho, R. H. Friend, and H. Sirringhaus, “Solution-Processed Zinc Oxide as High-Performance Air-Stable Electron Injector in Organic Ambipolar Light-Emitting Field-Effect Transistors,” *Advanced Functional Materials*, vol. 20, no. 20, pp. 3457–3465, 2010, doi: 10.1002/adfm.201000785.

[26] S.-M. Sun, W.-J. Liu, Y.-F. Xiao, Y.-W. Huan, H. Liu, S.-J. Ding, and D. W. Zhang, “Investigation of Energy Band at Atomic-Layer-Deposited ZnO/β-Ga2O3 Heterojunctions,” *Nanoscale Research Letters*, vol. 13, no. 1, 2018, doi: 10.1186/s11671-018-2832-7.

[27] J. Robertson, “Band offsets of wide-band-gap oxides and implications for future electronic devices,” *Journal of Vacuum Science & Technology B: Microelectronics and Nanometer Structures*, vol. 18, no. 3, p. 1785, 2000, doi: 10.1116/1.591472.

[28] J. Aarik, A. Aidla, A.-A. Kiisler, T. Uustare, and V. Sammelselg, “Effect of crystal structure on optical properties of TiO2 films grown by atomic layer deposition,” *Thin Solid Films*, vol. 305, no. 1–2, pp. 270–273, 1997, doi: 10.1016/s0040-6090(97)00135-1.

[29] F. P. Koffyberg and F. A. Benko, “A photoelectrochemical determination of the position of the conduction and valence band edges ofp-type CuO,” *Journal of Applied Physics*, vol. 53, no. 2, pp. 1173–1177, 1982, doi: 10.1063/1.330567.

[30] L. De Los Santos Valladares, D. H. Salinas, A. B. Dominguez, D. A. Najarro, S. I. Khondaker, T. Mitrelias, C. H. W. Barnes, J. A. Aguiar, and Y. Majima, “Crystallization and electrical resistivity of Cu2O and CuO obtained by thermal oxidation of Cu thin films on SiO2/Si substrates,” *Thin Solid Films*, vol. 520, no. 20, pp. 6368–6374, Aug. 2012, doi: 10.1016/j.tsf.2012.06.043.

[31] N. Alimardani and J. F. Conley, “Step tunneling enhanced asymmetry in asymmetric electrode metal-insulator-insulator-metal tunnel diodes,” *Applied Physics Letters*, vol. 102, no. 14, p. 143501, 2013, doi: 10.1063/1.4799964.

[32] D. A. Weerakkody, “Engineered high-K oxides,” The University of Liverpool, *PhD thesis*, 2016.

[33] B. J. Hopkins and J. C. Rivière, “The Work Function of Polycrystalline Tungsten Foil,” *Proceedings of the Physical Society*, vol. 81, no. 3, pp. 590–592, 1963, doi: 10.1088/0370-1328/81/3/129.

[34] M. M. Abdullah, F. M. Rajab, and S. M. Al-Abbas, “Structural and optical characterization of Cr2O3nanostructures: Evaluation of its dielectric properties,” *AIP Advances*, vol. 4, no. 2, p. 027121, 2014, doi: 10.1063/1.4867012.

[35] J. Singh, V. Verma, R. Kumar, and R. Kumar, “Structural, optical and electrical characterization of epitaxial Cr2O3thin film deposited by PLD,” *Materials Research Express*, vol. 6, no. 10, p. 106406, 2019, doi: 10.1088/2053-1591/ab3543.

[36] A. Miura, Y. Uraoka, T. Fuyuki, S. Yoshii, and I. Yamashita, “Floating nanodot gate memory fabrication with biomineralized nanodot as charge storage node,” *Journal of Applied Physics*, vol. 103, no. 7, p. 074503, 2008, doi: 10.1063/1.2888357.

[37] V. R. Shinde, S. B. Mahadik, T. P. Gujar, and C. D. Lokhande, “Supercapacitive cobalt oxide (Co3O4) thin films by spray pyrolysis,” *Applied Surface Science*, vol. 252, no. 20, pp. 7487–7492, 2006, doi: 10.1016/j.apsusc.2005.09.004.

[38] K. Xing, S. Zhang, A. Tsai, H. Xiao, D. L. Creedon, S. A. Yianni, J. C. McCallum, C. I. Pakes, and D.-C. Qi, “High-electron-affinity oxide V2O5 enhances surface transfer doping on hydrogen-terminated diamond,” *Diamond and Related Materials*, vol. 108, p. 107865, 2020, doi: 10.1016/j.diamond.2020.107865.

[39] S. Thiagarajan, M. Thaiyan, and R. Ganesan, “Physical property exploration of highly oriented V2O5 thin films prepared by electron beam evaporation,” *New Journal of Chemistry*, vol. 39, no. 12, pp. 9471–9479, 2015, doi: 10.1039/c5nj01582k.

[40] V. V. Afanas'ev, S. Shamuilia, M. Badylevich, A. Stesmans, L. F. Edge, W. Tian, D. G. Schlom, J. M. J. Lopes, M. Roeckerath, and J. Schubert, "Electronic structure of silicon interfaces with amorphous and epitaxial insulating oxides: Sc2O3, Lu2O3, LaLuO3," *Microelectronic Engineering*, vol. 84, no. 9–10, pp. 2278–2281, 2007, doi: 10.1016/j.mee.2007.04.113.

[41] S. Hosseini, M. Vahedpour, M. Shaterian, and M. A. Rezvani, "Investigation of structural and optoelectronic properties of sc2o3 Nanoclusters: A DFT study," *Physical Chemistry Research*, vol. 6, no. 3, pp. 493–504, 2018, doi: 10.22036/PCR.2018.113197.1451.

[42] M. Abdel-Rahman, K. Issa, M. F. Zia, M. Alduraibi, M. Siraj, A. Ragheb, and S. Alshebeili, "High sensitivity vanadium–vanadium pentoxide–aluminium metal–insulator–metal diode," *Micro & Nano Letters*, vol. 13, no. 5, pp. 680–683, 2018, doi: 10.1049/mnl.2017.0728.

[43] E. W. III Cowell, E. William, J. F. Wager, B. J. Gibbons, and D. A. Keszler. "Amorphous multi-component metallic thin films for electronic devices.", *Google Patents*, *U.S. Patent 8,436,337*, 2013.

[44] S. Shriwastava and C. C. Tripathi, "Metal–Insulator–Metal Diodes: A Potential High Frequency Rectifier for Rectenna Application," *Journal of Electronic Materials*, vol. 48, no. 5, pp. 2635–2652, 2019, doi: 10.1007/s11664-018-06887-9.

[45] I. Wilke, Y. Oppliger, W. Herrmann, and F. K. Kneubühl, "Nanometer thin-film Ni-NiO-Ni diodes for 30 THz radiation," *Applied Physics A Solids and Surfaces*, vol. 58, no. 4, pp. 329–341, 1994, doi: 10.1007/bf00323606.

[46] C. Fumeaux, W. Herrmann, F. K. Kneubühl, and H. Rothuizen, "Nanometer thin-film Ni–NiO–Ni diodes for detection and mixing of 30 THz radiation," *Infrared Physics & Technology*, vol. 39, no. 3, pp. 123–183, 1998, doi: 10.1016/s1350-4495(98)00004-8.

[47] P. C. D. Hobbs, R. B. Laibowitz, and F. R. Libsch, "Ni–NiO–Ni tunnel junctions for terahertz and infrared detection," *Applied Optics*, vol. 44, no. 32, p. 6813, Nov. 2005, doi: 10.1364/ao.44.006813.

[48] C. Zhuang, L. Wang, Z. Dai, and D. Yang, “High Frequency Ni-NiO-Ag Metal-Insulator-Metal Tunnel Diodes Fabricated via Anodic Aluminum Oxide Templates,” *ECS Solid State Letters*, vol. 4, no. 5, pp. P39–P42, 2015, doi: 10.1149/2.0021505ssl.

[49] P. Esfandiari, G. Bernstein, P. Fay, W. Porod, B. Rakos, A. Zarandy, B. Berland, L. Boloni, G. Boreman, B. Lail, B. Monacelli, and A. Weeks, “Tunable antenna-coupled metal-oxide-metal (MOM) uncooled IR detector (invited paper),” *SPIE Proceedings*, 2005, doi: 10.1117/12.606874

[50] S. Krishnan, E. Stefanakos, and S. Bhansali, “Effects of dielectric thickness and contact area on current–voltage characteristics of thin film metal–insulator–metal diodes,” *Thin Solid Films*, vol. 516, no. 8, pp. 2244–2250, 2008, doi: 10.1016/j.tsf.2007.08.067.

[51] S. Zhang, L. Wang, C. Xu, D. Li, L. Chen, and D. Yang, “Fabrication of Ni-NiO-Cu Metal-Insulator-Metal Tunnel Diodes via Anodic Aluminum Oxide Templates,” *ECS Solid State Letters*, vol. 2, no. 1, pp. Q1–Q4, 2012, doi: 10.1149/2.001301ssl.

[52] I. Azad, M. K. Ram, D. Y. Goswami, and E. Stefanakos, “Fabrication and characterization of NiO based metal−insulator−metal diode using Langmuir-Blodgett method for high frequency rectification,” *AIP Advances*, vol. 8, no. 4, p. 045219, 2018, doi: 10.1063/1.5034455.

[53] E. C. Kinzel, R. L. Brown, J. C. Ginn, B. A. Lail, B. A. Slovick, and G. D. Boreman, “Design of an MOM diode-coupled frequency-selective surface,” *Microwave and Optical Technology Letters*, vol. 55, no. 3, pp. 489–493, 2013, doi: 10.1002/mop.27363.

[54] J. A. Bean, B. Tiwari, G. H. Bernstein, P. Fay, and W. Porod, “Thermal infrared detection using dipole antenna-coupled metal-oxide-metal diodes,” *Journal of Vacuum Science & Technology B: Microelectronics and Nanometer Structures*, vol. 27, no. 1, p. 11, 2009, doi: 10.1116/1.3039684.

[55] M. R. Abdel-Rahman, F. J. González, and G. D. Boreman, “Antenna-coupled metal-oxide-metal diodes for dual-band detection at 92.5 GHz and 28 THz,” *Electronics Letters*, vol. 40, no. 2, p. 116, 2004, doi: 10.1049/el:20040105.

[56] P. C. D. Hobbs, R. B. Laibowitz, F. R. Libsch, N. C. LaBianca, and P. P. Chiniwalla, “Efficient waveguide-integrated tunnel junction detectors at 1.6 µm,” *Optics Express*, vol. 15, no. 25, p. 16376, 2007, doi: 10.1364/oe.15.016376.

[57] A. B. Hoofring, V. J. Kapoor, and W. Krawczonek, “Submicron nickel-oxide-gold tunnel diode detectors for rectennas,” *Journal of Applied Physics*, vol. 66, no. 1, pp. 430–437, 1989, doi: 10.1063/1.343841.

[58] M. Bareiß, B. N. Tiwari, A. Hochmeister, G. Jegert, U. Zschieschang, H. Klauk, B. Fabel, G. Scarpa, G. Koblmuller, G. H. Bernstein, W. Porod, and P. Lugli, "Nano Antenna Array for Terahertz Detection," in IEEE Transactions on Microwave Theory and Techniques, vol. 59, no. 10, pp. 2751-2757, 2011, doi: 10.1109/TMTT.2011.2160200.

[59] K. Bhatt, S. Kumar, and C. C. Tripathi, “Highly sensitive Al/Al2O3/Ag MIM diode for energy harvesting applications,” *AEU - International Journal of Electronics and Communications*, vol. 111, p. 152925, 2019, doi: 10.1016/j.aeue.2019.152925.

[60] S. Shriwastava, D. Singh Arya, S. Sharma, K. Singh, P. Singh, and C. C. Tripathi, “A laser patterned zero bias Au/Al2O3/Mo metal-insulator-metal diode rectifier for RF detection,” *Solid-State Electronics*, vol. 171, p. 107870, Sep. 2020, doi: 10.1016/j.sse.2020.107870.

[61] S. B. Tekin, A. D. Weerakkody, N. Sedghi, S. Hall, M. Werner, J. S. Wrench, P. R. Chalker, and I. Z. Mitrovic, “Single and triple insulator Metal-Insulator-Metal diodes for infrared rectennas,” *Solid-State Electronics*, vol. 185, p. 108096, 2021, doi: 10.1016/j.sse.2021.108096.

[62] S. Shriwastava and C. C. Tripathi, “Metal–Insulator–Metal Diodes: A Potential High Frequency Rectifier for Rectenna Application,” *Journal of Electronic Materials*, vol. 48, no. 5, pp. 2635–2652, 2019, doi: 10.1007/s11664-018-06887-9.

[63] J. A. Bean, A. Weeks, and G. D. Boreman, “Performance Optimization of Antenna-Coupled Al/AlO$_x$/Pt Tunnel Diode Infrared Detectors,” *IEEE Journal of Quantum Electronics*, vol. 47, no. 1, pp. 126–135, 2011, doi: 10.1109/jqe.2010.2081971.

[64] L. E. Dodd, S. A. Shenton, A. J. Gallant, and D. Wood, “Improving Metal-Oxide-Metal (MOM) Diode Performance Via the Optimization of the Oxide Layer,” *Journal of Electronic Materials*, vol. 44, no. 5, pp. 1361–1366, 2015, doi: 10.1007/s11664-015-3624-9.

[65] R. Urcuyo, D. L. Duong, H. Y. Jeong, M. Burghard, and K. Kern, “High Performance Graphene-Oxide-Metal Diode through Bias-Induced Barrier Height Modulation,” *Advanced Electronic Materials*, vol. 2, no. 9, p. 1600223, 2016, doi: 10.1002/aelm.201600223.

[66] A. Singh, R. Ratnadurai, R. Kumar, S. Krishnan, Y. Emirov, and S. Bhansali, “Fabrication and current–voltage characteristics of NiOx/ZnO based MIIM tunnel diode,” *Applied Surface Science*, vol. 334, pp. 197–204, 2015, doi: 10.1016/j.apsusc.2014.09.160.

[67] A. A. Khan, G. Jayaswal, F. A. Gahaffar, and A. Shamim, “Metal-insulator-metal diodes with sub-nanometre surface roughness for energy-harvesting applications,” *Microelectronic Engineering*, vol. 181, pp. 34–42, 2017, doi: 10.1016/j.mee.2017.07.003.

[68] I. Azad, M. K. Ram, D. Y. Goswami, and E. Stefanakos, “Fabrication and Characterization of ZnO Langmuir–Blodgett Film and Its Use in Metal–Insulator–Metal Tunnel Diode,” *Langmuir*, vol. 32, no. 33, pp. 8307–8314, Aug. 2016, doi: 10.1021/acs.langmuir.6b02182.

[69] M. F. Zia, M. R. Abdel-Rahman, N. F. Al-Khalli, and N. A. Debbar, “Fabrication and Characterization of Vanadium/Vanadium Pentoxide/Vanadium (V/V2O5/V) Tunnel Junction Diodes,” *Acta Physica Polonica A*, vol. 127, no. 4, pp. 1289–1291, 2015, doi: 10.12693/aphyspola.127.1289.

[70] M. Dagenais, K. Choi, F. Yesilkoy, A. N. Chryssis, and M. C. Peckerar, “Solar spectrum rectification using nano-antennas and tunneling diodes,” *SPIE Proceedings*, 2010, doi: 10.1117/12.845931

[71] K. Choi, F. Yesilkoy, A. Chryssis, M. Dagenais, and M. Peckerar, “New Process Development for Planar-Type CIC Tunneling Diodes,” *IEEE Electron Device Letters*, vol. 31, no. 8, pp. 809–811, 2010, doi: 10.1109/led.2010.2049637.

[72] P. Periasamy, J. J. Berry, A. A. Dameron, J. D. Bergeson, D. S. Ginley, R. P. O'Hayre, and P. A. Parilla, “Fabrication and characterization of MIM diodes based on Nb/NB2O5 via a rapid screening technique,” *Advanced Materials*, vol. 23, no. 27, pp. 3080–3085, 2011.

[73] M. L. Chin, P. Periasamy, T. P. O'Regan, M. Amani, C. Tan, R. P. O'Hayre, J. J. Berry, R. M. Osgood, P. A. Parilla, D. S. Ginley, and M. Dubey, “Planar metal–insulator–metal diodes based on the Nb/Nb2O5/X material system,” *Journal of Vacuum Science & Technology B, Nanotechnology and Microelectronics: Materials, Processing, Measurement, and Phenomena*, vol. 31, no. 5, p. 051204, Sep. 2013, doi: 10.1116/1.4818313.

[74] M. N. Gadalla, M. Abdel-Rahman, and A. Shamim, “Design, Optimization and Fabrication of a 28.3 THz Nano-Rectenna for Infrared Detection and Rectification,” *Scientific Reports*, vol. 4, no. 1, 2014, doi: 10.1038/srep04270.

[75] M. Inac, A. Shafique, M. Ozcan, and Y. Gurbuz, “Device characteristics of antenna-coupled metal-insulator-metal diodes (rectenna) using al2O3, tio2, and cr2O3as insulator layer for energy harvesting applications,” SPIE Proceedings, 2015, doi: 10.1117/12.2188161

[76] M. Aldrigo, M. Dragoman, M. Modreanu, I. Povey, S. Iordanescu, D. Vasilache, A. Dinescu, M. Shanawani, and D. Masotti, “Harvesting Electromagnetic Energy in the V-Band Using a Rectenna Formed by a Bow Tie Integrated with a 6-nm-Thick Au/HfO2/Pt Metal-Insulator-Metal Diode,” *IEEE Transactions on Electron Devices*, vol. 65, no. 7, pp. 2973–2980, 2018, doi: 10.1109/ted.2018.2835138.

[77] S. Almalki, S. B. Tekin, N. Sedghi, S. Hall, and I. Z. Mitrovic, “Applicability of Sc2O3 versus Al2O3 in MIM rectifiers for IR rectenna,” *Solid-State Electronics*, vol. 184, p. 108082, 2021, doi: 10.1016/j.sse.2021.108082.

[78] G. L. Gutsev, P. Jena, H.-J. Zhai, and L.-S. Wang, “Electronic structure of chromium oxides, CrOn− and CrOn (n=1–5) from photoelectron spectroscopy and density functional theory calculations,” *The Journal of Chemical Physics*, vol. 115, no. 17, pp. 7935–7944, 2001, doi: 10.1063/1.1405438.

[79] S. Grover and G. Moddel, “Engineering the current–voltage characteristics of metal–insulator–metal diodes using double-insulator tunnel barriers,” *Solid-State Electronics*, vol. 67, no. 1, pp. 94–99, 2012, doi: 10.1016/j.sse.2011.09.004.

[80] P. Maraghechi, A. Foroughi-Abari, K. Cadien, and A. Y. Elezzabi, “Enhanced rectifying response from metal-insulator-insulator-metal junctions,” *Applied Physics Letters*, vol. 99, no. 25, p. 253503, 2011, doi: 10.1063/1.3671071.

[81] I. Nemr Noureddine, N. Sedghi, I. Z. Mitrovic, and S. Hall, “Barrier tuning of atomic layer deposited Ta2O5and Al2O3in double dielectric diodes,” *Journal of Vacuum Science & Technology B, Nanotechnology and Microelectronics: Materials, Processing, Measurement, and Phenomena*, vol. 35, no. 1, p. 01A117, 2017, doi: 10.1116/1.4974219.

[82] A. Belkadi, A. Weerakkody, and G. Moddel, “Demonstration of resonant tunneling effects in metal-double-insulator-metal (MI2M) diodes,” *Nature Communications*, vol. 12, no. 1, 2021, doi: 10.1038/s41467-021-23182-0.

[83] B. Pelz and G. Moddel, “Demonstration of distributed capacitance compensation in a metal-insulator-metal infrared rectenna incorporating a traveling-wave diode,” *Journal of Applied Physics*, vol. 125, no. 23, p. 234502, 2019, doi: 10.1063/1.5083155.

[84] A. Y. Elsharabasy, A. S. Negm, M. H. Bakr, and M. J. Deen, “Global Optimization of Rectennas for IR Energy Harvesting at 10.6 µm,” *IEEE Journal of Photovoltaics*, vol. 9, no. 5, pp. 1232–1239, 2019, doi: 10.1109/jphotov.2019.2927142.

[85] D. Matsuura, M. Shimizu, and H. Yugami, “High-current density and high-asymmetry MIIM diode based on oxygen-non-stoichiometry controlled homointerface

structure for optical rectenna," *Scientific Reports*, vol. 9, no. 1, 2019, doi: 10.1038/s41598-019-55898-x.

[86] A. H. Alshehri, A. Shahin, K. Mistry, K. H. Ibrahim, M. Yavuz, and K. P. Musselman, "Metal-Insulator-Insulator-Metal Diodes with Responsivities Greater Than 30 A W −1 Based on Nitrogen-Doped TiO x and AlO x Insulator Layers," *Advanced Electronic Materials*, vol. 7, no. 11, p. 2100467, 2021, doi: 10.1002/aelm.202100467.

[87] P. Maraghechi, A. Foroughi-Abari, K. Cadien, and A. Y. Elezzabi, "Enhanced rectifying response from metal-insulator-insulator-metal junctions," *Applied Physics Letters*, vol. 99, no. 25, p. 253503, 2011, doi: 10.1063/1.3671071.

[88] I. N. Noureddine, N. Sedghi, J. Wrench, P. Chalker, I. Z. Mitrovic, and S. Hall, "Fabrication and modelling of MInM diodes with low turn-on voltage," *Solid-State Electronics*, vol. 184, p. 108053, 2021, doi: 10.1016/j.sse.2021.108053.

[89] G. Moddel, "Will Rectenna Solar Cells Be Practical?," *Will Rectenna Solar Cells Be Practical? | Springer*, 2013.

[90] I. Z. Mitrovic, A. D. Weerakkody, N. Sedghi, S. Hall, J. F. Ralph, J. S. Wrench, P. R. Chalker, Z. Luo, and S. Beeby, "(Invited) Tunnel-Barrier Rectifiers for Optical Nantennas," *ECS Transactions*, vol. 72, no. 2, pp. 287–299, 2016, doi: 10.1149/07202.0287ecst.

[91] A. Y. Elsharabasy, M. H. Bakr, and M. J. Deen, "Towards an optimal MIIM diode for rectennas at 10.6 μm," *Results in Materials*, vol. 11, p. 100204, 2021, doi: 10.1016/j.rinma.2021.100204.

[92] P. Maraghechi, A. Foroughi-Abari, K. Cadien, and A. Y. Elezzabi, "Observation of resonant tunneling phenomenon in metal-insulator-insulator-insulator-metal electron tunnel devices," *Applied Physics Letters*, vol. 100, no. 11, p. 113503, 2012, doi: 10.1063/1.3694024.

[93] H. Deng, K. Endo, and K. Yamamura, "Comparison of thermal oxidation and plasma oxidation of 4H-SiC (0001) for surface flattening," *Applied Physics Letters*, vol. 104, no. 10, p. 101608, Mar. 2014, doi: 10.1063/1.4868487.

[94] D. Maurya, A. Sardarinejad, and K. Alameh, “Recent Developments in R.F. Magnetron Sputtered Thin Films for pH Sensing Applications—An Overview,” *Coatings*, vol. 4, no. 4, pp. 756–771, Dec. 2014, doi: 10.3390/coatings4040756.

[95] N. H. Rased, B. Vengadaesvaran, S. R. S. Raihan, and N. A. Rahim, “Introduction to solar energy and its conversion into electrical energy by using dye-sensitized solar cells,” *Energy Materials*, pp. 139–178, 2021, doi: 10.1016/b978-0-12-823710-6.00006-6.

[96] C. Wirtz *et al.*, “Atomic layer deposition on 2D transition metal chalcogenides: layer dependent reactivity and seeding with organic ad-layers,” *Chemical Communications*, vol. 51, no. 92, pp. 16553–16556, 2015, doi: 10.1039/c5cc05726d.

[97] A. Pimpin and W. Srituravanich, “Review on Micro- and Nanolithography Techniques and their Applications,” *Engineering Journal*, vol. 16, no. 1, pp. 37–56, Jan. 2012, doi: 10.4186/ej.2012.16.1.37.

[98] M. Kaestner *et al.*, “Advanced electric-field scanning probe lithography on molecular resist using active cantilever,” *Journal of Micro/Nanolithography, MEMS, and MOEMS*, vol. 14, no. 3, p. 031202, Jun. 2015, doi: 10.1117/1.jmm.14.3.031202.

[99] J. Kischkat, S. Peters, B. Gruska, M. Semtsiv, M. Chashnikova, M. Klinkmüller, O. Fedosenko, S. Machulik, A. Aleksandrova, G. Monastyrskyi, Y. Flores, and W. Ted Masselink, “Mid-infrared optical properties of thin films of aluminum oxide, titanium dioxide, silicon dioxide, aluminum nitride, and silicon nitride,” *Applied Optics*, vol. 51, no. 28, p. 6789, 2012, doi: 10.1364/ao.51.006789.

[100] A. Parretta, M. K. Jayaraj, A. Di Nocera, S. Loreti, L. Quercia, and A. Agati, “Electrical and Optical Properties of Copper Oxide Films Prepared by Reactive RF Magnetron Sputtering,” *Physica Status Solidi (a)*, vol. 155, no. 2, pp. 399–404, 1996, doi: 10.1002/pssa.2211550213.

[101] M. R. Querry, *Optical constants*. Aberdeen Proving Ground, MD: US Army Armament, Munitions & Chemical Command, Chemical Research & Development Center, 1985.

[102] L.-Y. Xie, D.-Q. Xiao, J.-X. Pei, J. Huo, X. Wu, W.-J. Liu, and S.-J. Ding, “Growth, physical and electrical characterization of nickel oxide thin films prepared by plasma-enhanced atomic layer deposition using nickelocene and oxygen precursors,” *Materials Research Express*, vol. 7, no. 4, p. 046401, 2020, doi: 10.1088/2053-1591/ab82c9.

[103] A. Kashir, H.-W. Jeong, G.-H. Lee, P. Mikheenko, and Y. H. Jeong, “Dielectric Properties of Strained Nickel Oxide Thin Films,” *Journal of the Korean Physical Society*, vol. 74, no. 10, pp. 984–988, 2019, doi: 10.3938/jkps.74.984.

[104] W. Cho, S. S. Lee, T.-M. Chung, C. G. Kim, K.-S. An, J.-P. Ahn, J.-Y. Lee, J.-W. Lee, and J.-H. Hwang, “Nonvolatile Memory Effects of NiO Layers Embedded in Al2O3 High-k Dielectrics Using Atomic Layer Deposition,” *Electrochemical and Solid-State Letters*, vol. 13, no. 6, p. H209, 2010, doi: 10.1149/1.3380827.

[105] M. R. Abdel-Rahman, B. Monacelli, A. R. Weeks, G. Zummo, and G. D. Boreman, “Design, fabrication, and characterization of antenna-coupled metal-oxide-metal diodes for dual-band detection,” *Optical Engineering*, vol. 44, no. 6, p. 066401, 2005, doi: 10.1117/1.1929647.

[106] P. Das, A. Jones, J. T. Gibbon, V. R. Dhanak, T. Partida-Manzanera, J. W. Roberts, R. Potter, P. R. Chalker, S.-J. Cho, I. G. Thayne, R. Mahapatra, and I. Z. Mitrovic, “Band Line-up Investigation of Atomic Layer Deposited TiAlO and GaAlO on GaN,” *ECS Journal of Solid State Science and Technology*, vol. 9, no. 6, p. 063003, 2020, doi: 10.1149/2162-8777/aba4f4.

[107] M. D. Groner, J. W. Elam, F. H. Fabreguette, and S. M. George, “Electrical characterization of thin Al2O3 films grown by atomic layer deposition on silicon and various metal substrates,” *Thin Solid Films*, vol. 413, no. 1–2, pp. 186–197, 2002, doi: 10.1016/s0040-6090(02)00438-8.

[108] F. Argall and A. K. Jonscher, “Dielectric properties of thin films of aluminium oxide and silicon oxide,” *Thin Solid Films*, vol. 2, no. 3, pp. 185–210, 1968, doi: 10.1016/0040-6090(68)90002-3.

[109] S. W. Smith, K. G. McAuliffe, and J. F. Conley, “Atomic layer deposited high-k nanolaminate capacitors,” *Solid-State Electronics*, vol. 54, no. 10, pp. 1076–1082, 2010, doi: 10.1016/j.sse.2010.05.007.

[110] G. D. Wilk, R. M. Wallace, and J. M. Anthony, “High-κ gate dielectrics: Current status and materials properties considerations,” *Journal of Applied Physics*, vol. 89, no. 10, pp. 5243–5275, 2001, doi: 10.1063/1.1361065.

[111] P. D. Ye, , B. Yang, K. K. Ng, J. Bude, G. D. Wilk, S. Halder, and J. C. Hwang, “GaN metal-oxide-semiconductor high-electron-mobility-transistor with atomic layer deposited Al2O3 as gate dielectric,” *Applied Physics Letters*, vol. 86, no. 6, p. 063501, 2005, doi: 10.1063/1.1861122.

[112] J. Yota, H. Shen, and R. Ramanathan, “Characterization of atomic layer deposition HfO2, Al2O3, and plasma-enhanced chemical vapor deposition Si3N4 as metal–insulator–metal capacitor dielectric for GaAs HBT technology,” *Journal of Vacuum Science & Technology A: Vacuum, Surfaces, and Films*, vol. 31, no. 1, p. 01A134, 2013, doi: 10.1116/1.4769207.

[113] N. H. Langton and D. Matthews, “The dielectric constant of zinc oxide over a range of frequencies,” *British Journal of Applied Physics*, vol. 9, no. 11, pp. 453–456, 1958, doi: 10.1088/0508-3443/9/11/308.

[114] A. R. Hutson, “Hall Effect Studies of Doped Zinc Oxide Single Crystals,” *Physical Review*, vol. 108, no. 2, pp. 222–230, 1957, doi: 10.1103/physrev.108.222.

[115] Q. Cui, M. Sakhdari, B. Chamlagain, H.-J. Chuang, Y. Liu, M. M.-C. Cheng, Z. Zhou, and P.-Y. Chen, “Ultrathin and Atomically Flat Transition-Metal Oxide: Promising Building Blocks for Metal–Insulator Electronics,” *ACS Applied Materials & Interfaces*, vol. 8, no. 50, pp. 34552–34558, 2016, doi: 10.1021/acsami.6b11302.

[116] M. D. Stamate, “Dielectric properties of TiO2 thin films deposited by a DC magnetron sputtering system,” *Thin Solid Films*, vol. 372, no. 1–2, pp. 246–249, 2000, doi: 10.1016/s0040-6090(00)01027-0.

[117] N. Rausch and E. P. Burte, “Thin TiO2 Films Prepared by Low Pressure Chemical Vapor Deposition,” *Journal of The Electrochemical Society*, vol. 140, no. 1, pp. 145–149, 1993, doi: 10.1149/1.2056076.

[118] V. A. Shvets, V. N. Kruchinin, and V. A. Gritsenko, “Dispersion of the refractive index in high-k dielectrics,” *Optics and Spectroscopy*, vol. 123, no. 5, pp. 728–732, 2017, doi: 10.1134/s0030400x17110194.

[119] E. S. Andrés, M. Toledano-Luque, A. del Prado, M. A. Navacerrada, I. Mártil, G. González-Díaz, W. Bohne, J. Röhrich, and E. Strub, “Physical properties of high pressure reactively sputtered TiO2,” *Journal of Vacuum Science & Technology A: Vacuum, Surfaces, and Films*, vol. 23, no. 6, pp. 1523–1530, Nov. 2005, doi: 10.1116/1.2056554.

[120] M. Takeuchi, T. Itoh, and H. Nagasaka, “Dielectric properties of sputtered TiO2 films,” *Thin Solid Films*, vol. 51, no. 1, pp. 83–88, 1978, doi: 10.1016/0040-6090(78)90215-8.

[121] D.-D. Wang, F.-Z. Zhou, J.-X. Cao, L.-B. Li, and G.-L. Li, “Impact of Cu 2 O doping on high dielectric properties of CuO ceramics,” *Current Applied Physics*, vol. 17, no. 5, pp. 781–784, 2017, doi: 10.1016/j.cap.2017.02.024.

[122] D. C. Dube, D. Agrawal, S. Agrawal, and R. Roy, “High temperature dielectric study of Cr2O3 in microwave region,” *Applied Physics Letters*, vol. 90, no. 12, p. 124105, 2007, doi: 10.1063/1.2716336.

[123] P. H. Fang and W. S. Brower, “Dielectric Constant ofCr2O3Crystals,” *Physical Review*, vol. 129, no. 4, pp. 1561–1561, 1963, doi: 10.1103/physrev.129.1561.

[124] V. D. Wheeler, D. I. Shahin, M. J. Tadjer, and C. R. Eddy, “Band Alignments of Atomic Layer Deposited ZrO2and HfO2High-k Dielectrics with (-201) β-Ga2O3,” *ECS Journal of Solid State Science and Technology*, vol. 6, no. 2, pp. Q3052–Q3055, 2016, doi: 10.1149/2.0131702jss.

[125] J. F. Conley and N. Alimardani, “Impact of Electrode Roughness on Metal-Insulator-Metal (MIM) Diodes and Step Tunneling in Nanolaminate Tunnel Barrier

Metal-Insulator-Insulator-Metal (MIIM) Diodes," *Rectenna Solar Cells*, pp. 111–134, 2013, doi: 10.1007/978-1-4614-3716-1_6.

[126] B. Thomas and S. Jayalekshmi, "Dielectric properties of vanadium pentoxide thin films in the audiofrequency range," *Journal of Non-Crystalline Solids*, vol. 113, no. 1, pp. 65–72, 1989, doi: 10.1016/0022-3093(89)90319-0.

[127] A. Belosludtsev, Y. Yakimov, R. Mroczyński, S. Stanionytė, M. Skapas, D. Buinovskis, and N. Kyžas, "Effect of Annealing on Optical, Mechanical, Electrical Properties and Structure of Scandium Oxide Films," *physica status solidi (a)*, vol. 216, no. 18, p. 1900122, 2019, doi: 10.1002/pssa.201900122.

[128] L. V. Yakovkina, T. P. Smirnova, V. O. Borisov, V. N. Kichai, and V. V. Kaichev, "Synthesis and properties of dielectric (HfO2)1 − x (Sc2O3) x films," *Inorganic Materials*, vol. 49, no. 2, pp. 172–178, 2013, doi: 10.1134/s0020168513020234.

[129] J. Kim, R. Mehandru, B. Luo, F. Ren, B. P. Gila, A. H. Onstine, C. R. Abernathy, S. J. Pearton, and Y. Irokawa, "Inversion behavior in Sc2O3/GaN gated diodes," *Applied Physics Letters*, vol. 81, no. 2, pp. 373–375, 2002, doi: 10.1063/1.1492852.

Chapter 3

3. Modelling of rectenna devices

According to the conservation of energy law, a particle can either overcome a barrier or bounce back after hitting it in classical mechanics where the total amount of kinetic and potential energy must be conserved. Therefore, when the energy of the barrier is greater than the particle's kinetic energy (KE), electrons cannot pass through the barrier and no transportation occurs. However, in quantum mechanics (QM), it is explained that the particles can propagate through the potential barriers as wavefunctions via the physical phenomenon called tunnelling. In a QM system, the propagation of these wavefunctions are explained by the Schrödinger equation which was discovered by Erwin Schrödinger in 1926 [1,2].

Understanding the conduction mechanisms of dielectric films is essential for the successful utilization of these materials. In dielectric films, there are mainly two different types of conduction mechanisms: bulk-limited and electrode-limited. In the bulk-limited conduction, the electrical characteristics of the actual dielectric affect the current transport. This mechanism helps to determine a number of crucial physical properties of the dielectric films such as relaxation time (the time it takes for a material's polarisation to respond to a change in an external electric field), density of states (DOS) in the conduction band (the number of available energy levels for charge carriers within a material's conduction band), carrier drift mobility (the ability of charge carriers to move through a material in response to an applied electric field), trap level (the energy level within the electronic band gap of a material where charge carriers can become trapped), trap spacing (the separation between different trap sites at which charge carriers can become trapped), and the trap density (the density of electronic states within a material that can capture and trap charge carriers, preventing them from travelling freely). On the other hand, in the electrode-limited, the conduction is governed by the electrical behaviour at the electrode/dielectric interface where the barrier height or effective mass of the dielectric films can be extracted [3]. In this chapter, several conduction mechanisms that can affect the performance of single (MIM) and multiple (MI^{n}M) dielectric diodes are explained.

3.1 Conduction mechanisms in MIM diodes

In a rectenna system, the rectifier can either be semiconductor (p-n junction or Schottky diode) or dielectric based (MIM diode). By using Schottky diode-based rectennas, it has previously been demonstrated that rectennas are quite efficient at radio-frequency (RF) and micro wave (MW) frequencies, but they still have a number of drawbacks when it comes to harvesting infrared (IR) energies. Semiconductor-based diodes are insufficient for high frequency rectification (in THz). As stated by Hall *et al*. [4], p-n junction diodes use minority carrier (electrons in p-type material) injection to drive current during forward bias. When a reverse bias is applied, there is a recovery time needed for the minority carrier charges to be removed, during which a non-rectifying current flow. Therefore, removal of electrons occurs through a reverse current and recombination with majority carriers (holes), both of which are relatively slow processes. For this reason, p-n junction diodes cannot efficiently operate in the THz region.

As another semiconductor-based diode, Schottky diodes outperform p-n junction diodes at high frequencies because majority carriers (electrons for a metal-n-type semiconductor structure) carry the current, which is injected into the metal side of the diode junction. Metals do not store charge, so the electrons are stored within the dielectric relaxation time of the metal, which is determined by its conductivity and permittivity. The initial limiting factor for the Schottky diode's frequency response is its junction capacitance. Besides this, at high THz frequencies, another limitation is the dielectric relaxation response of the n-type material, which depends on its conductivity, doping density, and charge carrier mobility. These constraints make the semiconductor based diodes inefficient for functioning in THz spectrum [4].

However, the MIM diode is a promising contender for high frequencies since it functions based on the quantum mechanical tunnelling of electrons through the insulator. The transmission time of charge carriers across the dielectric is inversely proportional with the tunnelling probability and it is in the femtosecond (fs) range. Therefore, if the parasitic capacitance is decreased sufficiently the device can operate at THz frequencies [4,5]. For these reasons, it is crucial to suppress the effect of thermionic conduction mechanisms and have dominant quantum mechanical tunnelling in the MIMs to have more efficient THz applications [6].

3.1.1 Schottky emission (SE)

In Schottky emission (SE), which is an electrode-limited conduction mechanism, the electrons in the metal can pass over the energy barrier at the metal/insulator interface and go to the insulator region when they obtain sufficient energy through thermal activation. SE in an MIM diode is shown in Fig. 3.1 under an applied negative bias to the top metal.

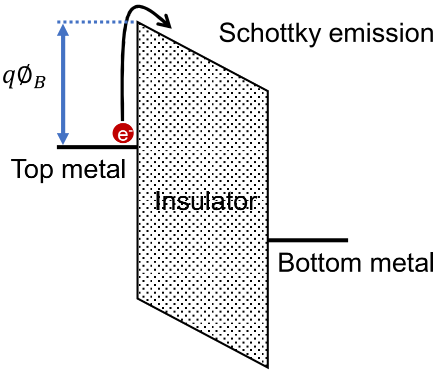

Figure 3.1. Energy band diagram of Schottky emission (SE) in MIM diodes.

The Schottky effect, also known as the image force can reduce the height of the energy barrier at the metal/insulator interface. The term "thermionic emission" or "Schottky emission" refers to this type of metal-to-dielectric conduction mechanism. In dielectric films, particularly at relatively high temperatures, this is one of the most frequently seen conduction mechanisms [3,7]. The current density (J_{SE}) generated by Schottky emission can be expressed by

$$J_{SE} = A^{*}T^{2}exp\left[\frac{-q\left(\emptyset_B-\sqrt{qE/4\pi\varepsilon_r\varepsilon_0}\right)}{kT}\right] \quad (3.1)$$

$$A^{*} = \frac{4\pi qk^{2}m^{*}}{h^{3}} = \frac{120m^{*}}{m_0} \quad (3.2)$$

where A^{*} is the effective Richardson constant, T is the absolute temperature, q is the electron charge, $q\emptyset_B$ is the Schottky barrier height, E is the electric field in the insulator, ε_r is the dynamic permittivity of dielectric (which is equal to n^2, where n is the refractive index at a specific frequency), ε_0 is the dielectric permittivity of free space, k is Boltzmann's constant, h is Planck's constant, m^{*} is the electron effective mass constant of the insulator, m_0 is the electron effective mass. In order to calculate the ε_r, natural logarithm of both sides of the expression (3.1) has to be taken

$$ln(J) = ln(A^*T^2)\left[\frac{-q(\emptyset_B-\sqrt{qE/4\pi\varepsilon_r\varepsilon_0})}{kT}\right] \tag{3.3}$$

Then, the equation can be written in a linear form for the square root of the electric field ($\sqrt{E}$) and the inverse temperature $(1/T)$

$$ln\left(\frac{J}{T^2}\right) = \frac{q(\sqrt{q/4\pi\varepsilon_r\varepsilon_0})}{kT}\sqrt{E} - \frac{q\emptyset_B}{kT} + ln(A^*) \tag{3.4}$$

Therefore, the slope of $ln\left(\frac{J}{T^2}\right)$ vs $\sqrt{E}$ becomes

$$SE_{Slope} = \frac{q(\sqrt{q/4\pi\varepsilon_r\varepsilon_0})}{kT}. \tag{3.5}$$

In order to confirm a Schottky conduction mechanism, the dynamic permittivity should be close to the square of the optical refractive index of the dielectric layer ($\varepsilon_r = n^2$). Then, the barrier height can be obtained from the intercept of the Schottky plot as

$$y - intercept = ln(A^*) - \frac{q\emptyset_B}{kT} \tag{3.6}$$

3.1.2 Poole-Frenkel emission (PF)

A bulk-limited conduction mechanism that results from defect energy states (traps) in the dielectric is Poole-Frenkel (PF) emission as shown in Fig. 3.2.

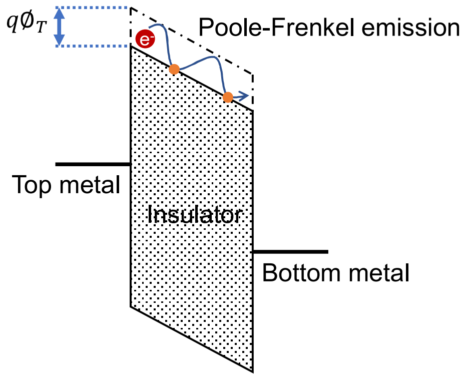

Figure 3.2. Energy band diagram of Poole-Frenkel (PF) emission in MIM diodes.

This mechanism is similar to SE where the electrons that have been thermally excited may emit from trap centres into the dielectric's conduction band [3,7]. These trap energy levels are important parameters in this mechanism. The Coulomb potential energy of an electron in a trapping centre can be lowered by an applied electric field across the dielectric layer. The thermal emission probability of an electron excited from the traps to the insulator's conduction band is increased by this decrease in barrier height. The current density (J_{PF}) resulting from the Coulombic attraction between these traps and the electrons is written as follows,

$$J_{PF} = qn_c\mu E\ exp\left(\frac{-q\phi_T - \sqrt{qE/\pi\varepsilon_r\varepsilon_0}}{k_BT}\right) \tag{3.7}$$

where n_c is the carrier density, μ is the electron drift mobility and $q\phi_T$ is the trap energy level. Similar to the SE, to examine the PF conduction mechanism, the dynamic permittivity (ε_r) can be extracted from the slope of the $ln\left(\frac{J}{E}\right)$ vs $\sqrt{E}$ which is

$$PF_{Slope} = \frac{q(\sqrt{q/\pi\varepsilon_r\varepsilon_0})}{kT}. \tag{3.8}$$

Also, the trap barrier height can be calculated from

$$y - intercept = ln(qn_c\mu E) - \frac{q\emptyset_T}{kT} \tag{3.9}$$

3.1.3 Trap-assisted-tunnelling (TAT)

As demonstrated in Fig. 3.3, trap-assisted-tunnelling (TAT) is a mechanism where the charge carriers tunnel from top metal to the bottom from the defects in the dielectric layer [8].

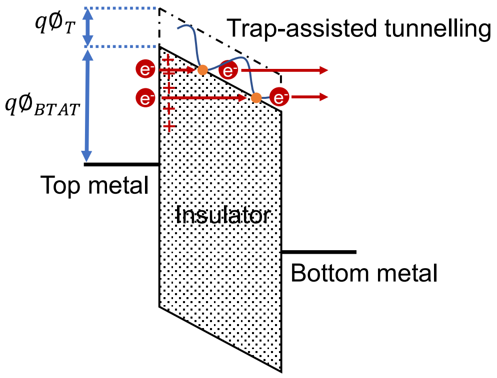

Figure 3.3. Energy band diagram of trap-assisted-tunnelling (TAT) in MIM diodes.

At low bias, electron injection into the bulk is prevented, which causes the interface to dominate the conduction. Therefore, the carrier transportation occurs when electrons from the electrode tunnel to the defect states close to the interface. This can be expressed as [7,9]

$$J_{TAT} = A_0 exp\left(-\frac{e}{kT}\emptyset_B\right)\ exp\left(\frac{-8\pi\sqrt{2em^*}\emptyset_{BTAT}^{3/2}}{3hE}\right) \tag{3.10}$$

where A_0 is constant and $\emptyset_{BTAT}$ is the trap-assisted barrier height.

At higher bias, the Eqn. 3.10 can be modified by including the Poole-Frenkel term in it to explain the temperature dependency of the conduction mechanism by

$$J = BEexp\left(\frac{-8\pi\sqrt{2em^*}\emptyset_{BTAT}^{3/2}}{3hE}\right) exp\left[-e\left(\emptyset_T - \frac{\sqrt{eE/\pi\varepsilon_r\varepsilon_0}}{kT}\right)\right] \tag{3.11}$$

where B is a constant and $\emptyset_T$ is the trap energy level coming from the PF term [9].

3.1.4 Fowler-Nordheim tunnelling (FNT)

When the applied electric field is sufficiently strong, the electron wave function can pass through the triangular potential barrier, resulting in Fowler-Nordheim tunnelling (FNT) [3,10] as shown in Fig. 3.4.

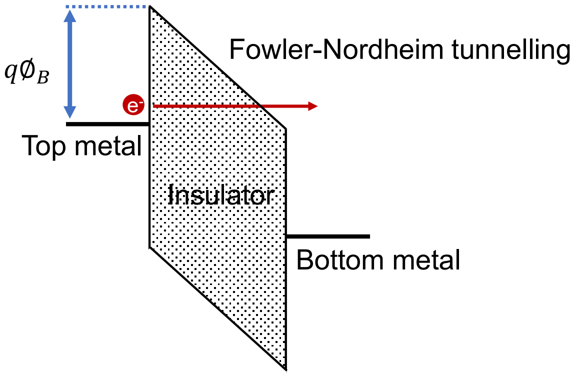

Figure 3.4. Energy band diagram of Fowler-Nordheim tunnelling (FNT) in MIM diodes.

The energy difference between the metal's Fermi level and the lowest edge of the oxide's conduction band is referred as the barrier height ($\emptyset_B$). The electrons can only tunnel through the triangular portion of the barrier when it is bent. The current density equation coming from FNT (J_{FNT}) can be written as

$$J_{FNT} = \frac{q^3 m E^2}{8\pi h q \emptyset_B m^*} exp\left[\frac{-8\pi(2qm^*)^{1/2}}{3hE}\emptyset_B^{3/2}\right] \tag{3.12}$$

where m^* is the effective mass in the dielectric and $\emptyset_B$ is the FNT barrier height.

For FN tunnelling to occur, the $ln(J/E^2)$ vs $1/E$ plot must be linear.

$$ln\left(\frac{J}{E^2}\right) = \left[\frac{-8\pi(2qm_T^*/m)^{1/2}}{3h}\emptyset_B^{3/2}\right]\frac{1}{E} + ln\left(\frac{q^3 m}{8\pi h q \emptyset_B m_T^*}\right) \tag{3.13}$$

Therefore, the FNT barrier height ($\emptyset_B$) can be calculated form the slope of this plot.

$$Slope = -6.83 \times 10^7 \sqrt{\left(\frac{m_T^*}{m_0}\right)\emptyset_B{}^3}\ (V/cm) \tag{3.14}$$

3.1.5 Direct tunnelling (DT)

In direct tunnelling (DT), the electrons can tunnel through the barrier at a lower bias than FNT if the barrier is ultra-thin (< 5 nm) as shown in Fig. 3.5.

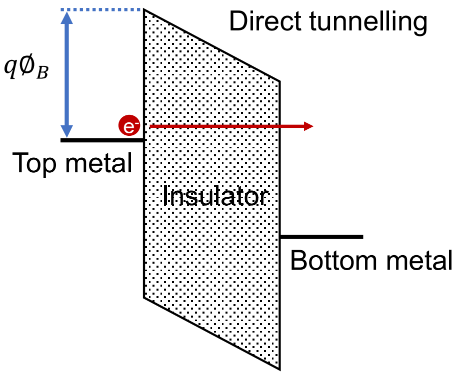

Figure 3.5. Energy band diagram of direct tunnelling (DT) in MIM diodes.

The approximated expression of DT can be written as [3,10]

$$J_{DT} = \frac{q^2}{8\pi^2 \hbar t}E^2\left(\phi_B - \frac{V_{app}}{2}\right) exp\left(\frac{-1.33\sqrt{2qm^*(\phi_B-(\phi_B^{3/2}-V_{app}))^3}}{\hbar E}\right) \tag{3.15}$$

where, t is the thickness of the dielectric and V_{app} is the applied bias.

3.1.6 Other conduction mechanisms in MIM diodes

Besides the summarised common conduction mechanisms in MIM diodes, there are several others that can been seen in dielectric films such as ohmic conduction. In this mechanism, the process occurs by the movement of the electrons and the holes in the conduction and the valence bands, respectively [3]. The current density (J) in ohmic conduction can be approximated as

$$J = \sigma E = n_C exp\left[\frac{-E_g}{2kT}\right] \tag{3.16}$$

where σ is the conductivity, n_C is the carrier density and E_g is the band gap of the dielectric.

Another mechanism that can be seen is the space-charge-limited conduction (SCLC) where the J vs V^2 plot should give a linear fit at any applied bias range for this mechanism to occur [11].

Besides these, the ionic conduction which is seen as a result of the migration of ions under an applied bias can be considered as a possible transport mechanism in dielectric films. The possible defects in the dielectric films can cause this movement of ions where they can travel through these defects under an external electric field [3]. The ionic conduction equation can be written as

$$J = J_0 exp\left(\frac{Eqd}{2kT} - \frac{q\phi_B}{kT}\right) \tag{3.17}$$

where J_0 is the proportional constant and d is the spacing between the defects. The other parameters have been defined in the above equations.

3.2 Conduction mechanisms in multiple dielectric MI^{n}M diodes

The use of multiple dielectric layers can improve the performance of MIM diodes taking the advantage of either resonant tunnelling (RT) or step tunnelling (ST). When compared to MIM diodes with a single insulator, MI^{2}M diodes with double insulators and different band offsets exhibit substantially higher responsivity and asymmetry values [12,13]. A detailed comparison has been done in Chapter 2. Figures 3.6 (a)-(b) show the formation of a quantum well (QW) in double and triple insulator diode configurations composed of different oxides, respectively.

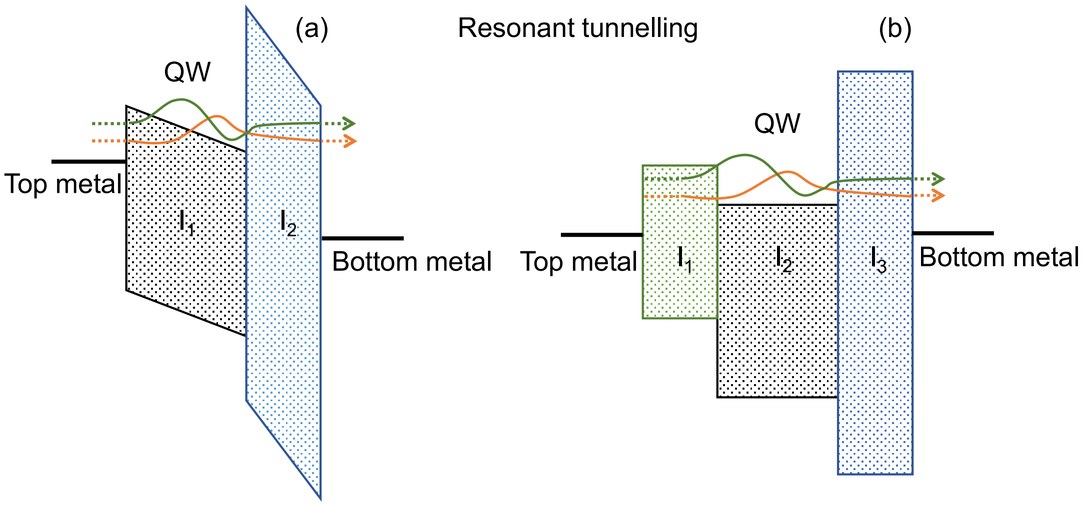

Figure 3.6. Schematics of band alignment for: (a) MI^2M diode under negative bias on top metal showing bound states in a quantum well and conditions for resonant tunneling to occur; (b) MI^3M diode under zero bias, showing existence of bound states in a quantum well.

In MI^2M configuration (Fig. 3.6 (a)), a triangular well forms at the interface of the two insulators when the Fermi level of the top metal is negatively biased. In Fig. 3.6 (b) an example of non-cascaded triple insulator configuration is shown where a natural quantum well occurs above the valence band of the middle insulating layer without any external bias. In both cases, there are localised eigenstates that are known as bound states, and electron waves can travel across these energy states by means of RT which improves current transmission [14,15].

For the step tunneling (ST) to occur, the metal Fermi level of the higher barrier side should overcome the conduction band of the lower barrier. This can be done with an applied reverse bias having opposite polarity on the top metal as shown in Fig. 3.7. This results in a sharp increase in current in one direction due to the decreased tunneling distance. The dominant mechanism in a particular device is determined by the metals, insulator materials, and thicknesses used [12,16–19].

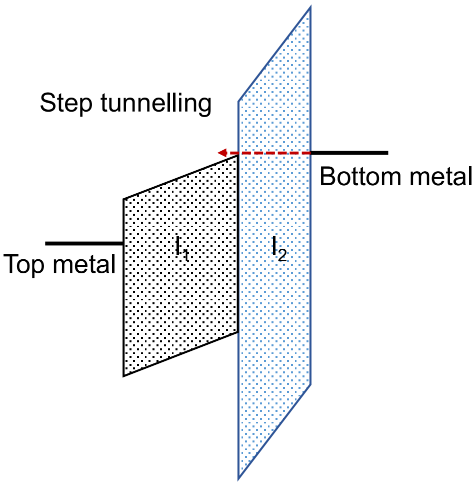

Figure 3.7. MI^{2}M diode under negative bias on the bottom metal showing step tunneling (ST).

For a better understanding of these two conduction mechanisms, the theoretical background of the in-house model developed for MI^{n}M device is given in the sequel.

3.3 MATLAB simulation model of MI^{n}M devices

As briefly mentioned before, for the RT to occur, the Fermi level of Metal 1 needs to be aligned with a bound state that exists in the quantum well (QW). This could be done by applying a negative voltage on Metal 1 and bending the left side of the barrier upwards as shown in Fig. 3.8 (a). Therefore, a maximum current transmission can be achieved.

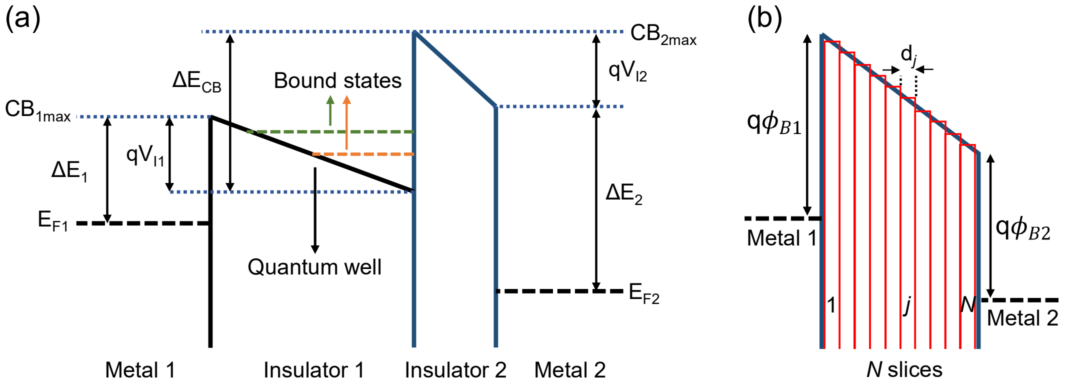

Fig. 3.8. (a) Energy band diagram of a MI^{2}M structure including the RT conduction under an applied negative bias on the Metal 1 and (b) energy barrier of a single dielectric divided into N slices.

The model for calculating the bound states in a quantum well is based on the Tsu–Esaki method [20] and the current density (*J*) is calculated using the transfer matrix method (TMM) where the insulator layers are assumed to consist of multiple slices with different barrier heights as shown in Fig. 3.8 (b). The number of slices (*N*) maintain the accuracy of the simulations and typically 50 slices per nanometer is sufficient for high accuracy. TMM method is used to calculate the transmission probability of electrons for tunneling through the barriers, while the tunnelling probability for each slice was determined by Wentzel-Kramers-Brillouin (WKB) approximation model

$$P_T(j) = exp\left[-\frac{2}{\hbar}\int_0^j \sqrt{2m^*\left(q\phi_{Bj} - E_{xj}\right)d_j}\right] \tag{3.18}$$

where m^* is the effective mass of electron, q is the electron charge, $\hbar$ is the reduced Planck's constant, k is the Boltzmann constant, E_x is the total energy of electrons in the tunneling direction, d_j is the thickness of the slice j.

As shown in Fig. 3.8 (a), the electrons on Metal 1 can be transmitted by tunneling through available energy states (bound states) in the QW. The current is determined by the Fermi-Dirac distribution of the average occupancy of each state as well as the density of the available states at each energy level. Assuming a potential difference between the Metal 1 ($V = V_{app}$) and Metal 2 ($V = 0$), the total current density (*J*) can be calculated by

$$J = \frac{m^*qkT}{2\pi^2\hbar^3}\int_0^\infty T_{coeff}(E_x)ln\left\{\frac{1+exp[(E_x-E_{F1})/kT]}{1+exp[(E_x-E_{F2}-qV_{app})/kT]}\right\}dE_x \tag{3.19}$$

where T is the temperature, T_{coeff} is the transmission probability, E_{F1} and E_{F2} are the Fermi levels of Metal 1 and Metal 2, respectively.

A MATLAB model was developed based on the theory of above-mentioned equations (3.18-3.19) by Liverpool group in the Department of Electrical Engineering and Electronics. The model was initially used for predicting the number of bound states in double insulator (MI^{2}M) structures and calculating the resulting current density due to resonant tunneling (RT) [14]. The model was then modified to predict the RT states in triple insulator (MI^{3}M) structures. Further details of the model have been published in several papers and theses which can be found in [10,11,14,15,21,22].

The MATLAB model was used to generate band diagram of several MI^{n}M (n = 1, 2, 3) structures to predict the RT states in a QW, as well as to plot the transmission and tunnelling probabilities leading to fitted I-V curve of associated device structure.

3.3.1 Modelling of MI^{2}M structures

As a demonstration for the MI^{2}M diodes with similar electrodes, the thickness of two oxides have been set as 4 nm and 1 nm, respectively. The 4 nm oxide layer was assumed to have a static dielectric permittivity (ε) of 25, while the ε of the 1 nm oxide was taken as 10. The ratio of the applied voltage of each specific layer (V_{ox}), as well as the band bending in the model is based on the series capacitance calculations [10] where

$$C_{eq} = \frac{C_{ox1}C_{ox1}}{C_{ox1}+C_{ox1}} \tag{3.20}$$

and

$$V_{ox1} = \frac{C_{eq}}{C1} \times V_{app}. \tag{3.21}$$

The capacitance of each layer is calculated using Eqn. 1.4. The barriers have been assumed to be 0.5 eV for the lower barrier (ϕ_{B1}), 2.5 eV for the higher (ϕ_{B2}) barrier and 2.0 eV for the well depth (ΔE_{CB}) which corresponds to the conduction band (CB) offset of two oxides. Figure 3.9 shows the flat band situation of a double insulator configuration without any external bias. A bound state can be formed in the quantum well under an applied bias V_{app} = 0.24 V as shown in Fig 3.10 (a). The M$_1$ work function (WF) was fixed at 0 eV and used as the reference point of the alignment. Therefore, the bands can be considered as bending with an applied of voltage (V_{app}) on M$_2$.

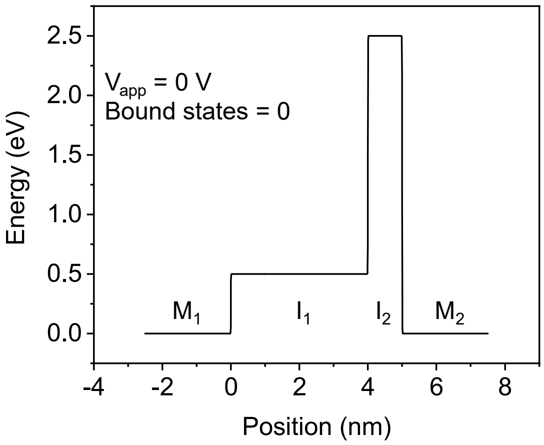

Figure 3.9. Energy band alignment of a MI^{2}M diode having 4:1 (nm) thickness and 25:10 ε ratios and same metal electrode work functions at zero-bias.

The energy of the bound state in the quantum well (E_{QW1}) was found to be 0.46 eV which also corresponds to the energy difference from the E_{F1}.

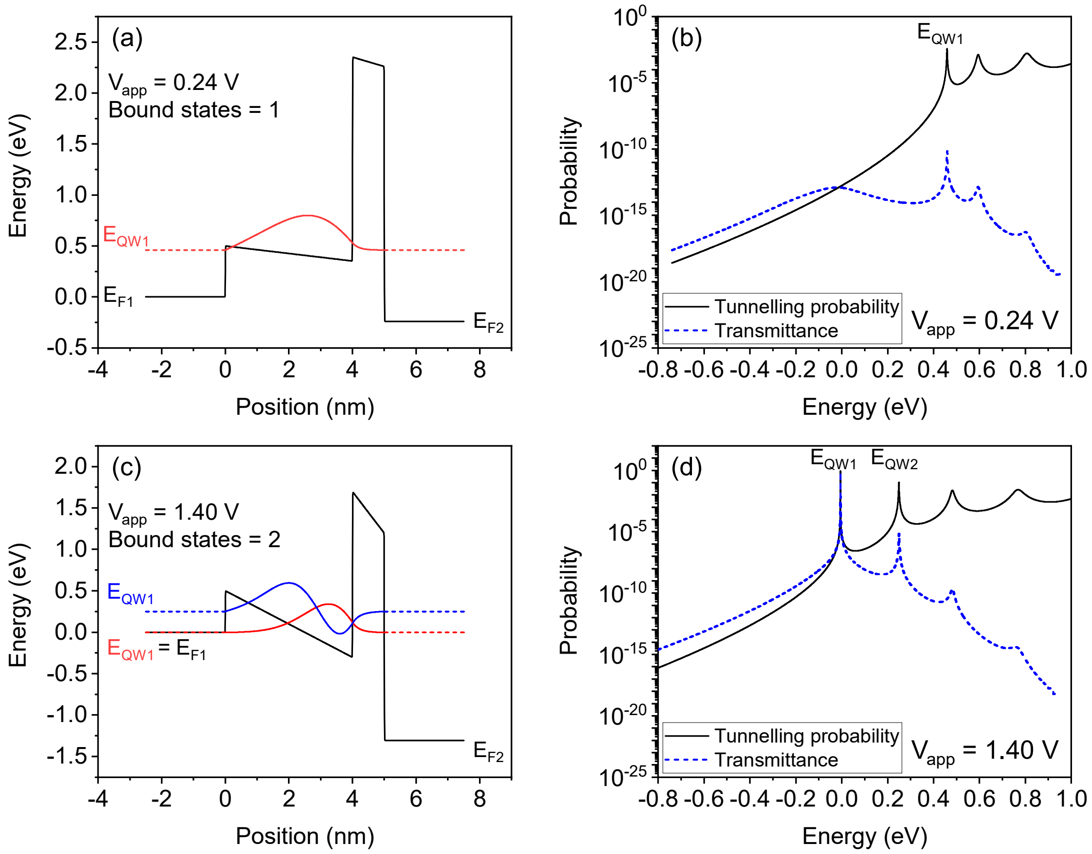

Figure 3.10. Energy band alignment of a MI^{2}M diode having 4:1 (nm) thickness and 25:10 ε ratios and same metal electrodes together with the associated transmission and tunneling probability plots (a)-(b) at 0.24 V and (c)-(d) 1.40 V.

It is also evident from the sharp peak at 0.46 eV in Fig. 3.10 (b) that there is a bound state in the QW however, with very low tunneling probability (4×10^{-3}) and transmittance (5.68×10^{-11}) values. This indicates that very small number of electrons are available to tunnel at this energy level as defined by Fermi-Dirac statistics. This is because of the large energy difference between the E_{F1} and E_{QW1}. If the V_{app} on M_2 is increased, the energy gap between E_{F1} and E_{QW1} can be decreased. This is shown in Fig. 3.10 (c) that when the V_{app} is 1.40 V, there are two bound states in the QW and there is no energy difference between E_{F1} and E_{QW1} which is also consistent with the tunneling probability (1) and the transmittance (1) and the values in Fig. 3.10 (d). This indicates that there is maximum current transmission at 1.4 V which is also seen in the fitted I-V characteristics of the associated diode in Fig. 3.11.

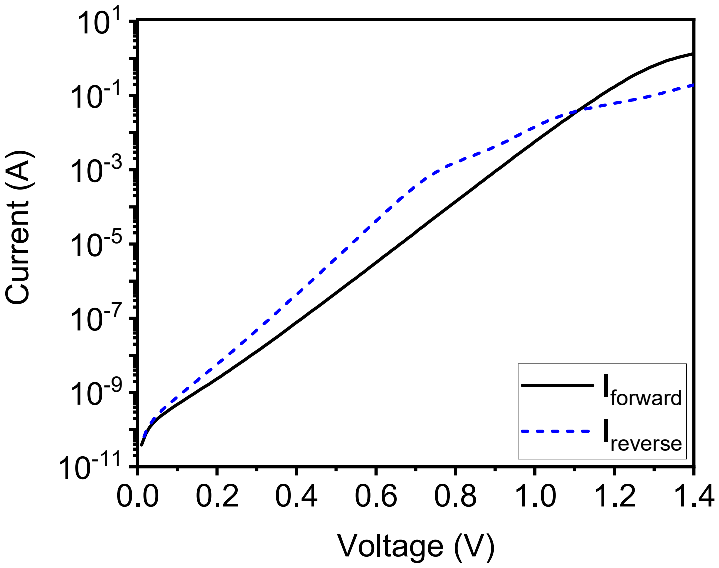

Figure 3.11. I-V curve of the MI^2M diode having 4:1 (nm) thickness and 25:10 ε ratios and same metal electrodes. The area and the effective mass ratio of the diode were considered as 10^4 μm^2 and $m^*=0.5m_0$

3.3.2 Modelling of MI^3M structures

Similar to MI^2M structures, MI^3M diodes can be modelled. Figure 3.12 shows two different formations of MI^3M diodes in cascaded and non-cascaded configurations with same electrode work functions at $V_{app} = 0$ V. In the cascaded from (Fig. 3.12 (a)), the insulators are aligned with an order of increasing barriers from left to right, while the lowest barrier is placed between two other insulators in the non-cascaded form (Fig. 3.12(b)).

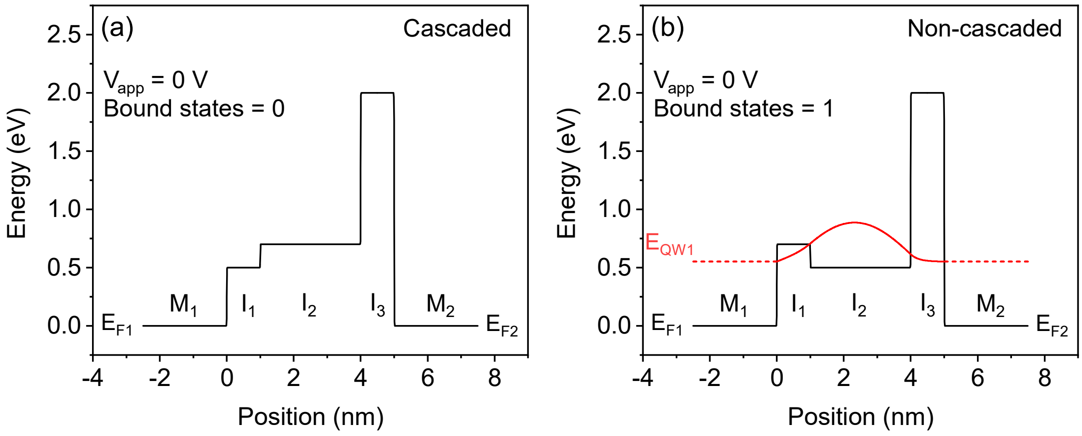

Figure 3.12. Energy band alignment of a MI^{3}M diode having 1:3:1 (nm) thickness and (a) 25:20:10 ε ratios for the cascaded and (b) 20:25:10 ε ratios for the non-cascaded. Both configurations have same metal electrode work functions and the V_{app} on M_2 is zero.

The barriers have been assumed to be 0.5 eV for the lowest, 0.7 eV for the middle, and 2.5 eV for the highest. At zero-bias, there is no QW in the cascaded formation, while a bound state with an energy of E_{QW1} = 0.55 eV is observed in the QW of the non-cascaded formation. As shown in Fig. 3.13 (a), the first bound state appears at V_{app} = 0.69 V and the corresponding energy E_{QW1} is 0.46 eV with a tunneling probability of 0.30 and transmittance of 6.3×10^{-9} (see Fig. 3.13 (b)). On the other hand, there are two bound states in the QW of the non-cascaded configuration where the energy gap between the E_{F1} and E_{QW1} is 0.26 eV as shown in Fig. 3.13 (c). Therefore, the tunneling probability (0.42) and the transmittance (2.1×10^{-5}) are higher as expected (see Fig. 3.13 (d)).

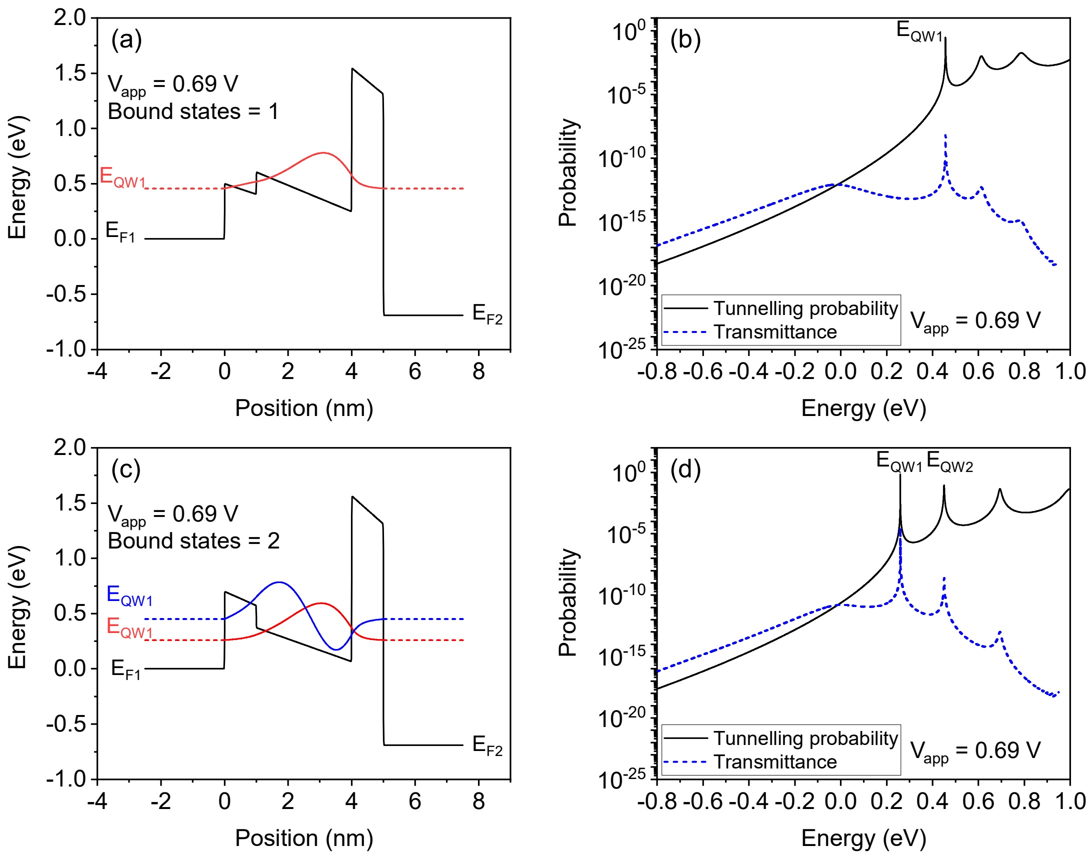

Figure 3.13. Energy band alignment together with the transmission and tunneling probability plots of (a)-(b) cascaded (c)-(d) non-cascaded MI^{3}M diodes having 1:3:1 (nm) thickness and same metal electrodes at 0.69 V.

For comparison, the I-V curves of these two configurations in forward bias (I_{forw}) are shown in Fig. 3.14. Maximum transmissions were seen at 1.75 V and at 1.40 V for the cascaded and non-cascaded configurations, respectively. It can be seen that the current density of the non-cascaded configuration is higher than for the cascaded one due to the difference in the band alignment between two configurations. In the non-cascaded configuration, the insulator with the highest electron affinity is placed between the other insulators which forms a natural quantum well and increase the tunneling probability at lower voltages. Further applications of the modelling presented here are shown in Chapter 6 for two different MI^{3}M configurations with the results compared to the experimental I-V data.

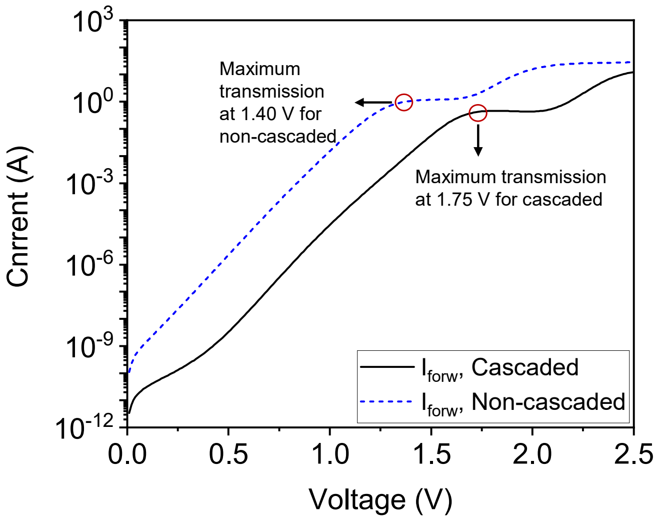

Figure 3.14. I-V characteristics in forward bias for cascaded and non-cascaded MI^3M diodes with same metal electrodes.

3.4 Circular-patch antenna design for 28.3 THz

In this thesis, a dipole microstrip circular patch antenna has been designed for the integration with the MIM didoes to detect and rectify 28.3 THz radiation. A 3-dimensional (3D) image of the dipole circular patch rectenna is shown in Fig. 3.15.

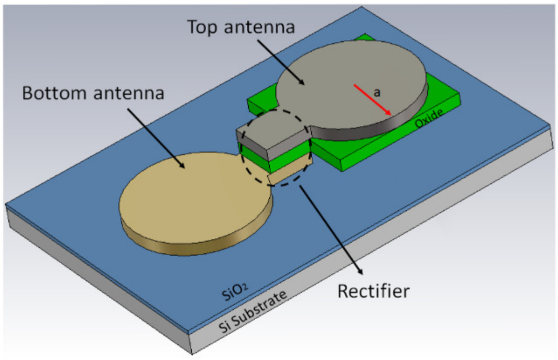

Figure 3.15. A rectenna structure with dipole (1 × 2) microstrip circular antenna patches on SiO_2/Si substrate.

In order to maximize the coupling efficiency of incident EM radiation to the receiving antenna, the antenna dimensions were optimised based on two main performance parameters. These are the S11 (reflection coefficient or return loss coefficient) and the voltage standing wave ratio (VSWR). The S11 parameter quantifies the amount of electromagnetic energy reflected back to the source when there is an impedance mismatch at the interface of two transmission lines or devices, such as an antenna and its feed line. It is expressed as decibels (dB) and has a negative value. In theory, S11 should close to infinity for a prefect impedance match. In practice, an S11 of -20 dB implies a very good impedance match. The typical acceptable limit for proper matching is -10 dB. Any value less than -10 dB is considered as mismatched [23].

VSWR is also a critical parameter to assess the performance of an antenna. The power transfer efficiency between an antenna and its transmission line is determined by the VSWR value. When an antenna is properly matched with the transmission line, the voltage at the input of the antenna becomes same as the voltage at the output of the transmission line. In this situation, The VSWR becomes 1, which means that no reflections or losses occur as the power is completely delivered from the transmitter to the antenna. For the majority of antenna applications, a VSWR value under 2 is deemed adequate. This means that the antenna has a good match with the transmission line and higher power is transferred to the antenna [23]. Therefore, when an antenna is poorly matched, it often implies that the VSWR value exceeds 2 for a certain frequency.

Based on the above mentioned performance parameters, the patch size was calculated using the following equations for 28.3 THz frequency [24]. The actual radius of a circular patch antenna is calculated by

$$a = \frac{F}{\left\{1+\frac{2h}{\pi\varepsilon_r F}\left[ln\left(\frac{\pi F}{2h}\right)+1.7726\right]\right\}^{1/2}} \tag{3.22}$$

$$F = \frac{8.791\times10^9}{f_r\sqrt{\varepsilon_r}} \tag{3.23}$$

where f_r is the resonant frequency, h and ε_r are the height and static dielectric permittivity of the underlying material. Since this equation does not consider the fringing effect (which makes the patch electrically larger), the effective patch radius is calculated by the following equation introduced by Balanis *et al.* [23].

$$a_e = \left\{1+\frac{2h}{\pi\varepsilon_r a}\left[ln\left(\frac{\pi a}{2h}\right)+1.7726\right]\right\}^{1/2} \tag{3.24}$$

The patch radius was initially calculated to be 1.57 μm for 28.3 THz frequency based on the Eqn. 3.24 and the dielectric permittivity (ε ~3.9) of SiO_2 substrate. After calculating the patch radius, for further optimisation, a dipole microstrip circular patch antenna made from copper (Cu) patches was designed on SiO_2 substrate material in CST Studio design and simulation tool using the calculated values. A discrete port was placed between the antenna patches, the S_{11} and VSWR parameters were checked in order to observe the reflected and the transmitted power on the antenna, respectively at 28.3 THz frequency. The optimized patch radius was found to be a_e=1.49 µm with a 100 nm gap between the circular patches in the simulations using the optimization tool of the CST studio software. The result is consistent with the antenna dimensions published in [24] for 28.3 THz frequency. The designed antenna structure and the radiation pattern is shown in Fig. 3.16.

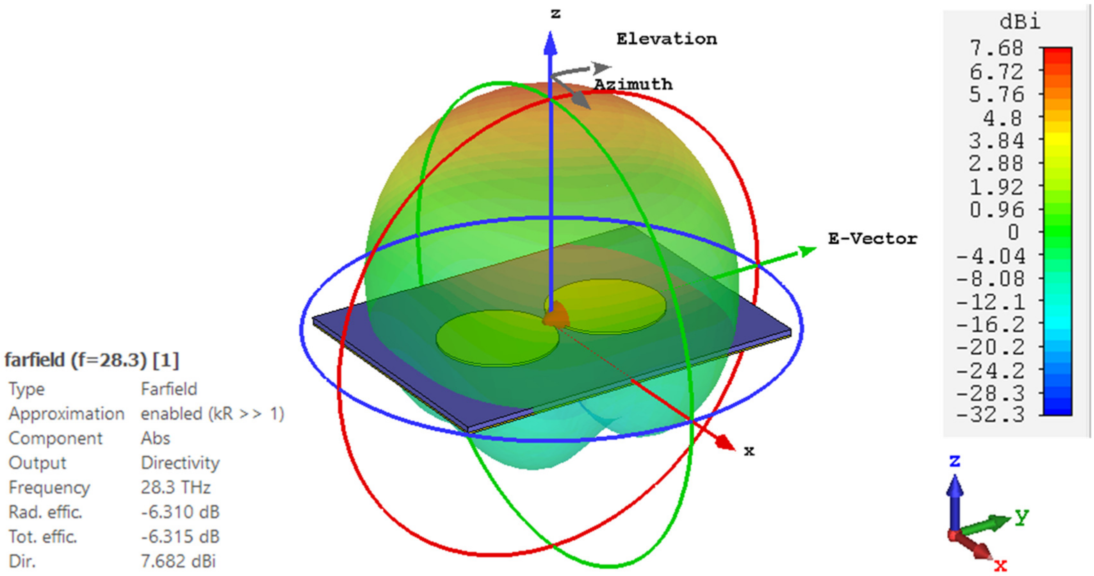

farfield (f=28.3) [1]

Type	Farfield
Approximation	enabled (kR >> 1)
Component	Abs
Output	Directivity
Frequency	28.3 THz
Rad. effic.	-6.310 dB
Tot. effic.	-6.315 dB
Dir.	7.682 dBi

Figure 3.16. CST simulations for a dipole microstrip circular patch antenna showing the directivity and the radiation pattern at 28.3 THz.

As shown in Fig. 3.17 (a), the S_{11} parameter is below -10 dB (-34 dB) around 28.3 THz which implies that the antenna can catch the incoming radiation at the desired frequency. The antenna bandwidth can also be determined from Fig. 3.17 (a).

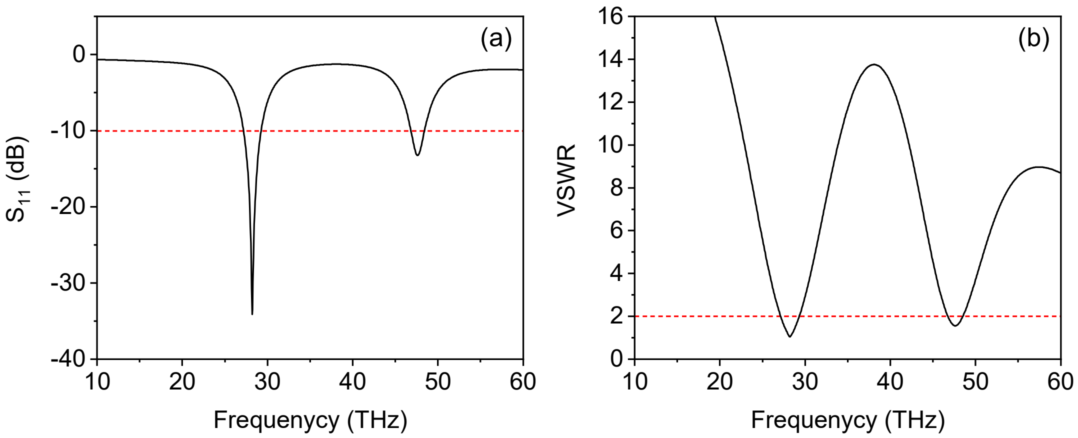

Figure 3.17. CST simulations for a 1×2 rectenna showing the (a) S_{11} and (b) VSWR at 28.3 THz for dipole microstrip circular patch antenna.

If the bandwidth is defined as the frequency range where S_{11} is to be less than -10 dB, then it would be 2 THz, with 29.2 THz high end and 27.2 THz low end of the frequency band. There is also another valley around 47.6 THz (-13 dB) with a similar bandwidth. A VSWR value of 1.04 (Fig. 3.17(b)) was also obtained for the designed antenna at 28.3 THz. The simulation results show the applicability of the design for 28.3 THz rectenna operation.

3.5 Conclusion

In this chapter, the conduction mechanisms and modelling of MI^nM diodes have been discussed. An in-house MATLAB model was used to observe the formation of QWs in double MI^2M and triple MI^3M insulator diode configurations. The location of bound states where the electron waves propagate by means of RT in the QW have been predicted. Therefore, the transmission and tunnelling probability of electrons through these bound states have been calculated using the TMM method and WKB approximation model. Then, the improved current transmission due to RT behaviour have been observed on the I-V curves. An MI^2M diode having 4:1 (nm) thickness and 25:10 ε ratios, as well as same metal electrode work functions was chosen to observe the RT characteristics. The left and right metal/oxide barriers were assumed to be 0.5 eV and 2 eV. It was seen that this configuration gives maximum current transmission at 1.40 V. For the triple MI^3M insulator diodes, two different configurations, cascaded and non-cascaded, have been modelled for 1:3:1 (nm) thickness ratios. The ε ratios were chosen as 25:20:10 for the cascaded and 20:25:10 ε ratios for the non-cascaded formations. The barriers for three insulators were assumed to be 0.5 eV for the lowest, 0.7 eV for the middle, and 2.5 eV for the highest. The maximum current transmission was seen at 1.40 eV for the non-cascaded and at 1.75 eV for the cascaded configuration. Also, the overall current magnitude of the non-cascaded diode was higher than for the cascaded one due to the formation of a natural QW at zero-bias which increases the tunnelling probability at lower voltages. Modelling different diode combination gives a useful idea of device performance prior to fabrication, as well as allows for the experimental results to be predicted. Furthermore, a dipole circular patch antenna was designed to integrate with the rectifier. The patch radius was calculated to operate at 28.3 THz frequency. Then, CST Studio software was used to simulate the designed antenna and optimize the performance. An S_{11} parameter was found to be -34 dB with a 2 THz band width, while a VSWR value of 1.04 was obtained for 1.49 μm patch radius and 100 nm patch gap. These two main performance parameters indicate that the designed antenna can efficiently operate at 28.3 THz.

References

[1] D. J. Griffiths and D. F. Schroeter, *Introduction to Quantum Mechanics*. 2018.

[2] E. Schrödinger, "An Undulatory Theory of the Mechanics of Atoms and Molecules," *Physical Review*, vol. 28, no. 6, pp. 1049–1070, 1926, doi: 10.1103/physrev.28.1049.

[3] F.-C. Chiu, "A Review on Conduction Mechanisms in Dielectric Films," *Advances in Materials Science and Engineering*, vol. 2014, pp. 1–18, 2014, doi: 10.1155/2014/578168.

[4] S. Hall, I. Z. Mitrovic, N. Sedghi, Y. C. Shen, Y. Huang, and J. F. Ralph, "Energy Harvesting Using THz Electronics," *Functional Nanomaterials and Devices for Electronics, Sensors and Energy Harvesting*, pp. 241–265, 2014, doi: 10.1007/978-3-319-08804-4_12.

[5] G. Moddel, "Will Rectenna Solar Cells Be Practical?," *Will Rectenna Solar Cells Be Practical? | Springer*, 2013.

[6] S. Krishnan, E. Stefanakos, and S. Bhansali, "Effects of dielectric thickness and contact area on current–voltage characteristics of thin film metal–insulator–metal

diodes,” *Thin Solid Films*, vol. 516, no. 8, pp. 2244–2250, 2008, doi: 10.1016/j.tsf.2007.08.067.

[7] S. M. Sze and K. K. Ng, *Physics of Semiconductor Devices*. Wiley-Blackwell, 2006. doi: 10.1604/9780471143239.

[8] C. Svensson and I. Lundström, “Trap-assisted charge injection in MNOS structures,” *Journal of Applied Physics*, vol. 44, no. 10, pp. 4657–4663, 1973, doi: 10.1063/1.1662016.

[9] S. A. Mojarad, K. S. Kwa, J. P. Goss, Z. Zhou, N. K. Ponon, D. J. Appleby, R. A. Al-Hamadany, and A. O’Neill, “A comprehensive study on the leakage current mechanisms of Pt/SrTiO3/Pt capacitor,” *Journal of Applied Physics*, vol. 111, no. 1, p. 014503, Jan. 2012, doi: 10.1063/1.3673574.

[10] D. A. Weerakkody, “Engineered high-K oxides,” The University of Liverpool, *PhD thesis*, 2016.

[11] I. N. Noureddine, “Resonant tunnelling nanostructures for THz energy harvesting,” The University of Liverpool, *PhD thesis*, 2018.

[12] I. Z. Mitrovic, S. Almalki, S. B. Tekin, N. Sedghi, P. R. Chalker, and S. Hall, “Oxides for Rectenna Technology,” *Materials*, vol. 14, no. 18, p. 5218, 2021, doi: 10.3390/ma14185218.

[13] S. Grover and G. Moddel, “Engineering the current–voltage characteristics of metal–insulator–metal diodes using double-insulator tunnel barriers,” *Solid-State Electronics*, vol. 67, no. 1, pp. 94–99, 2012, doi: 10.1016/j.sse.2011.09.004.

[14] N. Sedghi, J. W. Zhang, J. F. Ralph, Y. Huang, I. Z. Mitrovic and S. Hall, "Towards rectennas for solar energy harvesting," *2013 Proceedings of the European Solid-State Device Research Conference (ESSDERC)*, 2013, pp. 131-134, doi: 10.1109/ESSDERC.2013.6818836.

[15] N. Sedghi, J. F. Ralph, I. Z. Mitrovic, P. R. Chalker, and S. Hall, “Electron trapping at the high-κ/GeO2 interface: The role of bound states,” *Applied Physics Letters*, vol. 102, no. 9, p. 092103, 2013, doi: 10.1063/1.4794544.

[16] N. Alimardani and J. F. Conley, “Enhancing metal-insulator-insulator-metal tunnel diodes via defect enhanced direct tunneling,” *Applied Physics Letters*, vol. 105, no. 8, p. 082902, 2014, doi: 10.1063/1.4893735.

[17] P. Maraghechi, A. Foroughi-Abari, K. Cadien, and A. Y. Elezzabi, “Enhanced rectifying response from metal-insulator-insulator-metal junctions,” *Applied Physics Letters*, vol. 99, no. 25, p. 253503, 2011, doi: 10.1063/1.3671071.

[18] I. Z. Mitrovic, A. D. Weerakkody, N. Sedghi, S. Hall, J. F. Ralph, J. S. Wrench, P. R. Chalker, Z. Luo, and S. Beeby, “(Invited) Tunnel-Barrier Rectifiers for Optical Nantennas,” *ECS Transactions*, vol. 72, no. 2, pp. 287–299, 2016, doi: 10.1149/07202.0287ecst.

[19] A. D. Weerakkody, N. Sedghi, I. Z. Mitrovic, H. van Zalinge, I. Nemr Noureddine, S. Hall, J. S. Wrench, P. R. Chalker, L. J. Phillips, R. Treharne, and K. Durose, “Enhanced low voltage nonlinearity in resonant tunneling metal–insulator–insulator–metal nanostructures,” *Microelectronic Engineering*, vol. 147, pp. 298–301, 2015, doi: 10.1016/j.mee.2015.04.110.

[20] R. Tsu and L. Esaki, “Tunneling in a finite superlattice,” *Applied Physics Letters*, vol. 22, no. 11, pp. 562–564, 1973, doi: 10.1063/1.1654509.

[21] Z. Wang, J. Ralph, N. Sedghi, I. Z. Mitrovic, and S. Hall, “Bound states within the notch of the HfO2/GeO2/Ge stack,” *Journal of Vacuum Science & Technology B, Nanotechnology and Microelectronics: Materials, Processing, Measurement, and Phenomena*, vol. 31, no. 2, p. 021209, 2013, doi: 10.1116/1.4794378.

[22] I. Nemr Noureddine, N. Sedghi, J. S. Wrench, I. Z. Mitrovic, P. R. Chalker, and S. Hall, “Structural and electrical investigation of MI2M and MI3M diodes for improved non-linear, low bias rectification,” *Solid-State Electronics*, vol. 194, p. 108349, 2022, doi: 10.1016/j.sse.2022.108349.

[23] C. A. Balanis, *Antenna Theory*. Wiley-Blackwell, 2016.

[24] S. H. Zainud-Deen, N. A. Eltresy, H. A. Malhat, and K. H. Awadalla, “Single/Dual-Polarized Infrared Rectenna for Solar Energy Harvesting,” *Advanced Electromagnetics*, vol. 5, no. 2, p. 1, 2016, doi: 10.7716/aem.v5i2.327.

Chapter 4

4. Experimental methods

In this chapter, the primary experimental methods used in the fabrication and testing of MIM diodes are described. The sample preparation and processing techniques are covered in sections 4.1 and 4.2, while the testing methods including variable angle spectroscopic ellipsometry (VASE), X-ray photoelectron spectroscopy (XPS) and current voltage (I-V) electrical characterisation are addressed in section 4.3.

4.1 Material deposition

The surface cleaning methods of glass and SiO_2/Si samples, as well as the working principles of thermal evaporation, radio-frequency (RF) magnetron sputtering and atomic layer deposition (ALD) are explained in this section.

4.1.1 Sample preparation

The devices in this work were fabricated on ultra-smooth (0.32 nm rms roughness [1]) 4 cm × 4 cm Corning glass (CG) using shadow mask evaporation and on 300 nm SiO_2 on Si substrates using photolithography. 300 nm thick SiO_2/Si substrates were used to ensure insulation and uniformity of the bottom electrode contacts. For CG substrates, the cleaning process begins with dipping the glass slides in 10% Decon-90 surface active cleaning agent and 90% water concentration for a few hours. Then, the samples are washed under running de-ionised water (DIW) for a duration of 5-10 minutes. Nitrogen (N_2) gun is then used to blow dry the samples to remove any leftover water droplets. After that, the substrates are cleaned with acetone and isopropanol (IPA) in the ultrasonic bath for 10 minutes each and dried with N_2. Finally, they are placed UV ozone cleaner for 2 minutes to remove any remaining residues. The cleaning process is the same for SiO_2 on Si substrates except the Decon-90 and water solution step.

4.1.2 Thermal evaporation

Thermal evaporation, one of the physical vapor deposition processes, is widely used in the microfabrication process to deposit thin film material on the surface of a sample [2]. In the study presented in this thesis, a Moorfield minilab 60 thermal evaporator was mainly used for metal evaporation in which high temperature plays an important role. Au, Al and Cr metals were deposited using this technique. The difference in this method from other deposition techniques is the way of heating the target material. This technique generally consists of the steps of forming the vapor phase, evaporating the metal molecules from the source, accumulating the vaporised particles onto the substrate and condensing [3]. A basic representation of the thermal evaporation process is illustrated in Fig. 4.1. Thermal evaporation equipment has a vacuum chamber that is evacuated before and after the process. After the substrate and the basket filled with source material are placed in the vacuum chamber, it is expected to reach the desired pressure value, generally in the range of 1 $\times 10^{-6}$ mbar and ideally below. High vacuum is crucial to deposit high quality films by minimizing the gas particles in the chamber and preventing any collision between the vaporised and the other gas particles.

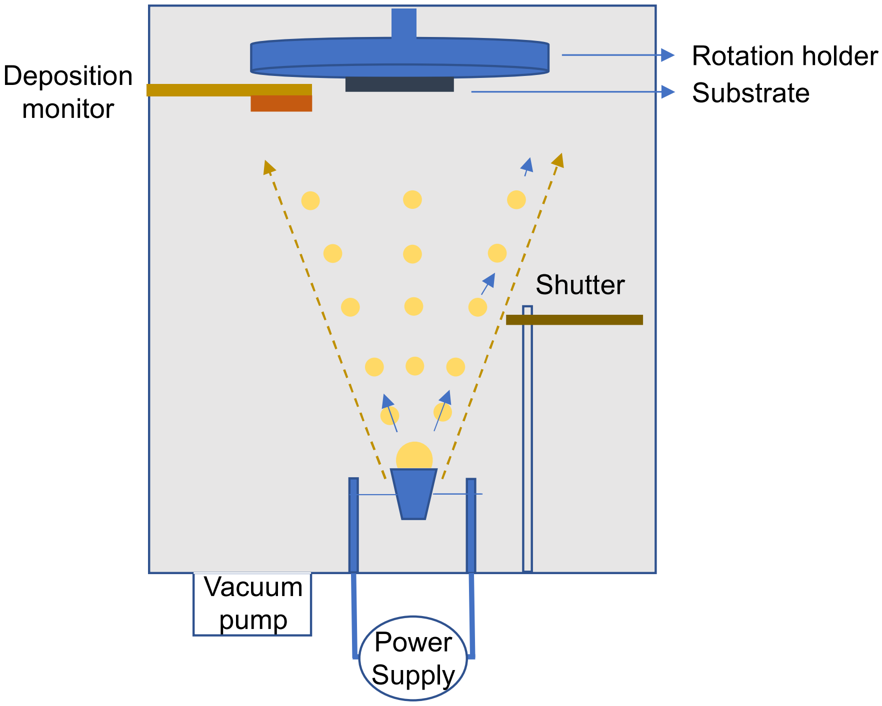

Figure 4.1. Basic schematics of a thermal evaporator [2].

Besides this, at low pressure, the mean free path of particles, which is the average distance a particle can travel, is greater than the distance between the evaporation source and the substrate material. Therefore, once the desired vacuum is obtained, the basket is heated by Joule heating with the applied current until the energy required for the separation of metal molecules from the source is reached. Since the target material will evaporate upwards as shown in the Fig. 4.1, the sample is attached under a plate (rotation holder) in the upside-down position above the evaporation source. For the films to be homogeneous, the plate containing the substrate is rotated at a certain speed. In order to obtain the desired thickness, the evaporation rate is monitored using the quartz sensor [4]. The ideal deposition rate for the metals is typically between 3-4 Å/s [1]. In addition, a shutter located between the basket and the substrate is used to prevent unwanted vaporized materials from reaching the substrate and to provide a controlled coating, and it is controlled from the outside of the vacuum chamber. As the particles accumulate on the substrate, the vapor particles finally form a nucleus. This core formation continues until a thin film of the material is formed [5].

4.1.3 Radio-frequency (RF) magnetron sputtering

Sputtering is another physical vapour deposition (PVD) technique, which is a type of vacuum deposition procedure used to produce thin films and coatings. The deposition includes coatings of light materials, often metals and oxides to a range of surfaces [6,7]. When intense particles (incoming ions) of a gas or plasma attack a substance, also known as a target, the sputtering phenomenon occurs. If the incoming ions create a series of collisions in the target materials and surpass the binding energy of the surface, the atoms are freed. There are several versions of this technique, such as direct-current (DC) magnetron sputtering, pulsed DC sputtering, and radio-frequency (RF) magnetron sputtering. A basic representation of RF magnetron sputtering is shown in Fig. 4.2.

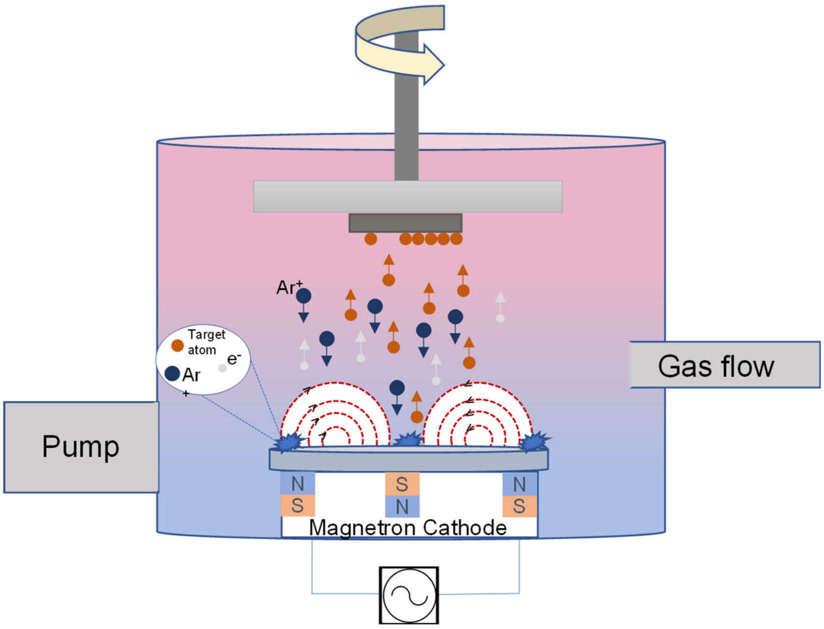

Figure 4.2. Basic schematics of an RF magnetron sputtering [6,7].

The main difference of the RF magnetron sputtering from the DC magnetron sputtering is that the target surface does not need to be electrically conductive. It may also sustain a plasma at a lower pressure (1-15 mTorr) throughout the chamber, considerably improving the growth rate [8]. This results in fewer ionised gas collisions and more effective deposition. The RF magnetron sputtering provides certain benefits which are faster deposition rates, cost-effectivity and production of higher quality films on the substrates over the DC sputtering. Furthermore, magnetron sputtering in general is a highly adaptable process for thin film deposition. Since the sputtering target does not need melting or vaporisation of the source material, sputter deposited films have a composition extremely close to the source material and stick on the substrate better than evaporated films [8]. In this work, a Moorfield NanoPVD RF Sputtering technology, which has several benefits as discussed above, was used to deposit the metal and oxide layers. ZnO, TiO_2 and NiO films were sputtered using an Ar gas flow rate of 4-5 sccm and 45 W power. The Ar gas flow rate was kept at 5 sccm for metal (Ti and Zn) sputtering and 52.5 W power was applied during the process. A base pressure of $< 1\times10^{-6}$ mBar was ensured before the deposition and the process pressure was kept at $3\text{-}4\times10^{-3}$ mBar.

The term "magnetron sputtering" refers to the employment of magnetic fields to influence the behaviour of charged particles during the deposition process of sputtering. It employs magnetic and electric fields to hold particles close to the target's surface, boosting particle density and resulting in a high sputtering rate. The electric potential supplied to the target material changes from positive to negative at a high frequency (13.56 MHz) in RF sputtering, allowing electrons to directly ionise the gas atom. Hence, this approach can be utilised for both conductive (metal) and non-conductive (insulator) materials [1,2,6]. Usually Argon (Ar) ions are accelerated by an RF electric field to interact with target made of the substance to be sputtered in RF magnetron sputtering. For repulsion, introducing a regulated flow of Ar gas into the vacuum chamber is required. The vacuum chamber is filled with free electrons. These electrons are captured by the magnetic field near the target's surface and spin around the target, then collide with the Ar atoms as they move through the high-density Ar gas, forming positive ions [9]. Since the target is negatively charged, the positively charged ions travel towards it and collide with its surface. These high-energy interactions have the potential to separate atoms from the source material. Sputtered atoms are not attracted by a negative charge or magnetic field as they are neutral. The target atoms can move freely via the vacuum chamber towards the substrate. As more and more atoms are released from the target, the substrate is covered by the source material. During the process, plasma flashes can be observed as a result of highly-energetic particles near the target. The sputtering rate depends on the pressure and the quantity of power. Collisions inside the plasma produce energetic ions to speed towards the target with enough kinetic energy (KE) to remove molecules, and the sputtered material travels through the vacuum chamber to coat the substrate [6,7,9].

4.1.4 Atomic layer deposition

An advanced chemical coating technique is known as atomic layer deposition (ALD) which can form a thin film in the size of a single atom layer in a certain period of time. The fact that ALD has a self-limiting structure sets it apart from other thin film deposition techniques [10–12]. The reaction reaches saturation and stops after the formation of a single atomic layer. In this way, it becomes possible to control the coated thickness, realize a homogeneous coating and deposit even on the most difficult geometric surfaces. A sequential process (Fig. 4.3) is applied to ensure that all reactions take place on the surface. The processes end when an atomic layer has developed on every surface, and the resulting films are usually stoichiometric. ALD uses several different sources such as Al, Ti, Zn, and Hf depending on the deposited material. Two or more chemical vapour or gas precursors are progressively sent into the growth chamber during the deposition, where the reaction takes place and the substrate is coated.

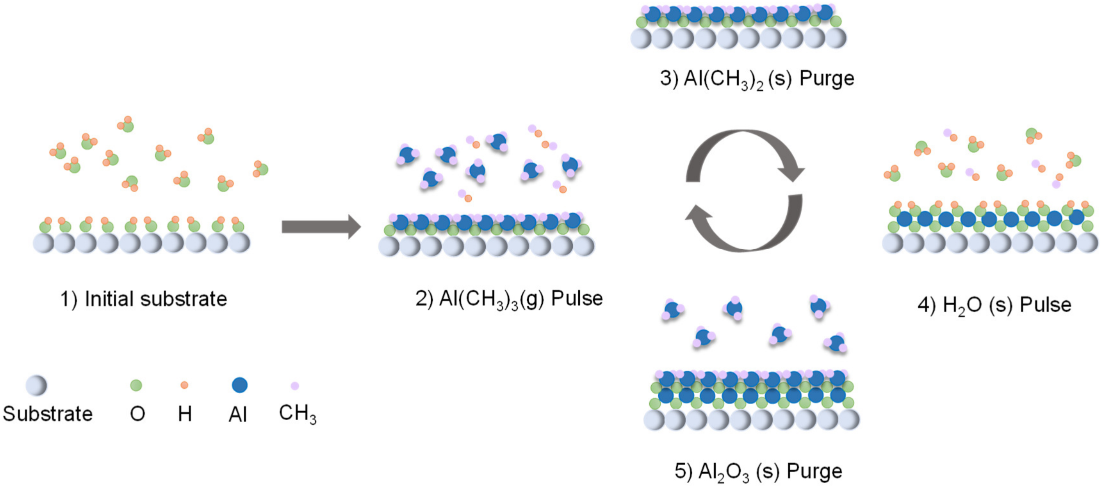

Figure 4.3. Overview of an ALD process [10–12].

As shown in Fig. 4.3, the source material for ALD is added to the reactor while it is still in the gas phase (1). The purge and evacuation periods come after this process, respectively. A full cycle requires two cycles of pulse and purge in order to eliminate the by-products created in the time of pulse step. Each precursor forms a monolayer as it saturates on the substrate surface. The thickness of this monolayer is related to how reactive the precursor is to the substrate surface. The remaining cycle consists of four phases (2)-(5), as seen in the (Fig 4.3). By repeating this cycle several times, the necessary film thickness can be attained. The precursors are chemically adsorbed on the surface, and once the surface is saturated, they stop adhering to it. The resulting film's formation is self-contained. In other words, each cycle results in the same quantity of material being deposited onto the film. This feature makes ALD advantageous over CVD. A great conformation may be achieved by controlling the film's thickness in accordance with the number of cycles [10–12]. Based on these principles, it can be said that ALD has several advantages in the thin film growth mechanism. These advantages are being able to achieve excellent conformality, uniformity and precise film thickness.

The precursor material's vapour pressure also has an impact on the flexibility of the precursors. The vapour pressure of the majority of metal-containing precursors, which are either liquid or solid, is inadequate at ambient temperature. In order to raise the vapour pressure, the precursors are heated to temperatures lower than their decomposition temperature (~140°C). Molecular precursors are used in several ALD procedures because transforming the elemental precursors into the gas phase is not always viable. As a result, the ALD method only employs a relatively small number of elemental precursors. Although ALD deposits layers slower than other techniques, it is the best choice for creating a smooth, thin coating on a nano-structured surface since its superior conformation. The reaction chamber, where the ALD process is carried out, has a pressure range of 0.1 to 5 mbar, a temperature range of 50 to 400 °C, and a gas flow rate range of 0.3 to 1.0 SLM (standard litre per minute) [10–12]. A conventional thermal ALD using a Cambridge Nanotech Savannah reactor in Materials Science and Engineering Department at University of Liverpool was utilised to deposit Al_2O_3, Nb_2O_5 and Ta_2O_5 thin films in this study. The deposition conditions of these oxide are explained in Chapter 6 in detail.

4.2 Device patterning

Two different patterning techniques, which are shadow mask evaporation and photolithography, were used to fabricate the MIM diodes in this study. The details of both methods are explained in Sections 4.2.1 and 4.2.2, respectively.

4.2.1 Shadow mask evaporation process

In Fig. 4.4, the mask design for shadow mask evaporation process is shown. The mask was made from 4 cm × 4 cm magnetic nickel (Ni) metal sheets. Figure 4.4 (a) shows the bottom electrode pattern of the mask which includes 64 device patterns. For the fabrication process, the mask is initially placed on the CG substrates having the same dimensions and fixed with the aid of magnet sheets from the back side of the substrate. Therefore, the bottom electrodes can be formed by the metal deposition. The second step involves the oxide deposition. The whole substrate is coated with the thin insulating layer(s) including the contact parts. Then, mask is again placed on the sample by rotating 90° (Fig. 4.4 (b)) and using the alignment marks (4 squares in the corners) to overlap the bottom and the top electrodes and sandwich the oxide layer between them. The zoomed-in image of the overlapped single devices with 100 μm×100 μm areas are shown in Fig. 4.4 (c).

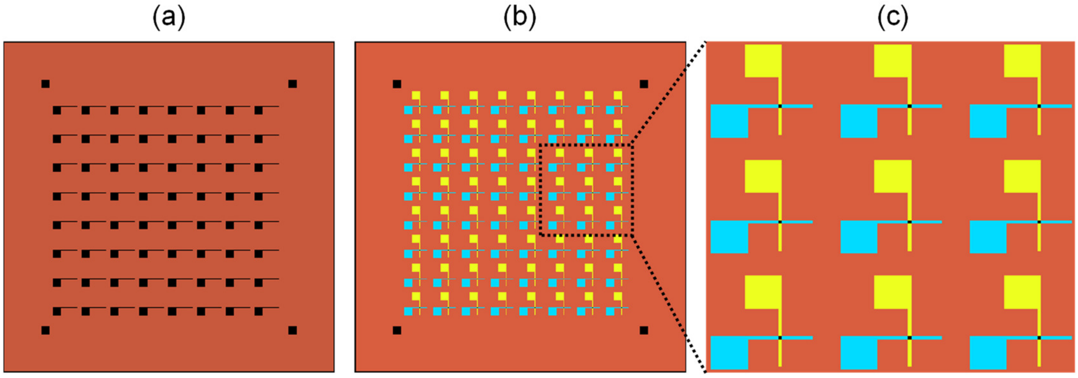

Figure 4.4 Shadow mask design; (a) bottom electrode pattern, (b) overlapped top and bottom electrodes and (c) zoomed-in image of the separate devices.

Since the deposited oxide layers are very thin, the oxide etching step for accessing the bottom contacts can be omitted. The probe station needles are used to scratch the oxide layer to have connection with the bottom contacts. The process flow of shadow mask evaporation and the MIM device cross-sections are shown in Fig. 4.5.

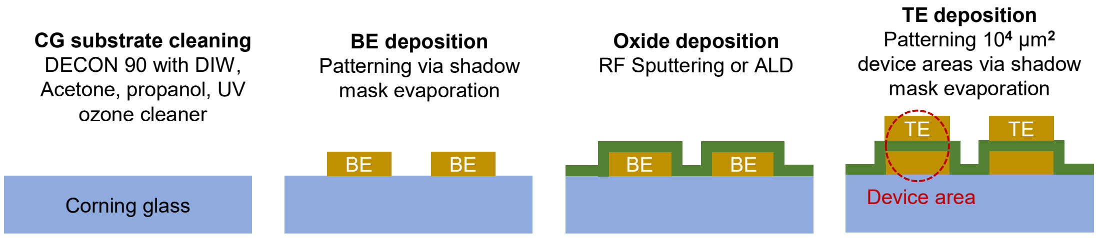

Figure 4.5. Process flow for patterning the MIM diodes using shadow mask.

4.2.2 Photolithography process

Two different photomasks (light field and dark field) each having 20 single rectenna elements were designed for the photolithography process. The patch radius of the circular antennas was determined as 339 µm using Eqns. 3.22-3.24 for detecting 76-81 GHz radiation based on the available radiation source to fabricate a proof-of-concept device. The mask has 3 main columns as shown in Fig. 4.6. Left column (Fig. 4.6 (a)) is the bottom electrode (BE) pattern for metal deposition using the UV aligner with a single photoresist layer, middle column (Fig. 4.6 (b)) is for oxide deposition/etching and the right column (Fig. 4.6 (c)) is for patterning the top electrodes (TE) with a final UV alignment on a single photoresist layer. In each layer, there are antenna arms attached to the patches and act as metal electrodes with line widths ranging from 1 µm, 2 µm, 4 µm and 8 µm to fabricate 1 µm^2, 4 µm^2, 16 µm^2 and 64 µm^2 devices when the TEs are overlapped with the BEs.

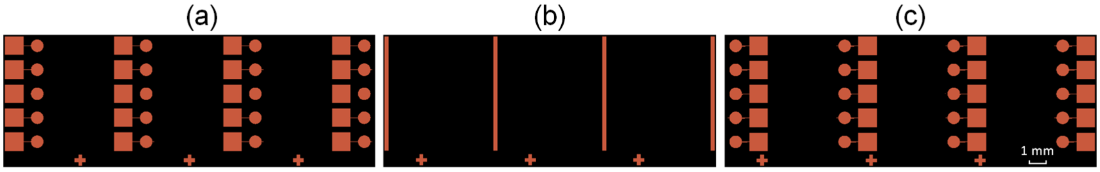

Figure 4.6. Mask layout for single rectenna devices showing (a) top contacts, (b) oxide etching layer and (c) bottom contacts.

The alignment steps for the BEs, oxide deposition and the TEs are shown in Fig. 4.7. After the BE patterning and the consequent metal deposition, the middle column (shown in Fig 4.6 (b)) is aligned at the edge of the bottom circular patches to cover the BEs. This step is shown in Fig. 4.7 (a) for the whole devices and in Fig. 4.7 (b) for a zoomed-in image of an individual device.

Then, depending on the process (light field and dark field), either lift-off or etching steps can be applied to open access for the bottom electrodes. This step can be omitted for the single devices similar to the shadow mask evaporation process and probe needles can be used to scratch the oxide layer and have contact with the bottom metal layer for ease of fabrication.

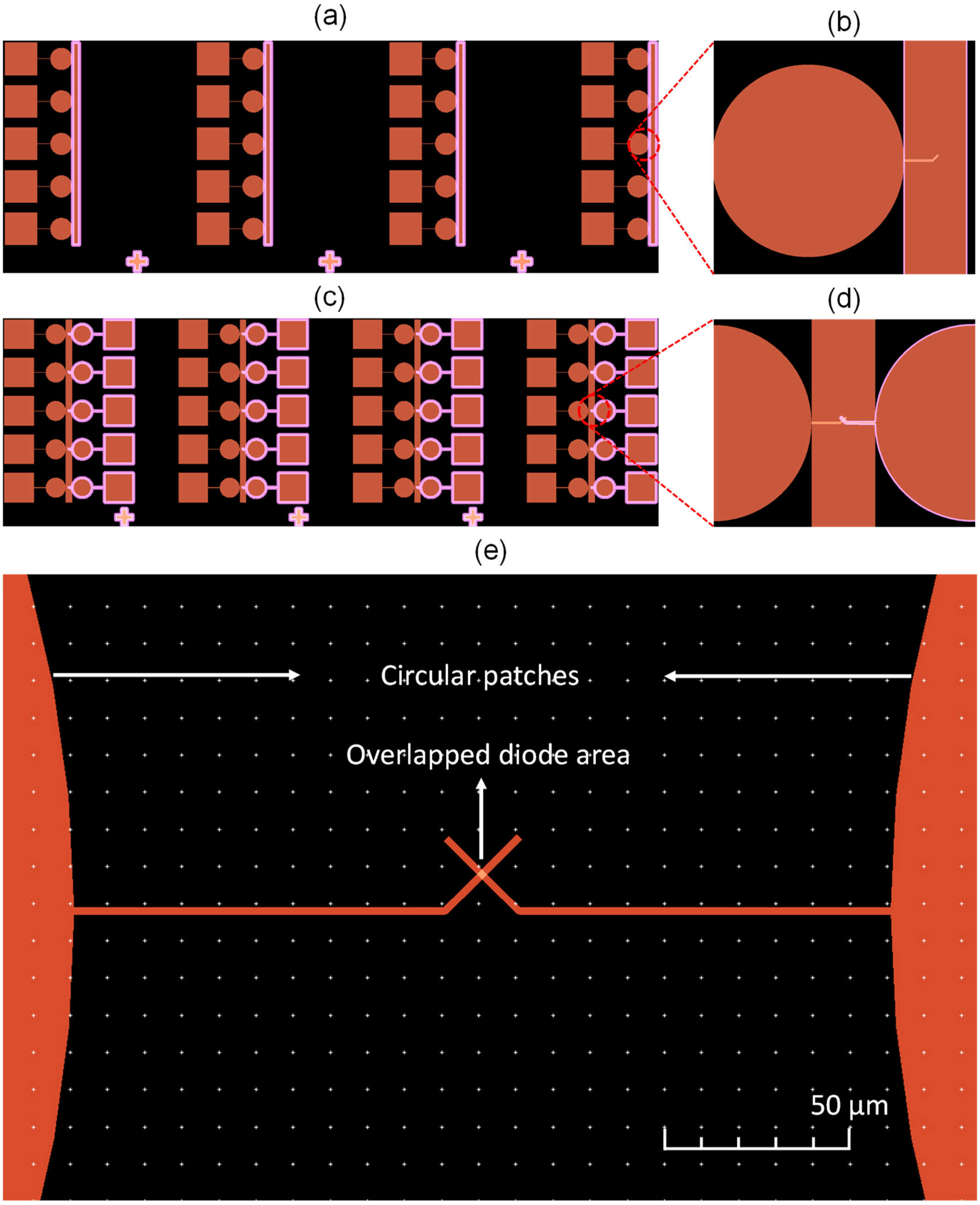

Figure 4.7. Different layers of the photomask showing (a)-(b) the alignment of BEs with the oxide etching layer, (c)-(d) alignment of TEs with the BE layers and (e) the overlapping bottom and top rectenna arms to form the diode area.

However, this step is necessary for fabricating arrays since the antennas must be interconnected in an array structure and need ohmic conduction for the current to flow. Fig. 4.7 (c) shows the last step of the alignment which is the TE patterning. The top layer is aligned on the BEs using the alignment marks, so that the oxide layer is sandwiched between the top and bottom antenna arms to from the MIM diode device. The cross-bar structure of the aligned metal electrodes is shown in the zoomed-in image in Fig. 4.7 (d). The detailed process flow and the device cross-sections at each step are shown in Fig. 4.8. After the standard cleaning procedures which were explained in Section 4.1, the process begins with spin coating of a single S1813 positive photoresist (PR) layer on the 300 nm SiO_2/Si substrate.

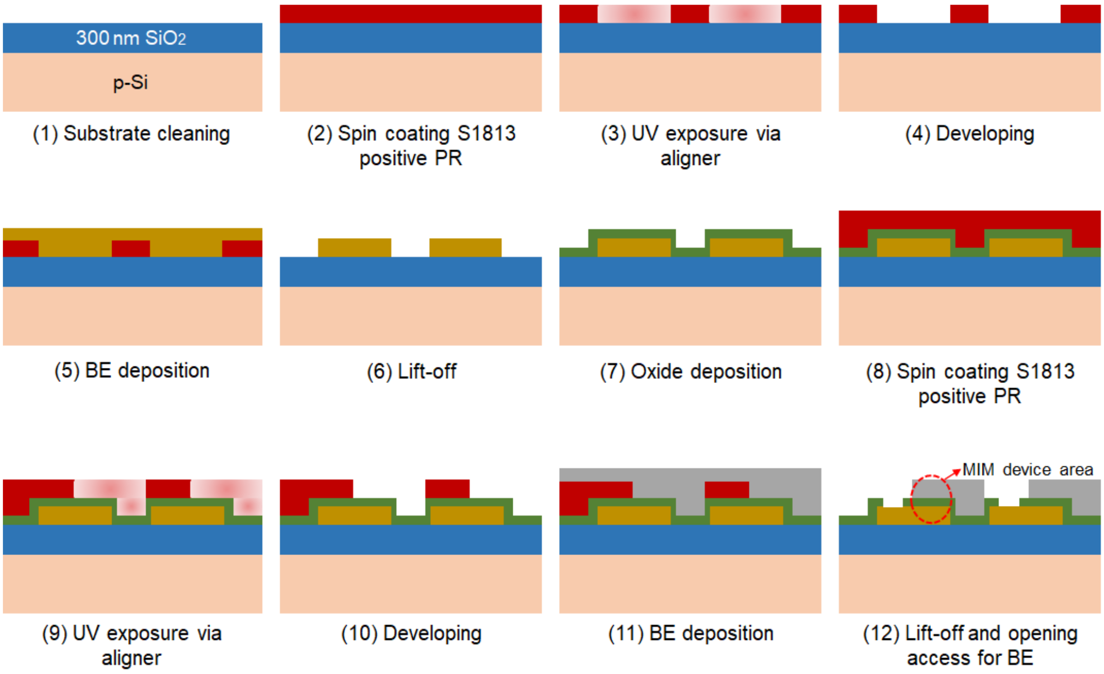

(1) Substrate cleaning

(2) Spin coating S1813 positive PR

(3) UV exposure via aligner

(4) Developing

(5) BE deposition

(6) Lift-off

(7) Oxide deposition

(8) Spin coating S1813 positive PR

(9) UV exposure via aligner

(10) Developing

(11) BE deposition

(12) Lift-off and opening access for BE

Figure 4.8 Process flow and the device cross-sections of single rectenna device.

The spin recipe includes spreading the PR for the first 5 seconds at 1000 rpm, and then coating the sample at 3000 rpm for 50 seconds. After that, the bottom layer is patterned by aligning, UV exposure for 20-22 seconds, developing the exposed parts in a Microposit developer concentrate for 50-60 seconds and then rinsing the sample with DIW. This is followed by the oxide deposition using either RF sputtering or ALD. The final TE layer is fabricated using the same steps as the BE fabrication. A Karl Suss mask aligner with a UV light source has been used for the photolithography processes in this study.

4.3 Characterisation methods

The deposited thin films and the fabricated devices have been assessed by several characterisation methods including, VASE, XPS, and electrical measurements. In this section, these processes are explained in detail.

4.3.1 Variable angle spectroscopic ellipsometry

The Spectroscopic ellipsometer (SE) is an optical characterisation tool that measures the change in the polarization of light when it refracts and reflects from a material [13]. The change in polarization is expressed by the amplitude ratio (ψ) and the phase difference (Δ). The obtained data depend on the optical properties of each material, as well as the thickness of the measured film. In this way, the SE can be used to determine the film thickness and the optical constants of the materials. In addition, the SE can be used to determine the composition, crystallization level, surface roughness, doping concentration and defect energy states of materials. Light with random parallel (p), perpendicular (s) components (planes) and phase of the electric field is called unpolarized light. On the other hand, the light that shows a certain orientation and shape at every point is called polarized light. The polarized light can be classified as three groups namely linear, circular and elliptical. The polarization of the light can be changed using a suitable polariser by absorbing light in a certain direction. If the light has two perpendicular s and p planes with uneven amplitudes and a 90° difference in phase, it is called an elliptically polarized light.

The working principle of ellipsometry can be explained as follows. The unpolarized light from the light source is converted into a linearly polarized light beam with the help of a polarizer. The electric field of the resulting light beam can be divided into s and p vector components in two planes. The p-plane contains the incident and passing rays, while the s-plane is perpendicular to this plane. The linearly polarized light is converted into circularly polarized by a compensator [14]. The electric field of the light beam reflected from the sample surface is also divided into p-plane and s-plane components. Reflected light is typically elliptically polarized. This is where the "ellipsometry" name comes from. An example of a SE measurement setup is shown in Fig. 4.9.

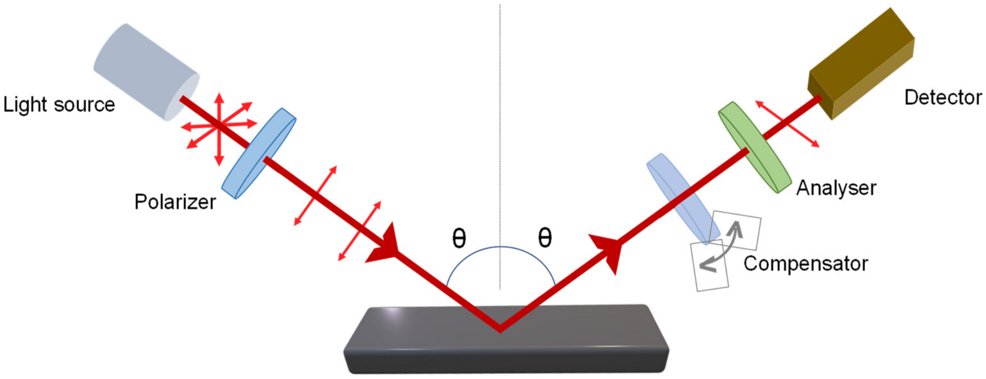

Figure 4.9. Schematic representation of a basic spectroscopic ellipsometry measurement setup [13].

The reflected light coming from the sample to the detector is analysed using change the polarization condition. The measured change in polarization gives the information about properties of the material. Mathematically, the change in polarization is denoted by;

$$\rho = tan(\psi)e^{i\Delta} = \frac{E_p^{out}/E_p^{in}}{E_s^{out}/E_s^{in}} = \frac{r_p}{r_s} \tag{4.1}$$

where r_p and r_s indicate the Fresnel reflection coefficients based on the p and s components of the polarised light wave, respectively. The SE measures ρ as a function of wavelength and angle of incidence. After the measurement, the data can be be analysed to determine the optical constants, layer thicknesses and other associated properties. The analysis is done based on a systematic procedure. Following the measurement, a suitable theoretical model is generated to match with the experimental data and describe the material. Then, the Fresnel equations, which give thickness and optical constants for each material, are utilised to compute the projected response using the model. For the initial calculation, estimated values are provided if these quantities are unknown. Following that, the calculated values are compared with the experimental results. To improve the fit between the experimental results and the theoretical model, the unknown material parameters might then be adjusted. However, the quantity of unknown variables in the experimental data should not exceed the number of known parameters [15]. In other words, the two data points of ψ and Δ can be obtained from a single wavelength SE measurement, allowing the determination of a maximum of two material parameters. Regression analysis is frequently used to determine the model's best fit with the experimental data. The difference between the theoretical and the experimental curves is calculated using an estimator, named as Mean Squared Error (MSE). In order to get the lowest MSE values, the unknown parameters are changed. Simultaneously, the optical parameters of the associated material are checked to have meaningful physical parameters within the optical range. The optical properties can be either defined by the complex refractive index ($\tilde{n}$) or complex dielectric functions ($\tilde{\varepsilon}$). These functions can be expressed as

$$\tilde{n} = n + ik \tag{4.2}$$

$$\tilde{\varepsilon} = \varepsilon_1 + i\varepsilon_2 \tag{4.3}$$

where n is the refractive index, k is the extinction coefficient, ε_1 is real and ε_2 is the imaginary parts of the complex dielectric function. The Kramers-Kronig consistency between the real and the imaginary part of the dielectric function should be preserved in the fittings [16].

The fitting can be done using a series of oscillator models usually based on Lorentz, Tauc-Lorentz and Gaussian transformations. The material losses, or the characteristics of the defects, are modelled by the oscillators. Each oscillator has a specific resonance frequency that is correlated with the location of the defect energy state within the band gap. These defect levels resonate at specific incident frequencies, exhibiting absorption in the material. These oscillators are responsible for the ψ and Δ values which help to find the defects.

The following Eqn. 4.4 is frequently used to describe the Cauchy relation in transparent materials.

$$n(\lambda) = A + \frac{B}{\lambda^2} + \frac{C}{\lambda^4} \tag{4.4}$$

where the terms A (amplitude), B (broadening), C (centre energy) are adjusted to the material's refractive index and λ represents the wavelength. The term A specifies the index range, whereas B and C determine the shape of the dispersion. Initially, the thickness and the amplitude of the theoretical and experimental ψ and Δ values are compared, and A is changed until they are in agreement. Then, the B parameter can be added in the fitting. The C parameter is fitted to see if the MSE value decreases by more than 10%, otherwise, it is not taken into account in the model. It is noted that the

KK consistency is not preserved in the Cauchy relation which can result in unphysical optical dispersion. Another typical model that is used in the transparent region is the Sellmeier relationship (Eqn. 4.5) which preserves the KK consistency and maintains a physical dispersion relation [14,15].

$$n = \sqrt{\varepsilon(\infty) + \frac{A\lambda^2}{\lambda^2 - B^2} - E\lambda^2} \tag{4.5}$$

where $\varepsilon(\infty)$ stands for the index offset, A for amplitude, B for centre energy and the E for the pole position in the infrared [15].

It is more challenging to assess the SE measurements in absorbing region of the materials than in the transparent region. This is due to the unknown optical constants (n, k) of the materials with respect to the wavelength prior to the measurements. Usually, the absorbing films also have a transparent region where the Cauchy or Sellmeier equations can be used for modelling. Nevertheless, the absorbing regions needs to be considered for the real (ε_1) and imaginary (ε_2) parts of the optical constants. There are several other methods for modelling the absorbing materials using basis spline (B-spline) and general oscillator (Gen-Osc) models. These two methods were also frequently used in the modelling of oxides films in this study.

The B-spline model is ideal for the films having partially transparent and absorbing regions which allows the ellipsometer to determine the beginning of the absorption. This method uses a set of control points that are evenly spaced in photon energy to specify the optical constants (n, k) or the real (ε_1) and imaginary (ε_2) parts of the dielectric function with respect to the wavelength. A spline function is composed of polynomial segments constructed in a way to retain continuity up to a specified degree of derivation. A B-spline function can be expressed as

$$B_i^0(x) = \begin{cases} 1 & t_i \leq x \leq t_{i+1} \\ 0 & otherwise \end{cases}, \tag{4.6}$$

$$B_i^0(x) = \left(\frac{x - t_i}{t_{i+k} - t_i}\right) B_i^{k-1}(x) + \left(\frac{t_{i+k+1} - x}{t_{i+k+1} - t_{i+1}}\right) B_{i+1}^{k-1}(x). \tag{4.7}$$

where the degree of the B-spline is denoted by k. The knots (t_i) on the x-axis indicate where the segments of the polynomial connect and defined by i. 0-degree B-spline functions are defined by Eqn. 4.6, and Eqn. 4.7 is used to generate higher degree basis functions. It is thus possible to create a spline curve S(x) by adding the linear sum of n number of basis functions using

$$S(x) = \sum_{i=1}^{n} c_i B_i^k(x) \tag{4.8}$$

where c_i are the coefficients for the i^{th} B-spline function. Numerous advantageous characteristics make B-spline curves ideal for modelling dielectric functions. B-spline curves are continuous, as are their derivatives up to the order of spline minus one. The node amplitudes that define the final curve are linearly independent because the basis functions only depend on the position of the nodes, considerably enhancing the efficiency of calculations. The B-spline recursion formula can be used to produce KK consistent basis functions by using the KK integral, such as the KK transform of ε_2 is used to determine the shape of the ε_1 curve [15,17,18].

The Gen-Osc layer is an additional technique for analysing absorbing films that can be employed independently or after preliminary B-Spline modelling. This layer defines the form of the absorption to model the absorbing features. There are several different oscillator models such as Pole, Gaussian, Lorentz, Drude, Harmonic, Tauc-Lorentz and Cody Lorentz. Despite the fact that they are all unique, they all perform similarly. In order to have a good match with the optical constants of actual materials, the oscillators have variable parameters. Oscillators having a centre energy (E_n), amplitude (A), and broadening (B) are used to define the ε_2 curve and the shape of the ε_1 is generated using the ε_2 values based on the KK consistency. In order to take into account the absorption features outside of the measured spectral region, there is additionally an ε_1 offset parameter which is a real constant introduced to ε_1. The definitions of typical Gen-Osc models are given as follows [15,19].

Oscillators with zero-broadening are defined by Poles. As a result, they only have an impact on the ε_1. They can be used to define the dispersion caused by the absorption out of the spectral region. The Poles can be expressed as

$$\varepsilon_n = \frac{A_n}{E_n^2 - E^2}. \tag{4.9}$$

Gaussian is another oscillator type which generates a Gaussian curve for ε_2 and a KK consistent ε_1 which are defined as

$$\varepsilon_1 = \varepsilon_\infty + \sum_i \left\{ A_i \left(\Gamma\left(\frac{\lambda - C}{k_g B}\right) + \Gamma\left(\frac{\lambda + C}{k_g B}\right) \right) + Z_i \left(\exp\left(-\left(\frac{\lambda - C}{k_g B}\right)^2 \right) + \exp\left(-\left(\frac{\lambda + C}{k_g B}\right)^2 \right) \right) \right\} \tag{4.10}$$

$$\varepsilon_2 = \sum_i \left\{ A_i \left(\exp\left(-\left(\frac{\lambda - C}{k_g B}\right)^2 \right) + \exp\left(-\left(\frac{\lambda + C}{k_g B}\right)^2 \right) \right) + Z_i \left(\Gamma\left(\frac{\lambda - C}{k_g B}\right) + \Gamma\left(\frac{\lambda + C}{k_g B}\right) \right) \right\} \tag{4.11}$$

where i is the number of oscillators, Γ is the convergence series function, A and Z are the real and imaginary parts of the amplitude, B denotes the broadening, C is the centre energy, λ is the wavelength at a specific photon energy (eV) and k_g is a constant. In this layer, the amplitude corresponds to the height of the ε_2 peak at the centre energy of the oscillator and the broadening defines the full width at half maximum (FWHM) of the oscillator. Therefore, if the type of an oscillator is changed, the new oscillator will maintain the same height and FWHM as the previous oscillator.

A fundamental line shape used to define the optical properties of absorbing materials is called a Lorentz oscillator. The definition of the Lorentz equation is as follows.

$$\varepsilon = \sum_j \left(\frac{(A_j + iZ_j) B_j C_j}{C_j^2 - \lambda^2 - iB_j\lambda} \right) + \varepsilon_\infty \tag{4.12}$$

The Drude model describes the impact of free carriers on the response of the dielectric layer. The shape of the Drude resembles a Lorentz oscillator without the resonance energy which is expressed as below.

$$\tilde{\varepsilon}(\lambda) = \varepsilon_\infty - \frac{i4\pi\hbar^2}{\rho(\hbar\lambda + i\lambda^2\tau)} \tag{4.13}$$

where $\hbar$ is the reduced Planck's constant, ρ is the DC resistivity and τ is the mean scattering time.

As another type, harmonic oscillators can be written as follows.

$$\varepsilon = \sum_j \left\{ (A_j + iZ_j) \frac{1}{2} B \left(\frac{1}{C_j - \lambda - i\left(\frac{1}{2}B_j\right)} + \frac{1}{C_j + \lambda - i\left(\frac{1}{2}B_j\right)} \right) \right\} + \varepsilon_\infty \tag{4.14}$$

A harmonic oscillator takes on the characteristics of a Lorentz oscillator when the broadening is significantly less than the centre energy.

Two other oscillator types, namely Tauc-Lorentz and Cody-Lorentz are also useful for modelling amorphous films. The key distinction between these two models is the way of modelling the absorption features at the energies just above the energy gap where the Tauc-Lorentz uses the Tauc law (Eqn. 4.15) and the Cody-Lorentz uses the Cody formulation (Eqn. 4.16) in this region. The expressions of these two types are written as follows.

$$\varepsilon_2(E) \propto \left(\left(E - E_g\right)^2 / E^2\right) \tag{4.15}$$

$$\varepsilon_2(E) \propto \left(E - E_g\right)^2 \tag{4.16}$$

For the Tauc-Lorentz oscillator, the fit parameters include the Amplitude (Amp), Broadening (Br), centre energy (E_0) and the band gap (E_g). The Cody-Lorentz oscillator additionally has E_p and E_t terms which are the transition energies where the absorption features change from Lorentzian to Cody and Cody to Urbach behaviour, respectively. The additional Urbach absorption term is part of the Cody-Lorentz type which is the inverse of the sub-gap absorption coefficient's logarithmic slope [15,19].

In this study, the variable angle spectroscopic ellipsometry measurements of reference oxide films were conducted using a J.A. Woollam M-2000 ellipsometer within a spectral range of 0.7-5.2 eV at angles 65-75° in 5° steps. The precision of ellipsometry measurements have been improved by changing the angle of incidence around the Brewster angle where the p-plane is only refracted but not reflected [16]. The “VASE” term comes from this application.

4.3.2 X-Ray Photoelectron Spectroscopy

X-ray photoelectron spectroscopy is a surface characterisation method which is carried out in a high vacuum chamber by targeting the sample surface with a monoenergetic X-ray source [20]. The photoelectric effect causes the emission of electrons from the sample as a result of the interaction with the X-rays. XPS enables the analysis of electrons that come from the core level to the valence levels, producing distinctive spectra for each identified element [21]. The following Eqn. 4.17 is used to determine the kinetic energy (KE) of these captured electrons.

$$KE = h\nu - BE - \phi_s \tag{4.17}$$

where $h\nu$ is the energy of the X-ray source, BE is the electron's binding energy, and ϕ_s is the spectrometer's work function. Mg (Mg kα) and Al (Al kα) sources are the two typically used X-ray sources, and their photon energies are 1253.6 eV and 1486.6 eV, respectively. The energy difference between the initial and the final states after the photoelectron has left the atom is known as the binding energy (BE) [21]. Due to the fact that every element has a distinct electron configuration, it is possible to identify the elements present in a sample by analysing their spectra. A basic schematic of an XPS setup is shown in Fig. 4.10.

Auger electrons may also be released and detected in addition to the electron emission from the photoelectric effect. The relaxation of the excited electrons following photoemission causes emission of the auger electron. A higher orbital electron relaxes into a hole that forms in the inner orbital caused by the photoelectric effect. Consequently, a photon with the same energy or an electron from the higher energy orbital is emitted. This happens within a few tens of femtoseconds (fs) when the sample emits a photoelectron. Additionally, the Auger electron energy is equal to the energy difference between the initial and double charged final ions. Thus, photo-ionization results in the emission of two electrons, whose combined KE is lower than or equal to the energy of the ionising photons [20–22].

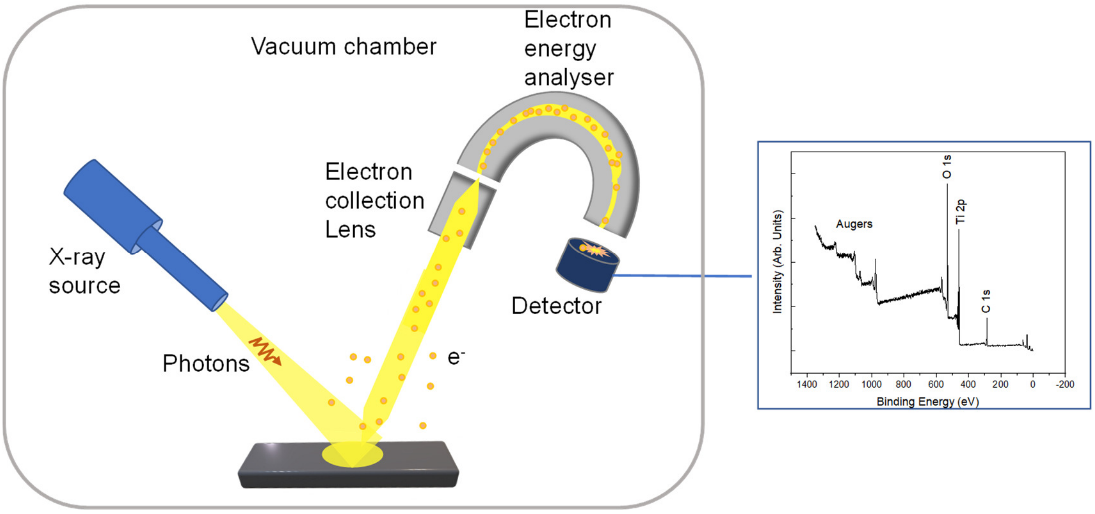

Figure 4.10. Basic components of an XPS system [20].

X-rays can penetrate to depths of a few micrometres, while XPS measurements are only accurate to a few nanometres. This is due to the interaction between electrons and matter, which allows electrons that are emitted a few nanometres below the surface to escape without colliding with other particles. An electron spectrometer detects the KE values of the electrons to identify those that are generated without any energy loss. Only electrons inside the defined energy window are detected by the analyser, which operates in a region known as the pass energy. For measurements, the analyser's acceptance energy is adjusted across the measurement range while the pass energy is fixed [20–22].

For the elemental analysis, there are several peak lines with various binding energies in the observed survey spectrum. Each observed peak is distinct and depends on the measured element's chemical composition as well as the spin orbital—s, p, d, or f—from which the electron is released. The strongest core levels can be used for elemental analysis. For example, Titanium (Ti) survey spectra is composed of 2s, 2p, 3s, 3p core levels and Ti 2p can be used to identify the element as a strong core level peak. Following the ionisation, orbital splitting occurs, resulting in the separation of the two binding energy lines that is specific to the element such as $p_{1/2}$, $p_{3/2}$, $d_{3/2}$, $d_{5/2}$, $f_{5/2}$ and $f_{7/2}$ [20]. The Ti 2p has two peaks those are Ti $2p_{1/2}$ and Ti $2p_{3/2}$ which correspond to energies around 464.5 eV and 458.8 eV, respectively. The CasaXPS software is used to analyse the measured core level spectra. Besides the elemental analysis; secondary electron cut-off (SEC), valence band maximum (VBM), as well as the electron affinity (χ) of materials can be extracted.

Secondary electron cut-off (SEC) measurements can be done by first biasing the sample to differentiate the SEC values of the sample and the analyser, with the nominal value of V_{app} (such as -10 V), and then measuring the SEC edge and a reference core level under the same conditions. This reference core level can then be compared to the non-biased core level to determine precisely the energy shift. Once adjusted for the energy shift, the SEC can be determined by linear intersection of the edge with the spectra background. The valence band edge was also determined in a similar way, by the linear intersection of the edge with the spectra background.

The electron affinity (χ) is then found using the extracted SEC, VBM and the applied bias during the measurements and expressed as

$$\chi = IE - E_g \tag{4.18}$$

where

$$IE = q\phi + VBM \tag{4.19}$$

and

$$q\phi = hv - SEC - qV_{app} \tag{4.20}$$

IE is the ionization energy, VBM is the valence band maximum found from the valence band edge and E_g is the band gap [23]. The XPS measurements in this study was done in Stephenson Institute at University of Liverpool using a SPECS monochromated Al k-α X-ray source (hv = 1486.6 eV) with energy step size of 0.03 eV and integration time of 0.25 s per step, operating at 150 W for core level (CL) and valence band scans, while 9 W for secondary electron cut off scans in an ultra-high vacuum chamber at a base pressure of ~10^{-10} mbar. A detailed XPS study on RF sputtered metal oxide layers including these analyses is conducted in Chapter 5.

4.3.3 Electrical Characterisation

Direct-current (DC) current-voltage (I-V) characteristics of the fabricated diodes were measured using an Agilent-B1500 semiconductor measurement unit (SMU) integrated with a probe station and an optical microscope in a dark screened environment. The DC I-V sweeps were performed from zero to negative and zero to positive voltages with the step voltage of 1-10 mV to observe the possible shifts in the origin of the curves, as well as to avoid any potential charging effect in the oxide layers. Investigating the rectification characteristics and the conduction mechanism of the rectifier structures is the purpose of the DC I-V experiments.

4.4 Conclusion

In this chapter, details of the experimental methods including sample cleaning, material deposition and characterisation equipment have been summarised. The metal electrodes in this work have been deposited using thermal evaporation and RF sputtering. Deposition rate of the thermal evaporation was maintained between 3-4 Å/s to avoid surface roughness and have uniform Au and Al metal electrodes. The Ar gas flow rate and the applied power for the sputtered metals (Ti and Zn) were 5 sccm and 52.5 W, respectively. The ZnO, TiO_2 and NiO layers were also deposited using RF sputtering at 4-5 sccm gas flow rate and 45 W power to control the thickness and have a repeatable deposition process. A base pressure of $< 1\times10^{-6}$ mBar was ensured before the deposition for both evaporation and sputtering processes to provide high quality deposition by preventing any collision between the vaporized material and the other particles in the vacuum chamber. ALD technique has also been used to deposit Al_2O_3, Nb_2O_5 and Ta_2O_5 thin films for MI^3M fabrication. It provided an excellent control in the film thickness and the oxide uniformity.

The devices have been patterned using two different methods which are shadow mask evaporation and photolithography. Shadow mask evaporation has the advantage of being fast and easy to process which is important to fabricate different diode combinations prior to photolithography. The device area of the shadow mask patterned diodes was 10,000 μm^2. A conventional photolithography tool was also used for fabrication of scaled devices to improve the diode coupling efficiency for high frequency operations. Devices having four different areas (1 μm^2, 4 μm^2, 16 μm^2 and 64 μm^2) have been fabricated using this technique to study the effect of device scaling on rectification performance.

VASE analysis has been used to determine the thickness, optical properties, band gap and the quality of the deposited oxide films. The reference samples of deposited oxide films on Si substrates were prepared simultaneously together with the actual devices in the ALD or RF sputtering chambers for the VASE analysis. The XPS measurements were used for elemental analysis of deposited thin films, as well as to determine their electron affinity. Finally, the fabricated diodes have been characterised by DC I-V measurements to assess their rectification performance such as dynamic resistance, responsivity, asymmetry and non-linearity using a semiconductor parameter analyser integrated with a probe station.

References

[1] D. A. Weerakkody, “Engineered high-K oxides,” The University of Liverpool, *PhD thesis*, 2016.

[2] J. E. Mahan, *Physical Vapor Deposition of Thin Films*. Wiley-Interscience, 2000. doi: 10.1604/9780471330011.

[3] R. F. Bunshah, Ed., *Handbook of Deposition Technologies for Films and Coatings: Science, Technology and Applications. Materials Science and Process Technology Series*. William Andrew, 1994.

[4] J. Handley, “Product Review: Quartz Crystal Microbalances,” *Analytical Chemistry*, vol. 73, no. 7, p. 225 A-229 A, 2001, doi: 10.1021/ac012432d.

[5] H. Frey and H. R. Khan, Eds., *Handbook of Thin Film Technology*. Springer, 2016.

[6] R. Kukla, “Magnetron sputtering on large scale substrates: an overview on the state of the art,” *Surface and Coatings Technology*, vol. 93, no. 1, pp. 1–6, 1997, doi: 10.1016/s0257-8972(97)00018-2.

[7] P. J. Kelly and R. D. Arnell, “Magnetron sputtering: a review of recent developments and applications,” *Vacuum*, vol. 56, no. 3, pp. 159–172, Mar. 2000, doi: 10.1016/s0042-207x(99)00189-x.

[8] T. M. Adams and R. A. Layton, *Introductory MEMS: Fabrication and applications*. New York: Springer, 2010.

[9] P. D. Davidse, “Theory and practice of RF sputtering,” *Vacuum*, vol. 17, no. 3, pp. 139–145, 1967, doi: 10.1016/0042-207x(67)93142-9.

[10] R. W. Johnson, A. Hultqvist, and S. F. Bent, “A brief review of atomic layer deposition: from fundamentals to applications,” *Materials Today*, vol. 17, no. 5, pp. 236–246, 2014, doi: 10.1016/j.mattod.2014.04.026.

[11] S. M. George, “Atomic Layer Deposition: An Overview,” *Chemical Reviews*, vol. 110, no. 1, pp. 111–131, 2009, doi: 10.1021/cr900056b.

[12] J. Haemaelaeinen, M. Ritala, and M. Leskelae, “ChemInform Abstract: Atomic Layer Deposition of Noble Metals and Their Oxides,” *ChemInform*, vol. 45, no. 11, p. no-no, 2014, doi: 10.1002/chin.201411237.

[13] A. Rothen, “The Ellipsometer, an Apparatus to Measure Thicknesses of Thin Surface Films,” *Review of Scientific Instruments*, vol. 16, no. 2, pp. 26–30, 1945, doi: 10.1063/1.1770315.

[14] D. Gonçalves and E. A. Irene, “Fundamentals and applications of spectroscopic ellipsometry,” *Química Nova*, vol. 25, no. 6a, pp. 1050–1050, 2002, doi: 10.1590/s0100-40422002000600025.

[15] JA. Woollam , *CompleteEASE data analysis manual.*, New England United States Am.: JA Woollam Co Inc, 2011

[16] H. Tompkins and E. A. Irene, *Handbook of Ellipsometry*. William Andrew, 2005.

[17] B. Johs and J. S. Hale, "Dielectric function representation by B-splines," *physica status solidi (a)*, vol. 205, no. 4, pp. 715–719, Apr. 2008, doi: 10.1002/pssa.200777754.

[18] J. W. Weber, T. A. R. Hansen, M. C. M. van de Sanden, and R. Engeln, "B-spline parametrization of the dielectric function applied to spectroscopic ellipsometry on amorphous carbon," *Journal of Applied Physics*, vol. 106, no. 12, p. 123503, Dec. 2009, doi: 10.1063/1.3257237.

[19] D. I. Patel, D. Shah, J. N. Hilfiker and M. R. Linford, "A tutorial on spectroscopic ellipsometry (SE) 5.: Using the Tauc-Lorentz and Cody-Lorentz models to describe the absorption features of amorphous silicon (a-Si)", *Vac. Technol. Coating*, vol. 20, pp. 34-37, 2019.

[20] J. M. Hollander, and L. J. William, "X-ray photoelectron spectroscopy." *Accounts of chemical research*, vol. 3, no. 6, pp. 193-200. 1970.

[21] J. F. Moulder, W. F. Stickle, P. E. Sobol, and K. D. Bomben, *Handbook of X-Ray Photoelectron Spectroscopy*. 1992. doi: 10.1604/9780962702624.

[22] J. F. Watts, *X-ray photoelectron spectroscopy.*, *Surface science techniques*, vol. 45, no. 5, 1994.

[23] I. Z. Mitrovic, A. D. Weerakkody, N. Sedghi, J. F. Ralph, S. Hall, V. R. Dhanak, Z. Luo, and S. Beeby, "Controlled modification of resonant tunneling in metal-insulator-insulator-metal structures," *Applied Physics Letters*, vol. 112, no. 1, p. 012902, 2018, doi: 10.1063/1.4999258.

Chapter 5

5. Physical and electrical characterisation of metal oxide thin films

In this chapter, film quality and material properties of deposited oxides have been studied using several experimental techniques. These include VASE, XPS and I-V measurements. Initially, a sub-band gap analysis has been carried out on SiO_2/Si samples to evaluate the gate oxide for inclusion in Si power MOSFETs. The samples were prepared by Nexperia semiconductor company using different oxidation (including wet and dry oxidation) methods for comparison. Furthermore, TiO_2, ZnO and NiO films were deposited on bare Si substrates using RF sputtering method. These samples were measured by VASE and XPS to analyse thin oxide films optical properties (n, k), as well as to extract their band gap values (E_g). Additionally, a band gap analysis was done on two different plasma-enhanced (PE) and thermal ALD TiO_2 thin films prepared by AMO, Germany for comparison with the in-house RF sputtered TiO_2 films. The I-V characterisation was carried out on two different 3 nm ALD Al_2O_3 based MIM diodes with Au/Au and Au/Ti electrodes prepared by shadow mask to examine their conduction mechanisms. The VASE and XPS results on the RF sputtered oxide films in this chapter have been submitted to Journal of Applied Physics. The manuscript has been accepted for publication after minor revision.

5.1 VASE analysis on oxide thin films

5.1.1 VASE analysis on SiO_2/Si wafers for Si power MOSFET gate oxide layers

A particularly important class of power switching transistors are silicon power metal-oxide-semiconductor field-effect transistors (Si power MOSFETs). They are produced with drain voltage ratings ranging from approximately 8 V to 1 kV [1–3]. Si MOSFETs are expected to be in widespread usage for the near future, particularly at drain bias ratings under 200 V. The reliability of Si power MOSFETs has been improved over time including the reliability of the gate stack technology. It is known that power MOSFETs under gate bias stress can become unstable due to underlying changes in gate-oxide trapped charges and the formation of interface states. The occurrence of these charges due to the specifics of the gate oxidation process is less understood [1–6].

In this section, different oxidation methods that were used to produce SiO_2 gate oxides for power MOSFETs have been evaluated. The samples were prepared by Nexperia semiconductor company. It is well-known that gate bias stressing in power MOSFETs can lead to instability through underlying changes in gate oxide trapped charge and generation of interface states. Less well-known is the role played by details of the gate oxidation process in the manifestation of these effects. The VASE point-by-point analysis was performed to gain understanding of defects in these oxides.

A selection of thermal oxides shown in Table 5.1 were grown on bare (100) silicon wafers after the industry standard wet cleaning procedure of Nexperia. The growth process was carried out in the same manufacturing equipment that is used to develop the gate oxides of Nexperia power MOSFETs.

Table 5.1. Preparation methods, thicknesses, *n* and MSE values of the SiO_2 on Si samples measured by VASE at single points on the wafers.

Sample	**Deposition method**	**Thickness (± 0.1 nm)**	**n @ 1.96 eV**	**MSE**
Native oxide	-	1.37	-	1.32
Wet	100% wet oxidation at 800 °C	72.3	1.48	1.96
Wet-dry	Standard 50% wet oxidation at 800 °C then 50% dry dilute at 1100°C	74.4	1.46	1.67
Dry	900 °C dry oxidation	74.3	1.47	1.84
Dry-wet	50% dry dilute at 1100 °C then 50% wet oxidation at 800 °C (Order reversed compared to wet-dry)	75.8	1.47	1.79

The oxides (wet, wet-dry, dry and dry-wet SiO_2) were grown following the recipes stated in Table 5.1. The layers had the same nominal thickness of 75 nm. It can be seen from Table 5.1 that wet oxidation produced thinner oxide of ~72 nm. The SiO_2 thicknesses measured at single points around the centre area on the samples are shown in Table 5.1. In addition, Nexperia fabricated power MOSFET chips using the same gate oxide processes as those used in the samples for the ellipsometry measurements and performed electrical characterisation on their fabricated devices.

The test wafers were measured using J.A. Woollam M-2000 spectroscopic ellipsometer having a spectral range between 0.74 eV - 5.1 eV. Data acquisition was performed by the default CompleteEASE software and then transferred to the WVASE software for point-by-point analysis. For the point-by-point analysis, initially the native oxide thickness of bare Si substrate is determined and used in the oxide fittings as a usual SE fitting procedure. The thickness of the oxide layers is then modelled by a suitable theoretical model and fixed. In this analysis, Cauchy relation was used as the theoretical model since it was the most suitable way for modelling the transparent SiO_2 layers. As an example, the Cauchy model that was used for fitting wet oxidized SiO_2 on Si sample is shown in Fig. 5.1 (a). As explained by Eqn. 4.4, the A (Amplitude), B (Broadening) and C (Centre energy) are the Cauchy parameters to determine the thickness and the refractive index (*n*) of the layer. The k Amplitude, Exponent and Band Edge parameters in the model are normally used to determine the shape of the extinction coefficient (*k*) and they were not used in this fitting since the SiO_2 layer was only measured in the transparent region.

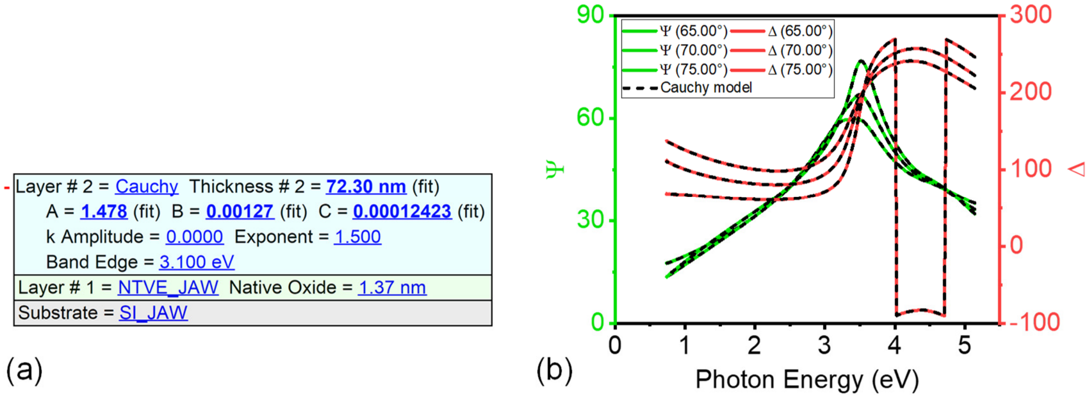
- Layer # 2 = Cauchy Thickness # 2 = **72.30 nm** (fit)
  A = **1.478** (fit) B = **0.00127** (fit) C = **0.00012423** (fit)
  k Amplitude = 0.0000 Exponent = 1.500
  Band Edge = 3.100 eV
Layer # 1 = NTVE_JAW Native Oxide = 1.37 nm
Substrate = SI_JAW

(a)

(b)

Figure 5.1. (a) Cauchy model and (b) experimental ψ (amplitude ratio) and Δ (phase difference) parameters measured at 65°, 70° and 75° angle of incidences fitted with theoretical models for SiO_2 on Si samples.

Other models such as default SiO_2.MAT, SiO_2.JAW and SiO_2 (Sellmeier) in the CompleteEASE software library were also checked for comparison but the Cauchy relation provided lowest Mean-squared-error (MSE) values. The MSE represents the accuracy of the fittings based on the standard deviation between the experimental data and the theoretical model. It is expressed by [7]:

$$MSE = \frac{1}{2N-M}\sum_{i=1}^{N}\left(\left(\frac{\psi_i^{model}-\psi_i^{experiment}}{\sigma_{\psi,i}^{experiment}}\right)^2 + \left(\frac{\Delta_i^{model}-\Delta_i^{experiment}}{\sigma_{\Delta,i}^{experiment}}\right)^2\right) \tag{5.1}$$

where N is the number of measured points of ψ and Δ, M is the total number of fit parameters, $\sigma_{\psi,i}^{experiment}$ and $\sigma_{\Delta,i}^{experiment}$ are the standard deviations of ψ and Δ parameters. The MSE value increases with the thickness and the complexity of the measured thin films. It also changes depending on the type of the substrate materials [8]. An MSE < 10 can be usually considered a good fit depending on these conditions [7,8]. For this sample set, MSE ≤ 2 can be considered acceptable. The resulting fits for the ψ and Δ parameters for the wet oxidized SiO_2 sample are shown in Fig. 5.1 (b) where they exhibited a good fit with an MSE value of 1.95. All the other measurement results also matched this criterion as shown in Table 5.1.

After the single point measurements, mapping analysis was done on each sample by scanning the wafers using the automated mapping tool of the ellipsometer to check the film uniformity. In this method, the results of the single point measurements were used as the reference models for the mapping analysis and the wafers were scanned at 70^o angle of incidence. The maps were formed by measuring 29 different points on each sample within an area of 63.6 cm^2. Initially, the reference Si substrate was scanned to check the surface uniformity (Fig. 5.2). As seen in Fig. 5.2 and Table 5.1, the native oxide layer on the reference Si wafer was uniform and had an average thickness of 1.4 nm. Therefore, this thickess value was used in the native oxide models during the mapping analysis of SiO_2 layers.

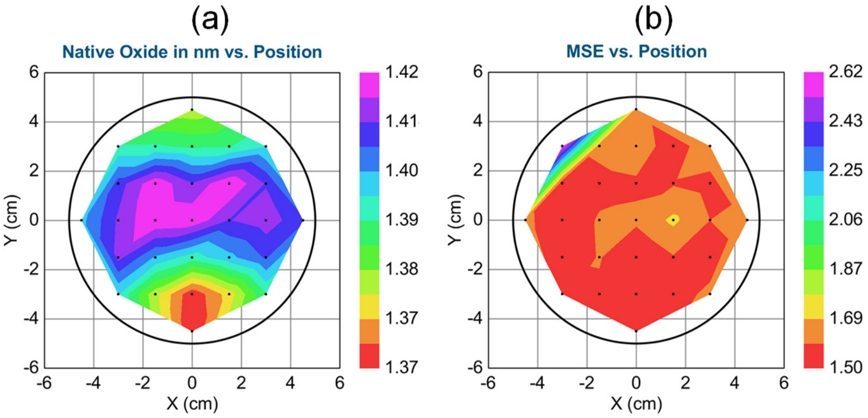

Figure 5.2. (a) Thickness, and (b) MSE mapping results for the native oxide layer on bare Si substrate within a scan area of 63.6 cm^2.

The thickness, n and MSE of the mapping results for each sample (wet, wet-dry, dry and dry-wet) are shown in Fig. 5.3. The results show that the SiO_2 layers grown with different methods have a good surface uniformity with a maximum standard deviation of 0.3 nm in thickness for the dry oxidized sample. The average *n* value also differs ± 0.02 between different oxidation methods and also consistent with the literature values (n = 1.46 for SiO_2 [9]). The highest average MSE value was found to be 2.4 for the dry-wet oxidized sample which is still acceptable.

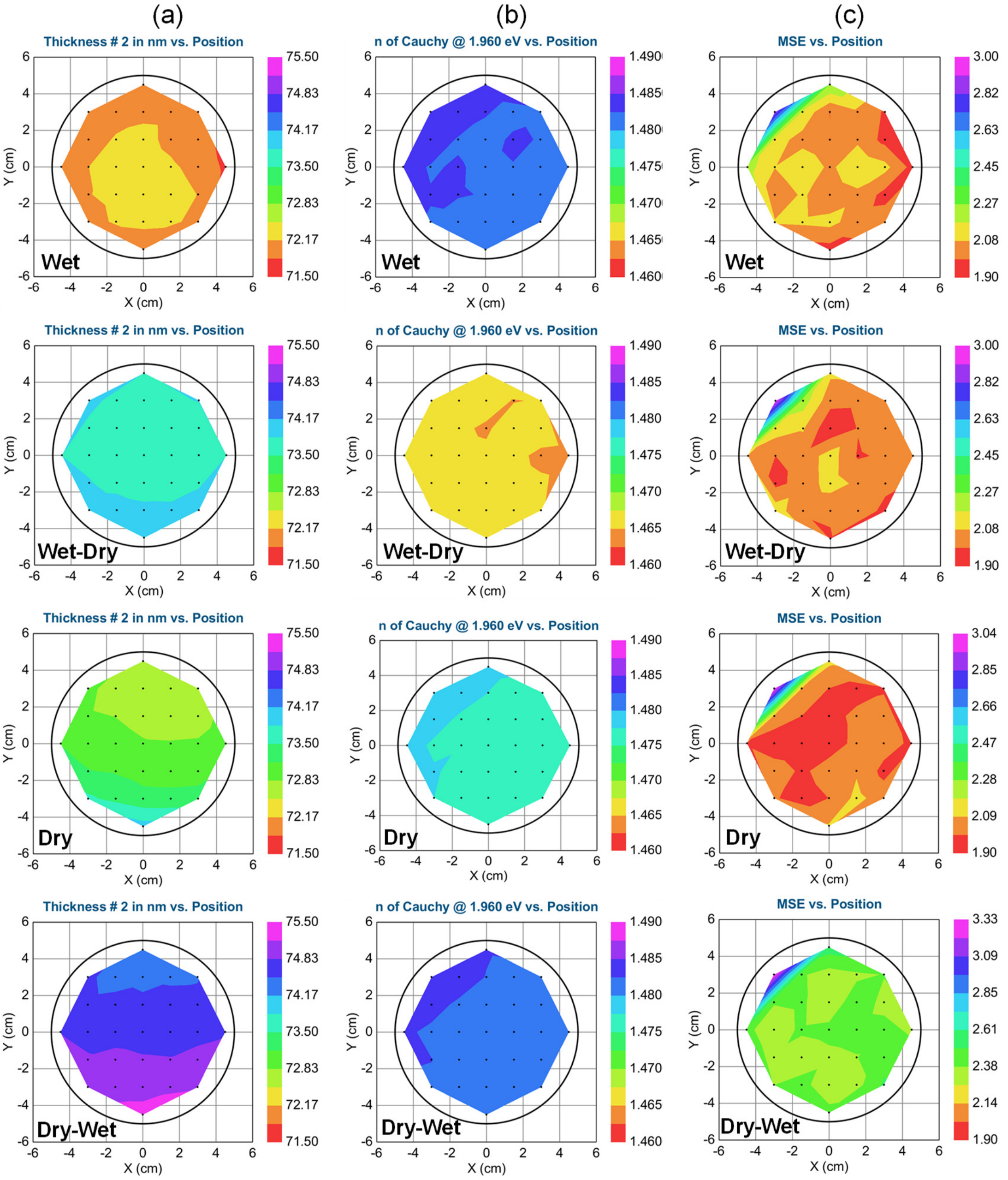

Figure 5.3. (a) Thickness, (b) *n* and (c) MSE mapping results for wet, wet-dry, dry and dry-wet samples within a scan area of 63.6 cm^2.

The details of the mapping measurements are summarised in Table 5.2.

Table 5.2. Mapping results of the SiO_2 on Si wafers including thickness, n and MSE values.

Sample	**Parameter**	**Average**	**Minimum**	**Maximum**	**Standard Deviation**
Native oxide	Thickness (nm)	1.40	1.37	1.42	0.01
	MSE	1.62	1.50	2.62	0.20
Wet	Thickness (nm)	72.11	71.77	72.30	0.13
	n @ 1.96 eV	1.48	1.48	1.49	0.00
	MSE	2.10	1.95	2.87	0.17
Wet-dry	Thickness (nm)	73.78	73.59	74.14	0.13
	n @ 1.96 eV	1.47	1.47	1.47	0.00
	MSE	2.07	1.92	2.97	0.19
Dry	Thickness (nm)	73.00	72.67	73.97	0.30
	n @ 1.96 eV	1.48	1.48	1.48	0.00
	MSE	2.04	1.90	3.04	0.20
Dry-wet	Thickness (nm)	74.75	74.37	75.28	0.24
	n @ 1.96 eV	1.48	1.48	1.49	0.00
	MSE	2.42	2.31	3.33	0.18

After these measurements, the point-by-point analysis was carried out on the SiO_2 layers. In this analysis, the optical properties are extracted by fixing all the variables in the modelling process except the real (ε_1) and imaginary (ε_2) parts of the dielectric function. A detailed account of point-by-point was done by Price *et al.* [10,11]. The method involves directly inverting the ellipsometry data to extract the optical constant for each wavelength measured independently. It can reveal certain defect energy levels within the band gap. Mitrovic *et al.* [12] also studied the sub-band gap absorption features of Tm_2O_3 on Ge using the same method. A detailed explanation of this method is illustrated in Fig. 5.4.

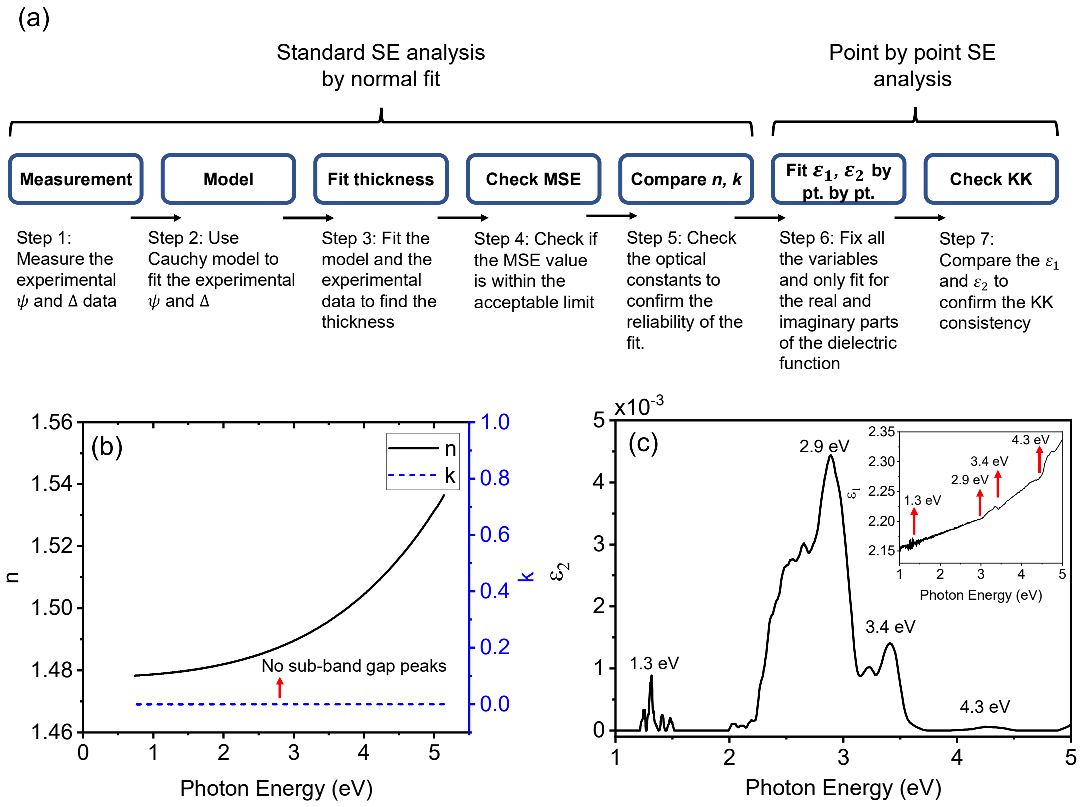

Step 1: Measure the experimental ψ and Δ data

Step 2: Use Cauchy model to fit the experimental ψ and Δ

Step 3: Fit the model and the experimental data to find the thickness

Step 4: Check if the MSE value is within the acceptable limit

Step 5: Check the optical constants to confirm the reliability of the fit.

Step 6: Fix all the variables and only fit for the real and imaginary parts of the dielectric function

Step 7: Compare the ε_1 and ε_2 to confirm the KK consistency

Figure 5.4. (a) Flow chart for normal and point-by-point SE analysis on SiO_2/Si sample, (b) optical constants (n, k) derived from normal fit and (c) imaginary (ε_2) part of the dielectric function showing the sub-band gap absorption peaks derived from point-by-point fitting. The inset figure shows the associated ε_1 peaks based on the KK consistency.

The analysis starts with measuring the samples to obtain the experimental ψ and Δ values within the spectral range of 0.74 eV - 5.1 eV (Step 1) as shown in Figure 5.4 (a). Initially, the native oxide thickness of the substrate (bare Si wafer in this study) is determined and used in SiO_2 fittings. Then, the actual oxide layers are measured and saved as another model (Cauchy) on the substrate (Step 2). The thickness of the SiO_2 layers is estimated from the non-absorbing (transparent) part of the spectra, modelled by the Cauchy relation (Eqn. 4.4) explained in section 4.3.1 and then fixed (Step 3). After finding the SiO_2 thickness, the MSE is checked to confirm the reliability of the fittings (Step 4). Once a low MSE value is obtained, the optical constants (n and k) are being checked and compared with the literature values (Step 5). Having determined the characteristics of the SiO_2 layers in the non-absorbing region, the optical properties are then extracted from the real (ε_1) and imaginary (ε_2) parts of the dielectric function

(Step 6). This is done by fixing all the variables including the thickness and only fitting for the ε_1 and ε_2 parameters with respect to the photon energy. Finally, the reliability of the sub-band gap peaks is checked by comparing the ε_1 and ε_2 based on the KK consistency which is determined by the following equations (Step 7) [13]:

$$\chi_1 = 1 + 2P\int_0^{+\infty} \frac{d\omega' \chi_2(\omega')}{\pi(\omega' - \omega)} \tag{5.2}$$

$$\chi_2 = -2P\int_0^{+\infty} \frac{d\omega' (\chi_1(\omega') - 1)}{\pi(\omega' - \omega)} \tag{5.3}$$

where P denotes the Cauchy principle number, which defines the function's limits when it diverges (such as $\omega' = \omega$). According to this principle, the absorption peaks seen in ε_2 should also be preserved in ε_1. The difference between the normal and point-by-point fittings in the absorbing region is shown in Figs. 5.4 (b) and (c). In Fig. 5.4 (b), no sub-band gap peak is observed using the normal fitting method, while in Fig. 5.4 (c) the peaks are seen in the absorbing region with the use of point-by-point method. The inset figure in Fig. 5.4 (c) shows the ε_1 peaks associated with the sub-band gap peaks in ε_2 based on the KK consistency.

Figure 5.5 shows a comparison of real (ε_1) and imaginary (ε_2) parts of the dielectric function between the set of wet, wet-dry (first wet and then dry), dry and dry-wet (first dry and then wet) SiO_2 on Si wafers obtained from VASE measurements. As shown in the Fig. 5.5, we consistently see the same peaks in the ε_2 graphs of all samples at around 1.3 eV, 2.9 eV and 3.4 eV. The reliability of the point-by-point data inversion method was checked by the KK consistency based on Eqns. 5.2 and 5.3. According to this method, the spectral features are seen at the same photon energies of 1.3 eV, 2.9 eV, 3.4 eV and 4.3 eV in both ε_1 and ε_2 which represents the preservation of KK consistency.

The peak at 1.3 eV is interpreted as the presence of the hydrogen bridge defect (Si-H-Si) [14,15] in the SiO_2 layers. This defect corresponds to oxygen vacancies in the SiO_2 and is likely to be homogeneous in wet oxide layers [16]. The Si-H-Si formation process is dependent on the compactness of the layer with wet-grown SiO_2 being less dense than the dry.

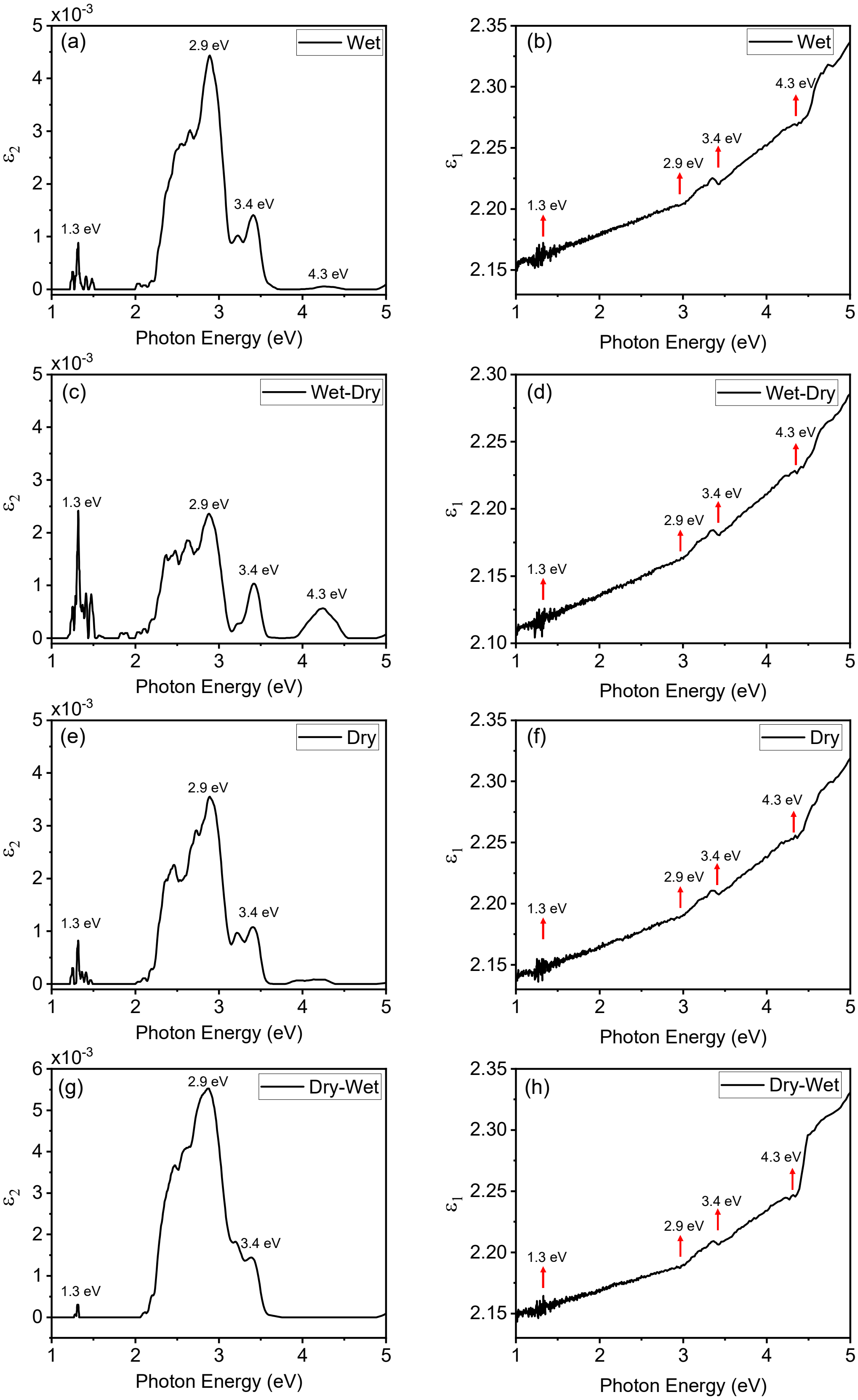

Figure 5.5. Comparison of real (ε_1) and imaginary (ε_2) parts of the dielectric function between the set of (a)-(b) wet, (c)-(d) wet-dry, (e)-(f) dry and (g)-(h) dry-wet SiO_2 on Si wafers.

Therefore, films grown purely wet (Figs. 5.5 (a)-(b)) and those wet-dry (Figs. 5.5 (c)-(d)) should show higher signals than those grown dry and dry-wet as in those cases, wet grown material is closer to the surface [16]. This is apparent in our results. The absorption at 2.9 eV has been found as intrinsic to the interface and refers to optical transitions associated with negatively charged oxygen vacancies in the interfacial SiO_x layer. The peaks at 3.4 eV and 4.3 eV refer to the critical points of Si due to absorption in the substrate [10,11,14–16].

This study clearly demonstrates that the point-by-point VASE analysis can be an important tool to elucidate signature of defects in oxides and at oxide/semiconductor interface and hence in correlation with electrical characterization of associated devices provide useful diagnostics of reliability and operation of the Si power MOSFETs.

5.1.2 VASE analysis of RF sputtered oxides

In this section, TiO_2, ZnO, and NiO films deposited by RF sputtering on Si wafers were investigated by VASE to find their thickness, optical constants (*n*, *k*) and the band gap (E_g) values. The samples were prepared in-house using the cleaning procedures explained in section 4.1.1. This includes cleaning the samples with acetone and IPA in the ultrasonic bath for 10 minutes each and drying with N_2. Then, the samples are placed in the UV ozone cleaner for 2 minutes to remove any remaining residues. The oxide films were sputtered using an Ar gas flow rate of 4-5 sccm at 45 W RF power after reaching a base pressure of $< 1\times10^{-6}$ mBar prior to deposition and the process pressure was kept at $3\text{-}4\times10^{-3}$ mBar for each process. Initially, the reference Si wafer was measured to ascertain the thickness of the native oxide which was then used in subsequent fittings of oxide/Si samples. The measured oxide layers and the native oxide thicknesses are shown in Fig. 5.6. The native oxide thickness was measured as 1.96 nm for the Si substrate under the TiO_2 layer and it was found to be 1.74 nm for the layers under ZnO and NiO. Default TiO_2-Cody Lorentz and ZnO-GenOsc models have been used for the TiO_2 and ZnO fittings, respectively. For the NiO, B-spline model was used.

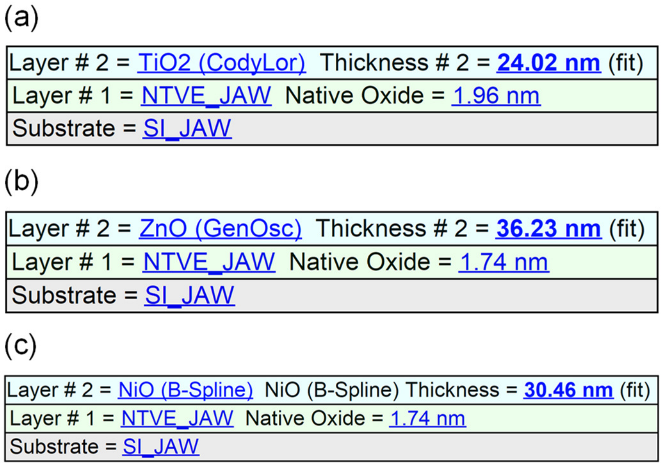

(a)

Layer # 2 = TiO2 (CodyLor) Thickness # 2 = **24.02 nm** (fit)
Layer # 1 = NTVE_JAW Native Oxide = 1.96 nm
Substrate = SI_JAW

(b)

Layer # 2 = ZnO (GenOsc) Thickness # 2 = **36.23 nm** (fit)
Layer # 1 = NTVE_JAW Native Oxide = 1.74 nm
Substrate = SI_JAW

(c)

Layer # 2 = NiO (B-Spline) NiO (B-Spline) Thickness = **30.46 nm** (fit)
Layer # 1 = NTVE_JAW Native Oxide = 1.74 nm
Substrate = SI_JAW

Figure 5.6. SE models used for measuring the thicknesses of (a) TiO_2 (CodyLor), (b) ZnO (GenOsc) and (c) NiO (B-Spline) thin films.

The default TiO_2 (CodyLor) model has only one Cody Lorentz harmonic oscillator, which was explained in Eqn. 4.16, to fit the n and k values of the TiO_2 layer. On the other hand, the ZnO (Gen-Osc) model includes three different harmonic oscillators, those are one parametrised semiconductor oscillator (PSemi) and two Gaussian oscillators. The equations for the Gaussian oscillator are given in Eqns. 4.10 and 4.11. The PSemi model mathematically represents dielectric functions as the sum of various Gaussian polynomials and poles occurs due to the absorption outside of the modelled region [17]. The reason behind using these two models is that they give the most accurate thickness values close to the target deposition thickness. Also, the lowest MSE values with physical optical constants (n, k) were obtained using these models. It should be noted that using other models, such as B-Spline, for these two films can result in lower MSE values however with a drawback of having unphysical n and k values. For the NiO film, since there was no available default model in the CompleteEase software, the modelling was started with fitting the ψ and Δ values of the NiO in the transparent (0.74 eV – 2.0 eV) region using the Cauchy relation. Then, the Cauchy model was parametrized to B-spline and fitted for the whole energy range to obtain the n and k characteristics in the full energy spectrum. The KK consistency between the real and the imaginary part of the dielectric function was preserved in all fittings.

The MSE between the experimental and theoretical (fitted) (ψ, Δ) versus photon energy data curves was monitored to assure a good quality fit. The MSE values were found to be 7.7 for TiO_2 (CodyLor), 1.8 for ZnO (GenOsc) and 2.5 for NiO (B-spline) models. The fitted ψ and Δ versus photon energy data for TiO_2, ZnO and NiO are shown in Fig. 5.7.

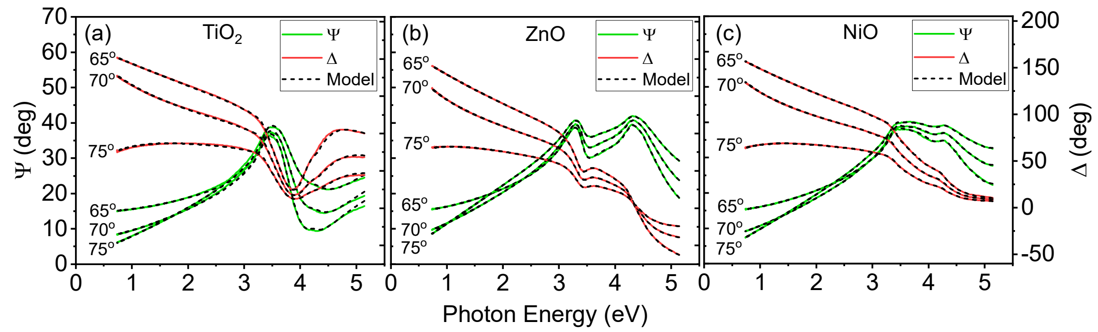

Figure 5.7. The experimental ψ (amplitude ratio) and Δ (phase difference) parameters measured at 65°, 70° and 75° angle of incidences fitted with theoretical models for (a) TiO_2, (b) ZnO and (c) NiO.

Figure 5.8 shows the measured *n* and E_g values derived from the Tauc plots for the bulk (>10 nm) oxides. The detailed values are shown in Table 5.3.

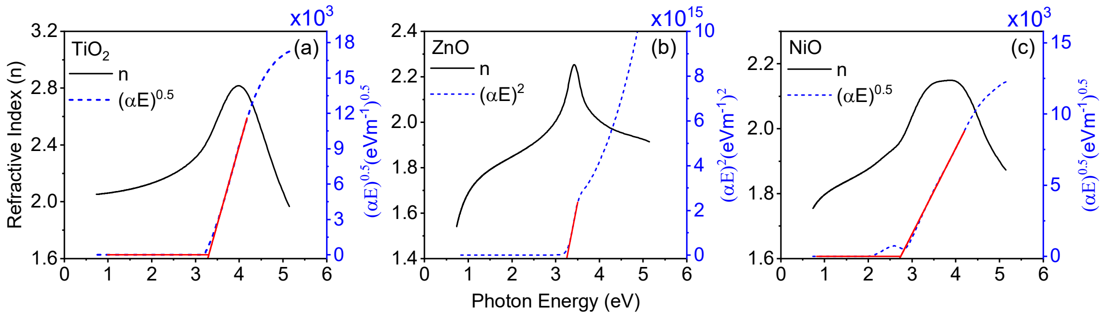

Figure 5.8. Refractive index (*n*) and Tauc, i.e. $(\alpha E)^{0.5}$ for indirect and $(\alpha E)^2$ for direct band gap, versus photon energy (E) plots (where α is absorption coefficient and E – photon energy) for: (a) TiO_2, (b) ZnO and (c) NiO films on Si substrates. The band gap (E_g) of each oxide was calculated from the linear extrapolation of the Tauc plot to the base line, as depicted.

The extracted band gaps of the TiO_2 (3.32 eV), ZnO (3.25 eV) and NiO (2.75 eV) films as well as *n* at 632.8 nm (1.96 eV) are consistent (±0.2) with the reported values archived in the CompleteEASE software [8] used for the VASE analysis and are summarized in Table 5.3.

Table 5.3. Summary of VASE analysis results for the ZnO, NiO and TiO_2 films.

Oxide	Substrate	Native oxide thickness (nm)	Deposition method	Model	MSE	Oxide thickness (nm)	Refractive index (n)	Band gap (E_g)
ZnO	Si	1.74	RF sputter	Gen-Osc	1.8	36.2	1.84	3.25
NiO	Si	1.74	RF sputter	B-spline	2.5	30.5	1.87	2.75
TiO_2	Si	1.96	RF sputter	Cody-Lorentz	7.7	24.0	2.13	3.32
	Si	6.32	PE-ALD		1.3	6.5	2.32	3.38
	Ti/Al/Si	-	PE-ALD		11.1	2.4	2.38	3.50
	Ti/Al/Si	-	Thermal ALD		9.9	5.7	2.44	3.39

5.1.3 VASE analysis of thermal and PE-ALD TiO_2 thin films

The plasma-enhanced (PE) and thermal ALD TiO_2 films were deposited at AMO GmbH research institute in Germany and measured at Liverpool by VASE. These TiO_2 films are to be used in metal-insulator-graphene (MIG) rectenna, an alternative device structure for THz energy harvesting introduced in section 1.3.4 [18]. The latest reported Ti/TiO_2/G device [18] was based on 5 nm TiO_2 grown by plasma-enhanced atomic layer deposition. The target thickness of the deposited thin films was 5 nm. The PE-ALD TiO_2 layers having a nominal thickness of 5 nm were grown on two different substrates: (i) a bare Si wafer and (ii) 50 nm Al/20 nm Ti metal coated Si substrate. On the other hand, the thermal ALD TiO_2 layers were deposited only on 50 nm Al/20 nm Ti metal coated Si substrates. The sample details, deposition methods as well as the VASE analysis results of these three samples are also summarised in Table 5.3.

Initially, the native oxide thickness of the reference Si wafer was measured to include in the oxide fittings. It should be noted that the native oxide thickness for the bare Si substrate was found to be 6.32 nm using the Cauchy model which indicates a highly oxidized substrate and can affect the surface uniformity of the deposited films. On the other hand, since the metals are opaque materials, it is not possible to measure the metal thickness via SE. Therefore, for the metal substrates, the actual thickness of Al and Ti layers were assumed to be 50 nm and 20 nm, respectively based on the nominal growth thickness values. Then, the optical constants (n, k) of Al and Ti were fitted until having a reasonable fit between the theoretical models and the experimental curves. After that, the measured TiO_2 layers were fitted using the Cody-Lorentz model in the CompleteEASE software library. Model layers for the three different samples are shown in Fig. 5.9.

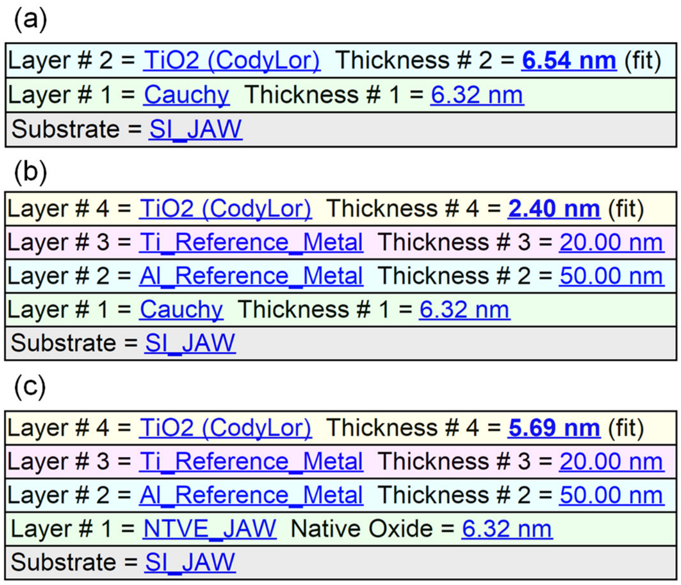
(a)

Layer # 2 = TiO2 (CodyLor) Thickness # 2 = **6.54 nm** (fit)
Layer # 1 = Cauchy Thickness # 1 = 6.32 nm
Substrate = SI_JAW

(b)

Layer # 4 = TiO2 (CodyLor) Thickness # 4 = **2.40 nm** (fit)
Layer # 3 = Ti_Reference_Metal Thickness # 3 = 20.00 nm
Layer # 2 = Al_Reference_Metal Thickness # 2 = 50.00 nm
Layer # 1 = Cauchy Thickness # 1 = 6.32 nm
Substrate = SI_JAW

(c)

Layer # 4 = TiO2 (CodyLor) Thickness # 4 = **5.69 nm** (fit)
Layer # 3 = Ti_Reference_Metal Thickness # 3 = 20.00 nm
Layer # 2 = Al_Reference_Metal Thickness # 2 = 50.00 nm
Layer # 1 = NTVE_JAW Native Oxide = 6.32 nm
Substrate = SI_JAW

Figure 5.9. SE models used for measuring the thicknesses of (a) PE-ALD TiO_2 on Si, (b) PE-ALD TiO_2 on metal and (c) thermal ALD TiO_2 on metal films.

The experimental ψ and Δ parameters measured at 65°, 70° and 75° angle of incidences and the theoretical fittings for 3 different samples are shown in Fig. 5.10.

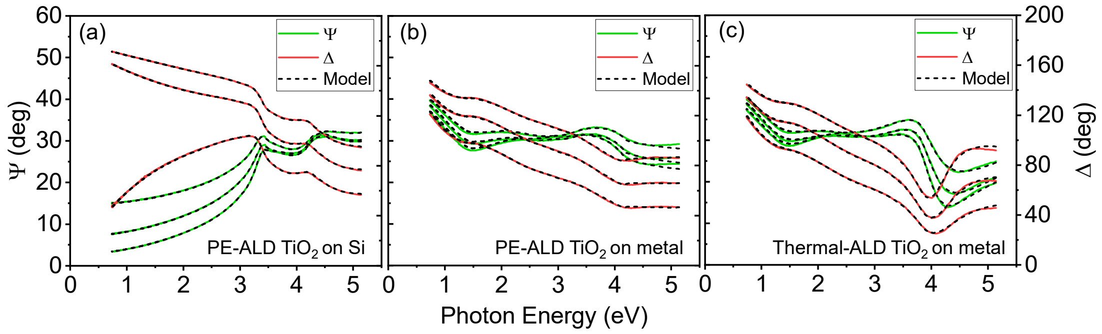

Figure 5.10. The experimental ψ (amplitude ratio) and Δ (phase difference) parameters measured at 65°, 70° and 75° angle of incidences fitted with theoretical models for (a) PE-ALD TiO_2 on bare Si, (b) PE-ALD TiO_2 on 20 nm Ti/50 nm Al/Si and (c) thermal ALD TiO_2 on 20 nm Ti/50 nm Al/Si substrates.

The measured oxide thicknesses were found to be 6.54 nm, 2.40 nm and 5.69 nm for PE-ALD TiO_2 on bare Si, PE-ALD TiO_2 on 20 nm Ti/50 nm Al/Si and thermal ALD TiO_2 on 20 nm Ti/50 nm Al/Si samples, respectively as shown in Table 5.3. It is seen that the thickness of the 2.40 nm PE-ALD TiO_2 on metal substrate deviates from the target thickness of 5 nm more than the other two samples. This can be attributed to the underlying metal layers since they are not ideal to be used as a substrate material. Normally, for a metal to be used as substrate, its thickness should be > 60 nm to be considered as a bulk layer. Therefore, the light beam cannot penetrate through the metal layer. Then, the ψ and Δ values of the metal substrate can be found by only fitting the optical constants (n, k). However, in these samples, there are two metal layers (20 nm Ti and 50 nm Al) and the thickness of the top Ti layer is not sufficient to be considered as bulk which can cause errors in the fitting of the TiO_2 layer. This is also supported by the high MSE value of ~11 coming from the fittings. On the other hand, the PE-ALD TiO_2 on Si substrate has a very good fit between the experimental data and the theoretical model with an MSE value of ~1. The thermal ALD TiO_2 on 20 nm Ti/50 nm Al/Si also has a relatively high MSE value ~9 because of being measured on the metal layers.

In order to check the uniformity of these films, mapping analysis was done by measuring 121 different point on the samples within a scan area of 1.5 × 1.5 cm^2. Initially, the reference Si substrates were scanned to check the surface uniformity as shown in Fig. 5.11. The details of the mapping results are also reported in Table 5.4.

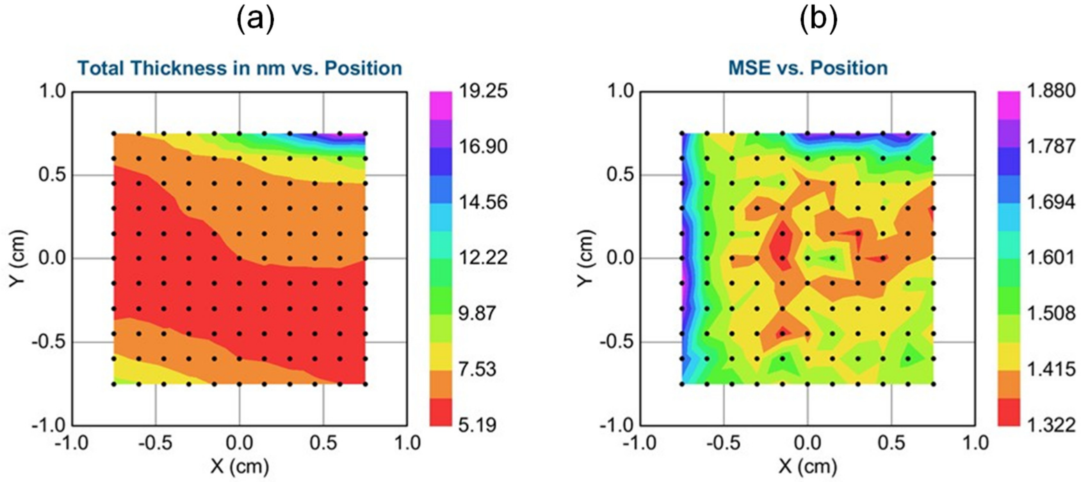

Figure 5.11. (a) Thickness, and (b) MSE mapping results for the native oxide layer on bare Si substrate within a scan area of 1.5 × 1.5 cm^2.

As seen in Fig. 5.11 and Table 5.4, the surface of the Si substrate is not uniform. The minimum and maximum native oxide thicknesses range from 5.19 nm to 19.25 nm towards the edge of the sample with an average thickness of 7.09 nm. Therefore, 6.32

nm native oxide thickness (measured in the centre of the sample) coming form the single point measurement result has been used in the mapping analyses.

After analysing the reference Si substrate, further mapping measurements were carried out on the actual TiO_2 layers. Results of the mapping analysis for PE-ALD on Si, PE-ALD on metal and thermal ALD on metal samples are shown in Fig. 5.12.

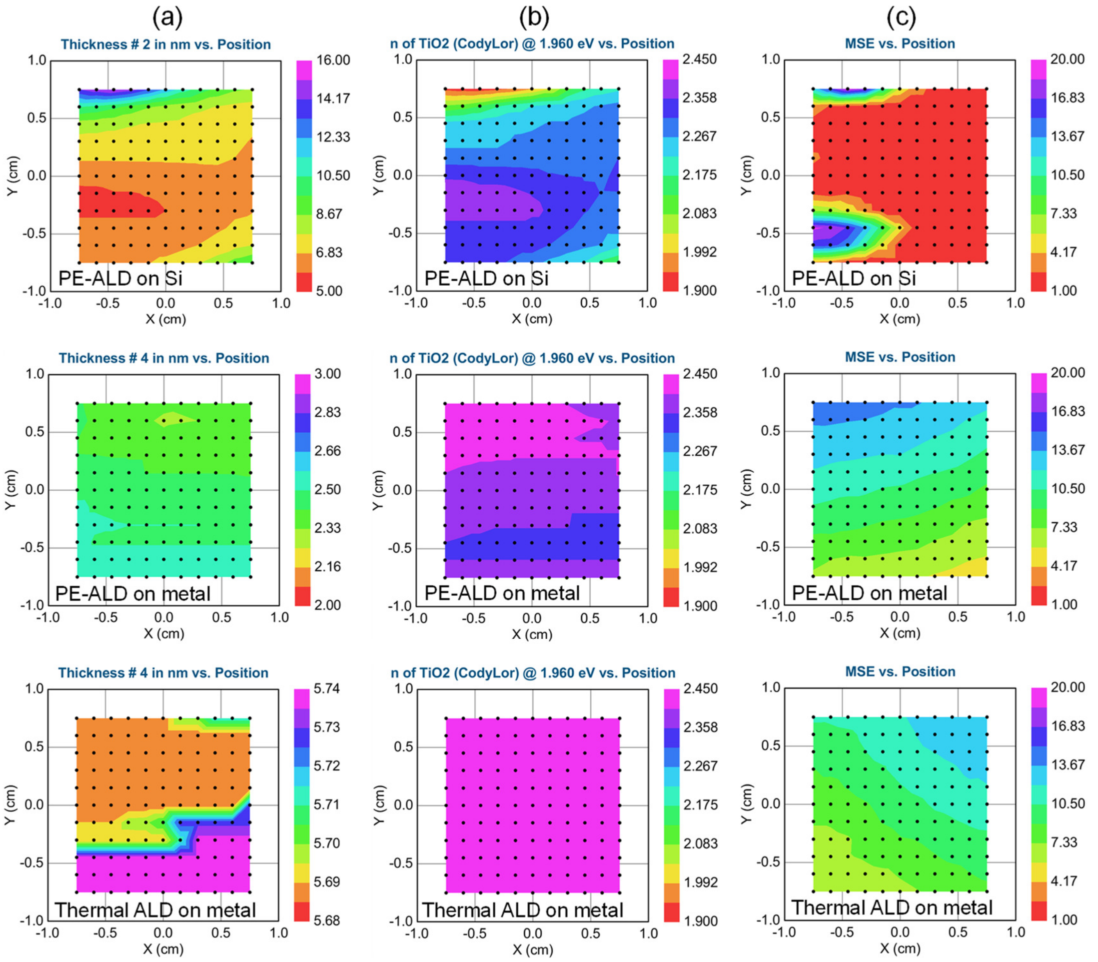

Figure 5.12. (a) Thickness, (b) *n* and (c) MSE mapping results for PE-ALD TiO_2 on Si, PE-ALD TiO_2 on metal and thermal ALD TiO_2 on metal samples within a scan area of 1.5 × 1.5 cm^2.

As seen in Fig. 5.12 and Table 5.4, the thickness and the *n* values of the PE-ALD TiO_2 on Si highly deviates which could be attributed to the thick and non-uniform native oxide thickness of reference Si since the TiO_2 layer was directly deposited on the substrate. This deviation is less prominent in the other two samples since there are 20 nm Al and 50 nm Ti layers between the TiO_2 and the Si substrate layers.

Table 5.4. Mapping results of the PE-ALD and thermal ALD TiO_2 samples including thickness, *n* and MSE values.

Sample	Parameter	Average	Minimum	Maximum	Standard Deviation
Reference Si substrate	Thickness (nm)	7.09	5.19	19.25	2.29
	MSE	1.50	1.32	1.88	0.13
PE-ALD on Si	Thickness (nm)	7.42	5.70	15.16	1.86
	n @ 1.96 eV	2.28	1.92	2.39	0.10
	MSE	3.58	1.57	19.33	3.58
PE-ALD on metal	Thickness (nm)	2.45	2.33	2.58	0.08
	n @ 1.96 eV	2.38	2.35	2.43	0.03
	MSE	10.02	4.87	14.65	2.59
Thermal ALD on metal	Thickness (nm)	5.71	5.69	5.74	0.02
	n @ 1.96 eV	2.44	2.43	2.45	0.01
	MSE	9.67	6.03	13.57	1.96

After determining the thicknesses and the film uniformity, further analysis has been carried out to extract the optical constants and the associated E_g values. The measured refractive index (n) and the band gap (E_g) values derived from the Tauc plots of three different TiO_2 films are shown in Fig. 5.13.

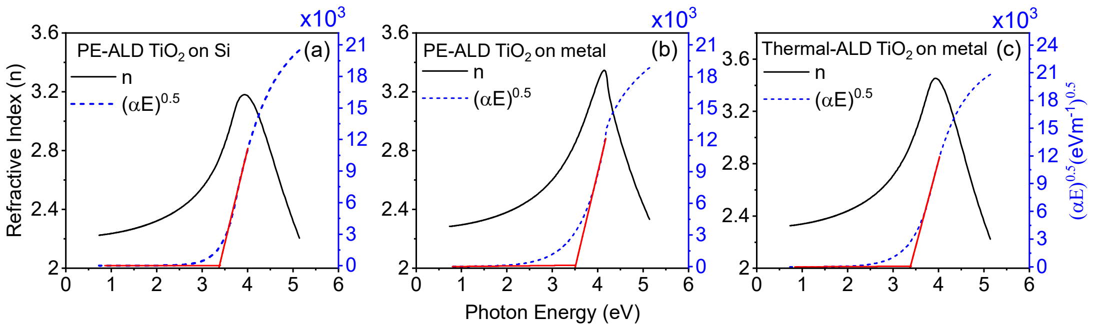

Figure 5.13. Refractive index (*n*) and Tauc, i.e. $(\alpha E)^{0.5}$ versus photon energy (E) plots (where α is absorption coefficient and E – photon energy) for: (a) PE-ALD TiO_2 on Si, (b) PE-ALD TiO_2 on metal and (c) Thermal ALD TiO_2 on metal substrates. The band gap (E_g) of each oxide was calculated from the linear extrapolation of the Tauc plot to the base line, as depicted.

The extracted E_g values of PE-ALD TiO_2 thin films were found to be 3.38 eV and 3.50 eV on Si and metal substrates, respectively. On the other hand, the E_g of thermal ALD TiO_2 was derived as 3.39 eV. Except the PE-ALD TiO_2 on metal sample, which is the most erroneous one with the highest MSE~11 due to being deposited on 20 nm Ti/50 nm Al metal substrate, the E_g values of plasma assisted and thermal ALD oxide thin films are consistent with each other. These values are also close to the E_g of RF sputtered TiO_2 thin films (3.32 eV) shown in Fig. 5.8 (a) and Table 5.3.

5.2 Stoichiometry and electron affinity analysis of RF sputtered oxide films

The XPS measurements were made on the in-house RF sputtered TiO_2 and NiO films using a SPECS monochromated Al k-α X-ray source ($h\upsilon = 1486.6$ eV) with energy step size of 0.03 eV and integration time of 0.25 s per step, operating at 150 W for core level (CL) and valence band scans, while 9 W for secondary electron cut off scans in an ultra-high vacuum chamber at a base pressure of $\sim 10^{-10}$ mbar. Photoelectron emission spectra were recorded with a PSP Vacuum Technology hemispherical electron energy analyser set to a constant pass energy of 10 eV. The spectrometer was calibrated using the core levels and Fermi line of a sputtered silver foil and was operated with an overall resolution of ±0.1 eV. Chamber pressure during measurements was $\sim 10^{-10}$ mbar.

The core level peaks were fitted using Voigt functions and a Shirley type background subtraction, performed within the CasaXPS software package. Adventitious carbon C 1s core level binding energy, calibrated to 284.6 eV, was used to account for any sample charging. Stoichiometry of the metal oxide films was determined by the relative sensitivity factor (RSF) adjusted area ratios of the metal core levels and their corresponding O 1s level. It should be noted that since XPS is a surface sensitive technique, the stoichiometry determined here refers to the surface composition. Besides the elemental analyses, the electron affinities (χ) of the oxides were found using Eqns. 4.18 – 4.20.

For the TiO_2 film, Fig. 5.14 (a) shows the Ti $2p_{3/2}$ peak at 458.76 eV and the O 1s lineshape is shown in Fig. 5.14 (b). The O 1s CL lineshape is fitted with two components: one for the oxygen in TiO_2 at 530.17 eV and a smaller broad peak at 531.51 eV attributed to adventitious carbon related oxide contamination. The quantitative analysis shows that this film is highly stoichiometric with Ti:O of 0.506:1 corresponding to $TiO_{1.98}$. Using the extracted parameters from XPS spectra shown in Figs. 5.14 (c) and (d), as well as V_{app} = 9.91 V allowed experimental determination of the ionization energy (IE) to be 6.88 eV for TiO_2 and the resulting χ was found to be 3.56 eV considering the E_g of 3.32 eV found from Tauc plot (Fig. 5.8 (a)).

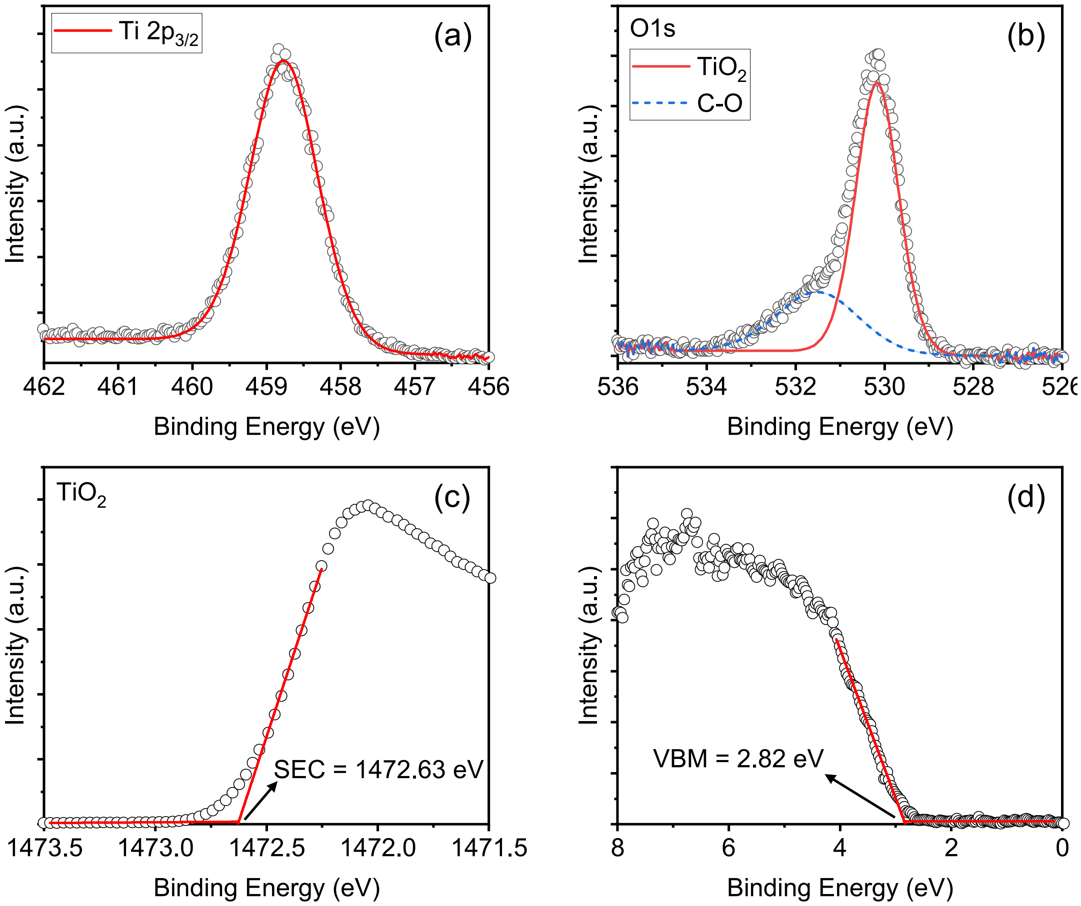

Figure 5.14. XPS intensity spectra of (a) Ti $2p_{3/2}$ core level, (b) O 1s spectrum, (c) SEC and (d) valence band edge for TiO_2 film.

In contrast to the TiO_2 film, for the NiO film (Fig. 5.15 (a)), the XPS lineshape is complicated due to the presence of multiple satellite features. Therefore, the lineshape requires multiple fit components. Qualitatively, the Ni $2p_{3/2}$ CL lineshape corresponds to Ni in the Ni^{2+} state as expected for NiO, with the Ni^{2+} binding energy determined to be 853.68 eV. The O 1s CL spectra (Fig. 5.15 (b)), show a component from NiO at 529.09 eV and two further broad peaks attributed to carbon contamination. It is noted that the contamination of the NiO films is significant in comparison to other oxide films. Furthermore, it should be noted that the stoichiometry calculation for NiO is challenging due to the above mentioned satellite peaks compared to other oxides and leads to a higher uncertainty in the result. Although the Ni 2p lineshape qualitatively indicates that the Ni is in the 2^+ state, Dong *et al.*[19] have mentioned that it is difficult to identify the different oxidation states of Ni due to the multiple peaks in the spectrum, and indeed there could be some Ni^{3+} state present as well.

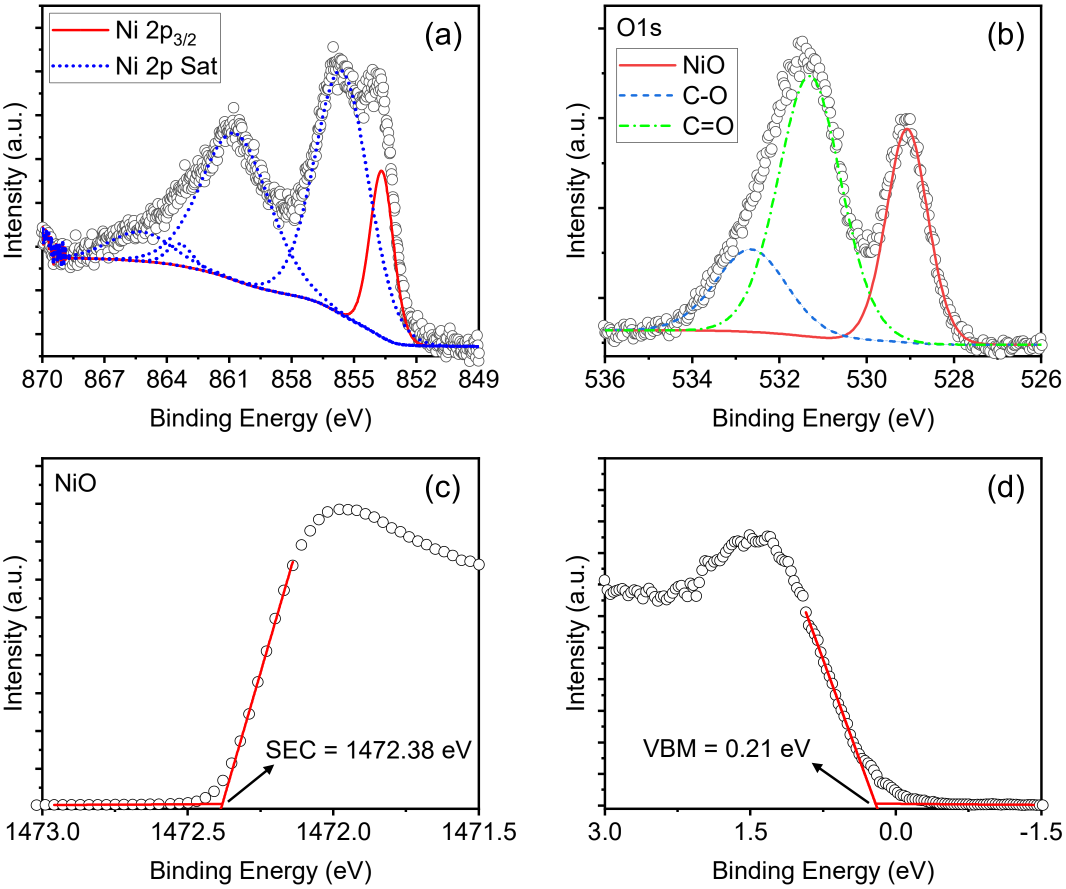

Figure 5.15. XPS intensity spectra of (a) Ni $2p_{3/2}$ core level, (b) O1s spectrum, (c) SEC and (d) valence band edge for NiO film.

Following Mansour *et al.*[20], the total area under the Ni 2p lineshape including the satellite peaks was used with the corresponding O 1s peak from the oxide to find the stoichiometry of the film and found to be $NiO_{0.70}$, similar to that found of ZnO and indicating some 3+ oxidation state characteristic. The χ of NiO was found to be 2.05 eV using the IE of 4.80 eV calculated form the SEC and VBM values in Fig. 5.15 (c) and (d) and the V_{app} of 9.63 V. The E_g of 2.75 eV (Fig. 5.8 (c)) for NiO was used in the calculations.

Besides the TiO_2 and NiO measurements, in the scope of a collaborative study, XPS analysis was done also on RF sputtered ZnO films to find the stoichiometry and electron affinity parameters. These values are summarised in Table 5.5. The electron affinity values correlate with literature values reported in Table 2.1 [21–23] within experimental errors, although it is noted that there are also smaller [24] and larger [25] values reported. Since these films are not perfectly stoichiometric, they are referred as NiO_x, and ZnO_x in this work.

Table 5.5. The experimentally determined electron affinities from XPS/VASE and FNT measurements of TiO_2, ZnO_x and NiO_x films are summarized together with reference values from literature. The thickness (t_{ox}), refractive index (n) and band gap (E_g) values are stated from VASE measurements. The XPS extracted parameters include key core level binding energies (BEs), stoichiometry, ionization energy (IE) and valence band maximum (VBM) of oxide films. The barrier heights (ϕ) between Al/oxide are listed as obtained from FNT plots.

Measurement method	Extracted parameters	TiO_2		ZnO_x		NiO_x	
		Ti $2p_{3/2}$	O 1s	Zn $2p_{3/2}$	O 1s	Ni 2p	O 1s
XPS	BE (± 0.1) (eV)	458.8	530.2	1021.3	529.7	853.7	529.1
	Area	1206.6	1338.2	12516.5	1418.0	4111.91	578.5
	RSF*	5.22	2.93	18.92	2.93	14.61	2.93
	Area (Adjusted)	231.15	456.71	661.55	483.97	281.45	197.4
	Metal:Oxygen	0.506:1		1.367:1		1.425:1	
	Stoichiometry	$TiO_{1.98}$		$ZnO_{0.73}$		$NiO_{0.70}$	
	IE (± 0.2) (eV)	6.88		6.71		4.80	
	VBM (± 0.2) (eV)	2.82		2.13		0.21	
	χ_{XPS} (±0.25) (eV)	3.56		3.46		2.05	
VASE	t_{ox} (±0.1) (nm)	24.0		36.2		30.5	
	n @1.96 (eV)	2.13		1.84		1.87	
	E_g (±0.1) (eV)	3.32		3.25		2.75	
FNT	$\phi_{Al/oxide}$ (eV)	0.62		0.56		1.82	
	χ (±0.3) (eV)	3.66		3.72		2.46	
Reference	χ (eV)	3.9 [26,27]		3.6 [23], 4.3-4.5 [25], 4.6 [26]		1.46 [24], 2.05 [21], 3.0 [26], 4.8 [28]	

* RSF taken from the CASA software to adjust the core level area.

5.3 Full band alignment of RF sputtered TiO_2, ZnO_x and NiO_x

In this section, the full band diagrams of RF sputtered TiO_2, ZnO_x and NiO_x are illustrated based on the VASE and XPS results in sections 5.1.2 and 5.2, respectively. As shown in Fig. 5.16, TiO_2 and ZnO_x films are found to be n-type, while the NiO_x is p-type. This was determined by observing the location of the fermi level (E_F) between the valence and conduction bands based on the extracted IE, E_g, χ and VBM values of these materials. The band gap values of stoichiometric TiO_2 ($E_g = 3.32$ eV) and non-stoichiometric ZnO_x ($E_g = 3.25$ eV) are consistent with the values reported in the literature (3.3 eV for TiO_2 [29] and 3.2 eV for ZnO [30]). The band gap of NiO_x ($E_g = 2.75$ eV) was found to be lower than some of the literature values such as 3.4 eV [28], however it was seen in Refs. [21,24] that the band gap, as well as the electron affinity of NiO can be increased or decreased depending on the surface treatment. Ratcliff *et al.* [21] reported E_g values of 3.1 eV, 0.4 eV and 3.6 eV for as-deposited, Ar-ion sputtered and O_2 plasma treated NiO_x films, respectively. Also, the electron affinities of these three oxides were derived to be 3.56 eV for TiO_2, 3.46 eV for ZnO and 2.05 eV for NiO. The χ results of ZnO_x and NiO_x are also in close agreement with the literature values which are 3.6 eV [23] for ZnO and 2.05 eV [21] for NiO. The χ of TiO_2 is seen to be slightly lower than the stated 3.9 eV in Refs. [26,27], but this value is based on theoretical calculations.

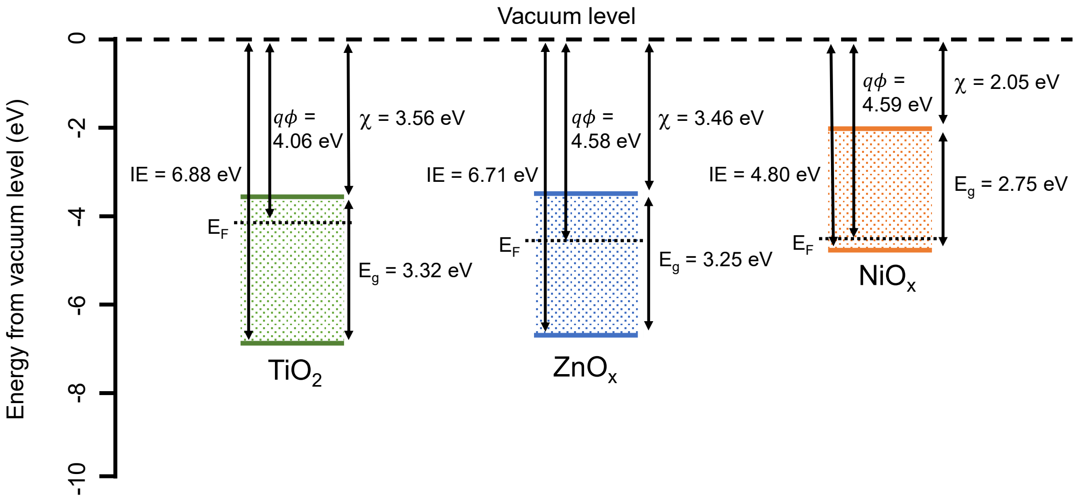

Figure 5.16. Band alignment of RF sputtered TiO_2, ZnO and NiO based on the VASE and XPS results.

The results of this section are used in Chapter 7 together with the derived χ values found from the FNT measurements at the Al/TiO_2, Al/ZnO and Al/NiO interfaces (explained in section 5.4) for assessing the I-V characteristics of TiO_2, ZnO and NiO based MIM diode structures.

5.4 Investigation of conduction mechanisms in oxide thin films

The device cut-off frequency (f_c) is an important parameter for the MIM rectifiers to operate at THz frequencies. The MIM diodes in this study were developed to have ultra-fast (fs) dominant QM tunnelling and avoid any other defect related or temperature dependent conduction. For this reason, ultra-thin (< 5 nm) oxide films were deposited using ALD and RF sputtering methods to maintain low defect density, superior uniformity and excellent film quality. Then, the conduction mechanism of the fabricated MIM diodes were examined using room temperature I-V measurements performed in a dark probe station integrated with an Agilent B1500 SMU. The voltage was swept from 0 V to 1.5 V (forward bias) and 0 V to -1.5 V (reverse bias) to avoid any breakdown in the oxide layers.

In this section, ALD deposited 3 nm Al_2O_3 based diodes with Au/Au and Au/Ti configurations were measured to examine any defect related Poole-Frenkel (PF) and temperature dependent Schottky emission (SE) conduction mechanisms. Figure 5.17 shows the PF plots for Au/Al_2O_3/Au and Au/Al_2O_3/Ti diodes, in both forward and reverse bias conditions, where a linear region of PF plots is seen between 210 MV/m and 500 MV/m corresponding to 0.63 V and 1.5 V, respectively. This linear relationship between $ln(J/E)$ and $(E)^{1/2}$, with an $R^2 \geq 0.999$, indicates a reliable fit [31] and the possibility of PF over the bias range.

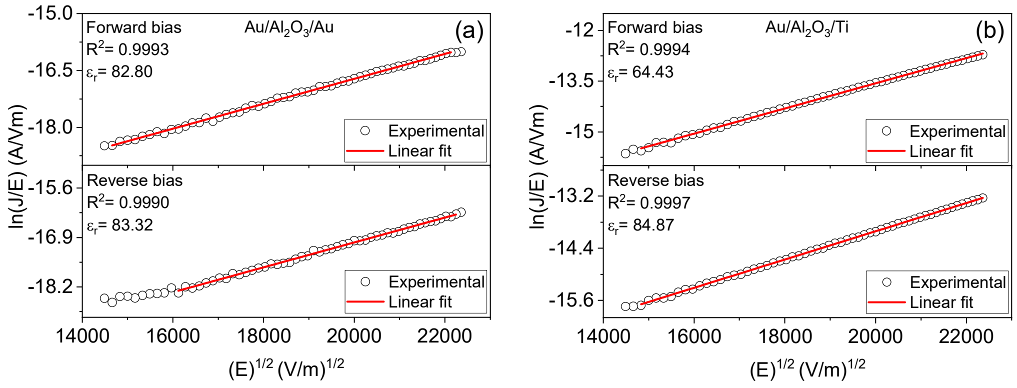

Figure 5.17. PF plots of (a) Au/Al_2O_3/Au and (b) Au/Al_2O_3/Ti diodes for the forward and reverse bias.

Then, the dynamic permittivity (ε_r) value of the Al_2O_3 layer associated with the possible trap emission in a dielectric layer was calculated using Eqn. 3.8 and the slope of the linearly fitted experimental $ln(J/E)$ and $(E)^{1/2}$ data for both diode configurations. The absolute temperature was measured as 294.1K in the lab and used for the calculations. Note that there are no consistent data available for the effective mass ratio of thin oxides and values reported in the literature vary between the range of values (0.1-1) [28,31–34] for ultra-thin (<5 nm) films. Therefore, the effective mass ratio (m^*/m_0) of Al_2O_3 was taken as 0.5, where m^* is the oxide effective mass and m_0 is the effective mass of electron.

The ε_r was found to be 82.80 and 83.32 for the forward and reverse biases in the Au/Al_2O_3/Au device. For the Au/Al_2O_3/Ti diode, the ε_r values were found to be 64.43 for the fowrard bias and 84.87 for the reverse bias. The difference in the ε_r values between the forward and reverse bias in this diode is expected due to the dissimilar (Au/Ti) electrode configurations. The forward bias was applied form the Au electrode where the electrons were injected from the Ti electrode to the Al_2O_3 layer. However, the ε_r values obtained from the Au/Al_2O_3 interface are consistent in both diode configurations.

On the other hand, the refractive index (n) value of Al_2O_3 was found from the VASE measurements and the associated dynamic permittivity ($\varepsilon_r = n^2$) was calculated to be 3.15 using the n value. Then, it was compared with the dynamic permittivity (ε_r) results obtained from PF fittings. As seen from the results, there is a large difference between the ε_r values obtained form the PF fittings and the VASE measurements for both diode configurations. Thus, PF cannot be considered as a dominant conduction mechanism in Al_2O_3 thin films.

Similar to the PF analysis, SE graphs were plotted in the same electric field region (210 MV/m and 500 MV/m) using the relationship between $ln(J/T^2)$ and $(E)^{1/2}$ as shown in Fig. 5.18. Then, the calculated dynamic ε_r values were compared with the VASE results.

The ε_r values were found to be 11.69 (forward bias) and 12.01 (reverse bias) for the Au/Al_2O_3/Au diode, while they were 9.77 (forward bias) and 11.96 (reverse bias) for the Au/Al_2O_3/Ti diode. Although the SE results are closer to the VASE results, they are still higher than expected values for a possible SE mechanism.

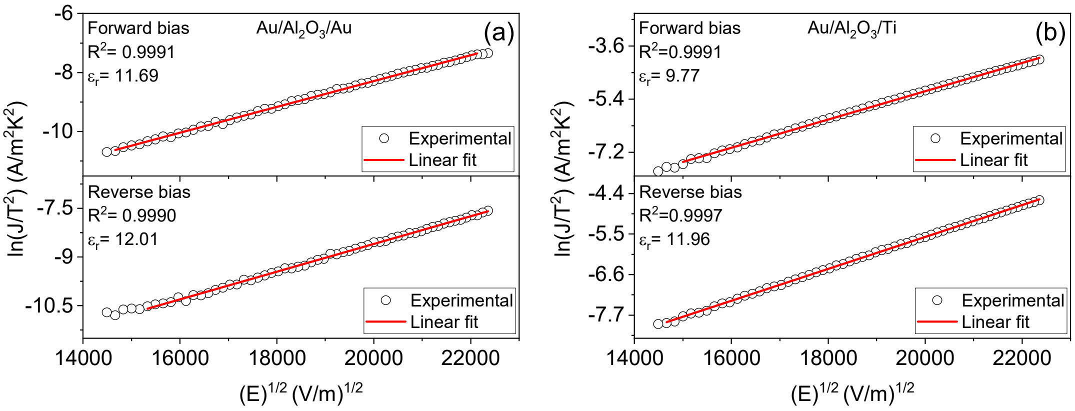

Figure 5.18. SE plots of (a) Au/Al_2O_3/Au and (b) Au/Al_2O_3/Ti diodes for the forward and reverse bias.

It should be noted that an FNT analysis could not be done on these devices due to the breakdown voltage being beyond 1.5 V and due to relatively large barrier heights at the Au/Al_2O_3 (3.5 eV) and Ti/Al_2O_3 (2.5 eV) interfaces based on the XPS values of Al_2O_3 electron affinity (1.6 eV, [7,32]) and the literature values of Au (5.1 eV, [35,36]) and Ti (4.1 eV, [35,37]) metal work functions. However, considering the ultra-thin (3nm) ALD Al_2O_3 layer, and not having a defect or temperature related conduction mechanisms, it is evident that there is a strong probability of having direct tunnelling (DT) as the dominant conduction mechanism in these films.

Further to the PF and SE analysis on ALD Al_2O_3 films, in the scope of the same collaborative work within the research group, a FNT analysis was done on RF sputtered TiO_2, ZnO and NiO thin films to confirm the electron affinity values derived from the combination of XPS and VASE measurements. Therefore, a set of MIM diodes were fabricated using shadow mask evaporation with 3.3 nm TiO_2, 3.0 nm ZnO and 3.9 nm NiO thin oxide films sandwiched between symmetrical Al/Al metal electrodes. A large enough bias was applied on the diodes to have the required electric field in the oxide of interest according to the static voltage ratio calculations, taking into account the effect of an unintentionally grown native AlO_x layer on the bottom Al electrodes. The barrier height ($\emptyset_B$) at the metal/oxide interface was extracted from the slope of FNT plots using Eqn. 3.14. Hence, using $\chi = WF_{Al} - \phi$, the oxide electron affinities deduced from FN barriers are (± 0.3 eV): 3.66 eV for TiO_2, 3.72 eV and

ZnO_x, 2.46 eV for NiO_x. All physical and electrical characterisation data are summarized in Table 5.5.

It can be seen that the electron affinities found from FNT analysis is consistent with that extracted from a combination of XPS and VASE techniques (termed as χ_{XPS}) for stoichiometric TiO_2, giving a consistent value of $\chi_{TiO2} = 3.6 \pm 0.1$ eV. An upward shift of up to 0.3 eV for ZnO_x and 0.4 eV for NiO_x films with the decreasing stoichiometry can be seen when FNT barriers were used to extract χ. This increase cannot be explained by a measurement error, as extrapolating the edge of the conduction band, valence band or absorption edge from Tauc plots is within ± 0.3 eV. This deviation is rather intrinsic to the different nature of XPS and FNT methods, where the XPS is much more surface sensitive as noted above.

5.5 Conclusion

This chapter summarises physical characterisation (VASE and XPS) parameters of thin oxide films to be used in modelling electrical properties of associated rectifiers in rectenna devices. Additionally, point-by-point VASE analysis has been demonstrated to be an efficient tool to extract a sub-band gap SiO_2 and SiO_2/Si features for oxides grown by different oxidation methods to be used in power MOSFETs. The signature of interface related defects has been found at 2.9 eV for samples processed by wet oxidation, being indicative of O_2 vacancies. As a result, higher current magnitude was observed from gate to source current vs time response measurements on associated devices.

The VASE analysis was done on the RF sputtered TiO_2, ZnO, and NiO thin films on Si wafers to find the thickness, surface uniformity, optical constants (*n*, *k*) and the band gap (E_g) of the thin films. The E_g of the oxide films were found to be 3.32 eV, 3.25 eV and 2.75 eV from the Tauc plots for the sputtered TiO_2, ZnO, and NiO respectively. The VASE measurements on thermal and plasma-enhanced ALD TiO_2 thin films show band gap values of 3.38 eV for PE-ALD and 3.39 eV for thermal ALD, similar to the value of RF sputtered TiO_2.

The XPS measurements show the electron affinities (χ) of TiO_2, ZnO, and NiO of 3.56 eV, 3.46 eV and 2.05 eV, respectively. The full band alignment of the RF sputtered

$TiO_{1.98}$, $ZnO_{0.73}$ and $NiO_{0.70}$ were also demonstrated based on the VASE and XPS results. The Al/TiO_2 (0.62 eV), Al/ZnO (0.56 eV) and Al/NiO (1.82 eV) barrier heights were also derived from the linear region of the FNT plots of associated MIM diodes. The resulting χ values of TiO_2, ZnO, and NiO were calculated as 3.66 eV, 3.72 eV and 2.46 eV considering the 4.28 eV work function of Al metal. It was observed that, the XPS and FNT results are in close agreement for the stoichiometric $TiO_{1.98}$ and deviate with the decreasing stoichiometry for $ZnO_{0.73}$ and $NiO_{0.70}$. The aim of this study was to experimentally determine physical parameters of MIM stack (band gap, electron affinity) to use in the I-V modelling in the next chapter.

Finally, Poole-Frenkel and Schottky emission conduction mechanisms have been examined on ALD deposited Au/Al_2O_3/Au and Au/Al_2O_3/Ti diodes to check any defect related and temperature dependent mechanisms. The inconsistency between the ε_r values obtained from VASE and PF/SE plots indicates that the oxides are of high quality. The current transport is rather based on tunnelling, particularly likely to be direct tunnelling due to the ultra-thin (3nm) ALD Al_2O_3 films.

References

[1] B. J. Baliga, *Advanced Power MOSFET Concepts*. Scholars Portal, 2010.

[2] A. Lidow, T. Herman, and H. W. Collins, “Power MOSFET technology,” *1979 International Electron Devices Meeting*, 1979, doi: 10.1109/iedm.1979.189545.

[3] R. K. Williams, M. N. Darwish, R. A. Blanchard, R. Siemieniec, P. Rutter, and Y. Kawaguchi, “The Trench Power MOSFET: Part I—History, Technology, and Prospects,” *IEEE Transactions on Electron Devices*, vol. 64, no. 3, pp. 674–691, Mar. 2017, doi: 10.1109/ted.2017.2653239.

[4] I. Starkov, H. Enichlmair, S. Tyaginov, and T. Grasser, “Analysis of the threshold voltage turn-around effect in high-voltage n-MOSFETs due to hot-carrier stress,” *2012 IEEE International Reliability Physics Symposium (IRPS)*, Apr. 2012, doi: 10.1109/irps.2012.6241937.

[5] G. Schindler, K.-H. Bach, P. Nelle, M. Deckers, A. Knapp, K. Ermisch, C. Feuerbaum, and W. V. Emden, “Impact of alpha-radiation on power mosfets,” *2016*

IEEE International Reliability Physics Symposium (IRPS), 2016, doi: 10.1109/irps.2016.7574553.

[6] K. Shenai, “Optimized trench MOSFET technologies for power devices,” *IEEE Transactions on Electron Devices*, vol. 39, no. 6, pp. 1435–1443, Jun. 1992, doi: 10.1109/16.137324.

[7] D. A. Weerakkody, “Engineered high-K oxides,” The University of Liverpool, *PhD thesis*, 2016.

[8] JA. Woollam , *CompleteEASE data analysis manual.*, New England United States Am.: JA Woollam Co Inc, 2011

[9] I. H. Malitson, “Interspecimen Comparison of the Refractive Index of Fused Silica*,†,” *Journal of the Optical Society of America*, vol. 55, no. 10, p. 1205, Oct. 1965, doi: 10.1364/josa.55.001205.

[10] J. Price, P. S. Lysaght, S. C. Song, H.-J. Li, and A. C. Diebold, “Identification of sub-band-gap absorption features at the HfO2⁄Si(100) interface via spectroscopic ellipsometry,” *Applied Physics Letters*, vol. 91, no. 6, p. 061925, 2007, doi: 10.1063/1.2769389.

[11] J. Price, G. Bersuker, and P. S. Lysaght, “Identification of interfacial defects in high-k gate stack films by spectroscopic ellipsometry,” *Journal of Vacuum Science & Technology B: Microelectronics and Nanometer Structures*, vol. 27, no. 1, p. 310, 2009, doi: 10.1116/1.3021045.

[12] I. Z. Mitrovic, M. Althobaiti, A. D. Weerakkody, N. Sedghi, S. Hall, V. R. Dhanak, P. R. Chalker, C. Henkel, E. Dentoni Litta, P.-E. Hellström, and M. Östling, “Interface engineering of Ge using thulium oxide: Band line-up study,” *Microelectronic Engineering*, vol. 109, pp. 204–207, 2013, doi: 10.1016/j.mee.2013.03.160.

[13] A. Shaw, “Atomic layer deposition zinc oxide devices for transparent electronics,” The University of Liverpool, *PhD thesis*, 2018.

[14] A. Alkauskas and A. Pasquarello, "Alignment of hydrogen-related defect levels at the interface," *Physica B: Condensed Matter*, vol. 401–402, pp. 546–549, 2007, doi: 10.1016/j.physb.2007.09.018.

[15] A. Alkauskas, P. Broqvist, A. Pasquarello, M. Caldas, and N. Studart, "Alignment of Defect Energy Levels at Si-SiO2 Interface from Hybrid Density Functional Calculations," *AIP Conference Proceedings*, 2010, doi: 10.1063/1.3295562.

[16] T. Bakos, S. N. Rashkeev, and S. T. Pantelides, "H2OandO2molecules in amorphousSiO2:Defect formation and annihilation mechanisms," *Physical Review B*, vol. 69, no. 19, 2004, doi: 10.1103/physrevb.69.195206.

[17] P. Janicek, K. M. Niang, J. Mistrik, K. Palka, and A. J. Flewitt, "Spectroscopic ellipsometry characterization of ZnO:Sn thin films with various Sn composition deposited by remote-plasma reactive sputtering," *Applied Surface Science*, vol. 421, pp. 557–564, Nov. 2017, doi: 10.1016/j.apsusc.2016.10.169.

[18] A. Hemmetter, X. Yang, Z. Wang, M. Otto, B. Uzlu, M. Andree, U. Pfeiffer, A. Vorobiev, J. Stake, M. C. Lemme, and D. Neumaier, "Terahertz Rectennas on Flexible Substrates Based on One-Dimensional Metal–Insulator–Graphene Diodes," *ACS Applied Electronic Materials*, vol. 3, no. 9, pp. 3747–3753, Aug. 2021, doi:10.1021/acsaelm.1c00134.

[19] M. D. Dong, J. Y. Shen, C. Y. Hong, P. X. Ran, R.-H. He, H. W. Chen, Q. Y. Lu, and J. Wu, "Modulation of the NiOx bandgap by controlling oxygen stoichiometry," *Journal of Applied Physics*, vol. 132, no. 17, p. 173901, 2022, doi: 10.1063/5.0109659.

[20] A. N. Mansour, "Characterization of NiO by XPS," *Surface Science Spectra*, vol. 3, no. 3, pp. 231–238, 1994, doi: 10.1116/1.1247751.

[21] E. L. Ratcliff, J. Meyer, K. X. Steirer, A. Garcia, J. J. Berry, D. S. Ginley, D. C. Olson, A. Kahn, and N. R. Armstrong, "Evidence for near-Surface NiOOH Species in Solution-Processed NiOx Selective Interlayer Materials: Impact on Energetics and the Performance of Polymer Bulk Heterojunction Photovoltaics," *Chemistry of Materials*, vol. 23, no. 22, pp. 4988–5000, 2011, doi: 10.1021/cm202296p.

[22] S. A. Chambers and P. V. Sushko, “Influence of crystalline order and defects on the absolute work functions and electron affinities of TiO2- and SrO-terminated n−SrTiO3(001),” *Physical Review Materials*, vol. 3, no. 12, 2019, doi: 10.1103/physrevmaterials.3.125803.

[23] M. C. Gwinner, Y. Vaynzof, K. K. Banger, P. K. H. Ho, R. H. Friend, and H. Sirringhaus, “Solution-Processed Zinc Oxide as High-Performance Air-Stable Electron Injector in Organic Ambipolar Light-Emitting Field-Effect Transistors,” *Advanced Functional Materials*, vol. 20, no. 20, pp. 3457–3465, 2010, doi: 10.1002/adfm.201000785.

[24] H. Wu and L.-S. Wang, “A study of nickel monoxide (NiO), nickel dioxide (ONiO), and Ni(O2) complex by anion photoelectron spectroscopy,” *The Journal of Chemical Physics*, vol. 107, no. 1, pp. 16–21, 1997, doi: 10.1063/1.474362.

[25] Z. Liu, Y. Liu, X. Wang, W. Li, Y. Zhi, X. Wang, P. Li, and W. Tang, “Energy-band alignments at ZnO/Ga2O3 and Ta2O5/Ga2O3 heterointerfaces by X-ray photoelectron spectroscopy and electron affinity rule,” *Journal of Applied Physics*, vol. 126, no. 4, p. 045707, 2019, doi: 10.1063/1.5112067.

[26] J. Robertson, “Band offsets, Schottky barrier heights, and their effects on electronic devices,” *Journal of Vacuum Science & Technology A: Vacuum, Surfaces, and Films*, vol. 31, no. 5, p. 050821, 2013, doi: 10.1116/1.4818426.

[27] J. Robertson, “Band offsets of wide-band-gap oxides and implications for future electronic devices,” *Journal of Vacuum Science & Technology B: Microelectronics and Nanometer Structures*, vol. 18, no. 3, p. 1785, 2000, doi: 10.1116/1.591472.

[28] A. Weerakkody, A. Belkadi, and G. Moddel, “Nonstoichiometric Nanolayered Ni/NiO/Al2O3/CrAu Metal–Insulator–Metal Infrared Rectenna,” *ACS Applied Nano Materials*, vol. 4, no. 3, pp. 2470–2475, 2021, doi: 10.1021/acsanm.0c03012.

[29] J. Aarik, A. Aidla, A.-A. Kiisler, T. Uustare, and V. Sammelselg, “Effect of crystal structure on optical properties of TiO2 films grown by atomic layer deposition,” *Thin Solid Films*, vol. 305, no. 1–2, pp. 270–273, 1997, doi: 10.1016/s0040-6090(97)00135-1.

[30] S.-M. Sun, W.-J. Liu, Y.-F. Xiao, Y.-W. Huan, H. Liu, S.-J. Ding, and D. W. Zhang, “Investigation of Energy Band at Atomic-Layer-Deposited ZnO/β-Ga2O3 Heterojunctions,” *Nanoscale Research Letters*, vol. 13, no. 1, 2018, doi: 10.1186/s11671-018-2832-7.

[31] N. Alimardani, S. W. King, B. L. French, C. Tan, B. P. Lampert, and J. F. Conley, “Investigation of the impact of insulator material on the performance of dissimilar electrode metal-insulator-metal diodes,” *Journal of Applied Physics*, vol. 116, no. 2, p. 024508, 2014, doi: 10.1063/1.4889798.

[32] I. Z. Mitrovic, A. D. Weerakkody, N. Sedghi, J. F. Ralph, S. Hall, V. R. Dhanak, Z. Luo, and S. Beeby, “Controlled modification of resonant tunneling in metal-insulator-insulator-metal structures,” *Applied Physics Letters*, vol. 112, no. 1, p. 012902, 2018, doi: 10.1063/1.4999258.

[33] E. W. Cowell, N. Alimardani, C. C. Knutson, J. F. Conley, D. A. Keszler, B. J. Gibbons, and J. F. Wager, “Advancing MIM Electronics: Amorphous Metal Electrodes,” *Advanced Materials*, vol. 23, no. 1, pp. 74–78, 2010, doi: 10.1002/adma.201002678.

[34] S. Grover and G. Moddel, “Applicability of Metal/Insulator/Metal (MIM) Diodes to Solar Rectennas,” *IEEE Journal of Photovoltaics*, vol. 1, no. 1, pp. 78–83, 2011, doi: 10.1109/jphotov.2011.2160489.

[35] I. Z. Mitrovic, S. Almalki, S. B. Tekin, N. Sedghi, P. R. Chalker, and S. Hall, “Oxides for Rectenna Technology,” *Materials*, vol. 14, no. 18, p. 5218, 2021, doi: 10.3390/ma14185218.

[36] H. B. Michaelson, “The work function of the elements and its periodicity,” *Journal of Applied Physics*, vol. 48, no. 11, pp. 4729–4733, 1977, doi: 10.1063/1.323539.

[37] W. F. Gale and T. C. Totemeier, Eds., *Smithells Metals Reference Book*. 2003. doi: 10.1604/9780750675093.

Chapter 6

6. Engineered MI^{n}M diode structures

In this chapter, tunnel-barrier rectifiers composed of single (MIM) and triple (MI^{3}M) insulator configurations have been fabricated by ALD and RF sputtering methods to investigate the insulator (Al_2O_3, ZnO, Ta_2O_5, Nb_2O_5) layer quality and rectification performance for their integration in rectennas for IR energy harvesting. For this purpose, the effect of metal work function difference and barrier height in the single insulator MIM diodes, as well as of resonant tunnelling in triple insulator MI^{3}M configurations on the rectification properties have been studied in detail. The key rectification parameters such as dynamic resistance (R_D), responsivity (β), asymmetry (η) and non-linearity (f_{NL}) have been assessed from the DC I-V measurements. Besides this, the bound states formed in the quantum well of MI^{3}M diodes were predicted by in-house simulation tool explained in Chapter 3, section 3.3 and the generated I-V curves were fitted with the experimental data. The main goal of the experiments is (i) to achieve high zero-bias responsivity (β_0) and maximum η using dissimilar metal electrodes and triple insulator configurations, as well as (ii) low zero-bias dynamic resistance (R_0) by reducing the metal/oxide barrier height. The outcomes of this chapter have been presented in Tekin *et al. EUROSOI-ULIS* 2020; Tekin *et al. Solid-State Electronics* 2021, 185, 108096; and partially in Tekin *et al.* 2022 *ECS Trans.* 108, 69.

6.1 Device fabrication and experimental details

The MIM and MI^{3}M diode structures were fabricated on 4 cm × 4 cm ultra-smooth Corning glass (CG) substrates as explained in Chapter 4. The gold (Au), and aluminium (Al) metal electrodes were deposited by thermal evaporationwhile the Titanium (Ti) and Zinc (Zn) metals were deposited by RF sputtering. The patterning was done using the shadow mask having 100 µm × 100 µm device area as explained in Section 4.2.1. The target thickness of the electrodes was ~50 nm. The Al_2O_3, Ta_2O_5 and Nb_2O_5 oxide thin films were deposited by conventional thermal ALD using the Cambridge Nanotech Savannah reactor. The precursors were water combined with either: trimethyl-aluminium (TMA), tantalum ethoxide ($Ta(OEt)_5$) and niobium ethoxide ($Nb(OEt)_5$) for the Al_2O_3, Ta_2O_5 and Nb_2O_5 respectively. The Ta and Nb precursors were heated to 140 °C to aid vapour transport into the reactor. Dose (0.2 s) and purge (4 – 10 s) times were chosen to ensure a self-limiting ALD reactions occurred, and the substrate temperature was 200 °C throughout. The H_2O source was pulsed for 0.04 seconds followed by a purge time of 4-10 seconds. This ALD cycle process was continued until the desired thicknesses were obtained. The ALD growth per cycle (nm/cycle) was 0.043 for Ta_2O_5, 0.04 for Nb_2O_5 and 0.125 for Al_2O_3. 5 sccm Ar gas flow rate and a power of 52.5 W was used for Ti and Zn and 45 W power was used for ZnO depositions using the Moorfield NanoPVD-S10A RF magnetron sputtering system. The energy band diagrams and the device pattern of the fabricated diodes are shown in Figs. 6.1 (a)-(g).

Electron affinities (χ) of the ALD deposited Al_2O_3 (1.57 eV [1,2]), Ta_2O_5 (3.54 eV [1,2]) and Nb_2O_5 (3.72 eV [1,2]) and the work function of Al metal (4.28 eV [1,2]) were calculated based on the previously measured XPS and FNT measurements within the group using the same deposition and characterisation techniques. As a result, the barriers were taken as 0.74 eV, 0.56 eV and 2.71 eV for the Al/Ta_2O_5, Al/Nb_2O_5 Al/Al_2O_3, respectively. The work functions of Au, Ti and Zn metals were considered as 5.1 eV [3,4], 4.1 eV [3,5] and 4.3 eV [4,5], respectively based on the widely used values in the literature. The electron affinity of RF sputtered ZnO was taken as 3.70 eV [6] for the barrier height calculation, XPS and FNT measurements were also carried out on this oxide and are explained in Chapter 5 in detail. Therefore, the barriers at the Au/Al_2O_3, Ti/Al_2O_3, Zn/Al_2O_3 and Au/ZnO were calculated to be 3.53 eV, 2.50 eV, 2.73 eV and 1.40 eV, respectively.

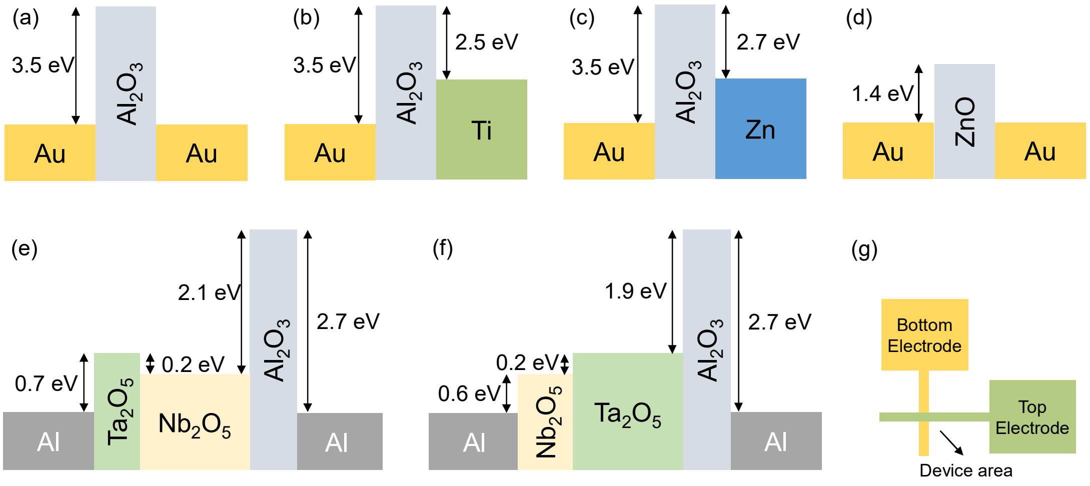

Figure 6.1. Band diagrams of (a)-(d) single and (e)-(f) triple insulator diodes with varying metal electrodes (Au, Ti, Zn and Al) and (g) the top view of a fabricated devices [7].

The barrier height values shown in Figs. 6.1 (a)-(f) are used in the simulations in this chapter. VASE measurements were used to determine the thickness and the optical constants (refractive index and extinction coefficient) of the dielectric layers. Four MIM diode structures having nominal 3 nm Al_2O_3 and ZnO insulating layers and ~50 nm metal electrode thicknesses were fabricated in symmetric and asymmetric configurations. The actual thicknesses of Al_2O_3 and ZnO layers measured by variable angle spectroscopic ellipsometry (VASE) are in good agreement (±0.1 nm for ALD and ±0.3 nm for RF sputtered) with the nominal values. Three MI^3M diode structures were fabricated; two in non-cascaded configuration $Al/Ta_2O_5/Nb_2O_5/Al_2O_3/Al$ by varying the insulator thicknesses (in nm) from 1/3/1 to 1.5/2.5/1, and one in cascaded configuration $Al/Nb_2O_5/Ta_2O_5/Al_2O_3/Al$ with thickness ratio (in nm) 1/3/1. Note that the total nominal thickness of the stack is maintained at 5 nm. In each single layer deposition process, a piece of Si wafer was placed in the chamber together with the CG substrates for VASE measurements and the thicknesses of the oxide layers were examined individually. Then, the same ratio of the precursors and the cycles were used for depositing the triple insulator layers. In this way, the thickness of non-cascaded nominal 1/3/1 and 1.5/2.5/1 MI^3M configurations were measured by VASE to be (in nm) 0.8/3.6/1.0 and 1.2/3.0/1.0, respectively. For the nominal 1/3/1 cascaded structure, the thicknesses were measured to be (in nm) 1.2/2.4/1.0.

6.2 Single insulator MIM diodes

The experimental I-V curves together with extracted rectification parameters of responsivity ($\beta = dI''(V)/2I'(V)$), dynamic resistance ($R_d = (dI/dV)^{-1}$), asymmetry ($\eta = |I_+/I_-|$ or $|I_-/I_+|$, where I_+ refers to forward bias current and I_- to reverse bias current) and non-linearity ($f_{NL} = (V/I)\times R_D$) were calculated for the MIM diodes. Figure 6.2. shows the rectification parameters of the $Au/Al_2O_3/Au$ diode. The voltage swept between -1.5 V and 1.5 V without having a breakdown in the oxide layer. The measurements were performed on several devices of the samples to ensure the I-V characteristics. Then, the noise of the plotted graphs was reduced by fitting the raw data with different orders of polynomial equations, an exponential equation and also by smoothing method. The quality of different fits was examined using two different ways to ensure the reliability of the fittings. The first way is to check the fit residue $(I_{raw} - I_{fit})$ which shows how well the raw data and the fits match with each other.

The second way is to compare the asymmetry values calculated from the raw and the fitted data. Therefore, according to the fit residues and the asymmetry plots, the most accurate fits were chosen for each device. Then, the rectification parameters were found using the corrected I-V curves. Zero-bias resistance (R_0) and responsivity (β_0) of Au/Al_2O_3/Au are found to be 83 MΩ and 0.1 A/W respectively (Fig. 6.2 (b)). Despite the ultra-thin (~3 nm) insulating layer, the high R_0 and relatively low β_0 are attributed to the high barrier height (~3.5 eV) between the Au/Al_2O_3 interface. The maximum responsivity β (Fig. 6.2 (b)) and asymmetry η (Fig. 6.2 (c)) were found to be 2.3 A/W at 0.53 V and 1.3 at 1.2 V, respectively. The device exhibits almost a symmetric behaviour as expected due to the same top and bottom metal electrode configuration.

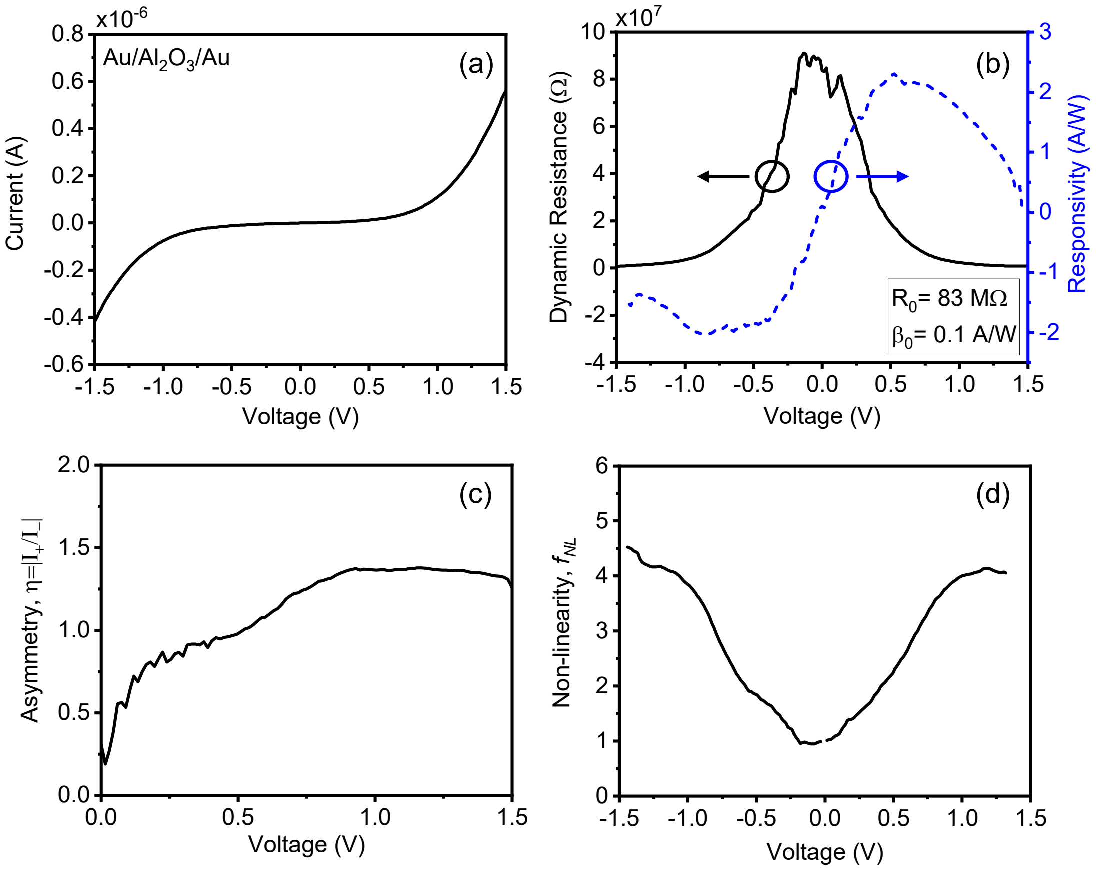

Figure 6.2. (a)-(d) Experimental I-V characteristics of Au/Al_2O_3/Au diode with associated extracted rectification parameters R_d, β, η and f_{NL}.

On the other hand, the work function difference of ~1 eV between Au/Ti metal electrodes has a considerable effect in improving MIM rectification as shown in Figs. 6.3 (a) and (b). There is approximately an order of magnitude increase in the current magnitude from symmetric (same electrode) to asymmetric (dissimilar electrode) diode which causes a reduction in the dynamic resistance of the Au/Al$_2$O$_3$/Ti diode and improves the antenna/diode coupling efficiency. There are also improvements in zero-bias responsivity, asymmetry and non-linearity in the asymmetric diode where it has an R_0 of 35 MΩ and β_0 of -0.6 A/W as shown in Fig. 6.3 (b). The maximum β (Fig. 6.3 (b)) and η (Fig. 6.3 (c)) were also found to be 5.0 A/W at 0.16 V and 1.7 at 1.5 V for this device. Furthermore, maximum f_{NL} at 1.2 V varies from 4.1 for Au/Al$_2$O$_3$/Au diode to 4.6 for Au/Al$_2$O$_3$/Ti diode as shown in Figs. 6.2 (d) and 6.3 (d).

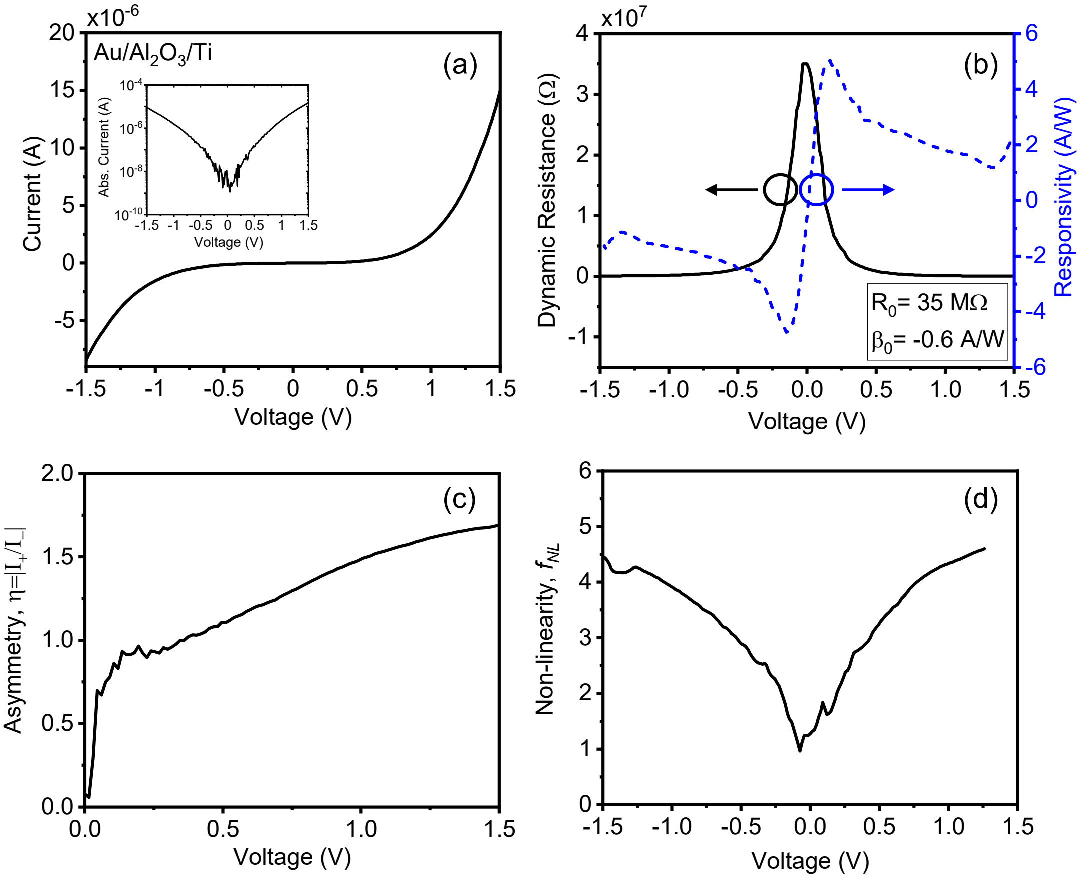

Figure 6.3. (a)-(d) Experimental I-V characteristics of the Au/Al$_2$O$_3$/Ti diode with associated extracted rectification parameters R_D, β, η and f_{NL}. Inset figure (a): Logarithmic scale of the raw I-V data.

A similar behaviour to the Au/Al$_2$O$_3$/Ti was observed for the Au/Al$_2$O$_3$/Zn diode which has an R_0 of 5.1 MΩ and β_0 of 1.60 A/W as shown in Fig. 6.4 (b). Since the breakdown voltage for this diode was less than 1 V, the I-V curve was swept between -0.75 V and 0.75 V. Therefore, the maximum β (Fig. 6.4 (b)) η (Fig. 6.4 (c)) and f_{NL} (Fig. 6.4 (d)) for this device were found as 2.29 A/W at 0.19 V, 1.7 at 0.25 V and 2.1

at -0.51 V, respectively. As seen in Figs. 6.3 (a) and 6.4 (a), Au/Al_2O_3/Ti and Au/Al_2O_3/Zn diodes have very similar current magnitude at the same applied voltage levels. Considering that they have the same 3 nm ALD Al_2O_3 layer and Au bottom electrodes, this shows that the Ti and Zn metals should have similar work functions. This is supported by the literature values of 4.1 eV - 4.3 eV for Ti and 4.3 eV for Zn [2,4,5]. It should be noted that, although the Ti can have ~0.2 eV smaller work function than Zn, the R_0 of Au/Al_2O_3/Zn diode is ~1 order of magnitude smaller than the Au/Al_2O_3/Ti. This could be attributed the highly noisy I-V curve (See inset I-V plot in Fig. 6.3 (a)) of the Au/Al_2O_3/Ti diode around to 0 V. However, it is seen that at higher bias (>0.58 V) the current magnitude of the Au/Al_2O_3/Ti diode becomes higher than the Au/Al_2O_3/Zn.

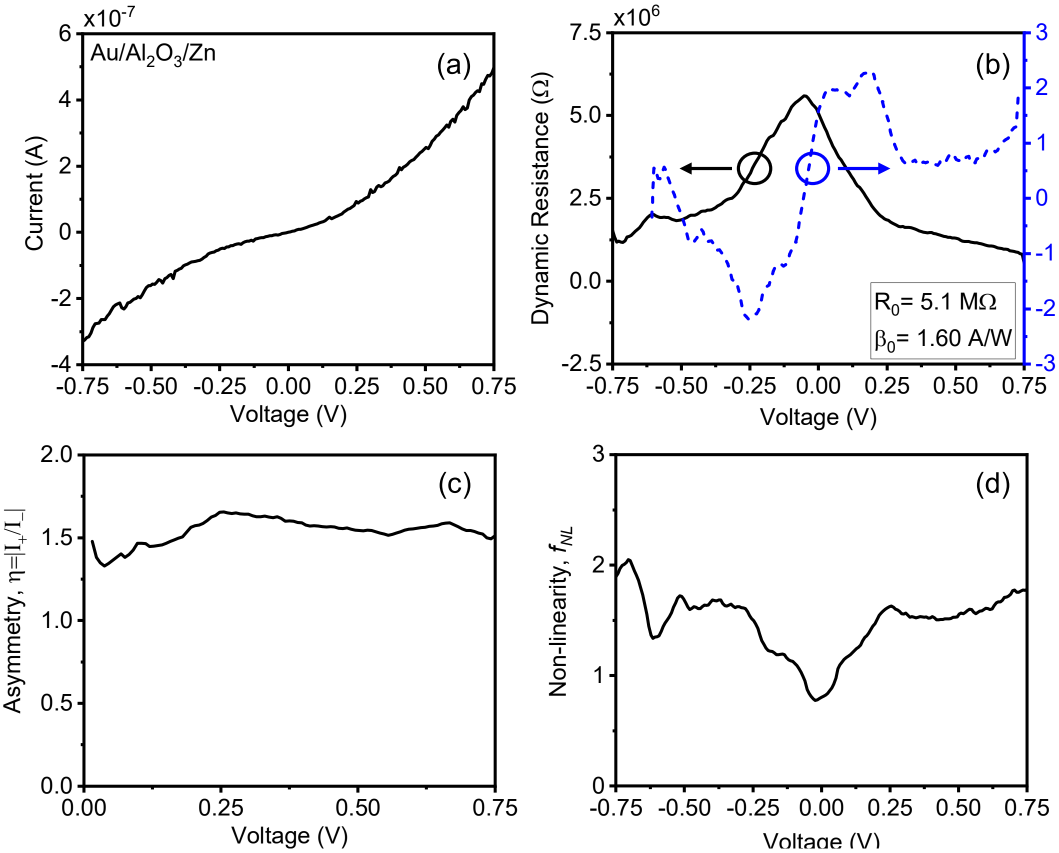

Figure 6.4. (a)-(d) Experimental I-V characteristics of the Au/Al_2O_3/Zn diode with associated extracted rectification parameters R_D, β, η and f_{NL}.

There has been no observation of critical improvement in asymmetry and non-linearity for Au/Al_2O_3/Ti and Au/Al_2O_3/Zn diodes likely to be due to direct tunnelling (DT) being dominant conduction mechanism within the voltage range of -1.5 V to 1.5 V (Fig. 6.3 (c)-(d)) and -0.75 V to 0.75 V (Fig. 6.4 (c)-(d)), respectively. Note that the

Fowler Nordheim tunnelling (FNT) could not be observed in these devices due to breakdown voltage being low. An improved asymmetry of ~1350 at 4.1 V has been reported for ZrCuAlNi/10 nm Al_2O_3/Al diode due to FNT [8]. The results on Au/Ti diode in this work are in line with the reported low asymmetry for 3.5 nm Al_2O_3 diode with dissimilar electrodes caused by DT at lower voltage levels [8].

Figure 6.5 shows the I-V behaviour and the extracted rectification parameters of the Au/ZnO/Au diode between -0.75 V and 0.75 V. Due to a smaller Au/ZnO barrier, there is a considerable increase of current for this diode (Fig. 6.5(a)) when compared to Au/Al_2O_3/Au, resulting in a very low R_0 of 540 Ω (Fig. 6.5(b)). The latter represents critical improvement to a state-of-the-art Ti/ZnO/Pt diode [9] with reported R_0 =1200 Ω and β_0 of ~0.1 comparable to β_0 of 0.06 in this work.

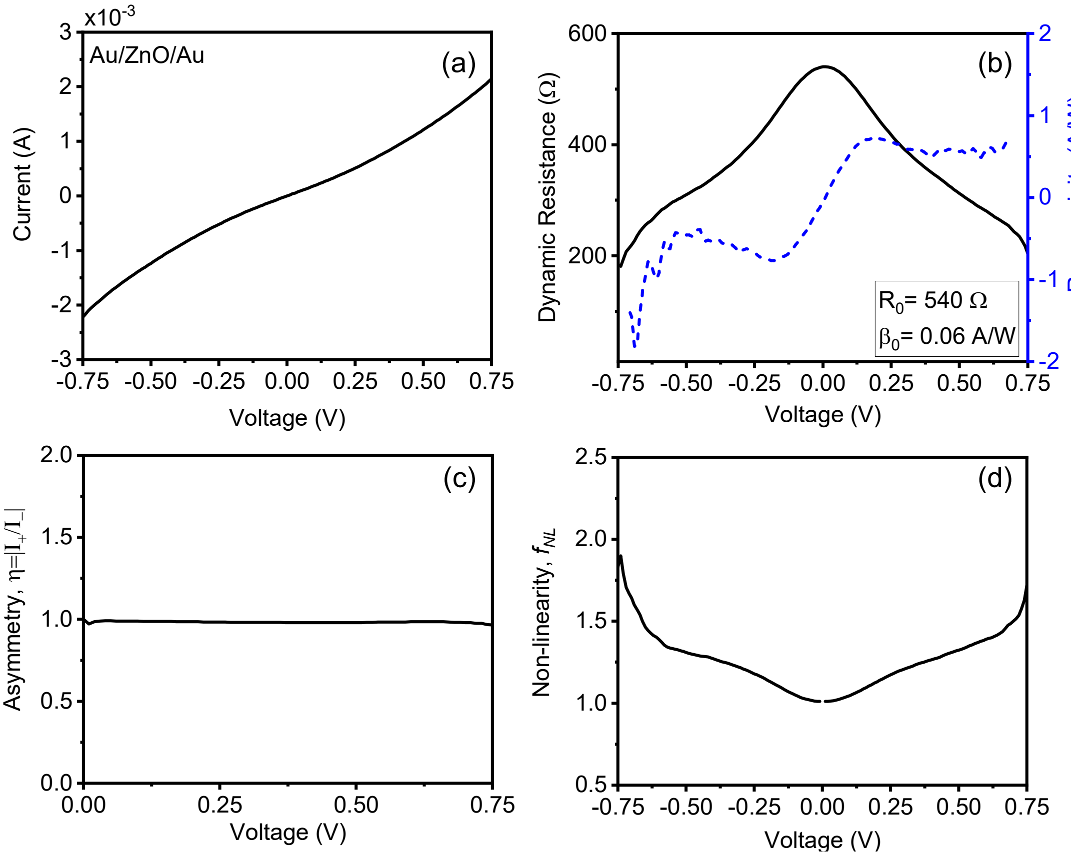

Figure 6.5. (a)-(d) Experimental I-V characteristics of the Au/ZnO/Au diode with associated extracted rectification parameters R_D, β, η and f_{NL}.

Although the device is symmetric (η~1, Fig 6.5 (c)) with a maximum β of 0.78 at 0.18 V and a maximum f_{NL} of 1.9 at -0.75 V (Fig. 6.5 (d)), it was already proved that the β_0, η and the f_{NL} values could be further improved using dissimilar metal electrodes

(Figs. 6.3-6.4). Therefore, a very low R_0 can be maintained at the same time using an oxide having high electron affinity and consequently low metal/oxide barrier height as in Au/ZnO.

For a better comparison, the experimental and theoretical I-V diagrams and the dynamic resistance curves of these four diode configurations were plotted together between -0.75 V and 0.75 V voltage range in Figs. 6.6 (a)-(d). Theoretical I-V characteristics using the same diode structures with their deduced barriers were generated using the in-house simulation model explained in section 3.3. The parameters used in simulations are as follows: The work functions of Au, Ti and Zn were taken as 5.1 [3,4], 4.1 eV [3,5] and 4.3 eV [4,5] respectively. The electron affinity of Al_2O_3 was 1.6 eV [1,2] and ZnO was 3.7 eV [6]. The dielectric constant of Al_2O_3 is 10 and ZnO is 9.4 based on Refs. [2,10–13], as well as the static dielectric permittivity calculations from C-V measurements. The electron effective mass is taken as $m_{eff} = 0.3m_0$, where m_0 is the free electron mass.

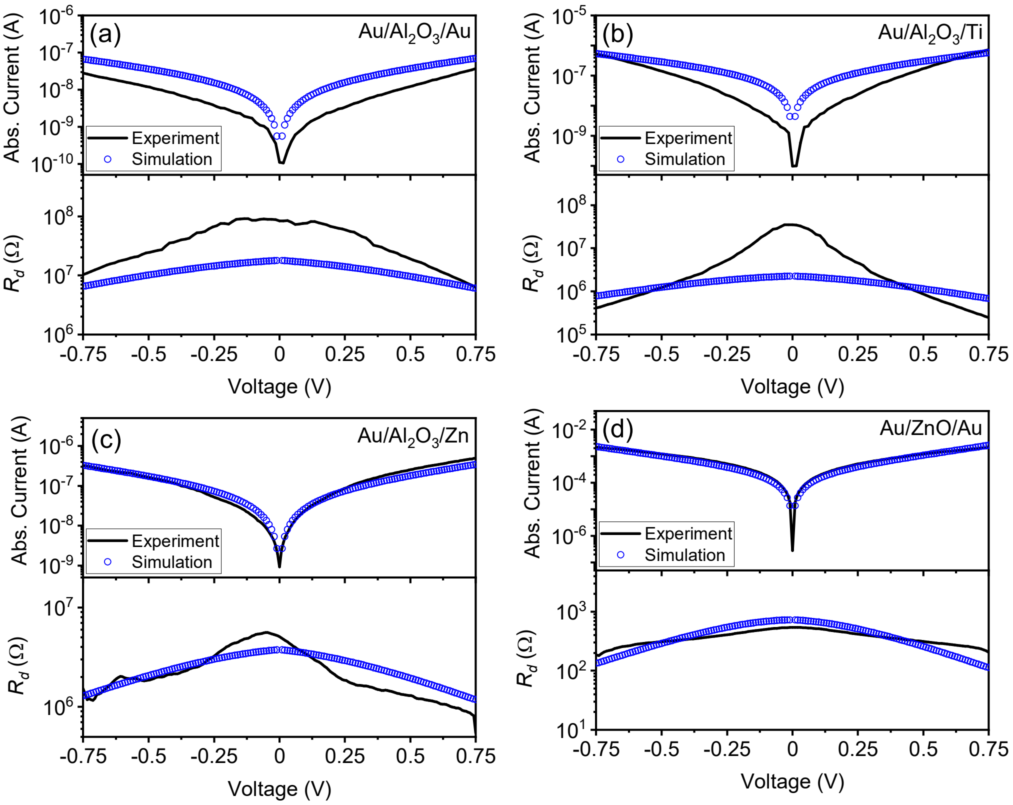

Figure 6.6. Experimental and simulated I-V characteristics of (a) $Au/Al_2O_3/Au$, (b) $Au/Al_2O_3/Ti$, (c) $Au/Al_2O_3/Zn$ and (d) Au/ZnO/Au diode structures with associated dynamic resistances (R_d).

A similar trend to the experimental I-V data shown in Figs. 6.6 (a)-(d) can be seen from the simulations. As seen from both experimental and theoretical I-V curves, lowering the barrier height between metal/oxide interface induces several orders of magnitude increase of current and causes a significant decrease in the device dynamic resistance. As mentioned before, the discrepancy in the experimental I-V curve of Au/Al_2O_3/Ti diode at low voltage range can also be seen from the simulation results. In the simulations, the current magnitude of the Au/Al_2O_3/Ti diode is higher than the Au/Al_2O_3/Zn for the whole voltage range due to the 0.2 eV difference in their electron affinities while in the experimental curve the Au/Al_2O_3/Ti starts to dominate the Au/Al_2O_3/Zn diode after 0.58 V.

Further improvement of rectification parameters can be achieved by lowering the barrier height by using metals with lower work functions or fabricating multiple insulator MI^{n}M diodes to achieve the RT conduction mechanism. Triple insulator (MI^{3}M) structures are investigated in the next section for this purpose.

6.3 Triple insulator non-cascaded MI^{3}M diodes

Energy band diagrams of the non-cascaded Al/Ta_2O_5/Nb_2O_5/Al_2O_3/Al structure, and the possible number of bound states formed in the potential well due to RT for each applied voltage are shown in Fig. 6.7. The alignment of the metal Fermi level with conduction bands of the insulators at a given external bias and the number of bound states were determined using the in-house simulation tool explained in section 3.3.

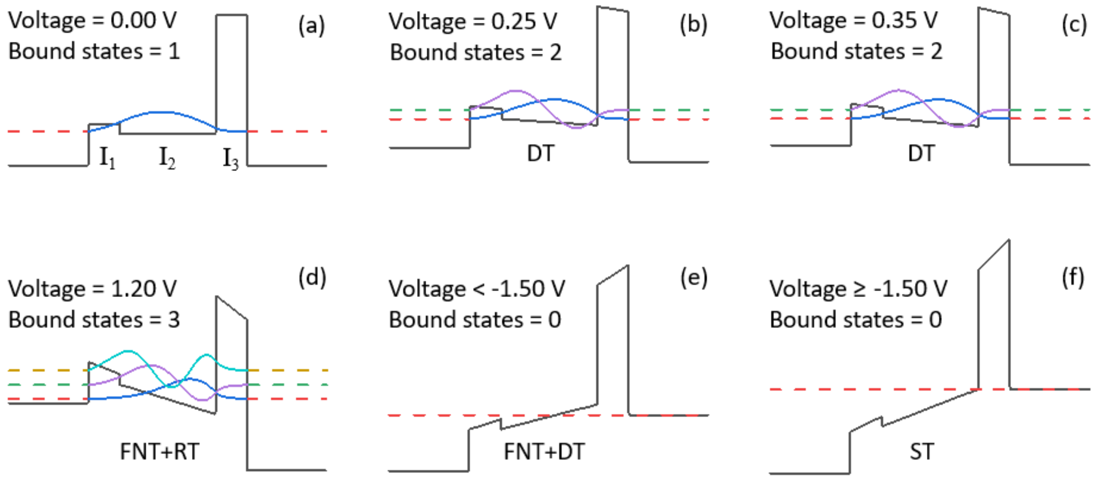

Figure 6.7. Band alignment for non-cascaded Ta_2O_5/Nb_2O_5/Al_2O_3 rectifier with thickness ratio (in nm) 1/3/1, under (a)-(d) positive bias, (e)-(f) negative bias.

It can be seen from Fig. 6.7 (a) that even when the applied voltage is zero, there is a bound state formed in the conduction band of Nb_2O_5. This is due to the barriers formed at the interfaces of Nb_2O_5/Ta_2O_5 (0.2 eV), and Nb_2O_5/Al_2O_3 (2.1 eV). As shown in Fig. 6.7 (b), there is the possibility of having another bound state when the applied bias reaches 0.25 V, but as can be seen from experimental data in Figs. 6.8 (a) and (b), the measured current levels are found to be low.

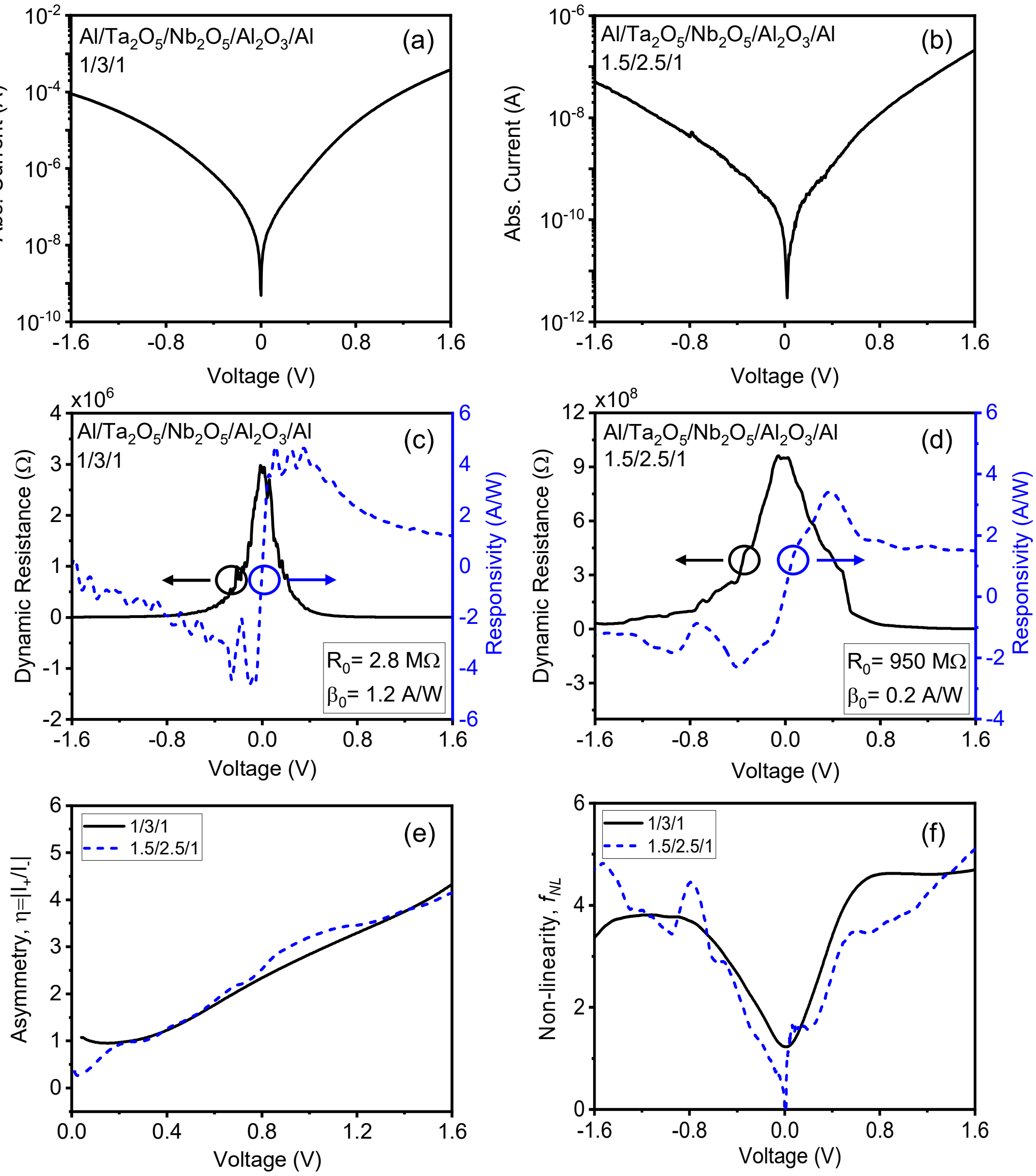

Figure 6.8. Experimental I-V characteristics for non-cascaded MI^3M diodes with $Ta_2O_5/Nb_2O_5/Al_2O_3$ thicknesses (in nm) (a) 1:3:1 and (b) 1.5:2.5:1 fabricated by ALD; their rectification parameters: (c)-(d) dynamic resistance and responsivity, (e) asymmetry and (f) non-linearity.

The latter is due to the very small number of electrons available to tunnel at this energy level as defined by Fermi-Dirac statistics; there is a large difference between the Fermi level of the metal and the energy level of the bound state. This is substantiated by simulations shown in Fig. 6.9 (a). Although there is a possibility of resonant tunnelling at two bound states located at 0.51 eV and 0.67 eV in Fig. 6.9 (a), the transmission probability is very low, ~10^{-11}. However, if the voltage is increased beyond 0.35 V (Fig. 6.7 (c)), it is possible to observe enhanced current due to resonance or in other words, a relatively larger number of electrons can tunnel via the bound state compared to the case of applied voltage of 0.25 V. This is clearly evident in the asymmetry plot in Fig. 6.8 (e).

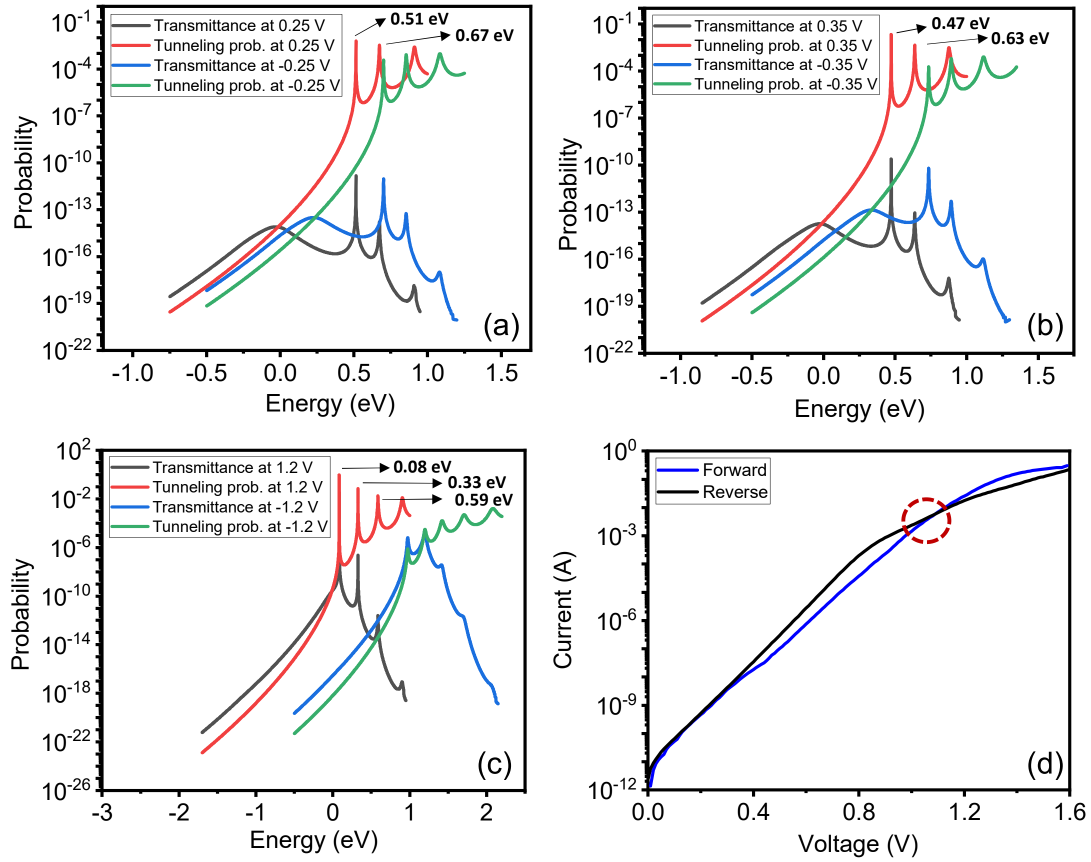

Figure 6.9. Transmittance and tunnelling probability curves generated at: (a) ± 0.25 V and (b) ± 0.35 V (c) ± 1.2 V for non-cascaded Al/1.0 nm Ta_2O_5/3.0 nm Nb_2O_5/1.0 nm Al_2O_3/Al diode. (d) simulated I-V curves for forward and reverse bias.

The asymmetry starts to increase from 1, for bias above 0.35 V. Furthermore, as shown in Fig. 6.9 (b), the bound states are located at 0.47 eV and 0.63 eV and are closer to the Al Fermi level. In this case, the transmission probability is higher (~10^{-10})

compared to the case of the applied voltage of 0.25 V. Nevertheless, due to the effect of large barrier height between Al/Nb_2O_5 interface (0.6 eV) (Fig. 6.1 (e), a pronounced effect of enhanced current due to RT cannot be observed in experimental data shown in Fig. 6.8 (a). For further increase of the bias to 1.2 V (Fig. 6.7 (d)), the Nb_2O_5 layer reaches the FNT and RT regimes. There are three bound states for external bias of 1.2 V, at 0.08 eV, 0.33 eV and 0.59 eV as shown in Fig. 6.9 (c). Aligning the Fermi energy of the metal with the bound states gives the maximum current transmittance in one direction. This is due to the transmittance being the product of Fermi-Dirac-like distribution of particles over energy states of the metal electrode and tunnelling probability. Dominance of forward current due to the resonant tunnelling can also been seen for bias above ~1.05 V in the simulations shown in Fig. 6.9 (d).

Figure 6.8 also shows the results for the 1.5:2.5:1 MI^3M diode structure, where the thickness of Nb_2O_5 is reduced by 0.5 nm and of Ta_2O_5 is increased by 0.5 nm to maintain the same total thickness of 5 nm. The voltage for strong resonance to occur is therefore higher in contrast to the 1:3:1 configuration. Note the significantly lower current for this device in Fig. 6.8 (b) compared to the 1:3:1 configuration shown in Fig. 6.8 (a). This is presumably due to the significant increase in tunnelling resistance with increase of Ta_2O_5 thickness. Furthermore, the effect of enhanced current due to resonance is less pronounced in 1.5:2.5:1 structure due to reduced potential across the thinner Nb_2O_5 layer. Therefore, a larger voltage must be applied on 1.5:2.5:1 structure to increase the depth of the triangular quantum well (QW) between Nb_2O_5/Al_2O_3 to achieve the same current level as in 1:3:1 diode configuration.

For reverse bias, the behaviour is very similar for both MI^3M diode configurations. The conduction in the films is dominated by DT and FNT when the applied bias is less than -1.5 V as can be seen in Fig. 6.7 (e). A QW is created in the conduction band of Nb_2O_5 as the bands are bent. However, as a result of the small barrier between Nb_2O_5 and Ta_2O_5 (0.2 eV), the bound state leaks to the left, resulting in the conduction in reverse bias to be dominated solely by DT and FNT. A potential of ~ -1.5 V must be applied for the metal Fermi level to overcome the conduction band (CB) of Ta_2O_5 and Nb_2O_5 to reach the step tunnelling regime (Fig. 6.7 (f)).

Dynamic resistance (R_d), responsivity (β), asymmetry ($\eta = |I_+/I_-|$ or $|I_-/I_+|$, where I_+ refers to forward bias current and I_- to reverse bias current) and non-linearity (f_{NL}) vs.

applied bias for the MI^{3}M devices are shown in Figs. 6.8 (c), (d), (e) and (f) respectively. The highest β_0 of 1.2 A/W was achieved for 1:3:1 MI^{3}M structure; while a peak η for this structure was found to be 4.3 at 1.6 V. A particular interest in enhanced zero bias responsivity is due to diode applications for IR energy harvesting where they need to operate at zero bias. Furthermore, the zero bias resistances of these two diodes structures are in the range of 10^6 to 10^8 Ω as shown in Figs. 6.8 (c)-(d). These large values are mainly due to the large barrier height of > 0.7 eV at the interface of Al/Ta_2O_5 (see Fig. 6.1 (d)). Reducing this barrier height could lower the resistance and this has been considered in the next section by adopting a cascaded insulator configuration.

6.4 Triple insulator cascaded MI^{3}M diodes

The energy band diagrams for cascaded A/Nb_2O_5/Ta_2O_5/Al_2O_3/Al MI^{3}M structure under positive and negative bias are shown in Fig. 6.10. As seen in Fig. 6.10 (a), no bound states exist in the cascaded structure for zero bias. Fig. 6.10 (b) illustrates that it is possible to obtain a bound state in the conduction bands of both Nb_2O_5 and Ta_2O_5 but the conduction process is dominated by DT in all three insulators when the applied bias is < 1.1 V.

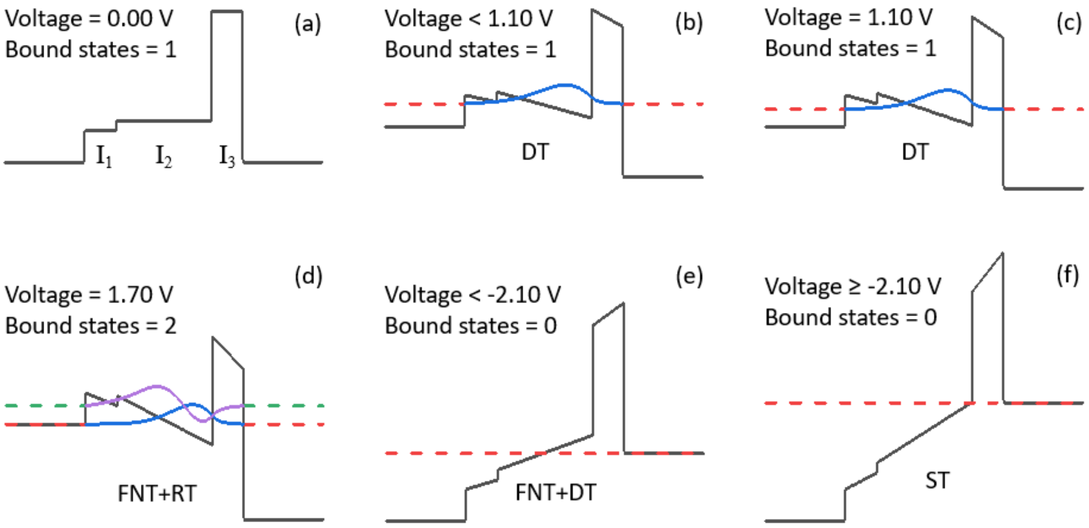

Figure 6.10. Energy band diagrams for cascaded MI^{3}M structure with Nb_2O_5/Ta_2O_5/Al_2O_3 thickness ratio (in nm) 1:3:1 under: (a) zero bias, (b)-(d) positive bias, (e)-(f) negative bias.

However, based on electrostatic calculations for 1:3:1 configuration, beyond 1.1 V (Fig. 6.10 (c)), the decreasing energy difference between the Al Fermi level and this bound state leads to an enhanced current due to resonance. The strong resonance is depicted for this structure from 1.7 V (Fig. 6.10 (d)). For reverse bias, the conduction below -2.1 V is dominated by DT and FNT (Fig. 6.10 (e)); further increase of voltage beyond -2.1 V leads to a step tunnelling regime (Fig. 6.10 (f)).

The experimental I-V characteristics for this device are shown in Fig. 6.11 (a), where measurements are taken from zero bias to either positive or negative bias (top graph) and also for continuous sweep, from negative to positive bias with a step voltage of 1.5 mV (bottom graph).

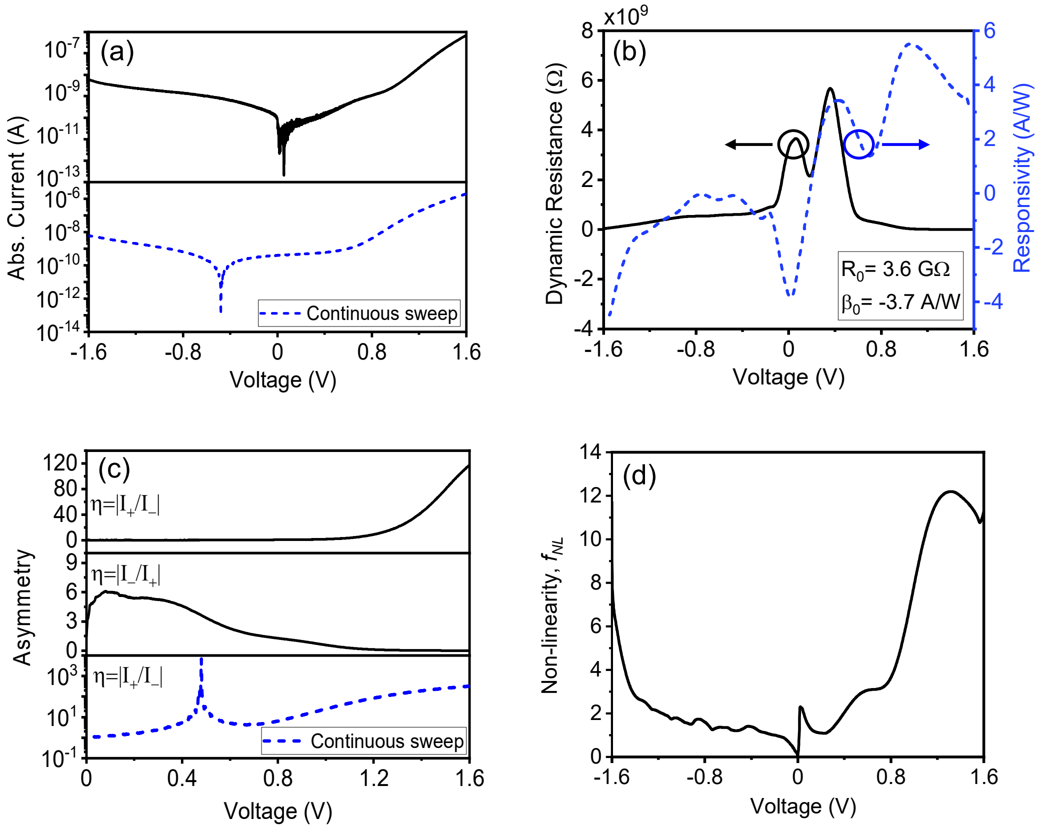

Figure 6.11. (a) Experimental I-V characteristics for cascaded MI^{3}M rectifier based on $Nb_2O_5/Ta_2O_5/Al_2O_3$ with thickness ratio (in nm) 1:3:1: (top) positive and negative bias sweeps start from 0 V; (bottom) continuous sweep from negative to positive bias; (b) dynamic resistance and responsivity, (c) asymmetry: $\eta = |I_+/I_-|$ for discontinuous sweep (top), $\eta = |I_-/I_+|$ for discontinuous sweep (middle), $\eta = |I_+/I_-|$ for continuous sweep; (d) non-linearity. The top and middle graphs in (c) are derived from I-V curve shown in top of (a); the graph at bottom of (c) is derived from I-V curve shown at the bottom of (a).

It can be seen that when sweeping from negative to positive voltage, the minimum current does not occur at 0 V, but there is a shift towards negative voltage level. The latter has been observed in Al/Al_2O_3/Ag diodes and the shift has been argued to be due to charge trapping or charge accumulation at Al/Al_2O_3 interface [14]. Further study of this effect is beyond the scope of this work [15], but the referring I-V characteristic has been presented here to illustrate that the erroneously high asymmetry value of ~10^4 at 0.5 V can be derived from such graph (see Fig. 6.11 (c),bottom). Therefore, the η, β and f_{NL} can only be considered accurate from the I-V plot shown in Fig. 6.11 (a) (top). The simulation results for the cascaded diode are depicted in Fig. 6.12. There is a strong effect of RT at 1.7 V as shown in Fig. 6.12 (a) with two bound states positioned at 0.00 eV and 0.33 eV. As shown in Fig. 6.12 (b), simulated rectification reversal point is seen at higher voltages ~1.55 V in comparison to non-cascaded configuration (~1.1 V, Fig. 6.9 (d)).

It can be seen from Fig. 6.11 (a) (top), that the rectification reversal and a change in curvature occurs at ~1 V in agreement with the band diagram shown in Fig. 6.10 (c) where the existence of a bound state can be observed in both potential wells. The increased current beyond 1 V is due to resonant tunnelling and leads to the high asymmetry of 117 at 1.6 V (Fig. 6.11 (c), top).

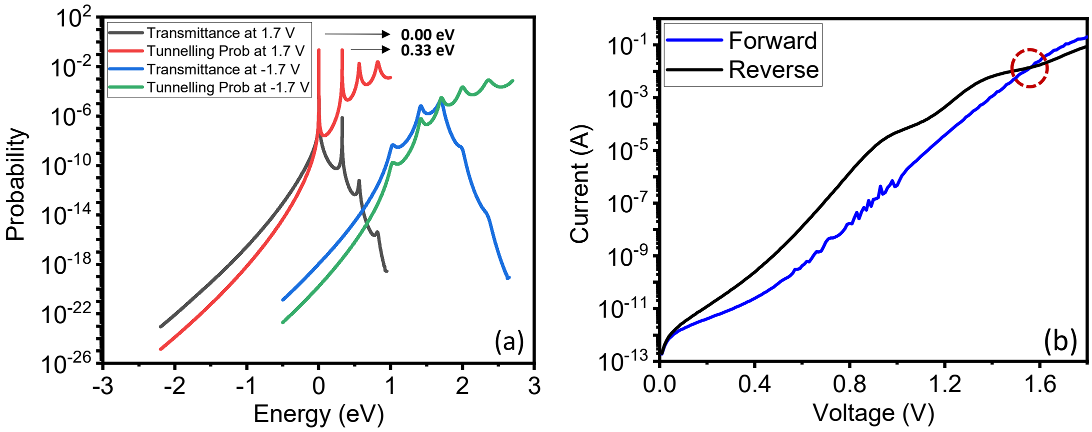

Figure 6.12. (a) Transmittance and tunnelling probability peaks at ± 1.7 V and (b) simulated I-V curves for cascaded Al/1.0 nm Nb_2O_5/3.0 nm Ta_2O_5/1.0 nm Al_2O_3/Al diode.

Note that by calculating asymmetry using the ratio of negative bias current to that of positive bias current, a peak asymmetry of 6 can be observed at 0.1 V as shown in Fig. 6.11 (c) (middle). The zero bias responsivity was found to be -3.7 A/W, while a peak value of 5.5 A/W at 1 V and the zero bias dynamic resistance of this device is ~10^9 Ω (Fig. 6.11 (b)). Finally, the maximum non-linearity is found to be 11.8 at 1.1 V as shown in Fig. 6.11 (d).

The rectification reversal, peak device η, maximum and zero-bias β values of fabricated MIM and MI^{3}M diodes in this section are summarised in Table 6.1.

Table 6.1. A summary of rectification parameters for fabricated MIM and MI^{3}M rectifiers fabricated by shadow mask evaporation.

Tunnel-barrier device	**Rectification Reversal**	**Maximum asymmetry**	**Maximum responsivity (A/W)**	**Zero-bias responsivity (A/W)**	**Zero-bias dynamic resistance (Ω)**
Au/Al_2O_3/Au	N/A	1.3 at 1.2 V	2.3 at 0.53 V	0.10	83 M
Au/Al_2O_3/Ti	N/A	1.7 at 1.5 V	5.0 at 0.16 V	-0.60	35 M
Au/Al_2O_3/Zn	N/A	1.7 at 0.25 V	2.3 at 0.19 V	1.60	5.1 M
Au/ZnO/Au	N/A	1 at 0.01 V	0.78 at 0.18 V	0.06	540
Ta_2O_5/Nb_2O_5/Al_2O_3 (1:3:1 non-cascaded)	0.35 V	4.3 at 1.6 V	4.3 at 0.35 V	1.20	2.8 M
Ta_2O_5/Nb_2O_5/Al_2O_3 (1.5:2.5:1 non-cascaded)	0.40 V	4.2 at 1.6 V	3.4 at 0.40 V	0.20	950 M
Nb_2O_5/Ta_2O_5/Al_2O_3 (1:3:1 Cascaded)	1.10 V	117 at 1.6 V; 6 at 0.1 V	5.5 at 1.0 V	-3.70	3.6 G

It is worth mentioning that the level of current in I-V simulations shown in Figs. 6.9 (d) and 6.12 (b) is much higher than that observed from the experiments in Figs. 6.8 (a) and 6.11 (a). This is due to limitations of the quantum-mechanical model and simulation that account only for the effect of the change in curvature of I-V curve due to the resonant tunnelling and available bound states from the energy band alignments as depicted in Figs. 6.7 and 6.10. To account for the effect of other conduction mechanisms and their effect in closely matching the level of current in theoretical to experimental I-V curves is outside of the scope of present work. It can be seen from Table 6.1 that the rectification performance from MI^{3}M diodes is superior to MIM diodes, especially the one in cascaded configuration where β_0 = -3.7 A/W and η = 6 at 0.1 V. Another significant result from this study is that although RT can be observed in non-cascaded MI^{3}M configuration in sub-V range, it has a small effect on enhancing current with asymmetry being less than 2 below 1 V and reaching ~4 at 1.6 V (see Fig. 6.8 (e) and Table 6.1). Further optimization of the MIM and MI^3M diodes needs to be considered in order to achieve lower zero bias dynamic resistance for rectenna applications.

6.5 Conclusion

In this chapter, optimized single M_1IM_2 and triple MI^3M diodes have been fabricated using ALD, RF sputtering and shadow mask evaporation techniques with the aim of improving the rectification performance. The device asymmetry (η), zero-bias responsivity (β_0), non-linearity (f_{NL}) and zero-bias dynamic resistance (R_0) have been enhanced in single insulator configurations using dissimilar metal electrodes (Au/Ti and Au/Zn) with different work functions. The Au/Al_2O_3/Zn diode exhibited a peak η of 1.7 at 0.25 V and a β_0 of 1.60 A/W while having around an order of magnitude decrease in the R_0 compared to the symmetric Au/Al_2O_3/Au configuration. A Au/ZnO/Au diode was also fabricated to particularly decrease the R_0 with the reduced barrier height using ZnO with a higher electron affinity value of ($\chi = 3.7$ eV) compared to Al_2O_3 ($\chi = 1.6$ eV). An extremely low R_0 of 540 Ω was obtained from the DC I-V measurements which is ~5 orders of magnitude lower than for the Au/Al_2O_3/Au configuration which makes ZnO as a promising candidate for THz MIM diodes.

Superior rectification performance (β, η, f_{NL}) in triple-insulator MI^3M in comparison to single M_1IM_2 rectifiers was also demonstrated in this work. Detailed electrical characterisation and simulation results show the effect of RT in thin (< 5 nm) insulator layers. The non-cascaded Ta_2O_5/Nb_2O_5/Al_2O_3 MI^3M structures with two different thickness ratios, and a cascaded Nb_2O_5/Ta_2O_5/Al_2O_3 device were fabricated and investigated. The evidence of RT can be found from a change of curvature and significant increase of current in the I-V characteristics. The RT was experimentally observed at ~0.35 V for non-cascaded and ~1 V for cascaded triple insulator MI^3M device. The strong RT effect has an impact on enhanced forward biased current and increased asymmetries (up to ~120) at higher voltages above 1 V. The highest low voltage asymmetry of 6 at 0.1 V and zero-bias responsivity of -3.7 A/W were observed for cascaded MI^3M structure which can be attributed to the effect of DT and FNT dominance on current transport. Although the dynamic resistances are too large for integration with the antenna part of the rectenna, lowering the metal/oxide barrier can pave the way for further optimization of triple insulator configurations together with dissimilar metal configurations ($M_1I^3M_2$).

References

[1] D. A. Weerakkody, “Engineered high-K oxides,” The University of Liverpool, *PhD thesis*, 2016.

[2] I. Z. Mitrovic, A. D. Weerakkody, N. Sedghi, J. F. Ralph, S. Hall, V. R. Dhanak, Z. Luo, and S. Beeby, “Controlled modification of resonant tunneling in metal-insulator-insulator-metal structures,” *Applied Physics Letters*, vol. 112, no. 1, p. 012902, 2018, doi: 10.1063/1.4999258.

[3] I. Z. Mitrovic, S. Almalki, S. B. Tekin, N. Sedghi, P. R. Chalker, and S. Hall, “Oxides for Rectenna Technology,” *Materials*, vol. 14, no. 18, p. 5218, 2021, doi: 10.3390/ma14185218.

[4] H. B. Michaelson, “The work function of the elements and its periodicity,” *Journal of Applied Physics*, vol. 48, no. 11, pp. 4729–4733, 1977, doi: 10.1063/1.323539.

[5] W. F. Gale and T. C. Totemeier, Eds., *Smithells Metals Reference Book*. 2003. doi: 10.1604/9780750675093.

[6] M. C. Gwinner, Y. Vaynzof, K. K. Banger, P. K. H. Ho, R. H. Friend, and H. Sirringhaus, “Solution-Processed Zinc Oxide as High-Performance Air-Stable Electron Injector in Organic Ambipolar Light-Emitting Field-Effect Transistors,” *Advanced Functional Materials*, vol. 20, no. 20, pp. 3457–3465, 2010, doi: 10.1002/adfm.201000785.

[7] S. B. Tekin, A. D. Weerakkody, N. Sedghi, S. Hall, M. Werner, J. S. Wrench, P. R. Chalker, and I. Z. Mitrovic, “Single and triple insulator Metal-Insulator-Metal diodes for infrared rectennas,” *Solid-State Electronics*, vol. 185, p. 108096, 2021, doi: 10.1016/j.sse.2021.108096.

[8] N. Alimardani and J. F. Conley, “Enhancing metal-insulator-insulator-metal tunnel diodes via defect enhanced direct tunneling,” *Applied Physics Letters*, vol. 105, no. 8, p. 082902, 2014, doi: 10.1063/1.4893735.

[9] A. A. Khan, G. Jayaswal, F. A. Gahaffar, and A. Shamim, “Metal-insulator-metal diodes with sub-nanometre surface roughness for energy-harvesting applications,”

Microelectronic Engineering, vol. 181, pp. 34–42, 2017, doi: 10.1016/j.mee.2017.07.003.

[10] P. D. Ye, B. Yang, K. K. Ng, J. Bude, G. D. Wilk, S. Halder, and J. C. Hwang, "GaN metal-oxide-semiconductor high-electron-mobility-transistor with atomic layer deposited Al2O3 as gate dielectric," *Applied Physics Letters*, vol. 86, no. 6, p. 063501, 2005, doi: 10.1063/1.1861122.

[11] J. Yota, H. Shen, and R. Ramanathan, "Characterization of atomic layer deposition HfO2, Al2O3, and plasma-enhanced chemical vapor deposition Si3N4 as metal–insulator–metal capacitor dielectric for GaAs HBT technology," *Journal of Vacuum Science & Technology A: Vacuum, Surfaces, and Films*, vol. 31, no. 1, p. 01A134, 2013, doi: 10.1116/1.4769207.

[12] A. D. Weerakkody, N. Sedghi, I. Z. Mitrovic, H. van Zalinge, I. Nemr Noureddine, S. Hall, J. S. Wrench, P. R. Chalker, L. J. Phillips, R. Treharne, and K. Durose, "Enhanced low voltage nonlinearity in resonant tunneling metal–insulator–insulator–metal nanostructures," *Microelectronic Engineering*, vol. 147, pp. 298–301, 2015, doi: 10.1016/j.mee.2015.04.110.

[13] N. H. Langton and D. Matthews, "The dielectric constant of zinc oxide over a range of frequencies," *British Journal of Applied Physics*, vol. 9, no. 11, pp. 453–456, 1958, doi: 10.1088/0508-3443/9/11/308.

[14] BJ. Eliasson, "Metal-insulator-metal diodes for solar energy conversion," University of Colorado at Boulder, *PhD thesis*, 2001.

[15] M. Kuhn and D. J. Silversmith, "Ionic Contamination and Transport of Mobile Ions in MOS Structures," *Journal of The Electrochemical Society*, vol. 118, no. 6, p. 966, 1971, doi: 10.1149/1.2408233.

Chapter 7

7. Optimization of MIM rectifiers for THz rectenna devices

In this chapter, it is aimed to further optimize the MIM diode configurations to achieve low zero-bias (R_0) resistance and increase coupling efficiency (η_c) with the antenna part. This is achieved by using rectenna contender oxides such as NiO, ZnO and TiO_2 and scaling down the devices. Thin (≤ 7 nm) insulating layers were fabricated using RF magnetron sputtering. Metal electrodes were deposited by thermal evaporation and RF sputtering using photolithography processes. The device areas range from 1 μm^2 to 64 μm^2 depending on the patterning process, to observe the effect of device scaling on the DC rectification properties. The DC I-V measurements were performed on fabricated diodes to evaluate key rectification parameters such as R_0, β_0 and η at zero-bias. Complementary theoretical calculations based on physical parameters extracted in Chapter 5 were carried out to substantiate the experimental results. The best rectification performance was achieved for a Au/2.6 nm ZnO_x/Cr diode, scaled down to 1 μm^2 device area, showing a zero-bias dynamic resistance of $R_0 = 71$ kΩ, zero-bias responsivity $\beta_0 = 0.28$ A/W and a coupling efficiency $\eta_c = 2.4 \times 10^{-5}$ % for rectification at 28.3 THz. The significance of this study is that it employs a methodology whereby key parameters of the MIM stack are derived from physical measurements which are then used to assist in the fitting of electrical current voltage data to produce a reliable appraisal of diode performance in an IR rectenna. The outcomes of this chapter have been submitted to Journal of Applied Physics together with the results of Chapter 5. The manuscript has been accepted for publication after minor revision.

7.1 Effect of device scaling on rectification behaviour of MIM diodes

Figure 7.1 shows I-V characteristics and associated rectification parameters of CrAu/7 nm NiO/CrAu diodes fabricated by photolithography using four different areas, from 64 μm^2 to 1 μm^2, to investigate the effect of scaling on the device rectification. As can be seen in Figs. 7.1 (a)-(b), reducing the device area causes decrease in the current level and an increase in the dynamic resistance as expected. The smallest R_0 was found to be 29 kΩ for the 64 μm^2 NiO-based diode, while values of 75.9 kΩ, 156.6 kΩ and 461.0 kΩ were observed for 16 μm^2, 4 μm^2 and 1 μm^2 devices respectively. The highest β_0 was found to be 0.76 A/W for 1 μm^2 diode being in advance to state-of-the-art values reported to be ~ 0.5 A/W [1–3]. The asymmetry, η (Fig. 7.1(d)) for all devices was found to be ~1 due to the symmetric metal electrode configurations and could be enhanced using dissimilar metals.

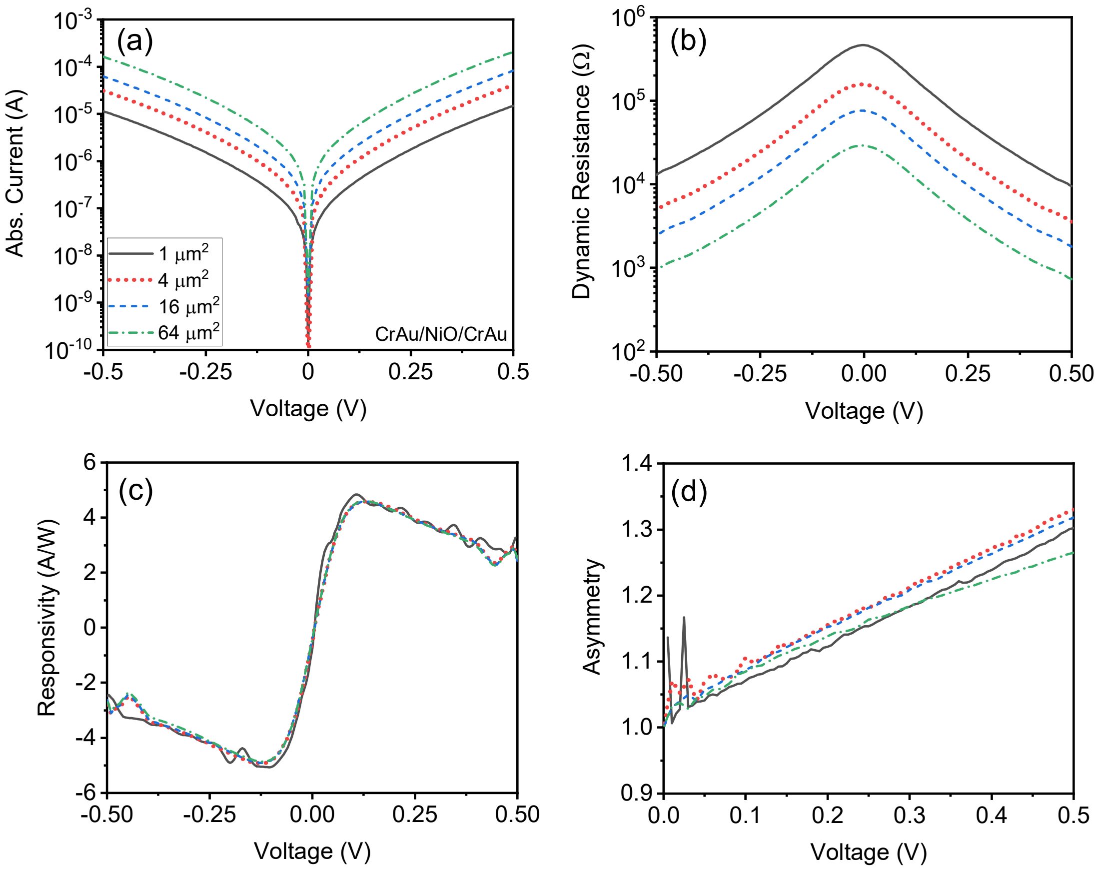

Figure 7.1. (a) The experimental I-V characteristics with associated extracted rectification parameters: (b) R, (c) β and (d) η for CrAu/NiO/CrAu diodes with varying areas, from 64 μm^2 to 1 μm^2. The nominal NiO thickness is 7 nm.

On the other hand, in Fig. 7.2, reduced NiO thickness (5 nm) with the same metal configuration (CrAu/CrAu) was compared with the thicker device (7 nm) for the same device area of 64 μm^2 with the aim of comparing the effect of reduced R_0 on the device coupling efficiency, η_c. The 2 nm thinner device exhibited ~1 order of magnitude high current magnitude and consequently a lower R_0 (5.6 kΩ). The β_0 = 1.81 A/W of the thinner diode was also found to be better than the thick one with a slightly higher asymmetry. However, although this diode has a lower R_0 and better β_0 than the 7 nm diode at the same 64 μm^2 area, the projected η_c of the 7 nm diode with 1 μm^2 device area is much higher the 5 nm-64 μm^2 one as shown in Fig. 7.3, where a similar η_c prediction as in Fig. 2.20 was done using the NiO based diodes at different areas and zero-bias dynamic resistances. The η_c was calculated using Eqn. 1.2 and assuming an antenna resistance of 100 Ω.

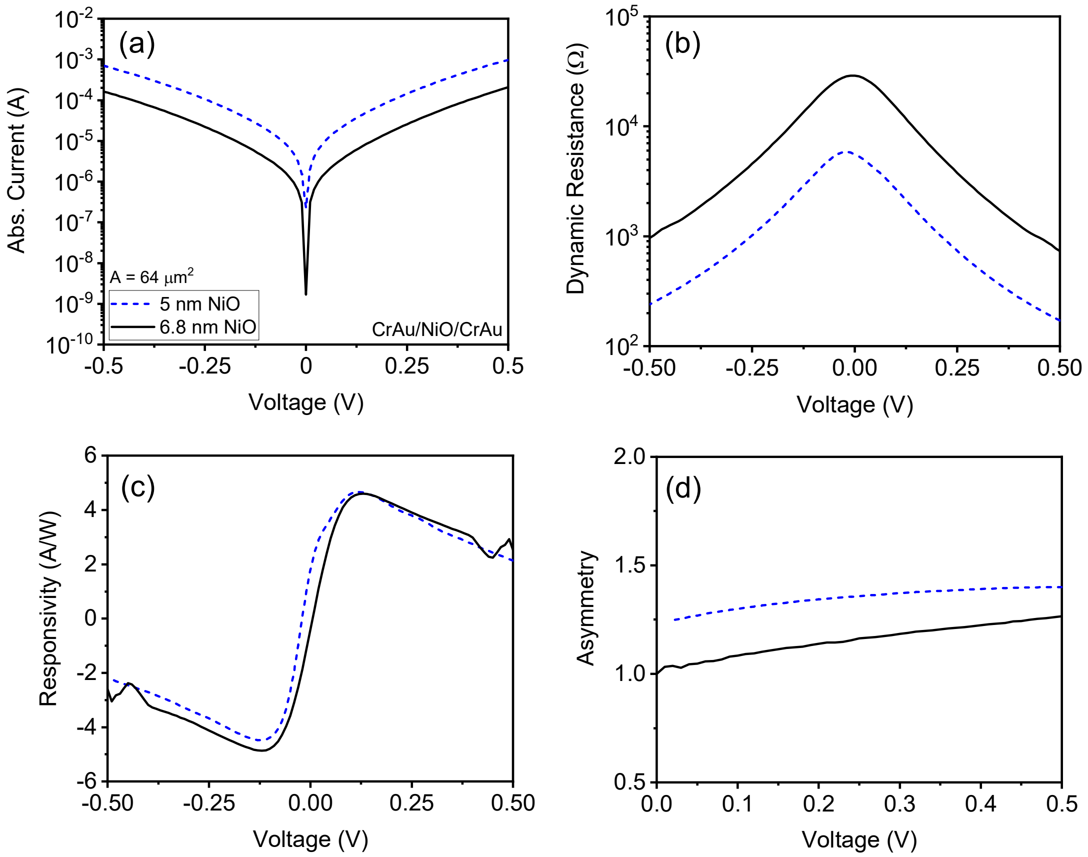

Figure 7.2. The experimental I-V characteristics with associated extracted rectification parameters: (b) R, (c) β and (d) η for 64 μm^2 CrAu/NiO/CrAu diodes with the nominal 5 nm and 7 nm NiO thicknesses.

As shown in Fig. 7.3, despite the highest R_0 (461 kΩ), $\eta_c = 1.5\times10^{-5}$ % was obtained for the 7 nm NiO based diode having 1 μm^2 device area which makes this device the most efficient among the others. The η_c is gradually decreasing with the increasing diode area down to 5.9 $\times10^{-8}$ % for the 64 μm^2 device area having 7 nm NiO thickness which is ~3 orders of magnitude lower than the η_c obtained for the smallest device area. It is also seen that reducing the thickness from 7 nm to 5 nm for the 64 μm^2 device causes ~ 1 order of magnitude decrease in the R_0 and consequently ~ 1 order of magnitude increase in the η_c up to 1.7×10^{-7} %. The results support the theoretical predictions done in Fig. 2.20 where the device area is much more critical than the diode resistance and shows the necessity of fabricating nano-scale devices.

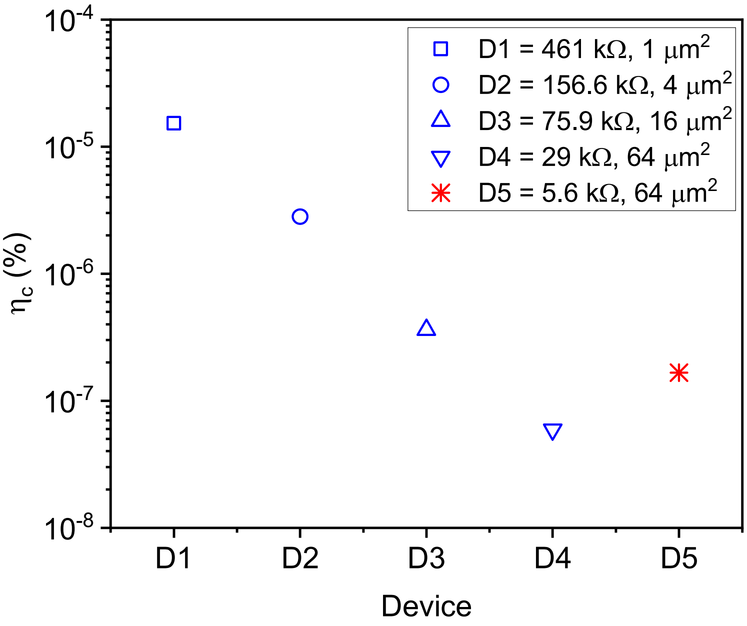

Figure 7.3. Projected η_c of the 7 nm (areas of 1 μm^2, 4 μm^2, 16 μm^2 and 64 μm^2) and 5 nm (64 μm^2) NiO based diodes compared to 100 Ω antenna resistance.

As reported in Table 7.1, the most recent data [1] demonstrates a scaled 0.025 μm^2 Ni/~1.5 nm NiO/CrAu diode, where the oxide is grown by plasma oxidation, with a much lower R_0 = 630 Ω in comparison to previously published data on similarly processed NiO-based MIM diodes. For example, a similar configuration with even a considerably larger area (1.45 μm^2) diode of Ni/3 nm NiO/Cr fabricated by Krishnan *et al*. [3], where the oxide is prepared by plasma oxidation, resulted in a R_0 of 500 kΩ. In another similar structure of Ni/NiO/Ni, fabricated by Choi *et al.*[2], with <4 nm thick plasma oxidized NiO and an aggressively scaled diode area of 0.018 μm^2, the resulting R_0 in is the order of megaohms, i.e. 42.4 MΩ, while β_0 is comparable (= 0.41 A/W) as in Ref. [1].

In this study, a large R_0 of 461 kΩ for 1 μm^2 scaled diode area on CrAu/~7 nm NiO/CrAu, where NiO was processed by radio frequency (RF) sputtering is also in line with the observed values in Ref. [3], while β_0 was found to be slightly improved to 0.76 A/W. An anomalously low R_0 in Ref. [1] has been interpreted to be due to very small Ni/NiO and CrAu/NiO barriers of 0.1 eV and 0.07 eV respectively. These values were deduced from simulating the theoretical current voltage (I-V) curve of the MIM stack with assumed band diagram values to match the experimental I-V data. This approach is often used in the literature but gives a wide range of values for metal/oxide band diagram parameters that do not agree with values extracted from physical characterization of associated thin films rendering difficulties in interpreting the results. In the case of Ref. [1], the electron affinity (χ) of NiO is deduced to be 4.8 eV from the theoretical I-V curve, while in Ref. [4] using the same fitting approach, χ of a similar plasma oxidized NiO film is estimated to be 2.05 eV. A similar uncertainty is also seen in Jayaswal *et al.* [5] work. Although the reported η_c is ~1.9×10^{-3} % for Au/Al_2O_3/Ti diode, as mentioned in Ref. [5], the electron affinity and the work function of the metals deviate significantly from the literature values (±2 eV) questioning the physical meaning of values extracted from I-V fittings and accuracy of predicted η_c. Looking at the published data [6,7] from ultraviolet and X-ray photoemission spectroscopy (UPS, XPS), the electron affinity of NiO has been measured to be 1.46 eV [6], while for as-deposited NiO_x χ is 2.1 eV [7]. These studies clearly point to a decrease or increase of electron affinity depending on the surface treatment of NiO, where the band gap structure also changes.

Table 7.1 A summary of MIM diode rectification figure of merits (R_0, β_0) of devices fabricated based on TiO_2, ZnO and NiO films and their comparison with the state-of-the-art. The stated coupling efficiency (η_c) values refer to 28.3 THz.

Device	Oxide deposition method	t_{ox} (nm)	Area (μm^2)	β_0 (A/W)	R_0 (Ω)	η_c (%)
Au/Al_2O_3/Ti [5]	ALD	1.5	$0.04^\dagger$	0.44	98 k	1.9×10^{-3}*
Ni/NiO/Ni [2]	Plasma ox.	<4.0	0.018	-0.41	42 M	1.5×10^{-4} *
Ni/NiO/Cr [3]	Plasma ox.	~2.5	1.45	0.50	500 k	1.3×10^{-6} *
Ni/NiO/CrAu [1]	Plasma ox.	1.5	0.025	0.41	630	2.9×10^{-1}
CrAu/NiO/CrAu (this work)	RF Sputtering	6.8	~1	0.76	461 k	1.5×10^{-5}
Ti/TiO_x/Pt [8]	Self-oxidation•	-	150	2.25	170 k	--
Ti/TiO_2/Pd [4]	in-situ oxidation	3	--	--	100 k	--
Au/TiO_x/Cr (this work)	RF Sputtering	2.5	~4	1.2	193 k	1.6×10^{-6}
Ti/ZnO/Pt [9]	ALD	4.0	9×10^4	0.125	1.2k	4.6×10^{-13} *
Au/ZnO_x/Cr (this work)	RF Sputtering	2.6	4	0.23	35 k	3.3×10^{-6}
Au/ZnO_x/Cr (this work)	RF Sputtering	2.6	~1	0.28	71 k	2.4×10^{-5}

* Coupling efficiency calculated based on the stated thickness, area and R_D values.

† Device area calculated based on stated dimensions.

• Oxidation in an elevated temperature and humidity.

Besides this, fitting the I-V curve with $\chi_{NiO} \sim 2$ eV to the same configuration as in Ref. [1] would result in ~6 orders of magnitude higher R_0 and projected much lower η_c of ~10^{-6} %. In order to confirm this, initially the I-V curve of the Ni/NiO/CrAu device was regenerated by the in-house model using the reported values of the diode properties in Ref. [1]. Then, the χ of NiO was changed from 4.80 eV to 2.46 eV and 2.05 eV based on the FNT and the XPS results of this work, respectively. The simulated I-V curves are shown in Fig. 7.4.

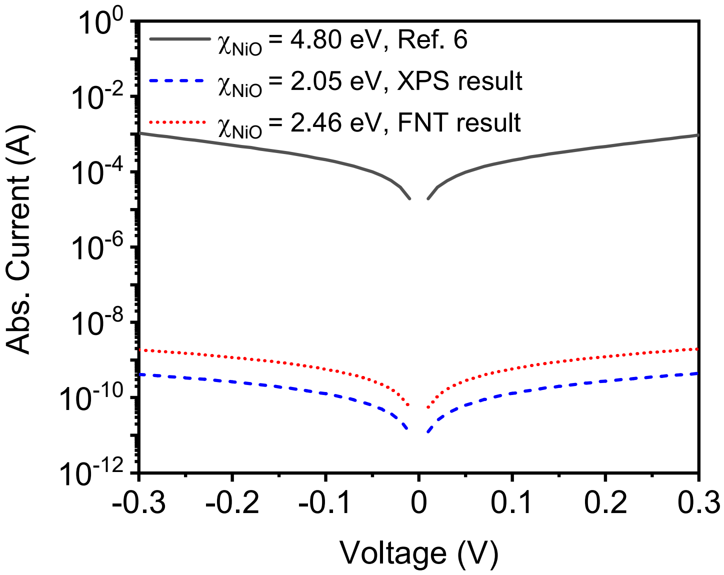

Figure 7.4. Simulated I-V curves of Ni/1.5 nm NiO/CrAu diode based on the results obtained in Ref. [1], FNT (χ = 2.46 eV) and XPS (χ = 2.05 eV) measurements.

Based on the above mentioned variety of supporting values in the literature [2,3,6,7,10], the results of this work raise the question regarding the repeatability of a very low barrier of ~0.1 eV between the Ni/NiO interface demonstrated in Ref [1].

7.2 Applicability of TiO_2 and ZnO thin films in 28.3 THz rectennas

In this section, MIM diodes have been fabricated based on (< 3 nm) TiO_2 and ZnO thin films to study their suitability for inclusion in 28.3 THz rectennas. The measured electron affinity values found in Chapter 5 were used to fit experimental I-V curves of associated MIM diodes. As explained in the literature review section of Chapter 2, the rectification at 28.3 THz has recently been demonstrated by rectenna devices based on MIM diodes using the Au/Al_2O_3/Ti [5] configuration. Although the results are promising, the overall conversion efficiency is low, 2.05×10^{-14} [5] mainly due to the poor rectification properties of the diodes. Khan *et al.*[9] have reported R_0 = 1.2 kΩ and β_0 = 0.125 A/W for Ti/4 nm ZnO/Pt diode, where the oxide is processed by ALD. However, due to the large diode area of 9×10^4 μm^2, this diode has a very low cut-off frequency (f_c) and hence low antenna/diode coupling efficiency. According to Table 7.1, the highest η_c = 2.9×10^{-1} % has been reported for Ni/NiO/CrAu [1] due to considerably smaller R_0 (~630 Ω) than the other reported values (500 kΩ [3,10], ~40 MΩ [2]) on similar diodes, which has been discussed in the previous section.

In this study, the experimental and theoretically fitted I-V curves of TiO_2 and ZnO_x based MIM devices fabricated by photolithography are shown in Figs. 7.5 (a)-(b) together with extracted rectification parameters of dynamic resistance (Fig. 7.5 (c)) and responsivity (Fig. 7.5 (d)).

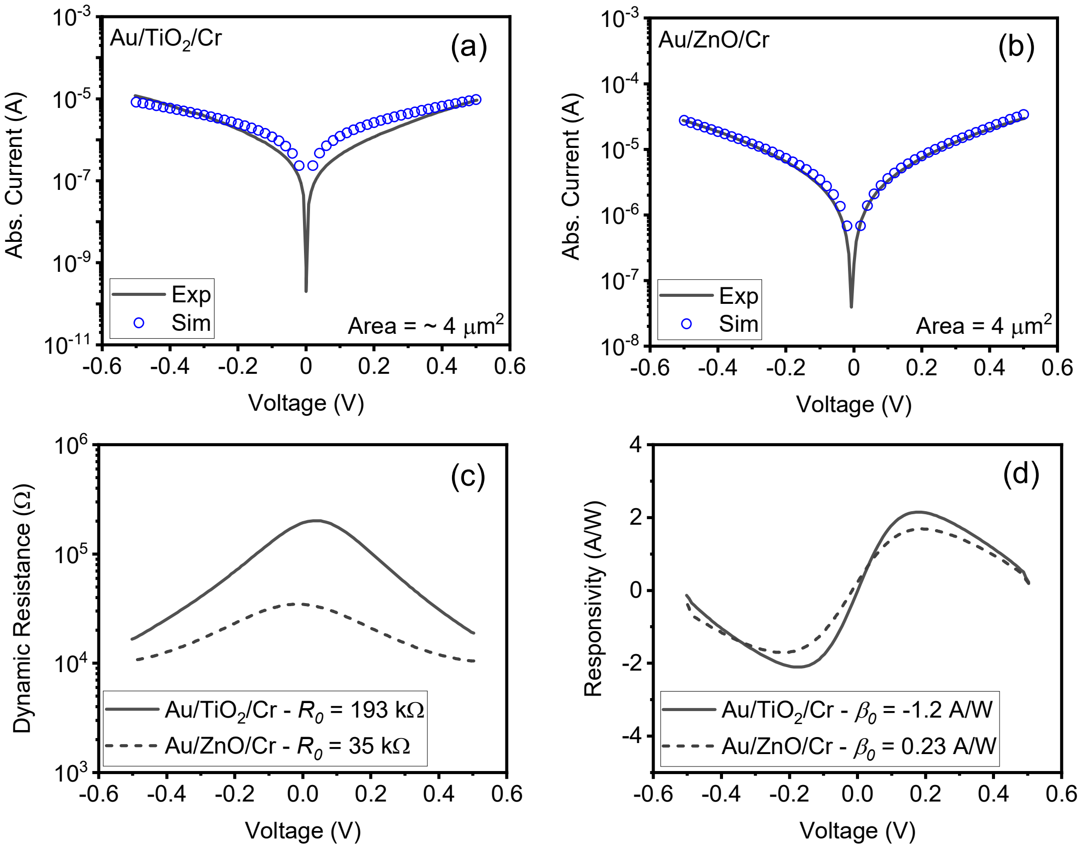

Figure 7.5. Experimental and fitted *I-V* characteristics of (a) Au/TiO_2/Cr, (b) Au/ZnO/Cr diodes with 4 μm^2 device area and their (c) dynamic resistance vs. applied bias; (d) responsivity vs. applied bias curves. The zero bias dynamic resistance (R_0) and zero-bias responsivity (β_0) are stated for each device.

The fitted I-V curves were generated using the in-house simulation model [11,12] which was explained in detail in section 3.2. The best fit to the experimental data in Fig. 7.5 (a)-(b) was achieved by inserting χ_{TiO2} = 3.6 eV and χ_{ZnOx} = 3.7 eV which is in agreement with values derived in Table 5.5. Other parameters used in simulations are as follows: work functions [13] of Au and Cr were taken as 5.1 eV and 4.5 eV, respectively; the static dielectric constant of TiO_2 was 25 [14] and of ZnO was 9.4 [15], while electron effective mass was $m^* = 0.3m_0$, where m_0 is the free electron mass.

Figures 7.5 (c)-(d) show the rectification parameters R_0 and β_0 of Au/2.5 nm TiO_2/Cr and Au/2.6 nm ZnO/Cr diodes with nominal device area of 4 μm^2 device. A smaller zero-bias dynamic resistance of R_0 = 35 kΩ can be seen for the ZnO based diode in comparison to 193 kΩ for TiO_2 based device. Even though the zero-bias responsivity of TiO_2 based diode (β_0=1.2 A/W) is higher than for the ZnO one (β_0=0.23 A/W), an order of magnitude lower R_0 makes the ZnO_x based diode more advantageous for rectenna due to better diode/antenna coupling efficiency.

In Figures 7.6 (a)-(b), it has been shown that further scaling of the ZnO_x based diode to a size of 1 μm^2 can result in β_0=0.28 A/W and R_0 = 71 kΩ. These diode metrics represent an advance on the previously reported state-of-the-art Ti/ZnO/Pt [9] device in terms of considerably higher coupling efficiency (η_c).

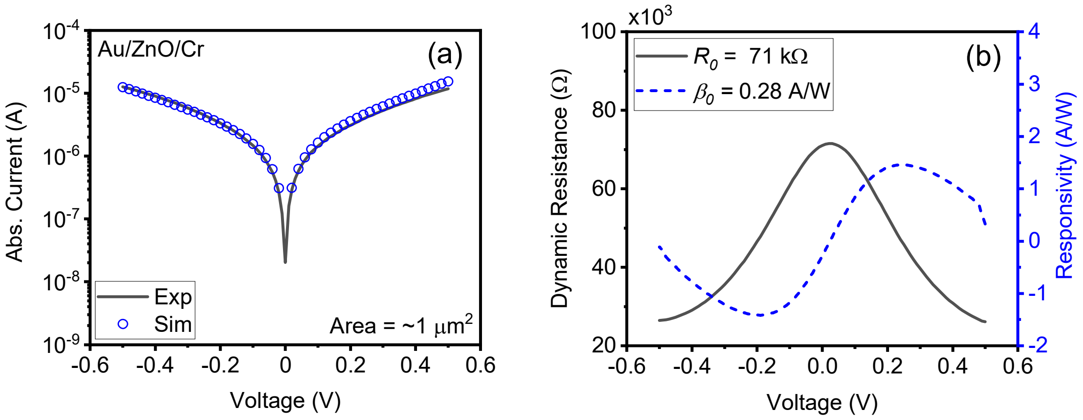

Figure 7.6. Experimental and fitted I-V characteristics of (a) scaled Au/ZnO/Cr diode with a nominal device area of 1 μm^2 with associated (b) dynamic resistance and responsivity vs. bias curves.

A projection of calculated η_c of these fabricated diodes is summarized in Table 7.1 and compared with η_c values reported in the literature. The high-frequency permittivity values of oxides [16] ($\varepsilon_\infty = n^2$, where n is the refractive index) were used for the capacitance calculations which are 1.4 for TiO_2 [17] 2.4 for ZnO [18] 3.24 for NiO [18], all at 28.3 THz. The best performing diode in this work (Au/ZnO_x/Cr with 1 μm^2 area) has η_c = 2.4×10^{-5} % which is 6 orders of magnitude higher than for previously demonstrated Ti/ZnO/Pt [9] diode with η_c = 4.6×10^{-13}%. The Au/TiO_2/Cr has an order of magnitude lower coupling efficiency than the ZnO based one (η_c=1.6×10^{-6}%).

Further to the evidence of our experimental results, ZnO and TiO_2 based MIM diodes can have a projected η_c > 1%. This could be achieved by fabricating thinner insulating layers (~1 nm) with a smaller area (~0.01 μm^2) and more asymmetric metal configurations such as Au/Ti or Au/Nb instead of Au/Cr to reduce the R_0 since Ti (4.1 eV [19]) and Nb (4.1 eV [20]) metals have smaller work function than Cr (4.5 eV[13]). For that reason, the I-V characteristics of Au/1 nm TiO_2/Ti and Au/1 nm ZnO/Ti diodes were simulated considering the electron affinity values experimentally measured on reference oxide samples as shown in Fig. 7.7.

These simulations results were compared with the experimental I-V curves of the diodes presented in Fig. 7.5. As can be seen in Figs. 7.7 (a)-(b), there is ~2 orders of magnitude increase in the current levels of both TiO_2 and ZnO based diodes with the increased asymmetry due to the difference in Au/Ti metal work functions of 1 eV (work functions of Au and Ti are taken as 5.1 eV [13] and 4.1 eV [19]), as well as the reduced oxide thickness of 1 nm despite the smaller area (0.01μm^2) compared to the experimental diodes having 4 μm^2 area. Figs. 7.7 (c) and (d) show the simulated R_0 values of Au/1 nm TiO_2/Ti and Au/1 nm ZnO/Ti diodes with an area of 0.01 μm^2 to be 1238 Ω and 783 Ω, respectively.

Considering the R_0 of these two diodes, the dynamic permittivity (1.4 for TiO_2 [17] and 2.4 for ZnO [18]) of these oxides at 28.3 THz [16] and an antenna resistance of 100 Ω, the coupling efficiency, η_c was calculated. According to these results, the Au/1 nm TiO_2/Ti and Au/1 nm ZnO/Ti configurations can have 5% and 3% η_c, respectively which can improve the efficiency ~1 order compared to the highest reported η_c=

0.29% [1] for the single insulator diodes. The projected η_c for TiO_2 based diode is higher than the ZnO based one due to its lower dynamic permittivity.

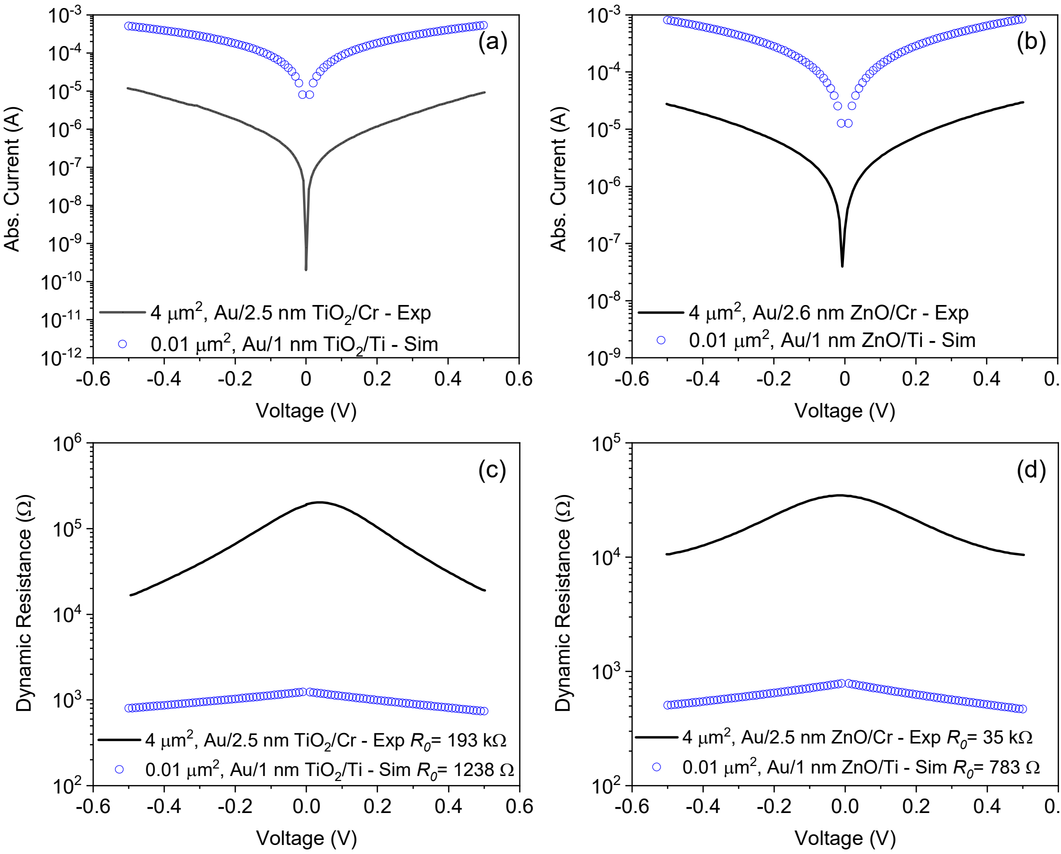

Figure 7.7. Comparison between the experimental and simulated I-V curves of (a) TiO_2 and (b) ZnO based single insulator diodes and (c)-(d) their calculated dynamic resistance.

For comparison, the η_c values for three different oxides are summarised in Fig. 7.8. It is also seen that the η_c for TiO_2 and ZnO based devices can be improved by ~6 orders of magnitude compared to our fabricated TiO_2 based diode (4 µm², 193 kΩ) and ~5 orders of magnitude in comparison with the ZnO based diode (1 µm², 71 kΩ), respectively with the proposed modifications.

However, for further increase in the β_0 while keeping a low R_0, double insulator MI^2M is crucial. As proposed in the theoretical work of Elsharabasy *et al.* [21] $Cr/TiO_2/ZnO/Ti$ configuration could be a potential candidate to have an efficient rectifier based on their simulated I-V characteristics. However, the electron affinities of TiO_2 and ZnO were considered as 4.20 eV and 4.30 eV in their simulations which are 0.6 eV higher than our experimentally found values for both oxides. This configuration would result in high metal/oxide barriers and consequently high R_0 according to the experimental results.

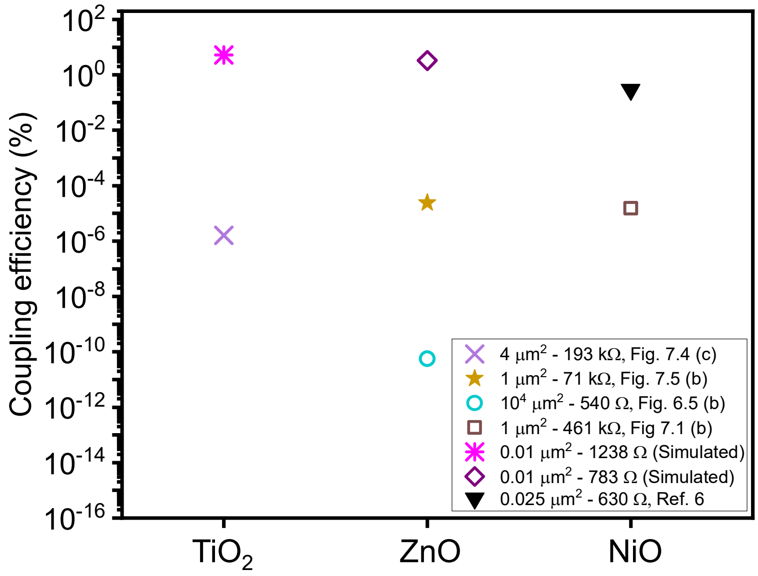

Figure 7.8. Projected η_c for TiO_2, ZnO and NiO based single insulator diodes with respect to 100 Ω antenna resistance.

As an alternative, metals having smaller work functions such as (Ti and Nb) can be chosen to combine with these two oxides. Another alternative is changing the growth parameters of the RF sputtered ZnO and TiO_2 layers to modulate the stoichiometry and consequently increase the electron affinity of the oxides such as in Ref [1]; or applying post-deposition treatment such as annealing of the thin films at high temperatures. Sharma *et al.* [22] reported an increase in the electron affinity of up to 0.5 eV between the spin coated ZnO thin films annealed at 150°C and 250°C. This could be a potential solution for having lower metal/oxide barrier heights. As mentioned in Ref [1], it is not straightforward to predict the projected η_c of the double insulator configurations without doing an actual optical measurement using a THz source since the high frequency behaviour of the diodes deviate from the DC I-V results more than the single insulator configurations, but the η_c can be experimentally increased >10% [21]. This could be done using metals having lower work functions. Another modification could be increasing the electron affinity of the oxides by either modifying the growth conditions to change the stoichiometry or applying post-deposition treatment methods, particularly annealing. By this way, the diode area can be reduced to nm scales while maintaining a low resistance which improves the η_c.

7.3 Conclusion

In this chapter, several scaled MIM devices were fabricated and tested using NiO, TiO_2, ZnO thin films with different metal configurations. The devices were fabricated using conventional photolithography tools to observe the effect of scaling on the device performance and calculate the coupling efficiency at 28.3 THz frequency.

CrAu/NiO/CrAu diodes with a nominal 7 nm NiO thickness were fabricated with four different devices areas including 64 μm^2, 16 μm^2, 4 μm^2 and 1 μm^2. A CrAu/NiO/CrAu diode having 64 μm^2 area was fabricated with a reduced NiO thickness of nominal 5 nm. It was experimentally observed that the device scaling has a considerably higher impact on the improved coupling efficiency compared to the reduced oxide thickness. Despite the higher dynamic resistance (R_0 = 461.0 kΩ), the 1 μm^2, 7 nm NiO based diode exhibited a projected coupling efficiency of $\eta_c = 1.5\times10^{-5}$ %, where it was calculated to be $\eta_c = 1.7\times10^{-7}$ % for the 64 μm^2, 5 nm NiO based diode having 5.6 kΩ R_0, which is ~2 orders of magnitude lower.

Further improvement in the coupling efficiency was obtained using scaled TiO_2 and ZnO based MIM diodes with Au/Cr metal combinations. The best achieved coupling efficiency was found to be $\eta_c = 2.4\times10^{-5}$ % for the Au/2.6 nm ZnO/Cr diode having a device area of nominal 1 μm^2 which is ~ 6 orders of magnitude in advance of the previously demonstrated ZnO based diode.

Furthermore, the calculations in this chapter provide evidence that by decreasing the oxide thickness, scaling down the area to nanometre scale and using metals with lower work function such as Ti or Nb, the η_c of the ZnO and TiO_2 based diodes can be increased up to ~ 5% at 28.3 THz. These modifications can also be applied in double insulator configurations and the efficiency can be improved beyond 10% which could merit practical application of rectennas.

References

[1] A. Weerakkody, A. Belkadi, and G. Moddel, "Nonstoichiometric Nanolayered Ni/NiO/Al2O3/CrAu Metal–Insulator–Metal Infrared Rectenna," *ACS Applied Nano Materials*, vol. 4, no. 3, pp. 2470–2475, 2021, doi: 10.1021/acsanm.0c03012.

[2] K. Choi, F. Yesilkoy, G. Ryu, S. H. Cho, N. Goldsman, M. Dagenais, and M. Peckerar, "A Focused Asymmetric Metal–Insulator–Metal Tunneling Diode: Fabrication, DC Characteristics and RF Rectification Analysis," *IEEE Transactions on Electron Devices*, vol. 58, no. 10, pp. 3519–3528, 2011, doi: 10.1109/ted.2011.2162414.

[3] S. Krishnan, H. La Rosa, E. Stefanakos, S. Bhansali, and K. Buckle, "Design and development of batch fabricatable metal–insulator–metal diode and microstrip slot antenna as rectenna elements," *Sensors and Actuators A: Physical*, vol. 142, no. 1, pp. 40–47, 2008, doi: 10.1016/j.sna.2007.04.021.

[4] A. Kaur and P. Chahal, "RF Characterization of NiO and TiO2 Based Metal-Insulator-Metal (MIM) Diodes on Flexible Substrates," *IEEE Access*, vol. 6, pp. 55653–55660, 2018, doi: 10.1109/access.2018.2871635.

[5] G. Jayaswal, A. Belkadi, A. Meredov, B. Pelz, G. Moddel, and A. Shamim, "Optical rectification through an Al2O3 based MIM passive rectenna at 28.3 THz," *Materials Today Energy*, vol. 7, pp. 1–9, 2018, doi: 10.1016/j.mtener.2017.11.002.

[6] H. Wu and L.-S. Wang, "A study of nickel monoxide (NiO), nickel dioxide (ONiO), and Ni(O2) complex by anion photoelectron spectroscopy," *The Journal of Chemical Physics*, vol. 107, no. 1, pp. 16–21, 1997, doi: 10.1063/1.474362.

[7] E. L. Ratcliff, J. Meyer, K. X. Steirer, A. Garcia, J. J. Berry, D. S. Ginley, D. C. Olson, A. Kahn, and N. R. Armstrong, "Evidence for near-Surface NiOOH Species in Solution-Processed NiOx Selective Interlayer Materials: Impact on Energetics and the Performance of Polymer Bulk Heterojunction Photovoltaics," *Chemistry of Materials*, vol. 23, no. 22, pp. 4988–5000, 2011, doi: 10.1021/cm202296p.

[8] L. E. Dodd, D. Wood and A. J. Gallant, "Optimizing MOM diode performance via the oxidation technique," *SENSORS, 2011 IEEE*, 2011, pp. 176-179, doi: 10.1109/ICSENS.2011.6127347.

[9] A. A. Khan, G. Jayaswal, F. A. Gahaffar, and A. Shamim, “Metal-insulator-metal diodes with sub-nanometre surface roughness for energy-harvesting applications,” *Microelectronic Engineering*, vol. 181, pp. 34–42, 2017, doi: 10.1016/j.mee.2017.07.003.

[10] S. B. Tekin, S. Almalki, A. Vezzoli, L. O’Brien, S. Hall, P. R. Chalker, and I. Z. Mitrovic, “(Digital Presentation) Optimization of MIM Rectifiers for Terahertz Rectennas,” *ECS Transactions*, vol. 108, no. 2, pp. 69–79, 2022, doi: 10.1149/10802.0069ecst.

[11] N. Sedghi, J. F. Ralph, I. Z. Mitrovic, P. R. Chalker, and S. Hall, “Electron trapping at the high-κ/GeO2 interface: The role of bound states,” *Applied Physics Letters*, vol. 102, no. 9, p. 092103, 2013, doi: 10.1063/1.4794544.

[12] N. Sedghi, J. W. Zhang, J. F. Ralph, Y. Huang, I. Z. Mitrovic and S. Hall, "Towards rectennas for solar energy harvesting," *2013 Proceedings of the European Solid-State Device Research Conference (ESSDERC)*, 2013, pp. 131-134, doi: 10.1109/ESSDERC.2013.6818836.

[13] H. B. Michaelson, “The work function of the elements and its periodicity,” *Journal of Applied Physics*, vol. 48, no. 11, pp. 4729–4733, 1977, doi: 10.1063/1.323539.

[14] Q. Cui, M. Sakhdari, B. Chamlagain, H.-J. Chuang, Y. Liu, M. M.-C. Cheng, Z. Zhou, and P.-Y. Chen, “Ultrathin and Atomically Flat Transition-Metal Oxide: Promising Building Blocks for Metal–Insulator Electronics,” *ACS Applied Materials & Interfaces*, vol. 8, no. 50, pp. 34552–34558, 2016, doi: 10.1021/acsami.6b11302.

[15] N. H. Langton and D. Matthews, “The dielectric constant of zinc oxide over a range of frequencies,” *British Journal of Applied Physics*, vol. 9, no. 11, pp. 453–456, 1958, doi: 10.1088/0508-3443/9/11/308.

[16] I. Z. Mitrovic, S. Almalki, S. B. Tekin, N. Sedghi, P. R. Chalker, and S. Hall, "Oxides for Rectenna Technology," *Materials*, vol. 14, no. 18, p. 5218, 2021, doi: 10.3390/ma14185218.

[17] J. Kischkat, S. Peters, B. Gruska, M. Semtsiv, M. Chashnikova, M. Klinkmüller, O. Fedosenko, S. Machulik, A. Aleksandrova, G. Monastyrskyi, Y. Flores, and W. Ted Masselink, "Mid-infrared optical properties of thin films of aluminum oxide, titanium dioxide, silicon dioxide, aluminum nitride, and silicon nitride," *Applied Optics*, vol. 51, no. 28, p. 6789, 2012, doi: 10.1364/ao.51.006789.

[18] M. R. Querry, *Optical constants*. Aberdeen Proving Ground, MD: US Army Armament, Munitions & Chemical Command, Chemical Research & Development Center, 1985.

[19] W. F. Gale and T. C. Totemeier, Eds., *Smithells Metals Reference Book*. 2003. doi: 10.1604/9780750675093.

[20] I. Z. Mitrovic, A. D. Weerakkody, N. Sedghi, J. F. Ralph, S. Hall, V. R. Dhanak, Z. Luo, and S. Beeby, "Controlled modification of resonant tunneling in metal-insulator-insulator-metal structures," *Applied Physics Letters*, vol. 112, no. 1, p. 012902, 2018, doi: 10.1063/1.4999258.

[21] A. Y. Elsharabasy, M. H. Bakr, and M. J. Deen, "Towards an optimal MIIM diode for rectennas at 10.6 µm," *Results in Materials*, vol. 11, p. 100204, 2021, doi: 10.1016/j.rinma.2021.100204.

[22] A. Sharma, S. E. Watkins, G. Andersson, and D. A. Lewis, "Effect of Annealing Temperature of ZnO on the Energy Level Alignment in Inverted Organic Photovoltaics (OPVs)," *Energy Technology*, vol. 2, no. 5, pp. 462–468, 2014, doi: 10.1002/ente.201300186.

Chapter 8

8. Conclusion and future work suggestions

8.1 Conclusion

This thesis is focused on THz energy harvesting applications using nano-rectenna devices as an alternative technology to the conventional photovoltaic solar cells. The main goal of this study was to model, fabricate and characterise MIM tunnel diodes for optimising these structures to efficiently work at 28.3 THz frequency.

In this scope, three novel contributions were provided as the outcome of this thesis. As the first novel contribution, an extensive physical (VASE and XPS) and electrical (I-V) characterisation study was conducted on different oxides including TiO_2, ZnO and NiO to find their physical parameters and reliably assess their performance in the fabricated devices. Majority of research studies use the wide range of reported physical values (such as E_g and χ) of these materials in the literature. However, it is critical to experimentally measure these values to understand the rectification behaviour of the fabricated devices, and hence to have a repeatable process.

Initially, a demonstration of point-by-point VASE analysis was also done on thermal SiO_2/Si wafers produced by Nexperia semiconductor company using various oxidation techniques with the aim of developing gate oxides for Si power MOSFETs. The purpose of this analysis was to observe any sub-band gap defects in the oxides and their effect on the electrical characteristics of the devices to have a better understanding of the gate oxide characteristics. Additional mapping analysis was also carried out on the SiO_2 on Si wafers to observe the film uniformity prior to point-by-point analysis. It was seen that the SiO_2 layers grown with different oxidation methods have a good surface uniformity with a maximum of 0.3 nm variation in thickness. Then, a sub-band gap ε_2 peak at 1.3 eV was observed in the point-by-point analysis which was associated with the O_2 vacancies in the SiO_2. At 2.9 eV, another sub-peak was observed and found to be as intrinsic to the interface which is explained by the optical transitions associated with negatively charged O_2 vacancies in the SiO_2 layer. Two other peaks at 3.4, 4.3 eV were referred to the critical points of Si due to absorption in the substrate. It has been observed that the identification of these defects in the oxide layers contributes to the explanation of the instabilities caused by variations in the trapped charges in the gate-oxide, as well as the emergence of interface states.

Further VASE analysis was carried out on the RF sputtered TiO_2, ZnO, and NiO to find their thickness, optical constants (*n*, *k*) and the band gap (E_g). The E_g values of these oxides were found to be 3.32 eV for TiO_2, 3.25 eV for ZnO, and 2.75 eV for NiO using the Tauc plots. Additional VASE measurements were also done on plasma-enhanced (PE) and thermal ALD TiO_2 thin films prepared by AMO, Germany which are utilised as the insulating layer in the fabrication of 1D metal-insulator-graphene (MIG) diodes. A E_g of 3.50 eV was obtained for the PE-ALD TiO_2 on metal sample. However, the MSE value for the fitting of this sample was high at ~11. On the other hand, for the PE-ALD TiO_2 on Si and thermal ALD TiO_2 on metal samples, the E_g values were found to be 3.38 eV and 3.39 eV, respectively which are closer to the E_g of the RF sputtered TiO_2 film.

An elemental XPS analysis was also done on the oxide films to find their stoichiometry. The metal:oxygen ratios of TiO_2, ZnO, and NiO were calculated as 0.506:1, 1.367:1 and 1.425:1, respectively which results in $TiO_{1.98}$, $ZnO_{0.73}$ and $NiO_{0.70}$. The electron affinity, χ values of TiO_2, ZnO, and NiO were determined to be 3.56 eV, 3.46 eV, and 2.05 eV, respectively from the XPS results. Based on the XPS and VASE results, the full band alignment of RF sputtered $TiO_{1.98}$, $ZnO_{0.73}$, and $NiO_{0.70}$ was also determined. These results were further correlated with the χ values found from an Folwer-Nordheim (FNT) analysis on the associated reference devices. The barrier heights between the Al/TiO_2, Al/ZnO and Al/NiO were extracted as 0.62 eV, 0.56 eV and 1.82 eV considering the Al work function of 4.28 eV. Therefore, the χ values were calculated as 3.66 eV for TiO_2, 3.72 eV for ZnO and 2.46 eV for NiO. Despite the fact that a deviation between the XPS and FNT values was observed with the decreasing stoichiometry of the oxides, the results were in close agreement. The obtained physical parameters (E_g and χ) were then used to model the I-V behaviour of the TiO_2, ZnO and NiO based MIM stacks and to compare with the experimental I-V results.

A conduction mechanism study was also done on 3 nm ALD deposited Au/Al_2O_3/Au and Au/Al_2O_3/Ti diodes to observe any possible defect related Poole-Frenkel (PF) or temperature dependent Schottky-emission (SE) transport in these devices. The dynamic permittivity (ε_r) value was derived from the PF and the SE plots of both diode configurations and then compared with the ε_r value found from the VASE measurements using the refractive index ($\varepsilon_r = n^2$). A large difference was observed between the ε_r values from the PF and SE plots compared to the VASE results (ε_r = 3.15) indicating that these two conduction mechanisms are not present in these devices. The FNT analysis could not be done on these devices due to the low breakdown voltage of > 1.5 V and relatively high barrier heights at the Au/Al_2O_3 (~3.5 eV) and Ti/Al_2O_3 (~2.5 eV). However, considering the absence of PF and SE mechanisms, as well as the ultra-thin (3 nm) ALD oxide layer, the conduction is most likely due to the direct tunnelling (DT) mechanism.

The second contribution is improving the rectification performance of tunnel rectifiers by engineering the MI^nM diode structures. To do this, shadow mask evaporation, ALD and RF sputtering processes were used to fabricate variety of single (MIM) and triple (MI^3M) insulator diodes having 10^4 μm^2 device area with the aim of investigating different metal/oxide combinations. Therefore, enhanced rectification performance in terms of device asymmetry (η), non-linearity (f_{NL}), zero-bias responsivity (β_0) and dynamic resistance (R_0) was targeted. The experimental results showed that using dissimilar metal electrodes such as Au/Ti and Au/Zn exhibits higher η and β_0, as well as ~1 order of magnitude lower R_0. A peak η of 1.7 at 0.25 V and a β_0 of 1.60 A/W with 5.1 MΩ were obtained using Au/Al_2O_3/Zn diode configuration. Besides this, it has been demonstrated that lowering the metal/oxide barrier height with the use of ZnO based diodes dramatically reduces the R_0 and consequently improve the coupling efficiency (η_c). The Au/ZnO/Au diode exhibited 540 Ω R_0 which is ~5 orders of magnitude lower than the R_0 of Au/Al_2O_3/Au device having the same oxide thickness due to the difference between the electron affinity values of ZnO (χ = 3.7 eV) and Al_2O_3 (χ = 1.6 eV). This made the ZnO one of the promising oxides in this study.

It was also shown that triple insulator MI^3M rectifiers exhibit better rectification performance (β, η, f_{NL}) than single insulator M_1IM_2 diodes. The effect of RT in triple insulator layers was demonstrated by detailed electrical characterisation and theoretical simulations. This was achieved using a cascaded $Ta_2O_5/Nb_2O_5/Al_2O_3$ diode with a nominal thickness ratio of 1/3/1 and two non-cascaded $Ta_2O_5/Nb_2O_5/Al_2O_3$ diodes with different thickness ratios as 1/3/1 and 1.5/2.5/1. All three structures had a total thickness of 5 nm. A change in curvature and a substantial increase in current on the I-V curve was used to identify the RT. It was observed that the RT is more dominant at lower voltages (~0.35 V) for the non-cascaded MI^{3}M device compared to the cascaded (~ 1 V). At higher voltages over 1 V, the RT has a significant impact on increasing the forward current and consequently the asymmetry up to ~120. The cascaded MI^{3}M structure showed the highest zero-bias responsivity of -3.7 A/W and the largest low voltage asymmetry of 6 at 0.1 V. This can be ascribed to the dominance of direct and Fowler-Nordheim tunnelling in current transportation. This is the first demonstration of extremely enhanced device responsivity and asymmetry using triple insulator MI^{3}M diode structures. The results open the way for further optimisation of triple insulator designs with the use of different metal electrodes ($M_1I^3M_2$) and reduced barrier heights, despite the fact that the dynamic resistances are too high for integration with the antenna component of the rectenna.

As a final novel contribution; TiO_2, ZnO and NiO based diodes were fabricated by photolithography and characterised by DC I-V measurements with the aim of observing the effect of device scaling on the rectification performance, particularly on the coupling efficiency at 28.3 THz frequency. It was seen that a CrAu/7 nm NiO/CrAu diode with 1 μm^2 device area has 461.0 kΩ R_0 which results in a projected coupling efficiency of η_c = 1.5×10^{-5} %. On the other hand, the η_c was calculated to be 1.7×10^{-7} % for CrAu/5 nm NiO/CrAu diode (based on 5.6 kΩ R_0) despite the relatively thinner oxide layer with a larger area (64 μm^2), which is ~2 orders of magnitude lower. The findings also demonstrate that NiO has a low electron affinity of 2.1–2.5 eV, which correlates with a high R_0 of ~500 kΩ for 1 μm^2 device area, making it questionable for use in a rectenna device. On the other hand, diodes made of TiO_2 and ZnO films have exhibited a better performance. The Au/2.6 nm ZnO/Cr diode, scaled down to a 1 μm^2 device area, had the highest rectification performance in terms of zero-bias dynamic resistance (R_0 = 71 kΩ), responsivity (β_0 =0.28 A/W), and coupling efficiency (η_c = 2.4 × 10^{-5} %), that is ~ 6 orders of magnitude higher than the previously demonstrated ZnO based devices for rectification at 28.3 THz.

Our simulation results have shown that the η_c of ZnO and TiO_2 based MIM diodes can be enhanced up to ~5% with the further modifications such as scaling down the device area to nm scale, modifying the growth conditions to increase the electron affinity, reducing the oxide thickness and using metals with lower work functions such as Ti and Nb. These modifications are also applicable to the multiple insulator MI^{n}M diodes where the resonant tunnelling mechanism is dominant. In this way, the η_c can be increased by more than 10 %, consequently the overall rectenna efficiency can be improved and competitive to current solar cell technology.

The low power coupling efficiency due to the inefficient diode structures continues to be the obstacle for producing MIM based THz rectennas. This underpins the need for more research into oxide thin films to develop a more reliable and repeatable processing method for rectenna technology. This thesis is a step towards the development of more efficient THz rectifiers.

8.2 A proposed solution for high efficiency THz rectifiers as future suggestion

The best performing rectenna devices made by using the photomask explained in section 4.2.1 were tested with an optical setup having an IWR1843 single chip radar with a 76-81 GHz radiation source attached. The source was aligned above the device under test on an optical bench with the suitable apparatus. An optic lens was used to converge the signal and focus on the rectenna. An optical chopper connected to a lock-in amplifier was placed between the lens and the sample to modulate the reference signal.

However, no output signal was detected for the tested samples. There could be several reasons behind this unsuccessful attempt. One of them is that the radiation source was not ideal for such an optical experiment since it was mainly developed to work as a radar by sending the radiation to an object and detecting the reflected signal. Therefore, the power of the signal was low for harvesting into DC current. However, the main issue was the efficiency of the fabricated rectenna devices. As mentioned in the previous sections, the fabricated device area was large (minimum 1 μm^2) which limits the coupling efficiency of the devices.

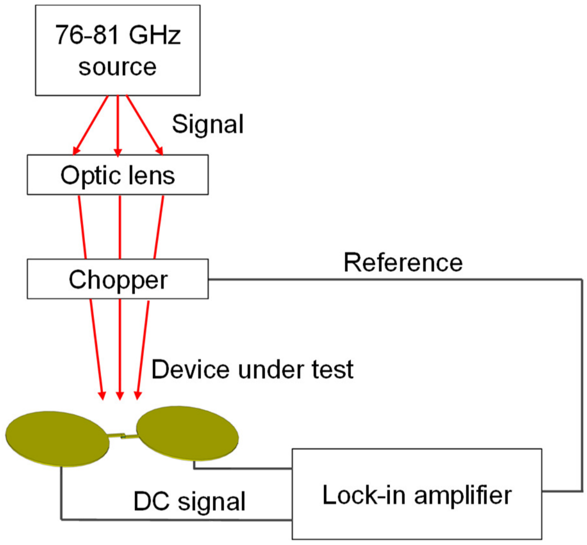

Figure 8.1. Schematics of a custom optical setup for testing rectenna devices.

In order to overcome this limitation, a new fabrication process is proposed for fabricating nm scale device areas using thermal scanning probe nanolithography tool called NanoFrazor that is available at University of Liverpool, Chemistry Department. This is an alternative way to other nanofabrication techniques (such as e-beam or nanoimprint lithography) as explained in section 2.3.1.3 (Refs. 97,98) and has the capability of patterning < 30 nm features.

The process flow of the proposed structure is shown in Fig. 8.2. The suggested rectenna array is made up of 12 linked, grid-like rectenna components, each made up of a MIM rectifier and a circular patch antenna. 300 nm thick SiO_2 on Si will be used as the substrate materials to ensure proper isolation and the uniformity of the device which is shown in the first step of the process flow chart. This will be followed by patterning and deposition of bottom circular patch metal and lift-off by conventional photolithography tool with a single layer positive photoresist and the deposition equipment.

Then, the antenna arms will be fabricated via the NanoFrazor tool with a bilayer lift-off (BLO) process. In the BLO process, the sample is first spin-coated with two polymer layers those are a lift-off resist and a thermal resist Polyphthalaldehyde (PPA). The NanoFrazor is then used to pattern the desired geometry into the PPA layer. After that, wet chemistry is used to develop the lift-off resist by immersing the sample in PMGI (*polydimethylglutarimide*) and IPA solution.

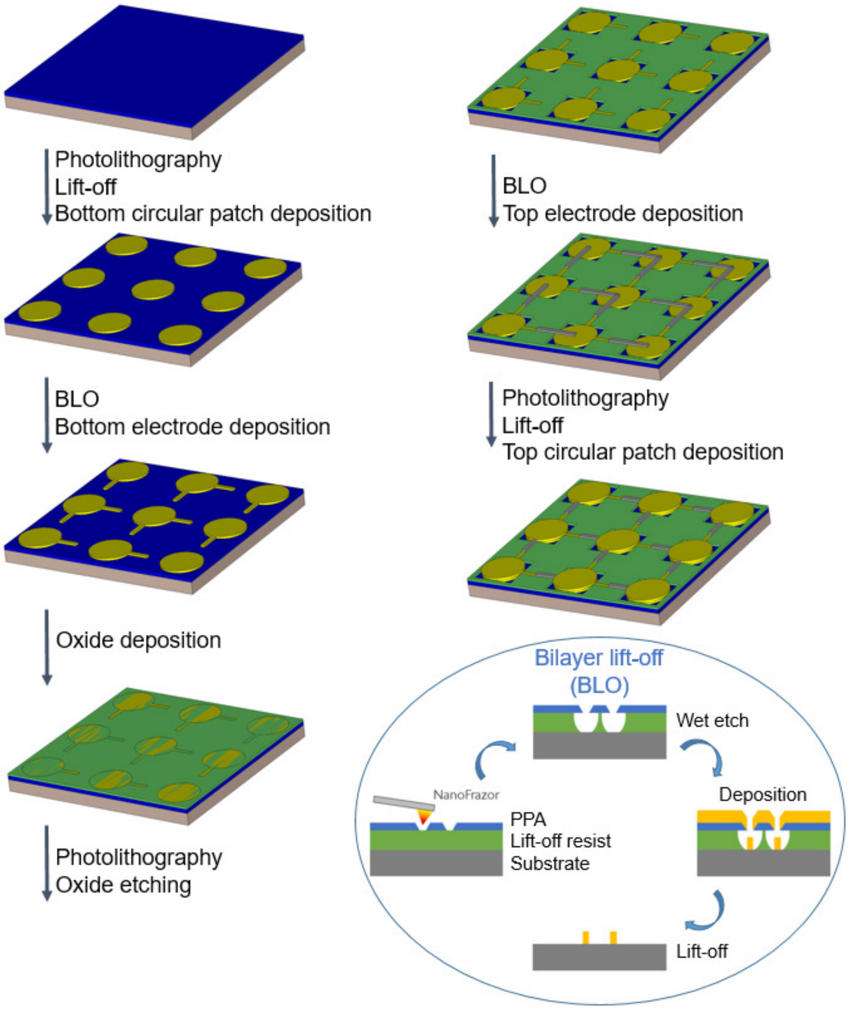

Figure 8.2. The process flow for patterning rectenna arrays using a combination of photolithography and thermal scanning probe lithography processes.

An undercut profile forms during the isotropic etching process. Then, the bottom metal layer is deposited. The lift-off resist and PPA are finally washed away together with the undesired sections of the deposited metal layer by immersing the sample in an NMP (N-Methyl-2-pyrrolidone) solvent. Hence, the geometry patterned in the PPA layer is transferred in the deposited material.

After the BLO, the oxides will be deposited via sputtering or ALD processes and then etched to have the electrical connection between the overlapping bottom and top circular patches. After the etching, the top antenna arms will be fabricated by following the same BLO steps and the device will be finalised with a last photolithography step and deposition of the top circular patches. The fabrication process can be modified by redesigning the microstrip antenna patches depending on the frequency of the input radiation.

In summary, by scaling down the devices into nm scale and engineering the tunnel barriers, it is aimed to increase the rectification efficiency (η_j) of the diodes including the responsivity, asymmetry and non-linearity parameters while decreasing the dynamic resistance to improve the coupling efficiency (η_c) at the same time.

On the other hand, it is also aimed to improve the coupling efficiency of the incident electromagnetic radiation (η_a) to the receiving antenna and the efficiency of the collected energy in the diode-antenna junction (η_s) with the designed circular patches explained in section 3.4. Single (1 × 2) rectenna structure can be used as a proof-of-concept for the circular patch rectennas, and it is expected to increase the overall conversion efficiency (η) further with the 3×3 array structure.